Stability Characteristics of Counter-Rotating Vortex Pairs
in the Wakes of Triangular-Flapped Airfoils

by

Jason Marc Ortega

B.S. (University of California, Berkeley) 1995
M.S. (University of California, Berkeley) 1998

A dissertation submitted in partial satisfaction of the

requirements for the degree of

Doctor of Philosophy

in

Engineering-Mechanical Engineering

in the

GRADUATE DIVISION

of the

UNIVERSITY of CALIFORNIA at BERKELEY

Committee in charge:

Professor Ömer Savaş, Chair
Professor Stanley Berger
Professor Alexandre Chorin

Spring 2001

The dissertation of Jason Marc Ortega is approved:

Chair   Date

                                                                                          Date

---
                                                                                          Date

University of California at Berkeley

2001

Stability Characteristics of Counter-Rotating Vortex Pairs

in the Wakes of Triangular-Flapped Airfoils

by

Jason Marc Ortega

Abstract

Stability Characteristics of Counter-Rotating Vortex Pairs

in the Wakes of Triangular-Flapped Airfoils

by

Jason Marc Ortega

Doctor of Philosophy in Engineering-Mechanical Engineering

University of California at Berkeley

Professor Ömer Savaş, Chair

A rapidly growing instability is observed to develop between unequal strength, counter-rotating vortex pairs in the wakes of airfoils with outboard triangular flaps. To investigate the physical mechanisms for this instability, a linear stability analysis is performed on a single vortex pair. This analytical model reveals that the instability is driven by the strain rate field from one vortex acting on the perturbations of its neighboring vortex. Another linear stability analysis is conducted to include the effects of the other counter-rotating vortex pair. The qualitative features of the instability, such as its wavelength and non-linear evolution, are examined by flow visualization measurements that are made in a towing tank facility at a chord-based Reynolds number of $O(10^5)$. From these observations, a sinuous instability is seen to develop on the weaker flap vortices and have a wavelength of order one wingspan. The instability wavelengths that are observed in the flow visualization data compare favorably with those predicted by the two- and four- vortex linear stability analyses, demonstrating that the analytical models capture the essential physics of the instability growth. Quantitative measurements of the vortex wakes are made with a PIV technique, allowing the vortex structure, trajectories, kinetic energy, and distribution to be assessed up to several hundred wingspans downstream of the airfoils. Additionally, the circulation-based Reynolds number is seen to be of $O(10^5)$. The PIV data indicate that the wake's two-dimensional kinetic energy decreases substantially as the instability transforms the two-dimensional nature of the wake into a three-dimensional one. Finally, the wake alleviation

properties of this instability are measured by computing the maximum rolling moment and downwash that a following wing might experience if it were placed in the wakes of these airfoils. These calculations show that by 75 wingspans, the wakes of the triangular-flapped airfoils have rolling moments and downwash that are always less than those of a conventional rectangular airfoil. This rapid reduction in the rolling moment and downwash leads to the conclusion that this instability between unequal strength, counter-rotating vortex pairs has the potential to solve the wake hazard problem.

_____

Ömer Savaş   Date

Contents

List of Tables

List of Figures

List of Symbols

50%c TF $=$		50%c triangular-flapped airfoil
75%c TF $=$		75%c triangular-flapped airfoil
$a =$		core radius of a Rankine vortex
A1, A2 $=$		anti- symmetric instability mode shapes for a four-vortex analysis
$b =$		span of the airfoil
$b^* =$		distance between the circulation centroids of two vortex pairs
$b_o^* =$		initial distance between the circulation centroids of two vortex pairs
$b_f =$		span of the following wing
$c =$		airfoil chord length
$c.c.(t) =$		average correlation coefficient from aLPT
$C_{l\alpha} =$		two-dimensional lift-curve slope
$Ci(x) =$		integral cosine
$d =$		separation distance between the vortices in a single vortex pair
$d\mathbf{L} =$		line increment directed along a vortex
$d_o =$		initial separation distance between the vortices in a single vortex pair
$D(y, z) =$		average downwash on a following wing of span, b_f
$D(t) =$		$min(D(x(t), y, z))$
$h =$		vertical vanishing point location
$h_o =$		streamwise offset of the Kodak camera from the light sheet
$high =$		upper cut-off parameter for image brightening
$k =$		perturbation wavenumber in the axial direction
$k_e =$		aLPT cut-off frequency
K.E. $=$		vortex kinetic energy
$l =$		horizontal vanishing point location
$low =$		lower cut-off parameter for image brightening
$m =$		perturbation wavenumber in the azimuthal direction
ML $=$		measuring line
$p =$		brightened pixel intensity
$p_o =$		original pixel intensity
ps $=$		port-side

$q =$ dimensional growth rate for a single vortex pair
$r_{ci} =$ distance from the circulation centroid to the perturbed location of vortex i
$r_{eff} =$ effective core size of a vortex
$r_{max} =$ radial location of maximum azimuthal velocity for a Lamb-Oseen vortex
$r_{n2p} =$ distance from vortex n to the perturbed location of vortex 2
$r_o =$ distance of the Kodak camera from the right-side of the measurement plane
$\hat{\mathbf{r}} =$ displacement eigenvector with components $(\hat{y}, \hat{z})$
$R(y,z) =$ average rolling moment on a following wing of span, b_f
$R(t) =$ $max|R(x(t),y,z)|$
$\mathbf{R} =$ distance between points on vortices
$s =$ position of an unperturbed vortex along the $\mathbf{e}_y$ direction
S1, S2 $=$ symmetric instability mode shapes for a four-vortex analysis
SP $=$ station point
ss $=$ starboard-side
$t =$ time variable
$u =$ axial velocity component
$U =$ velocity of a following wing
$u_\theta(r) =$ azimuthal velocity of a Lamb-Oseen vortex
$u_{\theta max} =$ maximum azimuthal velocity
$U_o =$ airfoil speed
$v =$ lateral velocity component
$v_{rel} =$ radial velocity of a vortex relative to a circulation centroid
$\mathbf{v}_c =$ velocity of the circulation centroids in a four-vortex analysis
$V_o =$ characteristic descent velocity of a vortex wake, $\Gamma_o/(2\pi b^*)$
VP $=$ vanishing point
$w =$ vertical velocity component
$w_o =$ lateral offset of the Kodak camera from the measurement plane
$x =$ axial direction in the vortex wake
$x(t)/b =$ downstream distance from the airfoil, $x(t) = U_o t$
$y =$ lateral direction in the vortex wake
$y_c =$ location of the circulation centroid for a single vortex pair, $\Gamma_1 d/(\Gamma_1 + \Gamma_2)$
$\mathbf{y}_c =$ vorticity centroid, (y_c, z_c)
$y_r =$ lateral circulation centroid location of the right-side vortex pair
$(\bar{y}, \bar{z}) =$ pixel location in the distorted camera view
$(y_i, z_i) =$ location of vortex i in a four-vortex analysis
$(y', z') =$ coordinate system that rotates with vortex 2 in the four-vortex analysis
$z =$ vertical direction in the vortex wake
$z_r =$ vertical circulation centroid location of the right-side vortex pair

Greek Characters

$$
\begin{aligned}
\alpha =&\ \text{dimensionless growth rate, } \tfrac{2\pi d^2}{\Gamma_2}q, \text{ for a single vortex pair; angle of attack} \\
\chi =&\ \text{mutual induction fuction} \\
\Delta t =&\ \text{time step of numerical integration} \\
\epsilon =&\ \text{vortex cut-off diameter} \\
\gamma =&\ \text{instability growth rate of the four-vortex analysis} \\
\gamma_e =&\ \text{Eulers constant, } 0.577721... \\
(\eta_n, \xi_n) =&\ \text{perturbations to vortex } n \text{ in the four-vortex analysis} \\
\Gamma =&\ \text{circulation strength ratio of the vortices in a single vortex pair;} \\
&\ \Gamma = \Gamma_1/\Gamma_2 \text{ or } \Gamma = \bar{\Gamma}_{of}/\bar{\Gamma}_{ot} \\
\Gamma_i =&\ \text{circulation stength of vortex } i \\
\Gamma_i =&\ \text{dimensionless vortex strength} \\
\Gamma_o =&\ \text{circulation strength of a vortex} \\
\Gamma(r) =&\ \text{circulation distribution of a Lamb-Oseen Vortex, } \Gamma_o(1 - e^{-r^2/\sigma^2}) \\
(\eta_n, \xi_n) =&\ \text{perturbations to vortex } n \text{ in a coordinate system that rotates with vortex } n \\
\kappa =&\ \text{non-linearity parameter for image brightening} \\
\lambda =&\ \text{instability wavelength} \\
\nu =&\ \text{kinematic viscosity} \\
\rho =&\ \text{fluid density} \\
\sigma =&\ \text{Lamb-Oseen vortex core size} \\
\tau =&\ \text{orbit period of a single vortex pair in a four-vortex analysis} \\
\tau_{single} =&\ \text{orbit period of a single, isolated vortex pair separated by a distance } d \\
\varpi =&\ \text{self-induced rotation rate given by the cut-off diameter model} \\
\bar{\varpi} =&\ \text{dimensional Kelvin/Saffman vortex self-induced rotation rate} \\
\varpi =&\ \text{dimensionless Kelvin/Saffman vortex self-induced rotation rate} \\
\varpi^* =&\ \text{dimensionless self-induced rotation rate, } \varpi d^2/a^2 \\
\omega =&\ \text{vorticity, } \nabla \times \mathbf{u} \\
\omega_{max} =&\ \text{maximum vorticity of a Lamb-Oseen vorticity profile} \\
\omega(r) =&\ \text{vorticity profile of a Lamb-Oseen vortex} \\
\Omega_o =&\ \text{rotational velocity of a single vortex pair, } (\Gamma_1 + \Gamma_2)/(2\pi d^2) \\
\Omega(t) =&\ \text{unsteady, rotational velocity of a single vortex pair in a four-vortex analysis} \\
\Omega_{rel} =&\ \text{angular velocity of a vortex relative to a circulation centroid} \\
\psi =&\ \text{mutual induction function} \\
\Psi_{rot} =&\ \text{streamfunction for solid-body rotation} \\
\Psi_{n2p} =&\ \text{streamfunction of vortex } n \text{ at the perturbed location of vortex 2} \\
\Psi_{rel} =&\ \text{streamfunction for the motion of vortex 2 relative to the right-side} \\
&\ \text{circulation centroid} \\
\Psi_c =&\ \text{streamfunction due to the downward velocity, } w_c(t), \text{ of a four-vortex system}
\end{aligned}
$$

Chapter 1

Introduction

The trailing vortex system in the wake of an airplane is a result of the lift generated by its finite-span airfoil. As the wing passes through the atmosphere, the high pressure fluid that exists beneath it travels outwardly and the low pressure fluid above it, inwardly. Combined with the free stream velocity, the resulting flow produces a sheet of swirling motion along the airfoil such as that in Figure 1.1. Within a few chord lengths downstream of the airfoil, the sheet rolls up into two distinct vortices, which rotate in opposite directions. At larger downstream distances, the trailing vortices continue to persist and, under the proper atmospheric conditions, can be seen behind an airplane when they entrain water vapor from the jet-engine exhaust (Figure 1.2). Typically, the trailing vortices decay by means of the Crow instability (Figure 1.3) [17]. This instability leads to sinusoidal perturbations along the lengths of the vortices and eventually causes them to link into closed vortex loops. The Crow instability requires several hundred wingspans to occur, allowing the vortices to exist several miles downstream of the airplane. It is this long life of the vortices that causes the wake hazard problem.

An airplane flying in the vortex wake of another airplane can experience motions anywhere from sudden upwash to downwash to rolling, depending on the airplane's orientation with respect to the wake. Near the ground, this can be especially dangerous, as the pilot has less time to recover from rapid changes in the airplane's attitude. This hazard is
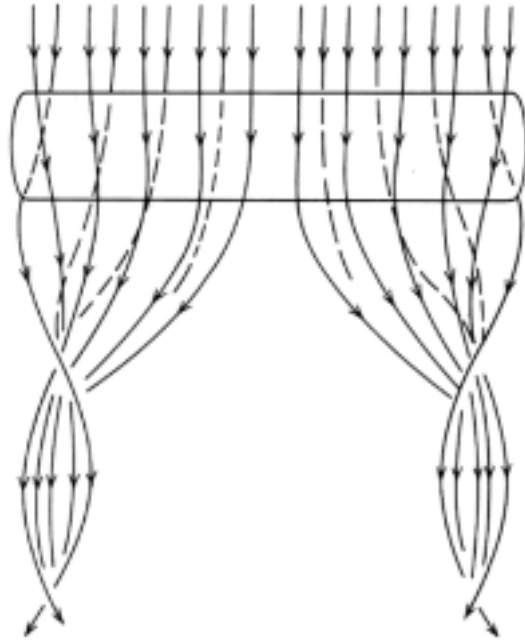
Figure 1.1: Vortex system in the wake of a finite aspect ratio wing [33]

further intensified at airports, where airplanes are continually landing and taking off in the vortex wakes of other airplanes. To deal with this wake vortex hazard, the Federal Aviation Administration (FAA) regulates the separation distances between successive airline flights, which presumably allows the following aircraft to avoid the previously generated vortices. To account for the fact that the vortices behave differently under various atmospheric conditions, these separation distances are often overly conservative, resulting in unnecessary flight delays and the associated costs to the public and airline companies. Consequently, there is an increasing need to develop a means of tracking or eliminating the trailing vortices. Unfortunately, the technology to precisely track or predict the location of the vortices under all weather conditions is currently unavailable. As a result, a considerable amount of research has been directed towards eliminating the trailing vortex hazard by modifying the airplane that generates them.

In the 1970's, NASA designed and tested a host of concepts and devices that were

Figure 1.2: Trailing vortices visible in the wake of a 747 airliner.
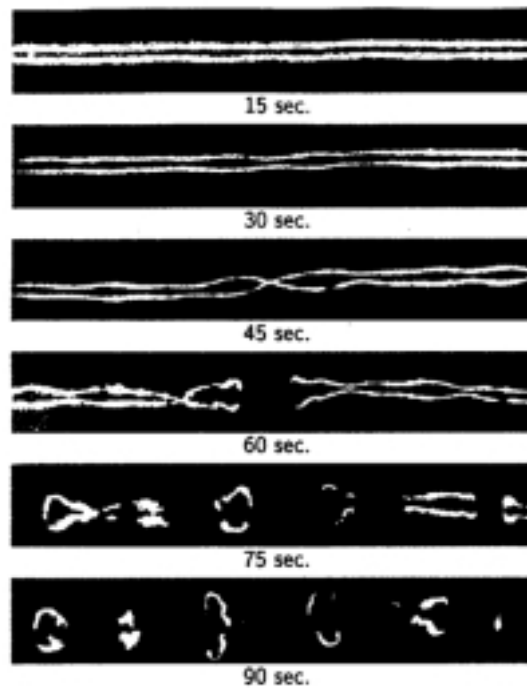
Figure 1.3: Crow instability in the wake of an aircraft. The numbers beneath each image indicate the number of seconds since the aircraft flew over [17].

intended to alleviate the wake hazard. Some of these designs, such as splines or wing-tip mounted engines [20, 21, 36, 37], were intended to force large amounts of turbulence into the vortices. The idea was that the additional turbulence would cause the vortices to break apart more quickly. Other concepts functioned by modifying the lift distribution of the wing in order to achieve a safer wake. Rossow [44] describes two such lift distributions: a saw-tooth wing loading and a tailored wing loading. Using the Betz roll-up theory, which relates the span loading to the rolled-up vortex structure, Rossow discovered that a saw-tooth wing loading leads to a vortex sheet that theoretically translates downward as a single unit with no concentrated vortices. Additionally, a tailored wing loading was shown to yield two tip vortices that rotate as rigid bodies. Other wake alleviation designs operated in an active manner and included such concepts as small, pulsatile jets located at the wingtips and spoilers or flaps that were periodically deployed in flight [21]. These devices were intended to pre-maturely excite the Crow instability and rapidly cause the linking of the oppositely-signed tip vortices. A final group of concepts are those that operated in a passive manner. Some of these ideas included wing-tip fences, control vortices, and wing-tip turning vanes [21, 36]. In spite of the large number of designs that were tested, none of them were implemented as a solution to wake hazard problem. Simply put, some of the concepts did not effectively reduce the wake hazard and for those that did, the price in airplane performance was too great to make them practical for every day use.

More recently, a few concepts have emerged as potential means to control the vortex wake. In 2000, Boeing went public with a design [5] that actively eliminates the wake hazard. By periodically oscillating the outer ailerons and spoilers, an instability is driven that destroys the inner and outer vortices on each wing. A similar idea was also demonstrated with numerical simulations in [43]. Another concept for reducing the intensity of wake vortices is based upon an application for military submarines. The research in [39, 40, 41, 42] over the past few years has been directed towards an idea called "vortex leveraging." This concept works by placing shape memory alloy (SMA) control surfaces on the submarine's sailplanes and periodically oscillating them. The control vortices generated by these surfaces interact with the sailplane vortices, causing an instability to rapidly occur. Though several

numerical simulations have been presented, experimental verification does not appear to be available in the open literature.

The third concept is the topic of the present work. In reviewing the wake alleviation devices that had been tested in the past, the author realized that one means of disrupting the coherence of the vortex wake is to render it three-dimensional. As long as the vortices remain parallel, they behave in a nearly two-dimensional fashion, which takes a relatively long time to decay. Perhaps, a robust means to bring about rapid changes in the wake would be to utilize control vortices in a passive fashion. The advantage of the control vortices is that they can be generated to contain a comparable amount of energy to that of the tip vortices. Consequently, the control vortices can effectively alter the behavior of the tip vortices. This was observed in previous towing tank studies [7, 9], which investigated the merger characteristics of co-rotating vortex pairs in the wakes of airfoils. By introducing flap vortices near the tip vortices, the trajectories of the tip vortices were altered so that they no longer descended in a near vertical manner, but orbited about the flap vortices in a helical fashion until the vortices merged. It was observed in these experiments that the closer the flap and tip vortices were to one another, the more quickly they merged. Since the merged vortices were just as coherent as the original flap and tip vortices, there was not much reduction in the wake hazard. In considering these results, the question then arose as to what would happen if oppositely-signed control vortices were utilized instead? Perhaps, by placing these control vortices close to the tip vortices, an instability between them would occur, transforming the two-dimensional nature of the wake into a three-dimensional one. Furthermore, the passive nature of such a concept would make it that much simpler to design and straightforward to test. Bilanin *et al.* [3] had already studied the wake of a similar type of airfoil. However, the short wind tunnel test section used in their investigation prevented their measurements from being made in the far wake of the airfoil.

During May 1999, several 15 cm spans airfoils were constructed to investigate the above idea. A set of preliminary experiments were conducted in a small-scale towing tank (1.8 m × 0.6 m × 0.6 m) in the U.C. Berkeley Fluid Mechanics Laboratory. Flow visualization of the vortex wakes was achieved by illuminating a cross-section of the seeded tank

with a light sheet and filming particle streaks with a video camera. Of all the 15 cm span airfoils that were investigated, one in particular (Figure 1.4) had a vortex wake that demonstrated three-dimensional characteristics most quickly. The oppositely-signed flap vortices interacted with the tip vortices, giving rise to a sudden out-of-plane flow. Because the flow was illuminated at only one vertical cross-section, it was difficult to determine exactly what was occurring in the vortex wake. To validate these results and better understand the flow physics, further flow visualization experiments [35] (see Appendix A) were performed at the U.C. Berkeley Richmond Field Station Towing Tank Facility in June 1999. For these tests, a larger, 40 cm span, similarly-shaped airfoil was towed down the length of the tank. Improved flow visualization was achieved by painting florescent dye on the upper surface of the flaps and wing tips. The test section of the towing tank was volumetrically illuminated by a CW laser. The results of these experiments revealed that the two, counter-rotating flap/tip vortex pairs undergo a rapidly growing instability within 50 spans downstream of the airfoil. Qualitatively, the vortex wake appears somewhat similar to Figures 17 of [14] and Figure 4 of [40] and, possibly, is being driven by the same instability mechanism.
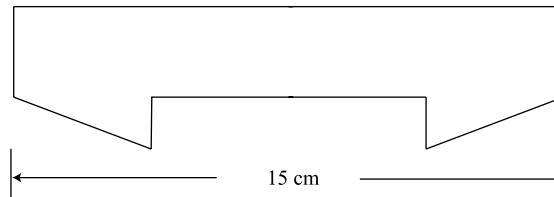
Figure 1.4: The airfoil that generated a wake with a rapidly growing instability.

With the observations of this rapidly growing instability, further research was conducted to better understand it. The purpose of this current work is to present the results of this research. As is often the case in fluid mechanics, the theoretical explanations for this instability came after the initial experimental observations. Chapter 2 discusses the fundamental physics of what causes this instability by comparing the stability properties

of counter- and co-rotating vortex pairs. Chapter 3 presents a linear stability analysis for two vortex pairs and determines the effects that the additional pair has on the stability properties of the original counter- and co-rotating pairs. In Chapter 4 the results of a more refined flow visualization experiment are discussed. Features of the instability, such as non-linear behavior, are presented. Chapter 5 discusses the PIV measurements that were made in the wakes of airfoils with triangular flaps. The data from these experiments provide a quantitative assessment of the circulation strengths of the vortices, their kinetic energy, internal structure, and trajectories up to several hundred spans downstream from the airfoils. Finally, in Chapter 6 the wake-alleviation properties of the triangular-flapped airfoils are discussed by comparing their wakes' rolling moment and downwash with those of a conventional, rectangular airfoil.

Chapter 2

Stability Characteristics of a Single Vortex Pair

2.1 Introduction

To begin analyzing the instability observed in the wake of the triangular-flapped airfoil, this chapter will consider the stability properties of a single flap/tip vortex pair. Although the following analyses neglect the effects of the other vortex pair, their simplicity highlights the underlying physics in a rather straightforward manner. For the sake of generality, the stability characteristics of both counter- and co-rotating vortex pairs will be discussed. In Section 2.2, a simplified stability model is presented to demonstrate how the rate of strain field and the vortex's self-induced rotation rate interact to bring about stability or instability to sinusoidal perturbations. In Section 2.3, a complete, linear stability analysis is performed on arbitrary strength counter- and co-rotating vortex pairs.

2.2 A Simplified Stability Model

The fundamental stability properties of a single counter-rotating or co-rotating vortex

pair can be explained through the use of a rather simple analytical model that is similar to that of Widnall *et al.* [50] . The vortex pair is represented by two infinitely long vortex filaments that are separated by a distance, d, and have strengths of Γ_1 and Γ_2 and equal core radii of a (Figures 2.1 and 2.2). For arbitrary Γ_1 and Γ_2, the centroid of the pair lies a distance $y_c = \Gamma_1 d/(\Gamma_1 + \Gamma_2)$ from vortex 2 and the two vortices orbit about this centroid at a constant angular velocity of $\Omega_o = (\Gamma_1 + \Gamma_2)/(2\pi d^2)$. The motion of the two vortices in this equilibrium state is steady and the vortices trace out circular paths as they orbit about their centroid. Let vortex 2 be sinusoidally displaced in the x-direction by a long-wavelength perturbation of wavenumber k. The (y, z) location of the perturbation is in a coordinate system that rotates with the unperturbed location of vortex 2. Regarding the stability of the perturbation, the question arises as to whether or not the disturbance amplitude, $r = \sqrt{y^2 + z^2}$, will grow or decay in time. To answer this question, it is necessary to determine how the rate of strain field at the perturbed position interacts with vortex 2's self-induced rotation rate, $\bar{\varpi}$. Sections 2.2.1 and 2.2.2 will discuss each of these effects individually. Sections 2.2.3 and 2.2.4 will describe how they work together to bring about stability or instability to counter- and co-rotating vortex pairs.
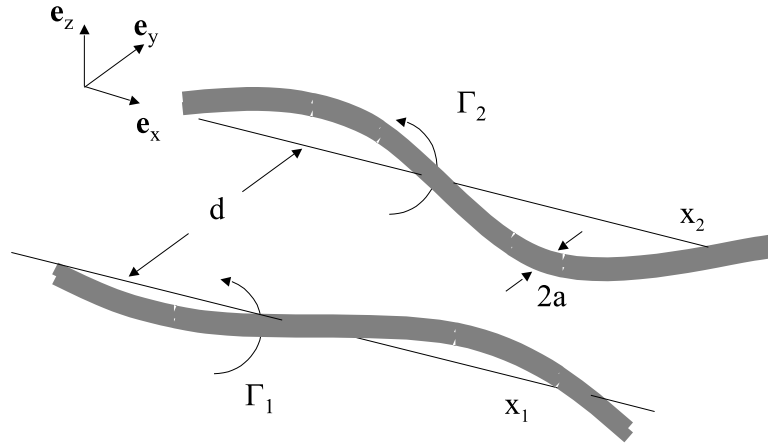
Figure 2.1: Schematic of a single vortex pair.
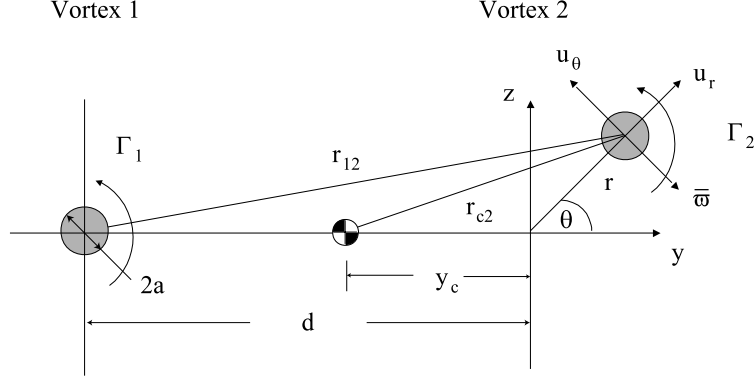
Figure 2.2: Cross-section of Figure 2.1 showing the perturbation of vortex 2 to the location (y, z). The (y, z) coordinate system is fixed with respect to the unperturbed position of vortex 2. Unlike Figure 2.1, vortex 1 is unperturbed in this view.

2.2.1 Rate of Strain Field

The rate of strain field at the perturbed location, (y, z), can be computed by considering the stream function of the flow. In the following calculations, it is assumed that vortex 1 is unperturbed, as shown in Figure 2.2. The streamfunction for vortex 1 is defined as

$$\Psi_1(y, z) = -\frac{\Gamma_1}{2\pi}ln(r_{12}) = -\frac{\Gamma_1}{2\pi}ln\sqrt{(y + d)^2 + z^2} \tag{2.1}$$

where r_{12} is the distance from vortex 1 to the perturbed location of vortex 2. The streamfunction, $\Psi_{rot}(y, z)$, for the rotating reference frame is given by

$$\Psi_{rot}(y, z) = -\frac{\Omega_o}{2}r_{c2}^2 = -\frac{\Omega_o}{2}[(y_c + y)^2 + z^2] \tag{2.2}$$

which is a solid body rotation about the circulation centroid. The variable r_{c2} is the distance from the centroid to the perturbed location of vortex 2. In a reference frame that rotates with the unperturbed position of vortex 2, the stream function of the flow is $\Psi = \Psi_1 - \Psi_{rot}$. The horizontal and vertical velocity components relative to this reference frame are given

by $(v, w) = (\frac{d\Psi}{dz}, -\frac{d\Psi}{dy})$. Performing the differentiation in this expression gives

$$v = \frac{z^3(\Gamma_1 + \Gamma_2) + y^2 z(\Gamma_1 + \Gamma_2) + 2yzd(\Gamma_1 + \Gamma_2) + \Gamma_2 z d^2}{2\pi d^2 [(y+d)^2 + z^2]} \tag{2.3}$$

$$w = \frac{-y^3(\Gamma_1 + \Gamma_2) - y^2 d(3\Gamma_1 + 2\Gamma_2) - yd^2(2\Gamma_1 + \Gamma_2) - \Gamma_1 z^2 d - yz^2(\Gamma_1 + \Gamma_2)}{2\pi d^2 [(y+d)^2 + z^2]} \tag{2.4}$$

Converting the velocity field to cylindrical coordinates, (r, θ), where $(y, z) = (r\cos\theta, r\sin\theta)$ and $(u_r, u_\theta) = (v\cos\theta + w\sin\theta, -v\sin\theta + w\cos\theta)$, yields,

$$u_r = \frac{-\Gamma_1(rd^2\sin 2\theta + r^2 d\sin\theta)}{2\pi d^2(r^2 + 2dr\cos\theta + d^2)} \tag{2.5}$$

$$u_\theta = \frac{-rd^2(\Gamma_2 + 2\Gamma_1 \cos^2\theta) - r^2 d\cos\theta(3\Gamma_1 + 2\Gamma_2) - r^3(\Gamma_1 + \Gamma_2)}{2\pi d^2(r^2 + 2dr\cos\theta + d^2)} \tag{2.6}$$

If it is assumed that the perturbation amplitude, r, is small $(r/d << 1)$, the velocity field in Eqs. 2.5 and 2.6 can be expressed in a more compact form,

$$u_r = -\frac{\Gamma_1}{2\pi d^2} r\sin 2\theta \tag{2.7}$$

$$u_\theta = -\frac{r(\Gamma_2 + 2\Gamma_1 \cos^2\theta)}{2\pi d^2} \tag{2.8}$$

The variable $\Gamma_1/(2\pi d^2)$ is the rate of strain on vortex 2 due to vortex 1. Because the equilibrium flow is steady, the streamlines given by Eqs. 2.7 and 2.8 are identical to the pathlines that a fluid element would follow in the flow.

2.2.2 Vortex Self-Induced Rotation Rate

The other important aspect of the simplified stability model is the self-induced rotation rate of vortex 2. To complete this simplified model, only the *direction* of rotation is needed. However, because the linear stability analysis that will be performed in Section 2.3 requires the quantitative values of the self-induced rotation rate, this section will analyze the self-induced rotation rate in its entirety.

Crow [17] analyzed the linear stability characteristics of equal strength, counter-rotating vortex pairs and utilized the expression

$$\frac{\Gamma}{2\pi}k^2\varpi(k\epsilon) = \frac{\Gamma}{2\pi}k^2\frac{1}{2}[(cos(k\epsilon)-1)/(k\epsilon)^2 + sin(k\epsilon)/(k\epsilon) - Ci(k\epsilon)] \tag{2.9}$$

for the self-induced rotation rate of a vortex. The variable ϵ is the vortex cut-off diameter. For a Rankine vortex, $\epsilon = 0.642a$. One problem with this self-induced rotation rate is that it becomes invalid for larger perturbation wavenumbers resulting in the spurious, high frequency modes plotted in the top graph of Crow's Figure 9. As a result, it is necessary to calculate an expression for the rotation rate that is valid for larger wavenumbers. Kelvin [26] originally accomplished this and, hence, the resulting instability, "Kelvin waves", bears his name. Saffman [47] also discusses this instability and, in the following paragraphs, his derivation will be followed.

Saffman computes a relationship for the rotation rate by performing a stability analysis on an isolated vortex, which has a uniform vorticity core with no axial flow. The radius of the vortex is taken to be a. The dispersion relationship that results is given by

$$\frac{1}{\eta a}\frac{J'_m(\eta a)}{J_m(\eta a)} = -\frac{K'_m(ka)}{kaK_m(ka)} - \frac{lm\sqrt{\eta^2+k^2}}{ka^2\eta^2} \tag{2.10}$$

where J_m are Bessel functions of the first kind and K_m are modified Bessel functions of the second kind. The variable m is the perturbation wavenumber in the azimuthal direction and k the perturbation wavenumber in the x-direction. The self-induced rotation rate is given by

$$\bar{\varpi} = \frac{\Gamma_i}{2\pi a^2}\varpi' = \frac{\Gamma_i}{2\pi a^2}\left(\frac{2kl}{\sqrt{\eta^2+k^2}} - m\right) \tag{2.11}$$

The variable $l = \pm 1$ determines whether or not the rotation direction is retrograde or co-grade. For $l = -1$, the angular velocity is co-grade and the perturbation rotates in a direction that is the same as that of the swirling flow about the vortex. For $l = 1$, the
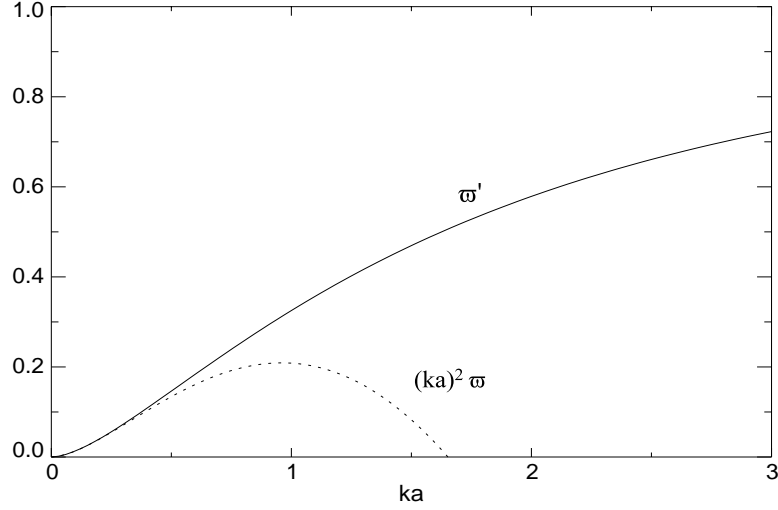
Figure 2.3: Comparison of the different self-induced rotation rates, ϖ (Eq. 2.9) and ϖ' (Eq. 2.11, $l = 1$), for of cylindrical vortex of core radius a. For large ka, $\varpi' \to 1$. Note that ϖ has been plotted as function of ka and not $k\epsilon$.

angular velocity is retrograde and the perturbation rotates in a direction opposite to that of the swirling flow about the vortex. The modes for which $m = 0$ are called "sausaging" modes because the disturbance is axisymmetric. When $m = 1$, the disturbance modes deform the axis of the vortex and are called bending modes. For $m \geq 2$, the disturbance is referred to as a "fluted" mode. In these instances, the cross-section of the vortex is deformed into an ellipse that rotates down the length of the vortex, giving the appearance of flutes. For computing the self-induced rotation rate, the bending modes that have $m = 1$ will be utilized. In order to solve for $\bar{\varpi}$ at a given value of ka, the dispersion relationship in Eq. 2.10 is first used to obtain the root, ηa. With this value of ηa, Eq. 2.11 can then be solved for $\bar{\varpi}$. As shown in Figure 12.1-3 of Saffman [47], there are an infinite number of roots to Eq. 2.10 for $l = \pm 1$. In the present analysis, only the lowest frequency roots are considered in the discussions to follow. Because there is no co-grade root for small ηa, the *retrograde* form of Eq. 2.11 is employed. The functional dependence of this lowest frequency, retrograde, bending mode is shown in Figure 2.3 along with that of Eq. 2.9. Figure 2.4 shows perspective and cross-sectional views of the this retrograde mode on a vortex filament. It can be seen in Figure 2.3 that $(ka)^2\varpi$ departs from the exact solution

as ka increases. When the self-induced rotation rate given by $(ka)^2\varpi$ becomes zero, the stability analysis misrepresents the true physics of the vortex.
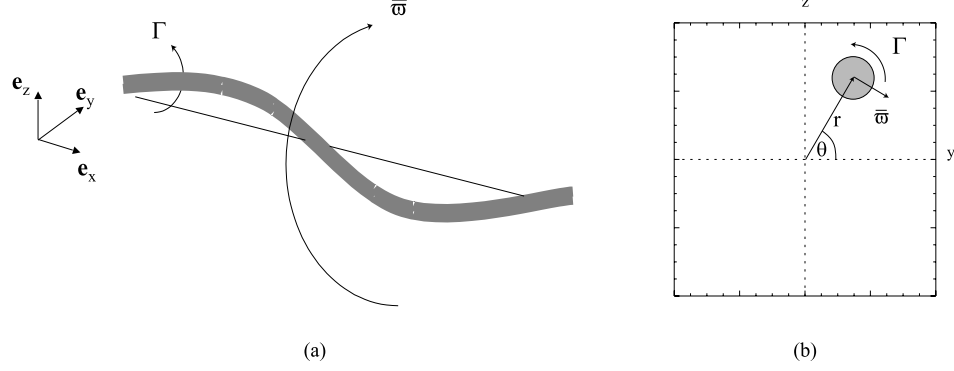
Figure 2.4: (a) Perspective and (b) cross-sectional views of the retrograde rotation rate, $\bar{\varpi}$, of a vortex filament.

2.2.3 Stability Characteristics of Counter-Rotating Pairs

With the rate of strain field, (u_r, u_θ), and the retrograde direction of the self-induced rotation rate, $\bar{\varpi}$, known, it is now possible to analyze the stability properties of single vortex pairs. For a counter-rotating pair $(\Gamma_1 < 0, \Gamma_2 > 0)$ that has circulation strengths of $|\Gamma_1| = O(|\Gamma_2|)$, the rate of strain field about vortex 2 generates a stagnation point flow as shown by the streamlines in Figure 2.5a. According to Eq. 2.8, the converging and diverging directions of the flow field, at which $u_\theta = 0$, occur at $\theta_o = cos^{-1}(\pm\sqrt{\frac{-\Gamma_2}{2\Gamma_1}})$. In some regions of the flow field, the azimuthal velocity and vortex 2's self-induced rotation rate are oriented in the same direction. In other regions, they are opposed to one another. If u_θ is equal and opposite to $\bar{\varpi}r$, vortex 2 becomes fixed at one orientation, θ_f, and diverges radially at a velocity of $u_r = -\Gamma_1 r sin2\theta_f/(2\pi d^2)$. The resulting perturbation amplitude grows exponentially as $r = r_o e^{\alpha t}$, where $\alpha = -\Gamma_1 sin2\theta_f/(2\pi d^2)$ and r_o is the initial perturbation amplitude. Therefore, vortex 2 is unstable to disturbances of this wavenumber, k. It can be seen in Eq. 2.8 that as the strength of vortex 1 is increased, the maximum azimuthal velocity about vortex 2 becomes more positive. As a result, u_θ balances only the larger

(a)   (b)
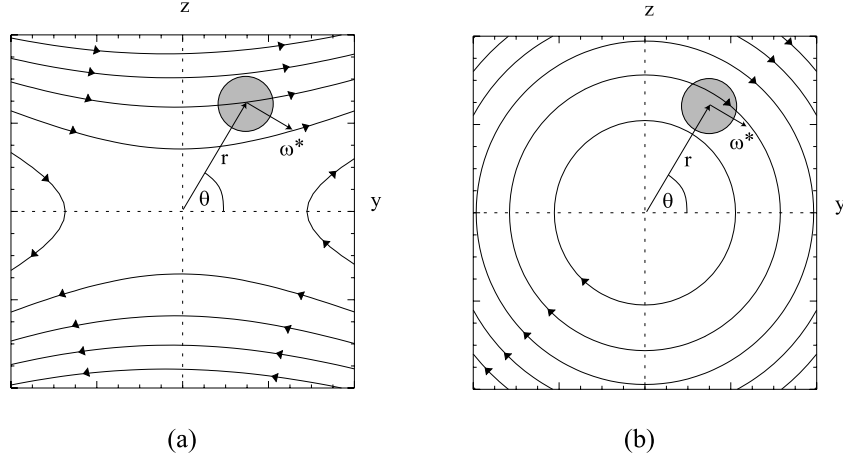
Figure 2.5: Rate of strain field relative to the equilibrium position of vortex 2 for a counter-rotating pair ($\Gamma_1 < 0$, $\Gamma_2 > 0$). (a) $|\Gamma_1| = O(|\Gamma_2|)$ (b) $|\Gamma_2| \gg |\Gamma_1|$.

self-induced rotation rates of vortex 2, which occur at higher wavenumbers (Figure 2.3). Thus, for the case of $|\Gamma_1| > |\Gamma_2|$, the unstable mode on vortex 2 has a higher frequency than that for case of $\Gamma_1 = -\Gamma_2$. When $\Gamma_1 = -\Gamma_2$, Eqs. 2.7 and 2.8 become identical to those in Widnall's [50] Eq. 1.

In the previous paragraph, the condition for instability is shown to be $u_\theta = \bar{\varpi} r$, where both quantities are assumed to be finite. However, an instability can also occur if the self-induced rotation rate is zero for a particular wavenumber. In this case, the stagnation point flow rotates vortex 2 to θ_o, at which $u_\theta = 0$, and causes the perturbation to radially diverge. Although the self-induction rate of $\bar{\varpi}$ does not exhibit the property of $\bar{\varpi} = 0$ for finite ka, there are higher wavenumber modes that do. Widnall [50] and Saffman [47] show that these modes have zero self-induced rotation rates at wavenumbers higher than that of the classic Crow instability [17], demonstrating that these instabilities are of a much shorter wavelength.

For the case of $|\Gamma_2| \gg |\Gamma_1|$, the rotation of the reference frame dominates Eq. 2.8 and a nearly circular velocity field is generated (Figure 2.5b). The azimuthal velocity is negative for all values of θ and, therefore, spins in the same direction as the self-induced rotation rate. Consequently, the perturbation on vortex 2 does not become fixed at one

(a)   (b)
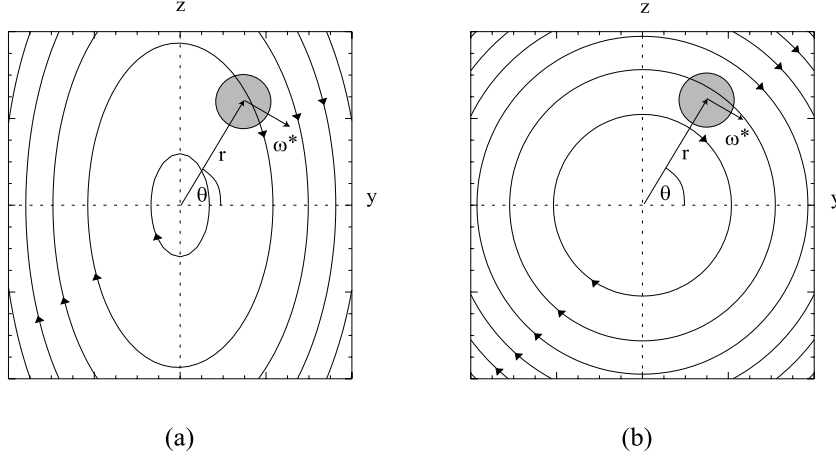
Figure 2.6: Velocity field relative to the equilibrium position of vortex 2 for a co-rotating pair ($\Gamma_1 > 0$, $\Gamma_2 > 0$). (a) $\Gamma_1 = O(\Gamma_2)$ (b) $\Gamma_2 >> \Gamma_1$.

orientation, but simply rotates with a nearly constant amplitude in a clockwise fashion. Thus, for the case of $|\Gamma_2| >> |\Gamma_1|$, vortex 2 is stable to long-wavelength perturbations.

2.2.4   Stability Characteristics of Co-Rotating Pairs

For a co-rotating pair ($\Gamma_1 > 0$, $\Gamma_2 > 0$), the azimuthal velocity in Eq. 2.8 is negative for all values of θ. Consequently, both u_θ and $\bar{\varpi}r$ work in concert to rotate the perturbations on vortex 2 clockwise. When $\Gamma_2 >> \Gamma_1$ (Figure 2.6b), the velocity field is very similar to that of the counter-rotating pair for the case of $|\Gamma_2| >> |\Gamma_1|$. However, when $\Gamma_1 = O(\Gamma_2)$ (Figure 2.6a), the strain field becomes elliptically-shaped and the perturbation amplitude varies with θ. Although the radial velocity provides an instantaneous growth rate that can be equal to that of the counter-rotating pair, the disturbance amplitude can only oscillate periodically and never decay to zero or grow exponentially large. Therefore, regardless of the relative strengths of the vortices, the co-rotating pair is linearly stable to long-wavelength perturbations. A similar conclusion was demonstrated by Jimenez [25], who utilized a more rigorous stability analysis for the case of $\Gamma_1 = \Gamma_2 = \Gamma > 0$.

2.3 Linear Stability Analysis of a Single Vortex Pair

In the previous section, a simplified stability model was employed to demonstrate the underlying physics that lead to instability growth on one of the vortices in a vortex pair. While this model is useful in describing the basic stability properties of counter- and co-rotating vortex pairs, it is not complete in that the perturbations on the other vortex are ignored. Therefore, the present section will extend the previous analysis by performing a complete linear stability calculation on single counter- and co-rotating vortex pairs and quantitatively computing the rate of instability growth as a function of the perturbation wavenumber.

2.3.1 Mathematical Formulation

The schematic of the vortices is shown in Figure 2.7, which for arbitrary Γ_1 and Γ_2, models a flap/tip vortex pair. As mentioned earlier, Crow [17] first computed the stability characteristics of an equal strength, counter-rotating vortex pair. Bristol [8] later extended Crow's analysis to include arbitrary strength counter-and co-rotating vortex pairs. The following calculations will follow Crow's derivation and incorporate the changes made by Bristol.
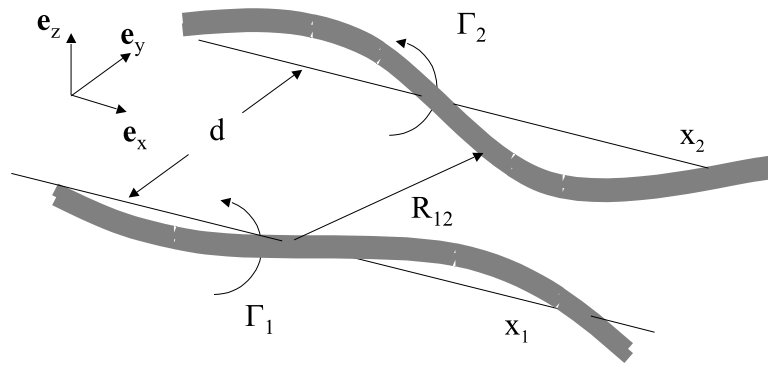
Figure 2.7: Schematic of the single vortex pair and the geometrical quantities used in the linear stability analysis.

The stability analysis begins with the Biot-Savart law, which relates the velocity field to a known vorticity field. The variable $\mathbf{R}_{mn}$, which is the distance from an element on vortex n to another element on vortex m, is given by

$$\mathbf{U}_n = \sum_{m=1}^{2} \Gamma_m \int \frac{\mathbf{R}_{mn} \times d\mathbf{L}_m}{4\pi |\mathbf{R}_{mn}|^3} \tag{2.12}$$

$$\mathbf{R}_{mn} = \mathbf{e}_x(x'_m - x_n) + \mathbf{e}_y(s_m - s_n) + (\mathbf{r}'_m - \mathbf{r}_n) \tag{2.13}$$

where the first two terms are the unperturbed vortex positions and the last is the radial perturbation from these positions. The primes in Eq. 2.13 are used to distinguish points that lie on the same vortex i.e., when $n = m$. The variable $d\mathbf{L}_n$ is the arc-length along vortex n and has the expression

$$d\mathbf{L}_n = (\mathbf{e}_x + \frac{\partial \mathbf{r}_n}{\partial x_n})dx_n \tag{2.14}$$

where

$$\mathbf{r}_n = \mathbf{e}_y y_n(x_n, t) + \mathbf{e}_z z_n(x_n, t) \tag{2.15}$$

are the displancements of vortex n in the lateral and vertical directions. The final equation in this analysis relates the velocity field to the motion of the vortices and comes from Helmholtz's first law of vortex motion. This law states that the vortex lines move with the fluid in an inviscid, barotropic flow under the action of conservative body forces. The equation that expresses this is

$$\frac{\partial \mathbf{r}_n}{\partial t} + u_n(\frac{\partial \mathbf{r}_n}{\partial x_n}) = \mathbf{e}_y v_n + \mathbf{e}_z w_n \tag{2.16}$$

where (u_n, v_n, w_n) are the velocity components of $\mathbf{U}_n - \Omega_o \mathbf{e}_x \times \mathbf{R}_n$, which is the motion of the vortices relative to the rotating frame. Note that the cross-product term is new in that it does not appear in Crow's derivation. The stability problem given in Eqs. 2.12, 2.13, 2.14, and 2.16 can be linearized by assuming that the perturbations are much smaller than the vortex separation, $|\mathbf{r}_n| \ll d$, and that the perturbation slopes remain small,

$|\partial \mathbf{r}_n/\partial x| << 1$. Equations 2.13 and 2.14 are substituted into Eq. 2.12, which is then linearized and substituted into the linearized form of Eq. 2.16. The resulting equation for the perturbation amplitudes is given by

$$\frac{\partial \mathbf{r}_n}{\partial t} = \sum_{m=1}^{2} \frac{\Gamma_m}{4\pi} \left\{ \mathbf{e}_y \int_{-\infty}^{\infty} \frac{[(z'_m - z_n) - (x'_m - x_n)\partial z'_m/\partial x'_m]}{[(x'_m - x_n)^2 + (s_m - s_n)^2]^{3/2}} dx'_m \; + \right.$$
$$\left. \mathbf{e}_z \int_{-\infty}^{\infty} \left(\frac{[3(s_m - s_n)^2(y'_m - y_n)]}{[(x'_m - x_n)^2 + (s_m - s_n)^2]^{5/2}} - \frac{[(y'_m - y_n) - (x'_m - x_n)\partial y'_m/\partial x'_m]}{[(x'_m - x_n)^2 + (s_m - s_n)^2]^{3/2}} \right) dx'_m \right\} \; - \Omega_o \mathbf{e}_x \times \mathbf{r}_n$$

(2.17)

which is similar to Crow's Eq. 6 except for the last term due to the rotation of the coordinate system. This equation has solutions of the form $\mathbf{r}_n(x_n, t) = \hat{\mathbf{r}} e^{(qt + ikx_n)}$, which when substituted into Eq. 2.17 gives

$$q\hat{y}_1 = -\frac{\Gamma_2}{2\pi}\hat{z}_1 \int_0^\infty \frac{dx}{(x^2+d^2)^{3/2}} \; + \; \frac{\Gamma_2}{2\pi}\hat{z}_2 \int_0^\infty \frac{coskx + kxsinkx}{(x^2+d^2)^{3/2}} dx \; +$$
$$\frac{\Gamma_1}{2\pi}\hat{z}_1 \int_\epsilon^\infty \frac{coskx + kxsinkx - 1}{x^3} dx \; + \; \Omega_o \hat{z}_1$$

(2.18)

$$q\hat{z}_1 = -\frac{\Gamma_2}{2\pi}\hat{y}_1 \int_0^\infty \frac{dx}{(x^2+d^2)^{3/2}} \; + \; \frac{\Gamma_2}{2\pi}\hat{y}_2 \int_0^\infty \frac{coskx}{(x^2+d^2)^{3/2}} dx \; -$$
$$\frac{\Gamma_1}{2\pi}\hat{y}_1 \int_\epsilon^\infty \frac{coskx + kxsinkx - 1}{x^3} dx \; - \; \Omega_o \hat{y}_1$$

(2.19)

along with an additional pair of equations that come about by transposing the subscripts 1 and 2. Evaluating the integrals in Eqs. 2.18 and 2.19, as well as the counterparts for vortex 2, yields

$$q\hat{y}_1 \;=\; -\frac{\Gamma_2}{2\pi d^2}\hat{z}_1 + \frac{\Gamma_2}{2\pi d^2}\psi\hat{z}_2 + \frac{\Gamma_1}{2\pi d^2}k^2 d^2 \varpi \hat{z}_1 + \Omega_o \hat{z}_1 \tag{2.20}$$

$$q\hat{y}_2 \;=\; -\frac{\Gamma_1}{2\pi d^2}\hat{z}_2 + \frac{\Gamma_1}{2\pi d^2}\psi\hat{z}_1 + \frac{\Gamma_2}{2\pi d^2}k^2 d^2 \varpi \hat{z}_2 + \Omega_o \hat{z}_2 \tag{2.21}$$

$$q\hat{z}_1 \;=\; -\frac{\Gamma_2}{2\pi d^2}\hat{y}_1 + \frac{\Gamma_2}{2\pi d^2}\chi\hat{y}_2 - \frac{\Gamma_1}{2\pi d^2}k^2 d^2 \varpi \hat{y}_1 - \Omega_o \hat{y}_1 \tag{2.22}$$

$$q\hat{z}_2 \;=\; -\frac{\Gamma_1}{2\pi d^2}\hat{y}_2 + \frac{\Gamma_1}{2\pi d^2}\chi\hat{y}_1 - \frac{\Gamma_2}{2\pi d^2}k^2 d^2 \varpi \hat{y}_2 - \Omega_o \hat{y}_2 \tag{2.23}$$

The terms, $\psi(kd)$ and $\chi(kd)$, are called mutual induction functions and are defined in Crow [17]. Figure 2.8 demonstrates the dependence of ψ and χ on kd. The term, ϖ, is the vortex self-induced rotation rate defined in Eq. 2.9.
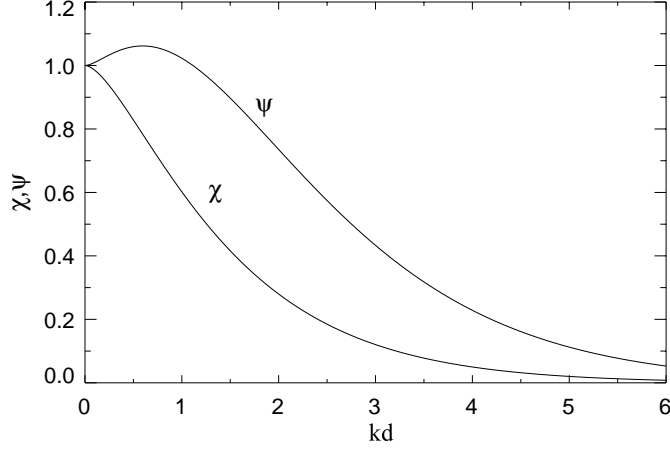
Figure 2.8: Dependence of the mutual induction functions, ψ and χ, upon the dimensionless perturbation wavenumber, kd.

As discussed in Section 2.2.2, one problem with this self-induced rotation rate is that ϖ becomes invalid for large perturbation wavenumbers. Consequently, the more accurate rotation rate, ϖ' (Eq. 2.11), will be used in the analysis to follow. Replacing the terms $k^2 d^2 \varpi$ in Eq.,'s 2.20-2.23 with $\varpi^* = \varpi' d^2 / a^2$ and non-dimensionalizing by $\Gamma_2 / (2\pi d^2)$ changes the form of the governing equations to

$$\alpha \hat{y}_1 = -\hat{z}_1 + \hat{z}_2 \psi + \Gamma \varpi^* \hat{z}_1 + (\Gamma + 1)\hat{z}_1 \tag{2.24}$$

$$\alpha \hat{y}_2 = -\Gamma \hat{z}_2 + \Gamma \hat{z}_1 \psi + \varpi^* \hat{z}_2 + (\Gamma + 1)\hat{z}_2 \tag{2.25}$$

$$\alpha \hat{z}_1 = -\hat{y}_1 + \hat{y}_2 \chi - \Gamma \varpi^* \hat{y}_1 - (\Gamma + 1)\hat{y}_1 \tag{2.26}$$

$$\alpha \hat{z}_2 = -\Gamma \hat{y}_2 + \Gamma \hat{y}_1 \chi - \varpi^* \hat{y}_2 - (\Gamma + 1)\hat{y}_2 \tag{2.27}$$

where $\alpha = \frac{2\pi d^2}{\Gamma_2} q$ and $\Gamma = \Gamma_1 / \Gamma_2$. Equations 2.24-2.27 represent an eigenvalue problem for the eigenvalue α and eigenvector $(\hat{y}_1, \hat{y}_2, \hat{z}_1, \hat{z}_2)^T$. For an equal strength, counter-rotating pair, $\Gamma = -1$ and the terms in Eqs. 2.24-2.27 take on a form similar to that of Crow's Eq. 8.

2.3.2 Interpretion of the Governing Equations

A useful exercise in understanding the stability properties of the vortex pair is to interpret the different columns in Eqs. 2.24-2.27. The column on the left-hand side of Eq. 2.24-2.27 denotes the rate of change of the perturbations with time. For purely imaginary α, the perturbations lead to neutrally stable oscillations. When α is positive and real, the perturbations exponentially increase in time, leading to a growing instability. The first column of terms on the right-hand side is the influence of the strain field from one vortex on the perturbations of the other vortex. If the instability analysis is conducted by including the left-hand side column and only the first column on the right-hand side of Eqs. 2.24-2.27, the eigenvalues for vortex 1 are ± 1 with corresponding modes $(-1, 0, 1, 0)^T$ and $(1, 0, 1, 0)^T$. The eigenvalues for vortex 2 would likewise be $\pm \Gamma$ with modes $(0, -1, 0, 1)^T$ and $(0, 1, 0, 1)^T$. Note that the modes grow or decay at $\pm 45^o$, the principle rate of strain directions of the vortices.

The second column of terms on the right-hand side of Eqs. 2.24-2.27 demonstrates how the perturbations of one vortex affect the velocity field at the other vortex. Consequently, this column provides a correction to the elements in the first column on the right-hand side of Eqs. 2.24-2.27. The simplified analysis in Section 2.2 neglected this effect. Employing the left-hand side column and only the first two columns on the right-hand side of Eqs. 2.24-2.27 in the stability calculation yields eigenvalues that have the form

$$\alpha^2 = \frac{1}{2}(\Gamma^2 + 1 + 2\Gamma\psi\chi) \pm \frac{1}{2}\sqrt{(\Gamma^2 + 1 + 2\Gamma\psi\chi)^2 - 4\Gamma^2(1 - \chi^2)(1 - \psi^2)} \qquad (2.28)$$

The effect of these velocity perturbations depends upon the value of the perturbation wavenumber. An example of this is shown in Figure 2.9, which plots the positive growth rates, α_{1+} and α_{2+}, from Eq. 2.28 for $\Gamma = -0.5$. For small wavenumbers, the velocity perturbations act to decrease the positive growth rates below the values of 1.0 and $-\Gamma = 0.5$, which effectively stabilizes the pair. However, as the wavenumber increases, the influence of the velocity perturbations diminishes and the growth rates asymptotically approach 1.0 and $-\Gamma$.
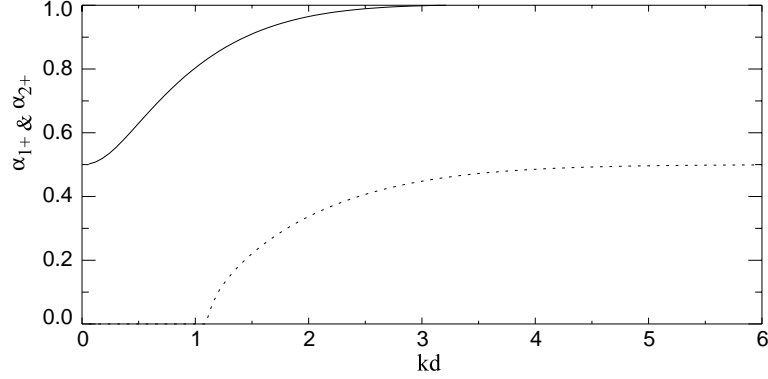
Figure 2.9: Effect of the velocity perturbations, ψ and χ, on the positive growth rates, α_{1+} and α_{2+}, of Eq. 2.28 ($\Gamma = -0.5$). Note these growth rates do not include the vortex self-induced rotation rate or the reference frame rotation.

The third column on the right-hand side of Eqs. 2.24-2.27 represents the self-induced rotation rate of the vortices. If this were the only term on the right-hand side of Eqs. 2.24-2.27, the eigenvalues would be $\pm\Gamma\varpi^*i$ and $\pm\varpi^*i$, all of which are purely imaginary. The vortices with these eigenvalues simply rotate in their self-induced velocity fields and exhibit neutrally stable oscillations in time. The final column of terms in Eqs. 2.24-2.27 is due to the rotation of the vortex pair about its vorticity centroid. If $\Gamma = -1$, as is the case in Crow's analysis, this column drops out because the vorticity centroid is infinite and the pair translates vertically downward. Performing a stability analysis with only this column on the right-hand side of Eqs. 2.24-2.27 results in the eigenvalues $\pm(\Gamma + 1)i$, which again give rise to neutrally stable oscillations.

To see how the rate of strain field, self-induction, and reference frame rotation affect the stability characteristics of the vortex pair, consider the equations Eqs. 2.24 and 2.26. If the the corrective terms, ψ and χ, are ignored and the variables y_1 and z_1 are eliminated, the equation that results for the eigenvalues is

$$\alpha^2 = 1 - [\Gamma\varpi^* + (\Gamma + 1)]^2 \tag{2.29}$$

The first term on the right-hand side of Eq. 2.29 is the contribution of the strain field that arises from the presence of the other vortex. Because this is the only positive term

in Eq. 2.29, it demonstrates that the *strain field is the driving mechanism of perturbation growth.* On the other hand, the second terms, which is the effect of self-induction and frame rotation, are negative. This shows that *self-induction and frame rotation contribute to stability.* The physical reason why these two terms stabilize the vortex pair is that they can rotate a perturbation out of the diverging portion of the strain field, preventing it from becoming "trapped" there by the u_θ velocity component (Section 2.2). For a co-rotating vortex pair, the neutrally stable oscillations arise from the disturbance rotating into and out of the converging and diverging regions of the strain field.

2.3.3 Solution to the Governing Equation

Solving the linearized eigenvalue problem in Eqs. 2.24-2.27 gives the stability characteristics of a vortex pair with arbitrary circulation strengths and vortex core sizes. The surfaces plotted in Figure 2.10 display the results of solving Eqs. 2.24-2.27 for $-1 \leq \Gamma \leq 1$ and $0 \leq a/d \leq 0.5$. The plot in Figure 2.10a is the maximum growth rate, α_{max}, while that in Figure 2.10b is the corresponding wavenumber, kd_{max}. It can be seen that α_{max} depends strongly on Γ and only weakly upon a/d. As Γ increases from -1 to 0, the maximum growth rate decreases to a minimum and then rises to a maximum value as $\Gamma \to 0^-$. This indicates that *counter-rotating vortex pairs with dissimilar circulation strengths have growth rates that are larger than those of pairs with nearly equal circulation strengths.* Note that regardless of the core size, the maximum growth rate has an upper value of 1.0, indicating that the perturbations grow no faster than the rate of strain, $\Gamma_2/(2\pi d^2)$, of vortex 2 on vortex 1. Another important feature in Figure 2.10a is that *co-rotating pairs ($\Gamma > 0$) are linearly stable to these long-wavelength perturbations.* This result is in agreement with Jimenez [25] and with the conclusion that was made in Section 2.2 with the simplified stability model.

Figure 2.11a shows a cut through the surface in Figure 2.10a at $a/d = 0.312$, which corresponds to a value of $\epsilon/d = 0.2$ from Crow's paper. The value of $\alpha_{max} = 0.79$ at $\Gamma = $ -1 is the growth rate for the Crow instability between two, counter-rotating vortices. The maximum growth rate reaches a minimum of 0.77 at $\Gamma = -0.89$ and does not exceed the
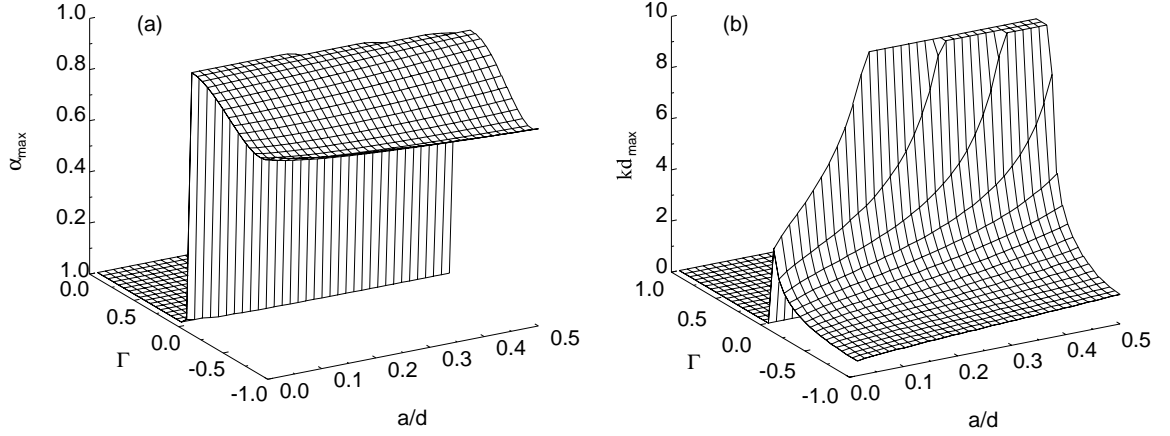
Figure 2.10: Surfaces of the (a) maximum growth rate, α_{max}, and (b) corresponding wavenumber, kd_{max} for a single vortex pair.

value for the Crow instability until $\Gamma \geq -0.77$. Therefore, if one were designing a vortex pair that had a linear growth rate greater than that of the Crow instability, it is essential that one of the counter-rotating vortices be at most 77% as strong as the other vortex when $a/d = 0.312$.

Figure 2.10b displays the surface of kd_{max}. For counter-rotating vortices, it is evident
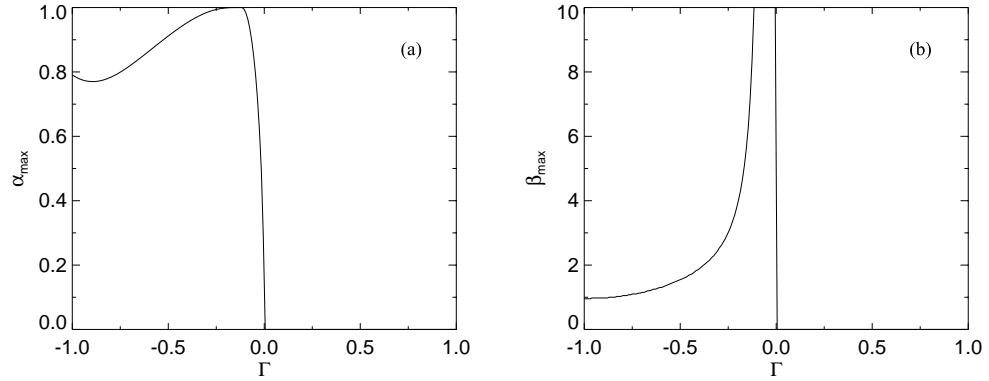
Figure 2.11: A plot through the (a) maximum growth rate surface and (b) most unstable, wavenumber surface in Figure 2.10 at $a/d = 0.312$.

that the most unstable wavenumber increases as Γ increases from -1 to 0. Consequently, the wavelength corresponding to the most unstable mode is smaller for dissimilar strength vor-

tices. Figure 2.11b further illustrates this by plotting kd_{max} vs. Γ at $a/d = 0.312$. It is also evident in Figure 2.11b that at a fixed value of Γ, the most unstable wavenumber increases with increasing a/d, demonstrating that fatter vortices are unstable to shorter wavelength perturbations. One feature in Figures 2.10b and 2.11b that requires an explanation is the behavior of kd_{max} for $\Gamma \to 0^-$. In reality, kd_{max} is becoming infinite as $\Gamma \to 0^-$. However, these figures do not show this due to the finite number of data points used in the calculation.

2.3.4 Growth Rate Curves and Unstable Mode Shapes for $\Gamma = -1$

The case of $\Gamma = -1.0$ was previously investigated by Crow [17], who used it to model the stability characteristics of oppositely-signed, equal strength tip vortices. In this section, a comparison is made between Crow's results, which utilize $(ka)^2 \varpi$ (Eq. 2.9) for the self-induced rotation rate, and the present analysis, which employs the Kelvin/Saffman model, ϖ' (Eq. 2.11), for the self-induced rotation rate. To make a proper comparison with Crow's $\epsilon/d = 0.2$, a/d is taken to be equal $a/d = \epsilon/d \frac{1}{2 \times 0.321} = 0.2 \frac{1}{0.642} = 0.312$, where Crow's Eq. 13 has been utilized. In Figure 2.12, is evident that Crow's analysis predicts two bands of instability, while the present analysis demonstrates only one. The higher band of unstable modes is caused by the rotation rate in Eq. 2.9 falsely going to zero at $ka = 1.7$ (Figure 2.3). Note that these spurious modes have a maximum growth rate at $kd = 5.3$, or $ka = kd \times a/d = 5.3 \times 0.312 = 1.7$, corresponding directly to the location at which $(ka)^2 \varpi$ in Figure 2.3 goes to zero. At $kd = 5.3$, the rate of strain field can freely rotate the perturbations to a region of the flow field where the azimuthal velocity is zero and there cause them to radially diverge. Because the rotation rate given by ϖ' remains finite for increasing ka (Figure 2.3), the stability analysis based on ϖ' does not yield the false band of instability.

Another difference between the two stability analyses is the behavior of the growth rate curves at smaller values of kd. Using Kelvin/Saffman's rotation rate shifts the growth rate curve slightly to the left and causes the band of instability to be narrower than that
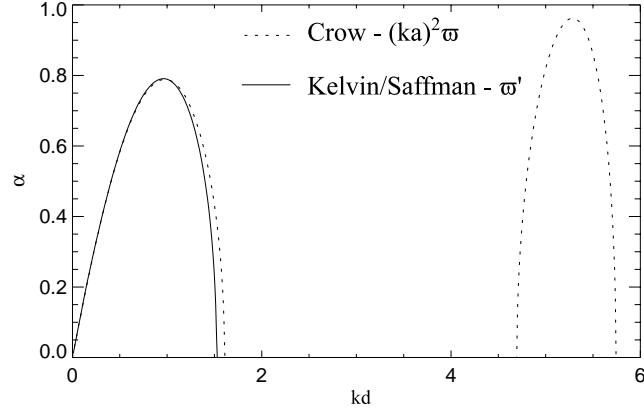
Figure 2.12: Growth rate curves for $\Gamma = -1.0$ based upon the two different self-induced rotation rate models.
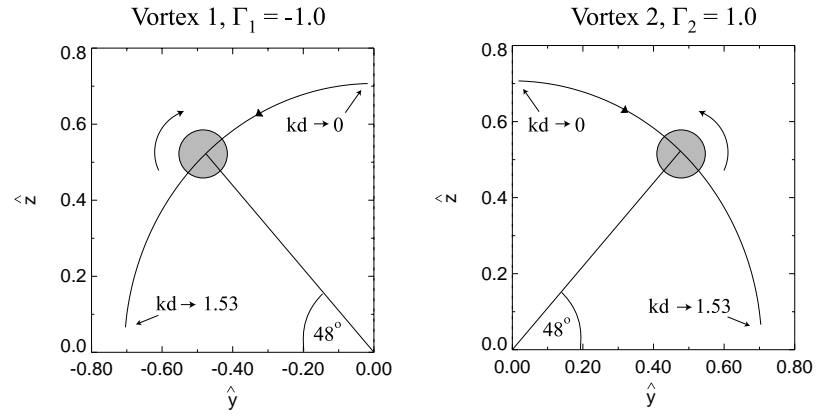
Figure 2.13: Shapes of the unstable modes as a function of perturbation wavenumber for $\Gamma = -1.0$ and $a/d = 0.312$. The lines at 48° denote the most unstable mode shape.

based on $(ka)^2 \varpi$. The reason for this can be explained by considering the trends of the two different rotation rate models. Within this range of wavenumbers, ϖ' is somewhat larger than that of $(ka)^2 \varpi$. Consequently, these larger rotation rates are better able to stabilize the flow, bringing about stability somewhat sooner.

Figure 2.13 displays the variation of the instability mode shapes as a function of kd for $\Gamma = -1$. These mode shapes are for the stability analysis based on Kelvin/Saffman's rotation rate formula. The unstable modes are symmetric, such that $\hat{y}_1 = -\hat{y}_2$ and $\hat{z}_1 = \hat{z}_2$. As kd increases from zero, the perturbations on vortices 1 and 2 are rotated counter-clockwise and clockwise by the increasing self-induced rotation rate. When $kd = 0.85$, the perturbations pass through the orientation at which the radial velocity componetn, u_r, is greatest, yielding a maximum growth rate of 0.81. At this wavenumber, vortices 1 and 2 are oriented at 48.0^o and 132.0^o. At $kd = 1.53$, the self-induced rotation rate becomes larger than the azimuthal velocity field. As a result, the flow is stable to perturbations of higher wavenumbers.

2.3.5 Growth Rate Curves and Unstable Mode Shapes for Γ = -0.25 and -0.5

To investigate the stability properties for vortex pairs with unequal circulation strengths, Eqs. 2.24-2.27 are solved for $\Gamma = -0.25$ and -0.5 with $a/d = 0.312$. The growth rate curves for these two cases, as well as that for $\Gamma = -1.0$, are plotted in Figure 2.14. An immediately apparent feature is that vortex pairs with greater disparity in circulation strengths are unstable over a larger range of perturbation wavenumbers. As discussed in Section 2.3.3, the most unstable modes have growth rates and wavenumbers that increase with increasing values of Γ.

Figure 2.15 demonstrates the shape of the unstable modes for $\Gamma = -0.5$ $(a/d = 0.312)$ as a function of the disturbance wavenumber. Note the difference in the horizontal and vertical scales that are used for vortices 1 and 2. The most unstable mode, which occurs at $kd = 1.54$, is indicated in by the lines that are oriented at 41° and 80°. As kd increases from zero, vortex 2, the stronger in the pair, rotates counter-clockwise from nearly
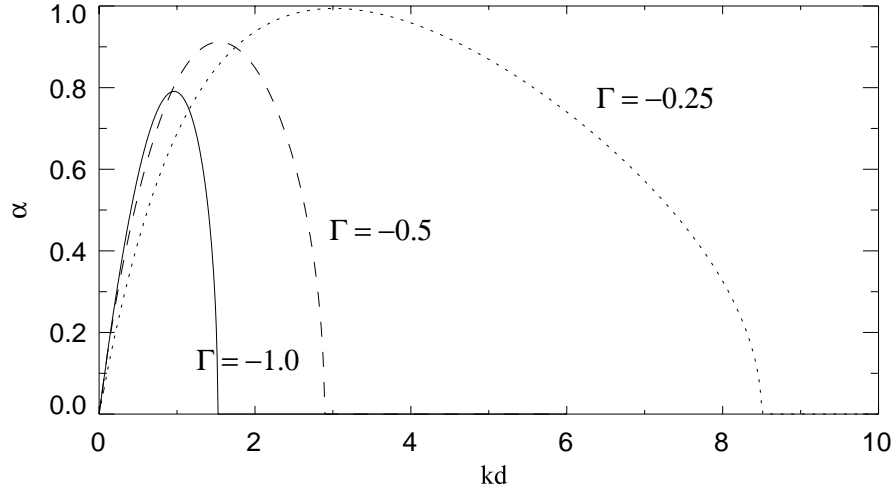
Figure 2.14: Growth rate curves for Γ = -0.25, -0.5, and -1.0 for $a/d = 0.312$.
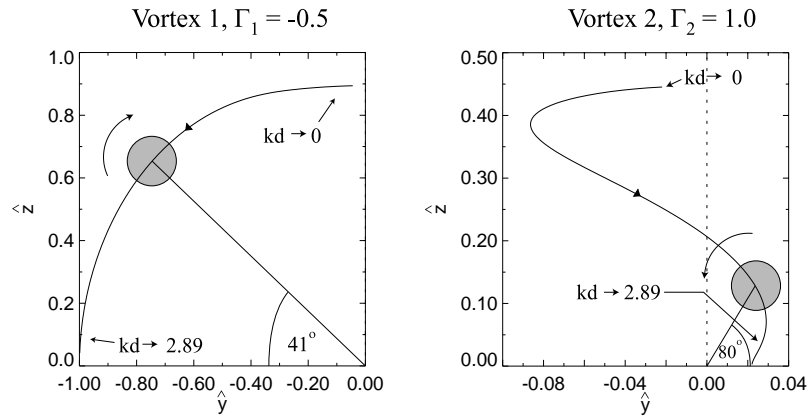
Figure 2.15: Shapes of the unstable modes as a function of perturbation wavenumber for $\Gamma = -0.5$ and $a/d = 0.312$. The lines at 41° and 80° denote the most unstable mode shape.
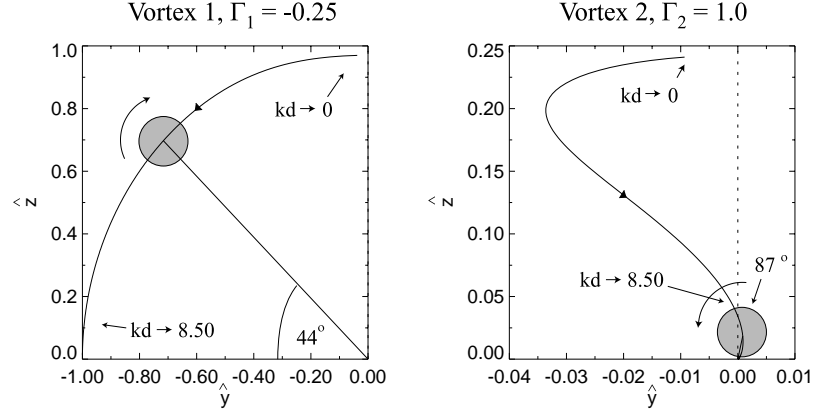
Figure 2.16: Shapes of the unstable modes as a function of perturbation wavenumber for $\Gamma = -0.25$ and $a/d = 0.312$. The lines at 44° and 87° denote the most unstable mode shape.

vertical orientation. The perturbation amplitude on vortex 2 decreases with increasing values of kd. Vortex 2 eventually reverses direction and begins to rotate clockwise with increasing kd. At the largest unstable wavenumber, $kd = 2.89$, vortex 2 is inclined at 0 degrees. Vortex 1, the weaker vortex, follows a different trend as kd varies. As kd is increased from zero, vortex 1 rotates counter-clockwise from a nearly vertical orientation. The amplitude of the perturbation on vortex 2 remains fairly constant as the disturbance wavenumber is increased. As kd approaches 2.89, vortex 1 becomes oriented at 180°. For higher wavenumbers, the effects of self-induction become dominant, rendering the pairs stable. The shape of the unstable modes for $\Gamma = -0.25$ follow similar trends as those for $\Gamma = -0.5$ as shown in Figure 2.16. One difference between Figures 2.15 and 2.16 that should be noted is that for $\Gamma = -0.25$, the perturbation amplitude on vortex 2 is smaller than that for the case of $\Gamma = -0.5$.

2.4   Closing Remarks

It has been shown in this chapter that arbitrary strength, counter-rotating vortex pairs are linearly unstable to long-wavelength perturbations, while co-rotating pairs are stable. Through the use of a simplified stability model, the underlying physics of instability

growth or decay were shown to depend upon the interaction of the rate of strain field at a vortex and the vortex's self-induced rotation rate. While the previous analyses are helpful in gaining an understanding of the stability properties of single vortex pairs, they do not completely model the four-vortex wakes observed in the towing tank. Hence, the next chapter will extend the above discussions to determine the effects that the additional vortex pair has upon the stability characteristics of the original pair.

Chapter 3

Stability Characteristics of Two Vortex Pairs

3.1   Introduction

In Chapter 2, the stability characteristics of a single vortex pair with arbitrary strength ratios were studied. Since the vortex wake of the triangular-flapped airfoil is comprised of two counter-rotating pairs, the present chapter will extend the analyses in Chapter 2 to include the other counter-rotating vortex pair. Additionally, the stability properties of two co-rotating pairs will be computed to determine whether or not an additional co-rotating pair destabilizes the original co-rotating pair to long-wavelength perturbations. In Section 3.2, a simplified stability model, similar to that in Section 2.2, will be employed. In Section 3.3, a complete linear stability calculation that follows the Crouch analysis [16] will be performed on several four-vortex systems.

3.2   A Simplified Stability Model

In Section 2.2, a simplified stability analysis was performed by calculating the rate of strain field about one vortex in a single vortex pair. This discussion illuminated the underlying physics of why a perturbation grows or decays on one of the vortices. In this section,

a similar analysis will be performed for a four-vortex system. Because the equilibrium flow
of the four-vortex system varies periodically in time, it is necessary to first solve for the
locations and velocities of the vortices. Then, the rate of strain field with respect to one of
the vortices can be found at various points in the orbit period.

A schematic of the wake is shown in Figure 3.1. The four vortices are modeled as
vortex filaments that have stream functions, $\Psi = \frac{-\Gamma}{2\pi} ln(r)$, where r is the distance from
the vortex center. The circulation centroids on either half of the wake are separated by a
distance, b^*, and the vortices within each pair by a distance, d.
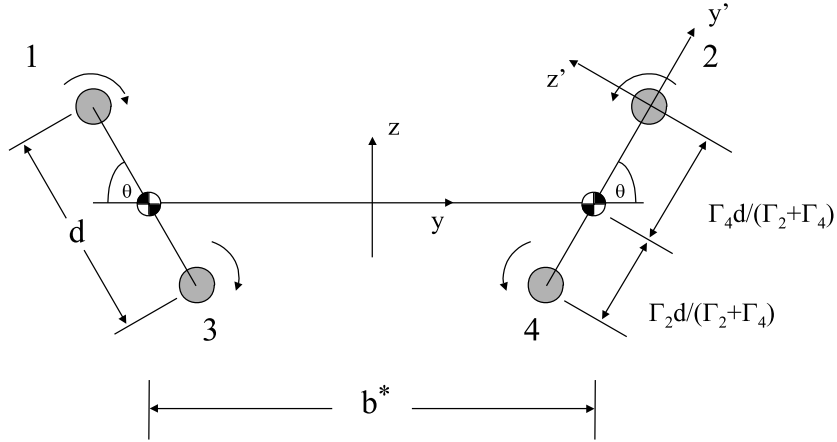
Figure 3.1: Schematic of the four vortex system. The (y', z') coordinate system rotates with
vortex 2.

The wake is symmetric about the centerline, such that $\Gamma_1 = -\Gamma_2$ and $\Gamma_3 = -\Gamma_4$.
Vortex 2 is located a distance $\Gamma_4 d/(\Gamma_2 + \Gamma_4)$ from the right-hand side centroid and vortex
4 a distance of $\Gamma_2 d/(\Gamma_2 + \Gamma_4)$ from the right-hand side centroid. The vortices within each
pair orbit about their circulation centroid at an angular velocity, $\Omega(t) = d\theta/dt$. For the
signs of Γ_n shown in Figure 3.1, $\Omega > 0$ for vortex pair 2-4 and $\Omega < 0$ for vortex pair 1-3.
The horizontal and vertical velocity components at vortex n are given by

$$\frac{dy_n}{dt} = \sum_{\substack{m=1 \\ m \neq n}}^{4} \Gamma_m \frac{z_{mn}}{r_{mn}^2} \tag{3.1}$$

$$\frac{dz_n}{dt} = \sum_{\substack{m=1 \\ m \neq n}}^{4} -\Gamma_m \frac{y_{mn}}{r_{mn}^2} \tag{3.2}$$

where $y_{mn} = y_m - y_n$, $z_{mn} = z_m - z_n$, and $r_{mn}^2 = y_{mn}^2 + z_{mn}^2$. The positions of the vortices are computed by numerically integrating Eqs. 3.1 and 3.2 with a fourth order Runge-Kutta scheme. The initial positions of the vortices are $y_2(0) = b + \Gamma_4 d/(\Gamma_2 + \Gamma_4)$, $y_4(0) = b - \Gamma_2 d/(\Gamma_2 + \Gamma_4)$, $y_1(0) = -y_2(0)$, $y_3(0) = -y_4(0)$, and $z_n(0) = 0, n = 1, 2, 3, 4$.

If the time-varying locations of the vortices are known, several additional quantities of the flow field can be obtained. The positions of the right-hand side centroids are calculated from

$$y_r = \frac{\Gamma_2 y_2(t) + \Gamma_4 y_4(t)}{\Gamma_2 + \Gamma_4} \tag{3.3}$$

$$z_r = \frac{\Gamma_2 z_2(t) + \Gamma_4 z_4(t)}{\Gamma_2 + \Gamma_4} \tag{3.4}$$

Because the wake is symmetric, the left-hand side centroids are given by $y_l = -y_r$, and $z_l = z_r$. The velocities, $\mathbf{v}_c = (v_c, w_c)$, of the circulation centroids are computed by taking the time derivative of Eqs. 3.3 and 3.4 with a central difference scheme. The angular velocity and radial velocity of vortex n relative to a circulation centroid is found by solving for Ω_{rel} and v_{rel} in

$$\mathbf{v}_n = \mathbf{v}_c + \Omega_{rel}\mathbf{e}_x \times r\mathbf{e}_r + v_{rel}\mathbf{e}_r \tag{3.5}$$

where $\mathbf{v}_n$ is the velocity of vortex n, $\mathbf{v}_c$ the velocity of the left or right circulation centroid, and r the distance from vortex n to the circulation centroid in the direction $\mathbf{e}_r$.

Using Eqs. 3.1 and 3.2, the positions of the vortices are solved over one orbit period. Table 3.1 shows the parameters for the four cases that are computed using the analysis described above. The variable Δt is the time step used in the numerical integration, $\tau_{single} = 4\pi^2 d^2/(\Gamma_2 + \Gamma_4)$ the orbit time for an isolated vortex pair, and τ the calculated orbit time. Further decreases in Δt for each of the four cases result in changes of $O(10^{-4})$. Cases 1 and

2 model counter-rotating vortex pairs that have circulation centroid spacings of $b^* = 6.0$ and $b^* = 10.0$. Cases 3 and 4 model co-rotating vortex pairs that have circulation centroid spacings of $b^* = 2.0$ and $b^* = 5.0$. For the counter-rotating pairs, $\Gamma_2 + \Gamma_4 > 0$, such that an airfoil with this type of wake generates positive lift.

Case	Γ_2 (cm^2/s)	Γ_4 (cm^2/s)	b^* (cm)	d (cm)	Δt (s)	τ (s)	τ_{single} (s)
1	1.0	-0.6	6	1	0.06	104.7	98.7
2	1.0	-0.6	10	1	0.06	100.1	98.7
3	0.4	1.0	2	1	0.02	41.2	28.2
4	0.4	1.0	5	1	0.02	29.4	28.2

Table 3.1: Parameters for each of the four-vortex systems.

3.2.1 Equilibrium Flow of the Counter-Rotating Pairs

Figure 3.2 shows the results for the counter-rotating vortex pairs in Case 1. The positions of the vortices over the orbit period are displayed in Figure 3.2a. The vortex trajectories are no longer circular as they are for a single vortex pair, but are distorted into an "α" shape due to the velocity induced by the additional pair. Furthermore, the presence of the other pair lengthens the orbit period (Table 3.1) so that it increases from a value of 98.7 s for a single vortex pair to 104.7 s for the four vortex system. The angular velocity of vortex 2 about the right-hand side circulation centroid is plotted in Figure 3.2b. The angular velocity, Ω, of vortex 2 is normalized by $\Omega_o = (\Gamma_2 + \Gamma_4)/2\pi d^2$, which is the angular velocity of a single 2-4 vortex pair separated by a distance d. Unlike the single vortex pair, vortex 2 orbits the centroid with an angular velocity that varies over the orbit period. When the two pairs are closely spaced at the beginning and end of the orbit cycle, the additional pair retards $\Omega(t)$. However, during the middle of the orbit period, the distance between the vortex pairs increases and the angular velocity tends to vary about a value close to that for an isolated vortex pair. Figure 3.2c depicts the velocity of vortex 2 relative to the right-
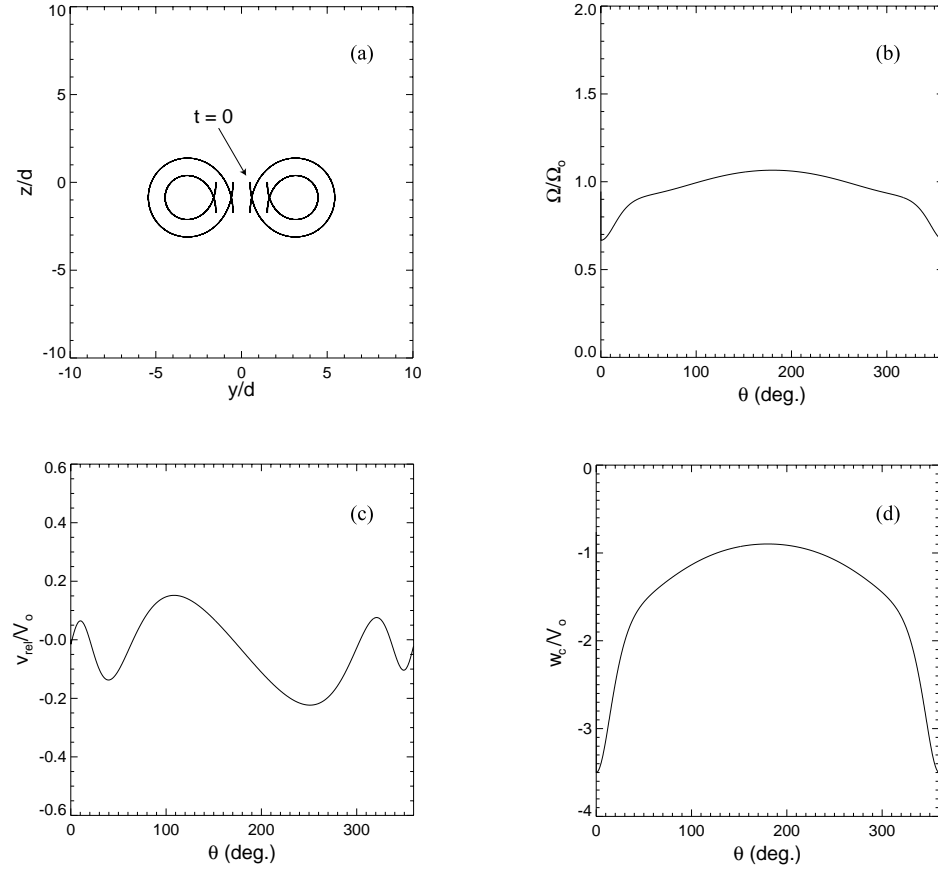
Figure 3.2: Results for the counter-rotating pairs in Case 1 ($\Gamma_2 = 1$ (cm^2/s), $\Gamma_4 = -0.6$ (cm^2/s), $b^* = 6$ (cm), $d = 1$ (cm)) over one orbit period: (a) mean vortex positions, (b) angular velocity and (c) relative velocity of vortex 2 with respect to the right-hand side circulation centroid, and (d) vertical descent velocity of the left- and right-hand side circulation centroids.
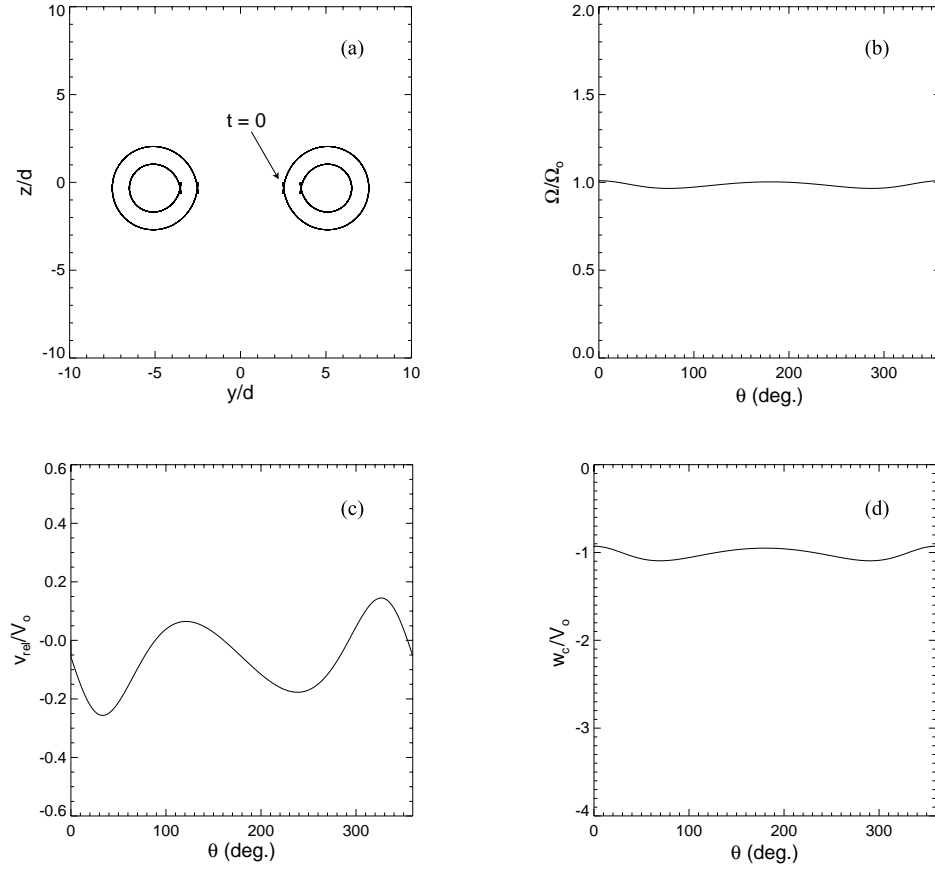
Figure 3.3: Results for the counter-rotating pairs in Case 2 ($\Gamma_2 = 1$ (cm^2/s), $\Gamma_4 = $ -0.6 (cm^2/s), $b^* = 10$ (cm), $d = 1$ (cm)) over one orbit period: (a) mean vortex positions, (b) angular velocity and (c) relative velocity of vortex 2 with respect to the right-hand side circulation centroid, and (d) vertical descent velocity of the left- and right-hand side circulation centroids.

hand side centroid along the y'-direction (Figure 3.1). While a single vortex pair has $v_{rel} = 0$ for all time, the additional pair causes v_{rel} to oscillate in time. As a result, vortex 2 moves towards and away from the centroid over the orbit period. The descent velocity of the vortex system is shown in Figure 3.2d. The variable $V_o = (\Gamma_2 + \Gamma_4)/2\pi b^*$ in this plot is the descent velocity of an equivalent counter-rotating vortex pair, where the vortices are located at the circulation centroids on either half of the wake. Rather than descending at a constant rate, as would be the case for two equal-strength, counter-rotating vortices, the four-vortex system descends at a velocity that varies strongly over the orbit period. When the vortex pairs are close to each other at the beginning and end of the orbit period, the descent velocity is larger than that of an equivalent counter-rotating system. In the middle of the orbit cycle, the normalized descent velocity becomes of $O(1)$ as the pairs reach their maximum separation distance.

The results for Case 2 are shown in Figure 3.3. The trends described for Case 1 are evident in Case 2, though they are less pronounced. For example, the vortex positions (Figure 3.3a) are more circular than those for Case 1 and the angular velocity, relative velocity, and descent velocity have oscillation amplitudes that are less than those in Figure 3.2b-d. Although the oscillation amplitude of v_{rel} in Figure 3.3c appears to be on the order of the oscillations in Figure 3.2c, it should be noted that V_o for Case 2 is 60% of that for Case 1. Finally, the orbit time for Case 2 (Table 3.1) is closer to that of a single vortex pair.

3.2.2 Equilibrium Flow of the Co-Rotating Pairs

Two co-rotating vortex systems are calculated in Cases 3 and 4. The results for Case 3 are plotted in Figure 3.4. As is the case for the counter-rotating vortex pairs, the presence of the additional vortex pair renders the vortex trajectories non-circular. When vortices 1 and 2 enter the downwash of the wake, they interact strongly and advect one another downwards, making the orbit period 46% longer than that of an isolated co-rotating pair. The angular velocity of vortex 2 about the right-hand side circulation centroid is displayed in Figure 3.4b. As the vortices orbit about one another, $\Omega(t)$ oscillates in a manner such
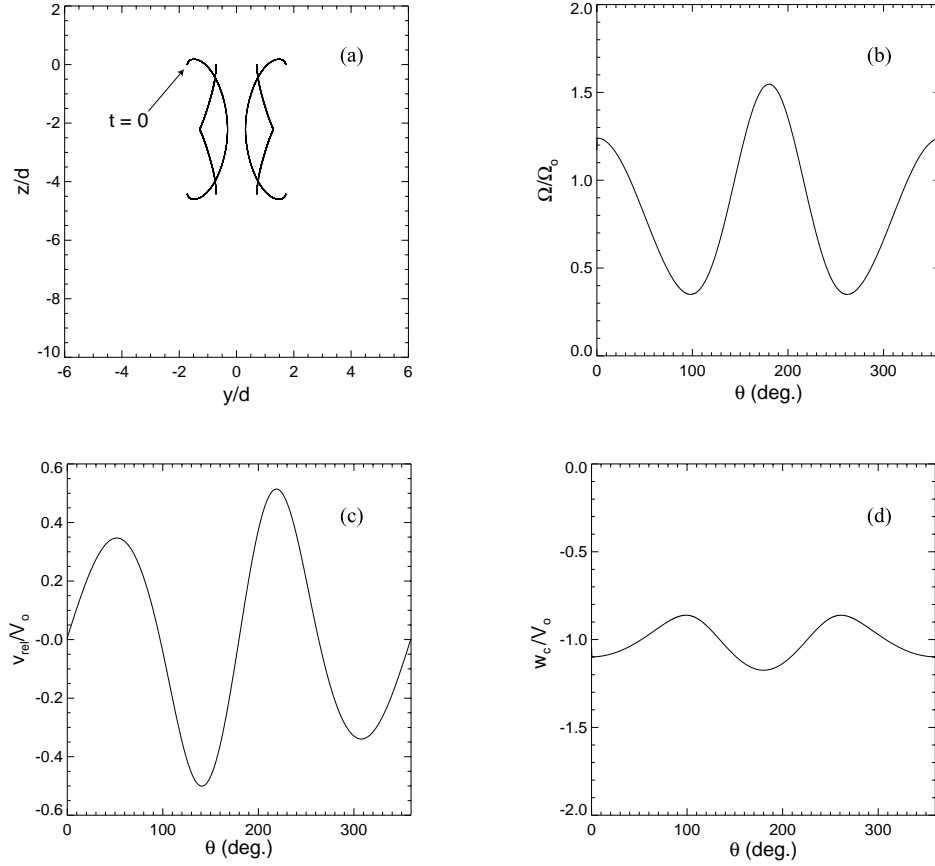
Figure 3.4: Results for the co-rotating pairs in Case 3 ($\Gamma_2 = 0.4$ (cm^2/s), $\Gamma_4 = 1$ (cm^2/s), b^* = 2 (cm), $d = 1$ (cm)) over one orbit period: (a) mean vortex positions, (b) angular velocity and (c) relative velocity of vortex 2 with respect to the right-hand side circulation centroid, and (d) vertical descent velocity of the left- and right-hand side circulation centroids.
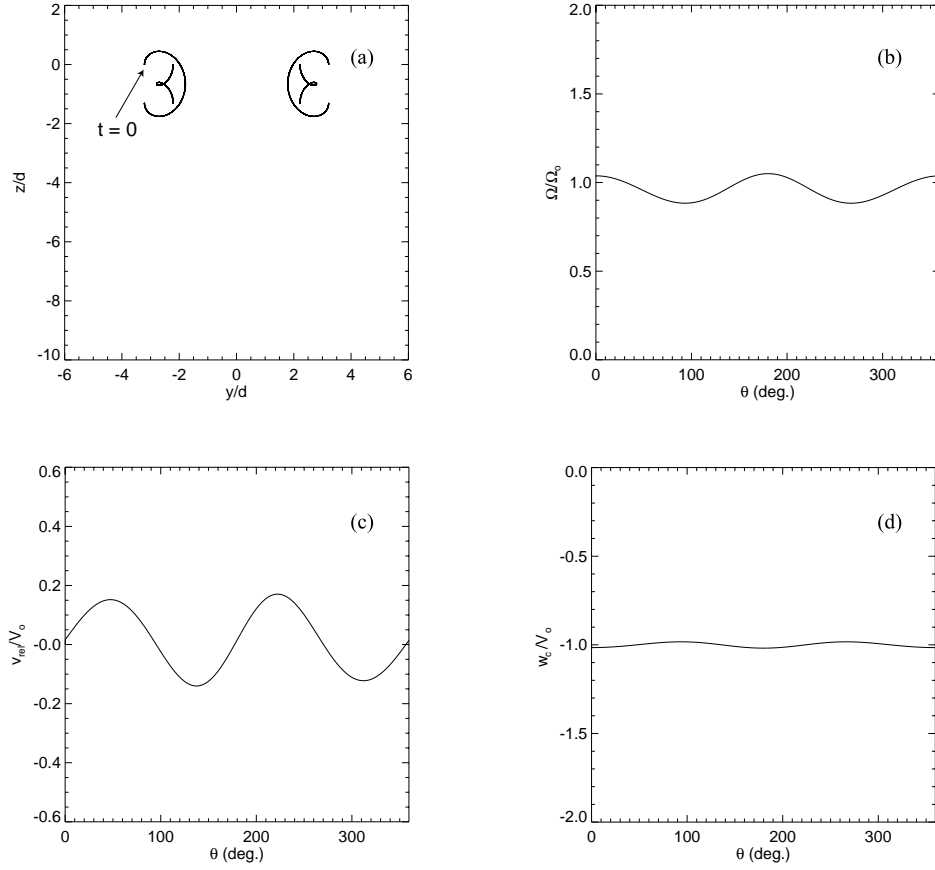
Figure 3.5: Results for the co-rotating pairs in Case 4 ($\Gamma_2 = 0.4$ (cm^2/s), $\Gamma_4 = 1$ (cm^2/s), b^* = 5 (cm), $d = 1$ (cm)) over one orbit period: (a) mean vortex positions, (b) angular velocity and (c) relative velocity of vortex 2 with respect to the right-hand side circulation centroid, and (d) vertical descent velocity of the left- and right-hand side circulation centroids.

that it attains its local extrema at $\theta \approx 0^o, 90^o, 180^o$, and 270°. At 0° and 180°, the four

vortices are co-linear and $\Omega(t)$ has local maxima. However, at 90° and 270°, vortices 1-3

and 2-4 are vertically aligned and $\Omega(t)$ has local minima. Figure 3.4c demonstrates the

velocity of vortex 2 relative to the right-hand side centroid in the y'-direction. Similar to

the counter-rotating vortex pairs, v_{rel} varies over the orbit cycle, but it does so in a fashion

that is different from that of the counter-rotating pairs. When vortices 1-2 or 3-4 are exiting

the downwash of the vortex system $(0^o < \theta < 90^o$ or $180^o < \theta < 270^o)$, $v_{rel} > 0$ and the

distance from vortex 2 to the right-hand side centroid is increasing. However, when vortices

1-2 or 3-4 are entering the downwash $(90^o < \theta < 180^o$ or $270^o < \theta < 360^o)$, $v_{rel} < 0$

and the distance between vortex 2 and the right-hand side centroid is decreasing. The

descent velocity of the vortex system (Figure 3.4d) oscillates during the orbit period and,

in a manner similar to $\Omega(t)$, it has local extrema at $\theta \approx 0^o, 90^o, 180^o$, and 270°. For $\theta \approx 0^o$

and 180°, the four vortices are co-linear and w_c has local minima. On the other hand, at θ

$\approx 90^o$ and 270°, vortices 1-3 and 2-4 are vertically aligned and w_c attains local maxima.

The results for Case 4, in which $b^* = 5.0$, are displayed in Figure 3.5. The primary

difference in the results of Case 3 and Case 4 is that the oscillation amplitudes of $\Omega(t)$, v_{rel},

and w_c are smaller over the orbit cycle. This indicates that the vortex pairs are behaving

more independently of one another. In fact, the orbit period for Case 4 is only 4.3% greater

than that of an isolated pair. An important conclusion can be drawn from the calculations

of these four cases: *as one might expect, the larger the distance between the vortex pairs,*

whether they be counter-rotating or co-rotating, the more the individual pairs behave as

isolated, single pairs.

3.2.3   Rate of Strain Field in the Vicinity of Vortex 2

With the time-varying vortex positions, descent velocities, and angular velocities

known, it is now possible to compute the streamlines and, hence, the rate of strain field in

a coordinate system that travels with one of the vortices. In a manner similar to that in

Section 2.2, assume that at a given angle, $\theta(t)$, vortex 2 is perturbed from its equilibrium

position by a distance (y', z') (Figure 3.1). The streamfunction, which is computed in a

reference frame that is fixed to the time-dependent position of vortex 2, is given by

$$\Psi(y', z', t) = \Psi_{12p} + \Psi_{32p} + \Psi_{42p} - \Psi_{rot} - \Psi_{rel} - \Psi_c \tag{3.6}$$

where Ψ_{n2p} is the value of the streamfunction of vortex n $(n \neq 2)$ at the perturbed location of vortex 2 and is defined as

$$\Psi_{n2p} = -\frac{\Gamma_n}{2\pi} ln(r_{n2p}) \tag{3.7}$$

The variable r_{n2p} is the distance from vortex n to the perturbed location of vortex 2 and is given by

$$r_{n2p} = \sqrt{[y_2(t) - y_n(t) + y'cos\theta - z'sin\theta]^2 + [z_2(t) - z_n(t) + y'sin\theta + z'cos\theta]^2} \tag{3.8}$$

The term

$$\Psi_{rot} = -\frac{\Omega(t)}{2} r_{c2p}^2 \tag{3.9}$$

in Eq. 3.6 is the streamfuction due to the solid-body rotation of vortex 2 about the right-hand side circulation centroid, where

$$r_{c2p} = \sqrt{[y_2(t) - y_c(t) + y'cos\theta - z'sin\theta]^2 + [z_2(t) - z_c(t) + y'sin\theta + z'cos\theta]^2} \tag{3.10}$$

is the distance from the right-side circulation centroid, $(y_c(t), z_c(t))$, to the perturbed location of vortex 2. The term

$$\Psi_{rel} = v_{rel} \ y' \tag{3.11}$$

is the streamfunction due to the motion of vortex 2 relative to the the right-side circulation centroid in the $\mathbf{e}_{y'}$ direction. Finally, the term

$$\Psi_c = w_c(t)z'sin\theta - y'w_c(t)cos\theta \tag{3.12}$$

is the streamfuction due to the downward velocity, $w_c(t)$, of the right-side circulation centroid.

With the introduction of the additional vortex pair, the question arises as to whether or not the strain rate field in vortex 2's reference frame will differ from that computed for a single vortex pair in Section 3.2.3. Previously, it was shown that a single counter-rotating

pair with vortices of comparable strengths has a stagnation point flow that counteracts the self-induced rotation rate of vortex 2, rendering it unstable. However, the single co-rotating pairs were shown to be stable because the fluid motion about them rotates clockwise, the same direction as vortex's self-induced rotation rate. Therefore, the perturbations oscillate periodically in time. In the present analysis, the stability or instability of vortex 2 is not quite as simple to determine by merely examining the streamline images. The reason is that because the equilibrium flow is unsteady, the streamlines found from Eq. 3.6 do not necessarily match the pathlines that a perturbation would follow. Therefore, in the discussion to follow, only the qualitative features of the streamlines that *may* lead to stability or instability are addressed.

Strain Fields for the Counter-Rotating Pairs

Figures 3.6 and 3.7 demonstrate the streamlines for the two counter-rotating cases. Each of the plots is rotated at its respective angle, $\theta(t)$, in order to better illustrate the orientation of vortex 2 in the orbit period. It can be seen in Figure 3.6 and Figure 3.7 that at $\theta = 0^o$, the streamlines are different from those of a single counter-rotating pair (Figures 2.5a) in that they are shifted slightly to the right. This effect is more apparent for Case 1 in which the 2-4 vortex pair is located more closely to the other pair. At the other points of the orbit cycle, the stagnation point flows in Figures 3.6 and 3.7 are very similar to that in Figure 2.5a. This implies that the effects of the additional vortex pair on the stability properties of vortex 2 are minimal. *It is hypothesized that the instability on one of the counter-rotating pairs is driven primarily by the strain rate field between the neighboring vortices within the pair and not by the strain rate field from the other vortex pair.*

Strain Fields for the Co-Rotating Pairs

The streamlines for the two co-rotating cases are shown in Figures 3.8 and 3.9. It is immediately apparent that there is a strong effect of the pair spacing on the streamline shapes. For Case 3, in which $b^* = 2.0$, the streamlines transition back and forth from an elliptical, clockwise flow ($\theta = 0^o, 180^o$) to a stagnation point flow ($\theta = 90^o, 270^o$). This
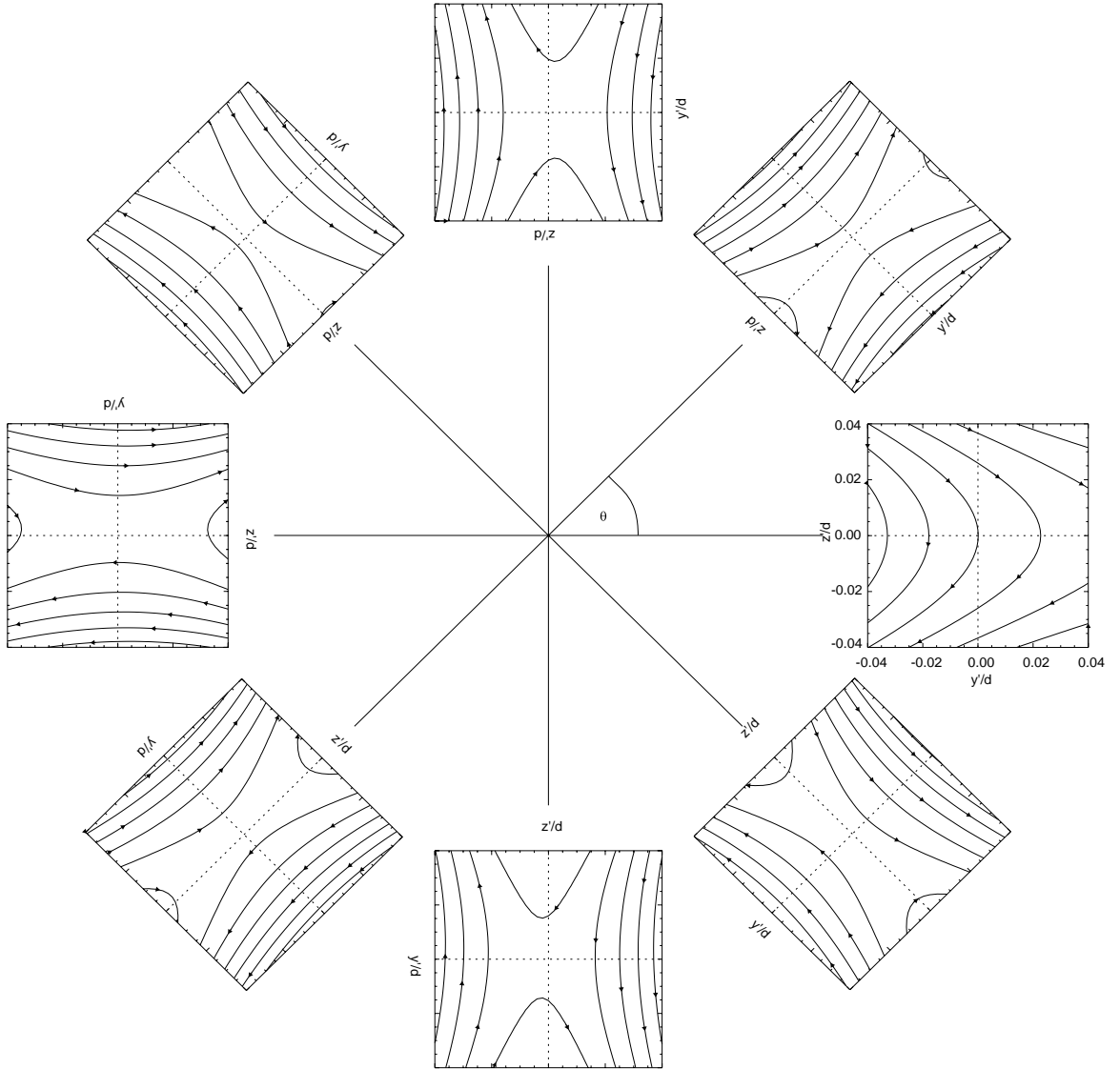
Figure 3.6: Rate of strain field about vortex 2 for the counter-rotating vortex pairs in Case 1 ($\Gamma_2 = 1$ (cm^2/s), $\Gamma_4 = $ -0.6 (cm^2/s), $b^* = 6$ (cm), $d = 1$ (cm)) at various orientations in the orbit period. The (y', z') coordinate system is fixed with respect to vortex 2.
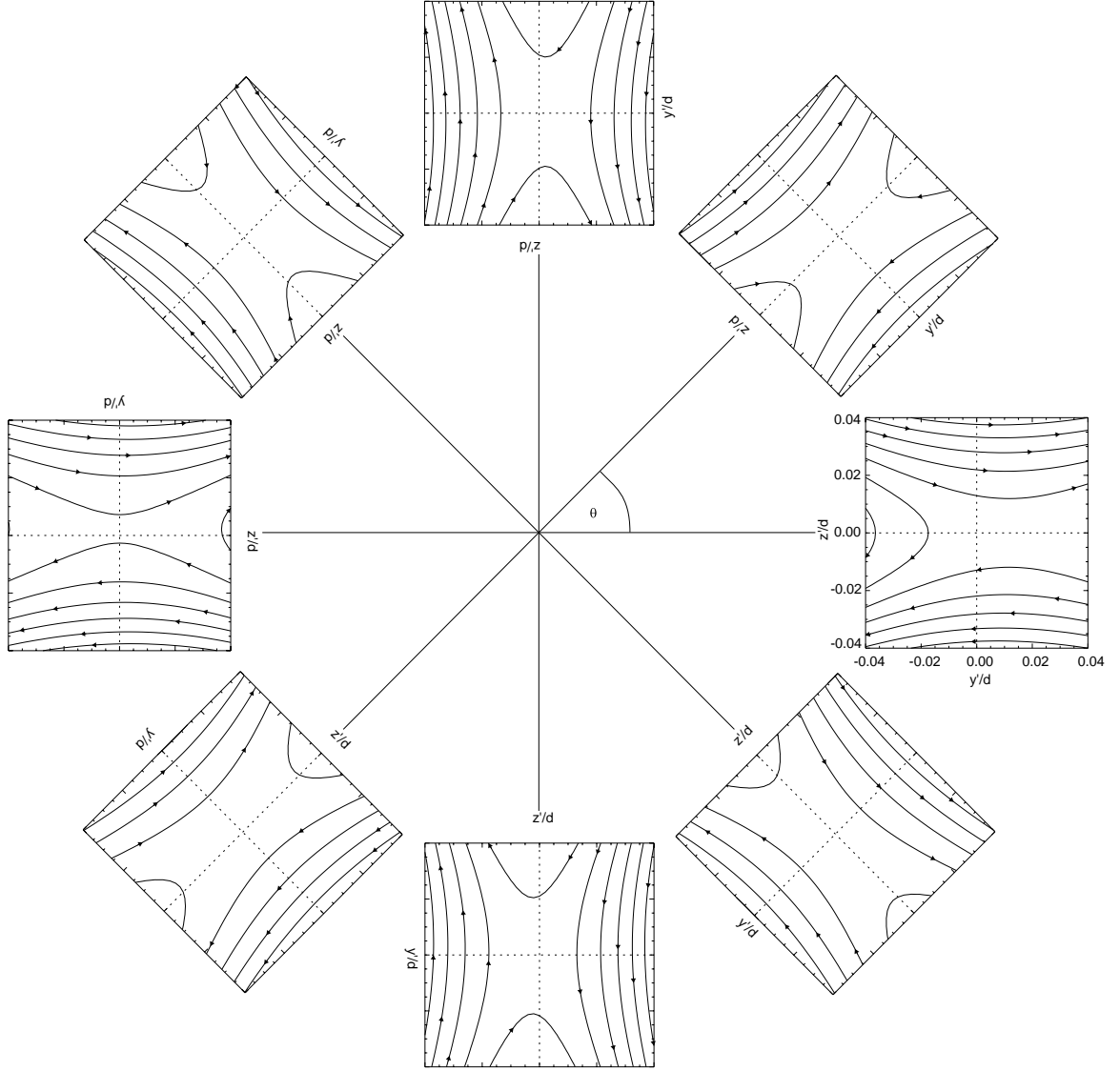
Figure 3.7: Rate of strain field about vortex 2 for the counter-rotating vortex pairs in Case 2 ($\Gamma_2 = 1$ (cm^2/s), $\Gamma_4 = $ -0.6 (cm^2/s), $b^* = 10$ (cm), $d = 1$ (cm)) at various orientations in the orbit period. The (y', z') coordinate system is fixed with respect to vortex 2.
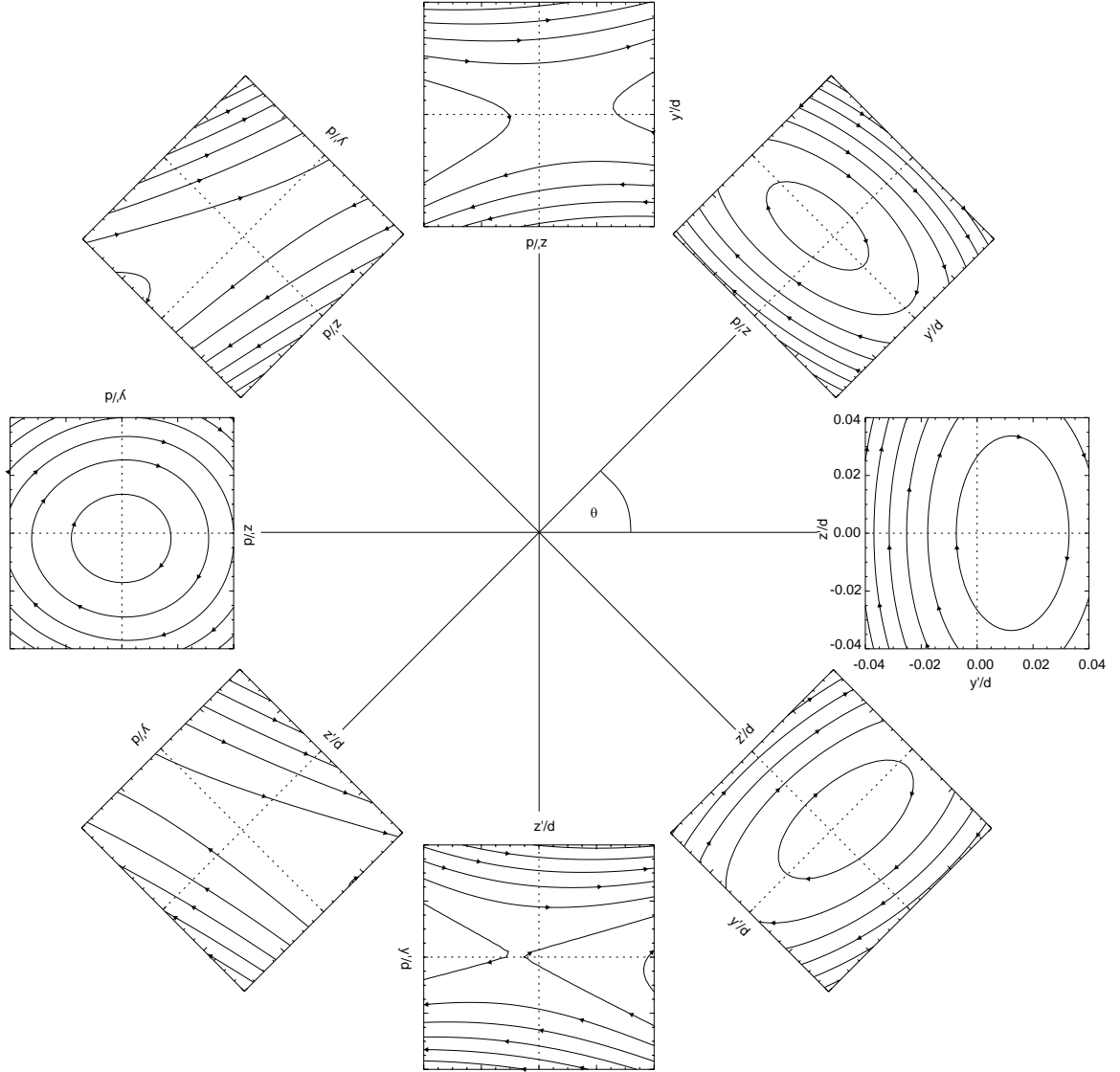
Figure 3.8: Rate of strain field about vortex 2 for the co-rotating vortex pairs in Case 3 (Γ_2 = 0.4 (cm^2/s), Γ_4 = 1 (cm^2/s), b^* = 2 (cm), d = 1 (cm)) at various orientations in the orbit period. The (y', z') coordinate system is fixed with respect to vortex 2.
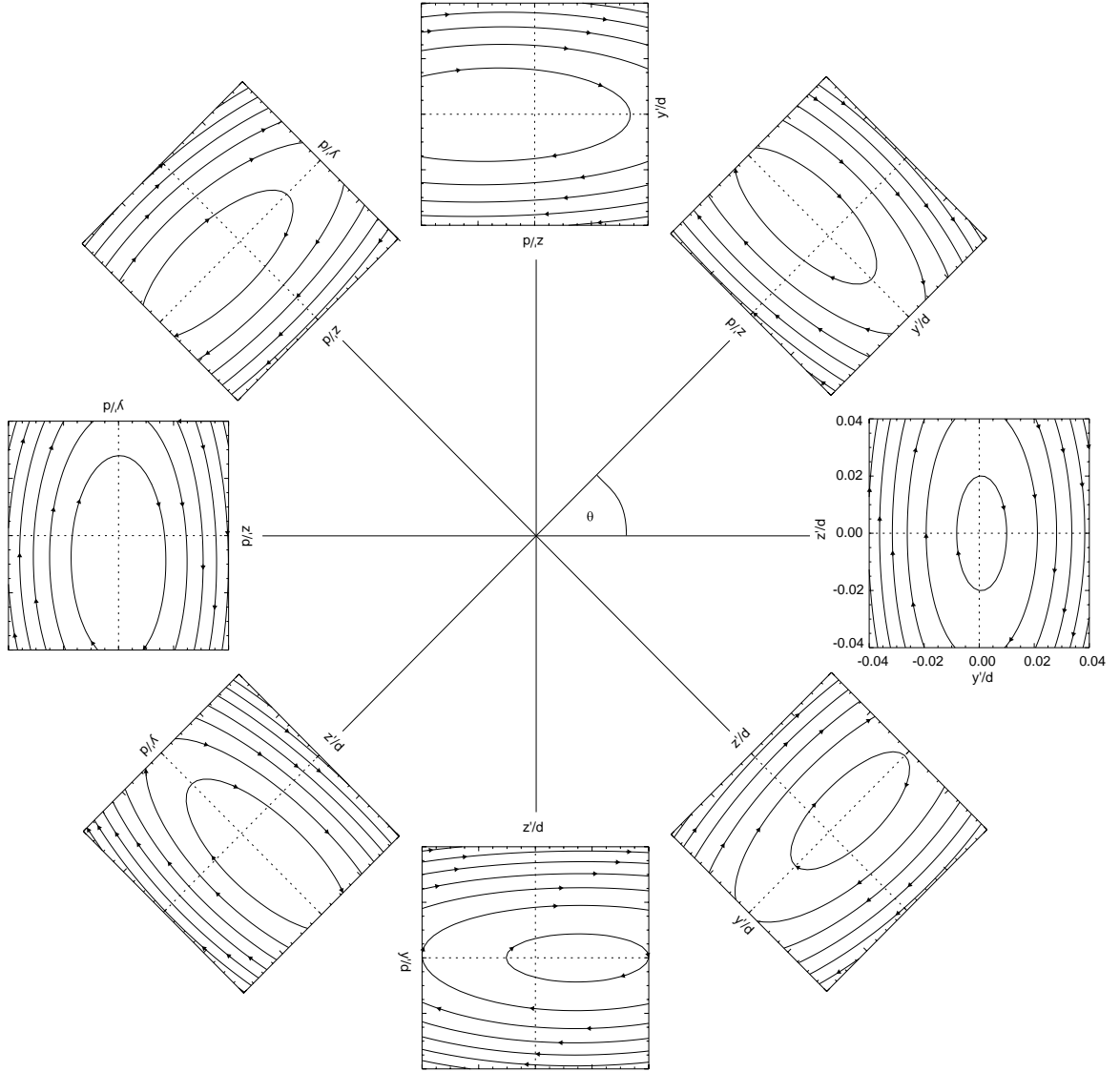
Figure 3.9: Rate of strain field about vortex 2 for the co-rotating vortex pairs in Case 4 (Γ_2 = 0.4 (cm^2/s), Γ_4 = 1 (cm^2/s), b^* = 5 (cm), d = 1 (cm)) at various orientations in the orbit period. The (y', z') coordinate system is fixed with respect to vortex 2.

transitioning is correlated with the angular velocity of vortex 2 about the right-hand side circulation centroid. It was shown in Section 2.3.2 that the angular velocity has a stabilizing effect on the stability characteristics of a single vortex pair, rendering the streamlines either elliptical or nearly circular. Judging from the flow patterns in Figure 3.8, $\Omega(t)$ appears to a have similar effect in the four vortex system. At $\theta = 0^o$, $\Omega(t)$ has a local maximum and the streamlines are elliptically shaped and directed clockwise. Furthermore, at $\theta = 180^o$, $\Omega(t)$ has a global maximum and the streamlines appear almost circular. However, at $\theta = 90^o$ and 270°, $\Omega(t)$ has local minima and, therefore, has less of a stabilizing influence on the flow. Consequently, a stagnation point flow is generated at these orientations.

The streamlines for Case 4 appear to be very similar to those of a single vortex pair (Figure 3.9). Regardless of θ, the only changes that occur to the streamlines are small displacements from the origin and slight angular shifts in the orientation of the major and minor axes of the elliptical flow. By comparing Case 3 with Case 4, one might infer that the presence of additional vortex pair destabilizes the original pair in Case 3, but has little effect upon the original pair in Case 4. However, without numerically calculating the amplitude of a perturbation over an orbit cycle, no definite conclusions can be drawn at this point. The linear stability analysis in the following section will provide quantitative results of whether or not an instability exists for these two co-rotating cases.

3.3 Linear Stability Analysis for Two Vortex Pairs

In this section, the linear stability analysis performed in Section 2.3 will be extended to include the effects of an additional vortex pair. The disturbance growth rate will be computed as a function of the perturbation wavenumber for the vortex systems discussed in the previous section. This will provide a quantitative assessment of the stability properties of Cases 1-4, which up to this point have only been analyzed in terms of the strain rate fields. Crouch [16] studied the linear stability properties of two co-rotating vortex pairs. His stability analysis will be implemented in this section and broadened to include counter-rotating pairs. The setup of Crouch's analysis is presented here, but for the sake

of brevity, the reader is referred to [16] for a thorough discussion of the stability theory. While ϖ (Eq. 2.9) is used in [16] for the vortex self-induced rotation rate, the more accurate Kelvin/Saffman rotation rate, $\bar{\varpi}$ (Eq. 2.11), will be utilized in the following section instead.

3.3.1 Mathematical Formulation

Crouch's model of the vortex wake is shown in Figure 3.10. As in Section 3.2, the tip vortices are labeled 1 and 2 and the flap vortices 3 and 4. Each of the vortices is modeled as a vortex filament of core radius a. The total positive circulation is $\Gamma_0 = \Gamma_2 + \Gamma_4$. The equations are non-dimensionalized by the length scale b^* and the time scale by $2\pi b^{*2}/\Gamma_0$. This normalization introduces two dimensionless variables: d/b^* and $\Gamma = \Gamma_2/\Gamma_4$. The initial positions of the vortices are

$$y_2(0) = \frac{1}{2} + \Gamma(d/b^*)/(1+\Gamma), \quad y_4(0) = \frac{1}{2} - (d/b^*)/(1+\Gamma) \tag{3.13}$$

$$y_1(0) = -y_2(0), \quad y_3(0) = -y_4(0), \quad z_n(0) = 0, \quad n = 1, 2, 3, 4 \tag{3.14}$$

The dimensionless flap and tip circulations are expressed as $\Gamma_2' = -\Gamma_1' = 1/(\Gamma + 1); \Gamma_4' = -\Gamma_3' = \Gamma/(\Gamma + 1)$. The perturbation wavenumber is denoted by kb^* and the instability growth rate by γ. The perturbations to vortex n in the $y-$ and $z-$directions are denoted by η_n and ξ_n (Figure 3.10). The linear stability analysis that follows is identical to that of Crouch's with only one change. Rather than using the self-induced rotation rate ϖ in Eq. 2.9, which is subject to errors for larger wavenumbers (Figure 2.3), the present analysis employs the rotation rate, $\varpi^* = \varpi' \, b^{*2}/a^2$ from Eq. 2.11. With this change, Eqs. 2.26-2.29 of Crouch [16] become

$$V_{1nn} = W_{1nn} = 0 \tag{3.15}$$

$$V_{2nn} = \Gamma_n' \varpi' b^{*2}/a^2 \tag{3.16}$$

$$W_{2nn} = -\Gamma_n' \varpi' b^{*2}/a^2 \tag{3.17}$$
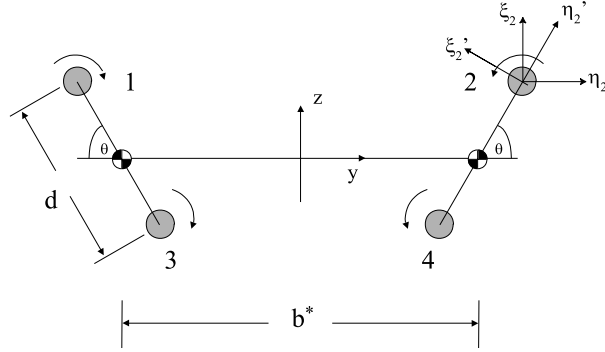
Figure 3.10: Schematic of the four-vortex system.

The counter-rotating and co-rotating vortex pairs discussed in Section 3.2.3 are now analyzed to quantitatively assess their stability properties. Table 3.2 displays the values of Γ, d/b^*, a/b^*, and orbit period, τ, of the vortex systems in terms of Crouch's notation. Note that the core sizes for each of the four cases are 15% of the flap/tip separation distances. The time steps, Δt, used for these vortex systems are also listed in Table 3.2. Further reductions in Δt lead to changes of $O(10^{-2})$ in the subsequent results. Table 3.2 lists the upper wavenumber, kb^*_{upper}, for which the calculations are made. These values are chosen such that $ka_{upper} = 0.3$ for all four cases. The maximum growth rate, γ_{max}, corresponding wavenumber, kb^*_{max}, and mode are also listed in Table 3.2 for each of the four cases.

Case	Γ	d/b^*	a/b^*	Δt	kb^*_{upper}	τ	kb^*_{max}	γ_{max}	$Mode_{max}$
1	-0.6	0.1666	0.025	0.0020	12.0	0.188	6.3	81.8	S1
2	-0.6	0.1000	0.015	0.0008	20.0	0.0648	10.0	209.3	A1
3	2.5	0.5000	0.075	0.0250	4.0	2.325	1.18	1.63	A2
4	2.5	0.2000	0.030	0.0030	10.0	0.264	5.07	1.48	A2

Table 3.2: Parameters for each of the linear stability analyses.

In computing the growth rate curves for Cases 1-4, the unstable eigenmodes are classified as being either symmetric or anti-symmetric as in [16]. A symmetric mode of vortices 1 and 2 is one in which the perturbations in the y-direction satisfy $\eta_1 = -\eta_2$ and

those in the z-direction $\xi_1 = \xi_2$. An anti-symmetric mode is one in which $\eta_1 = \eta_2$ and $\xi_1 = -\xi_2$. Two symmetric modes, S1 and S2, are defined, where the difference between them being that for the S1 mode

$$\eta_1\eta_3 + \xi_1\xi_3 > 0 \tag{3.18}$$

and for the S2 mode

$$\eta_1\eta_3 + \xi_1\xi_3 < 0 \tag{3.19}$$

Similarly, two anti-symmetric modes, A1 and A2, are defined, where A1 follows Eq. 3.18 and A2 Eq. 3.19. Examples of the four mode categories are illustrated in Figure 3.11.
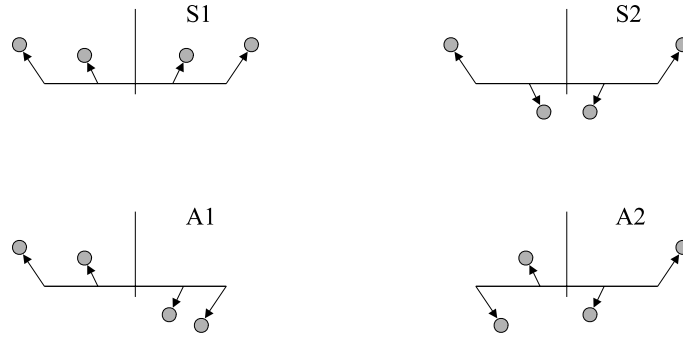
Figure 3.11: Classifications of the instability mode shapes.

3.3.2 Stability Properties of Counter-Rotating Pairs

The growth rate curves for Case 1 are demonstrated in Figure 3.12. The left-hand side and lower axes are the instability growth rate, γ, and perturbation wavenumber, kb^*, for the entire four-vortex system. Note that the growth rate γ is in terms of the strain rate field that one vortex pair produces on the other vortex pair. The right-hand side and upper axes are the corresponding growth rate, α, and perturbation wavenumber, kd, for a single vortex pair, as defined in Section 2.3. The growth rate, α, is the rate of strain from vortex 2 on vortex 4. Figure 3.12 demonstrates that all four modes are unstable over a certain range of wavenumbers. In a manner similar to the Crow instability, the smaller growth rate, S1
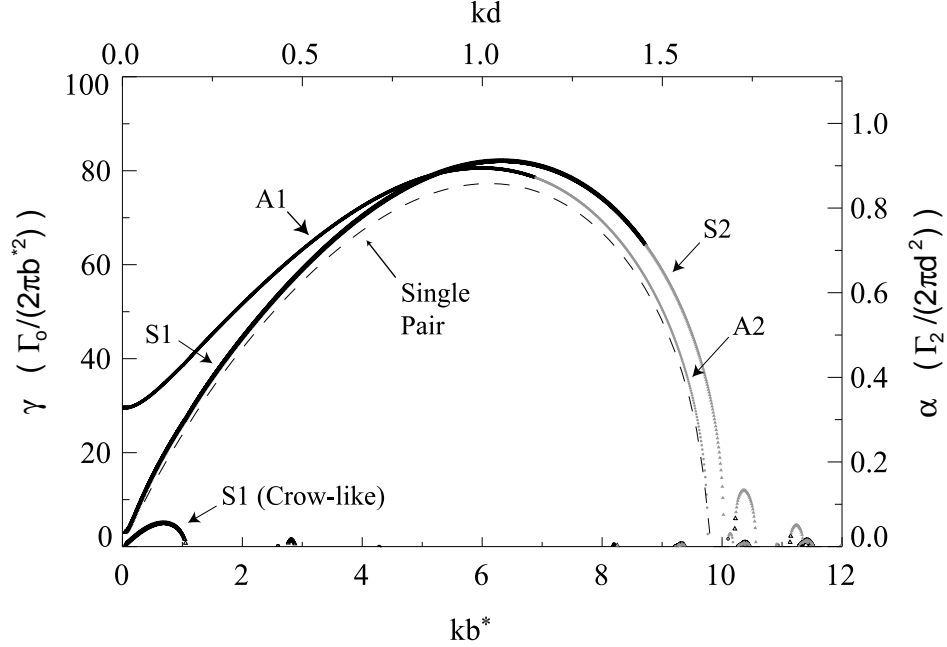
Figure 3.12: Growth rate curves for the counter-rotating vortex pairs in Case 1 ($\Gamma = -0.6$, $d/b^* = 0.1666$, $a/b^* = 0.025$). The S1 and A1 modes are denoted by black symbols and the S2 and A2 modes by gray symbols. The dashed line is the growth rate curve of a vortex pair comprised of vortices 2 and 4, where $\Gamma = -0.6$ and $a/d = 0.15$.

mode is unstable to perturbations of small wavenumbers. This S1 mode has a maximum growth rate of $\gamma = 4.7$ at a wavelength equal to $\lambda/b^* = 2\pi/kb^* = 2\pi/0.65 = 9.7$. Because the maximum growth rate, $\gamma = 4.7$, is greater than 1.0, the instability grows faster than it would if the two vortex pairs were replaced by two oppositely-signed vortices located at the left and right circulation centroids.

The most noticeable features of Figure 3.12 are the symmetric and anti-symmetric modes that are unstable over the majority of the calculated wavenumbers. At $kb^* = 6.3$, the S1 mode has a maximum growth rate of $\gamma = 81.8$, which is about 16 times larger than the Crow-like S1 instability discussed above. The large growth rate S1 mode is unstable at lower wavenumbers. Note that there are two growth rate curves for the S1 mode at low perturbation wavenumbers, indicating that the S1 mode manifests itself in two forms simultaneously. However, in an actual flow, the large growth rate S1 mode would grow

more quickly than the Crow-like S1 mode and probably become the dominate instability in the wake. At $kb^* \approx 9.5$, the S1 mode transitions to a S2 mode as Eq. 3.18 goes from being positive to negative. Around $kb^* \approx 10$, the S2 mode becomes stable. An interesting phenomena occurs for the anti-symmetric mode as $kb^* \to 0$. Rather than being stable as the symmetric modes are, the A1 mode exhibits instability to perturbations that have an infinite wavelength. Consequently, the four-vortex system is unstable to the A1 mode in a two-dimensional manner. To visualize how this type of instability evolves, the four-vortex system is perturbed with the A1 mode, $(\eta_1, \eta_2, \eta_3, \eta_4, \xi_1, \xi_2, \xi_3, \xi_4) = (0.00153, \ 0.00153,$ $0.00724, \ 0.00724, \ 0.00471, \ -0.00471, \ 0.00786, \ -0.00786)$, at a wavenumber of $kb^* = 10^{-4}$. This A1 mode is the eigenvector of the four-vortex system at $kb^* = 10^{-4}$. The total perturbation magnitude,

$$\sqrt{\sum_{n=1}^{4}(\eta_n^2 + \xi_n^2)} \tag{3.20}$$

is chosen to be 0.01666, or 10% of the separation distance between vortices 2 and 4. The transient behavior of the perturbations is obtained by solving Crouch's [16] Eqs. 2.32-2.37. Figure 3.13a shows the total perturbation magnitude (Eq. 3.20) over one orbit period. It can be seen that the perturbation magnitude quickly grows to 4.324 by the end of the orbit period at the predicted growth rate of $\gamma = 29.5$. Note that the assumption of small perturbation amplitudes ($|\eta_n|/(d/b^*) << 1$ and $|\xi_n|/(d/b*) << 1$) quickly becomes invalid during the orbit period. Figure 3.13b demonstrates the vortex positions over one orbit period. In this figure, the initial positions of the four vortices (Eqs. 3.13 and 3.14) have been displaced by the above A1 mode. These initial vortex positions are then numerically integrated in time through the use of Eqs. 3.1 and 3.2. It can be seen that the vortex positions are no longer symmetric about the z-axis as they are in Figure 3.2a. Notice that while the right vortex pair has completed almost 1.5 orbits, the left vortex pair is orbiting at a lower angular velocity and has not yet completed one orbit period.

A useful exercise is to compare the growth rate curves for Case 1 with those obtained from a linear stability analysis on a single vortex pair. This makes it possible to determine

the effect that the additional pair has on the stability properties of the four-vortex system. Repeating the analysis in Section 2.3 for a single vortex pair, which has Γ = -0.6 and a/d = 0.15, results in the dashed growth rate curve displayed in Figure 3.12. When the growth rate curves of the four-vortex system are scaled according to α and kd, a comparison can be made between the stability properties of the single vortex pair (vortices 2 and 4) and the entire four-vortex system. It can be seen in Figure 3.12 that except for small wavenumbers, both the symmetric and anti-symmetric modes closely follow the growth rate trends of the single vortex pair. *This confirms the statement in Section 3.2.3, which hypothesized that the instability of the two counter-rotating pairs is driven primarily by the strain rate field*
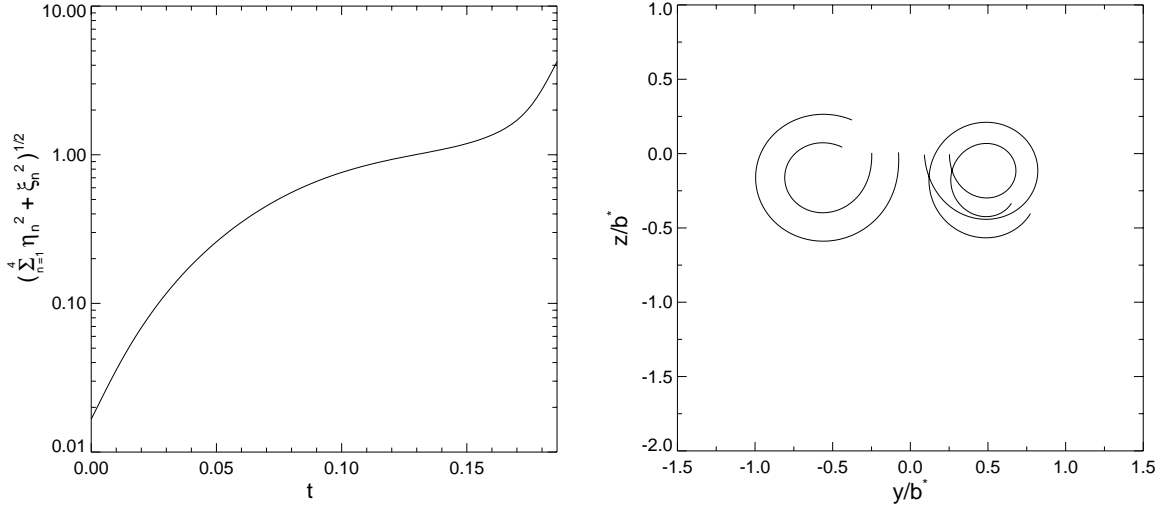
Figure 3.13: Two-dimensional instability for the A1 mode in Case 1. (a) Total perturbation magnitude (Eq. 3.20) over one orbit period when the vortex system is perturbed at $kb^* = 10^{-4}$ with the A1 mode, $(\eta_1, \eta_2, \eta_3, \eta_4, \xi_1, \xi_2, \xi_3, \xi_4) = (0.00153, 0.00153, 0.00724, 0.00724, 0.00471, -0.00471, 0.00786, -0.00786)$. (b) Transient vortex positions (Eqs. 3.1 and 3.2) for $0 \le t \le 0.188$, where the initial positions (Eqs. 3.13 and 3.14) have been displaced by the above A1 mode at $t = 0$.

Case	Γ	Max. Growth Rate, α_{max}	Most Unstable Wavenumber, kd_{max}
1	-0.6	0.91	1.05
2	-0.6	0.84	1.01
single	-0.6	0.86	1.01

Table 3.3: A comparison of the maximum growth rates and corresponding wavenumber for the counter-rotating vortex pairs in (a) Case 1 and (b) Case 2 with those a single counter-rotating pair. The dimensionless vortex core size for all three cases is $a/d = 0.15$. The maximum growth rates are in the units of $\Gamma_2/(2\pi d^2)$ and the most unstable wavenumbers are in the units of kd.

of the vortices within each pair and not by the strain rate field of the other vortex pair. Table 3.3 highlights some of these similarities. The most unstable wavelength for the S1 mode is $\lambda/d = 6.0$, while that of the single vortex pair is $\lambda/d = 6.22$. The maximum growth rates of the two- and four-vortex systems are also in close agreement. When scaled according to the growth rate α and wavenumber kd, the maximum growth rate of the four-vortex system is $\alpha = 0.91$, while that of a single pair is $\alpha = 0.86$. Figure 3.14a shows the shape of the most unstable eigenmode for the two- and four-vortex systems. It can be seen that the orientations of the flap and tip vortices in Case 1 are very similar to those of the single vortex pair.

The effects of decreasing the relative distance between the vortices from $d/b^* = 0.1666$ to $d/b^* = 0.1$ can be seen in the growth rate curves for Case 2 in Figure 3.15. At this smaller value of d/b^*, the long-wavelength, Crow-like, S1 instability between the two vortex pairs is less pronounced when compared to the larger growth rate modes. Although it is difficult to discern in Figure 3.15, the growth rates for the dominant symmetric and anti-symmetric modes coincide with one another for almost all wavenumbers. These modes also transition from S1 to S2 and A1 to A2 at $kb^* = 12.2$. It is near $kb^* = 0$ that the symmetric and anti-symmetric modes differ slightly from one another. Like in Case 1, the A1 mode is unstable as $kb^* \to 0$, while the S1 mode is stable. The growth rate curve for a single vortex pair (vortices 2 and 4) is indicated in Figure 3.15 by the dashed line. At this smaller relative
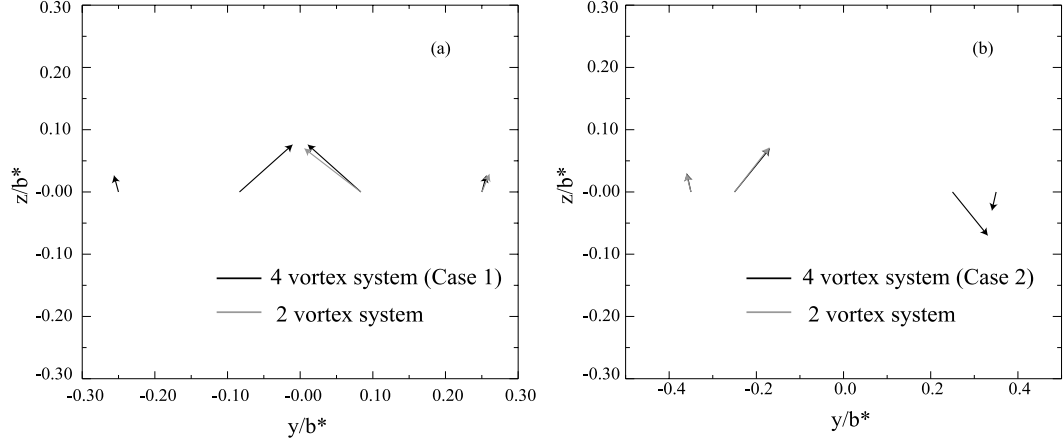
Figure 3.14: Most unstable mode shapes for the counter-rotating vortex pairs in (a) Case 1 ($\Gamma = -0.6$, $d/b^* = 0.1666$, $a/b^* = 0.025$, S1 mode at $kb^* = 6.3$) and (b) Case 2 ($\Gamma = -0.6$, $d/b^* = 0.1$, $a/b^* = 0.015$, A1 mode at $kb^* = 10.0$). The eigenvectors for the four-vortex systems are shown in black and that of an equivalent, single vortex pair ($\Gamma = -0.6$, $a/d = 0.15$) in gray.

separation distance, the growth rate curves of the four-vortex system are even closer to that of the single pair. The most unstable eigenmode (A1 at $kb^* = 10.0$) for Case 2 is shown in Figure 3.14b. Note that the perturbations to the single vortex pair are plotted on the left side of the wake for a better comparison with the perturbations to the four-vortex system. It can be seen that the eigenmode for the single pair coincides almost directly with that of the left-hand pair.

Two important conclusions can be made from the analysis of Cases 1 and 2. *First, the most rapidly growing instability of the two counter-rotating pairs is primarily driven by the strain rate field of the oppositely signed vortices within each pair.* Consequently, the unstable wavelengths and growth rates are well approximated by those of an isolated, counter-rotating pair. *Second, the primary instability of the four-vortex system grows faster and occurs at a wavelength that is shorter than that of the classic Crow instability.*
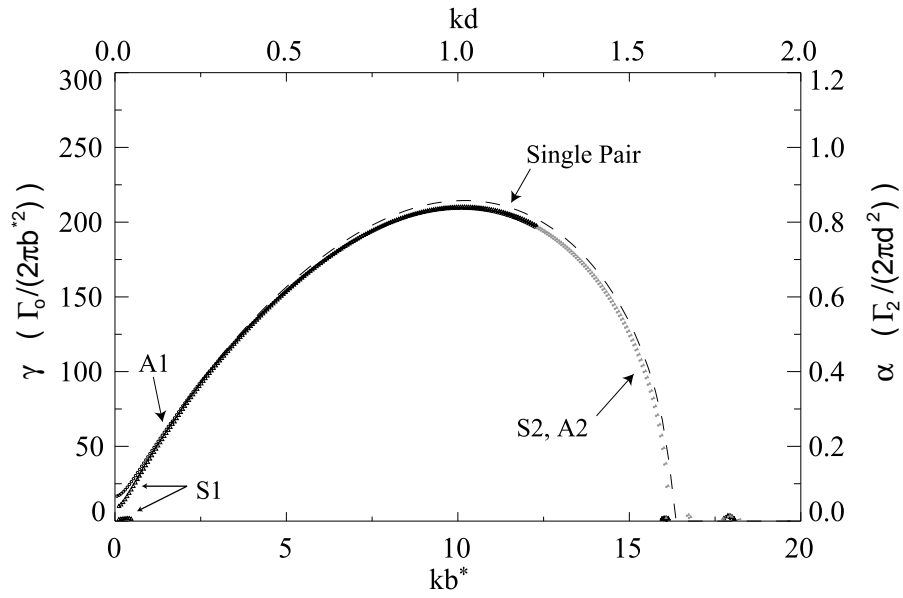
Figure 3.15: Growth rate curves for the counter-rotating vortex pairs in Case 2 ($\Gamma = -0.6$, $d/b^* = 0.1$, $a/b^* = 0.015$). The S1 and A1 modes are denoted by black symbols and the S2 and A2 modes by gray symbols. The dashed line is the growth rate curve of a vortex pair comprised of vortices 2 and 4, where $\Gamma = -0.6$ and $a/d = 0.15$.

3.3.3   Stability Properties of Co-Rotating Pairs

The growth rate curves for Case 3 are shown in Figure 3.16. Unlike a single, like-signed pair that is always stable to long-wavelength perturbations, the two co-rotating pairs are unstable over a significant range of wavenumbers. Therefore, the additional pair is the source of instability to long-wavelength disturbances. The S1 mode in Figure 3.16 is similar to the Crow instability, having a maximum growth rate of $\gamma = 0.71$ at $kb^* = 0.78$ or a wavelength of $\lambda/b^* = 8.06$. The S2 mode demonstrates instability several times over the range of calculated wavenumbers. For $kb^* \to 0$, the S2 mode is unstable in a two-dimensional sense and at moderate values of kb^*, has a peak growth rate of $\gamma = 1.15$. At larger wavenumbers, the S2 mode becomes unstable again and appears to attain a local maximum at $kb^* \approx 4$. The most unstable mode for Case 3 is A2, which has a maximum growth rate of $\gamma = 1.63$ at $kb^* = 1.18$. The shape of this most unstable mode is plotted in Figure 3.17a. In a manner similar to the S2 mode, the A2 mode exhibits instability as $kb \to 0$ and at larger wavenumbers. One observation from Figure 3.16 is that the growth rate curves of the S2 and A2 modes both rise above a value of 1.0 over a certain range of wavenumbers. *Physically, this means that the instability is growing faster than it would if the vortex pairs were replaced by two equivalent strength, counter-rotating vortices located at the right and left circulation centroids. Therefore, the vortices within each of the pairs or the vortices from different pairs must be interacting with each other during the orbit period and generating strain rate fields that have extensional components greater than $\Gamma_o/2\pi b^{*2}$.*

Reducing the relative separation distance between the co-rotating pairs from $d/b^* = 0.5$ to $d/b^* = 0.2$ results in the growth rate curves for Case 4 shown in Figure 3.18. Although the rate of strain fields in Section 3.2.3 might have left the impression that Case 4 is stable, the two co-rotating pairs are unstable over certain values of kb^*. The S1 mode has a peak growth rate of $\gamma = 0.82$ at $kb^* = 0.70$. The S2 and A2 modes are unstable over a narrow band of wavenumbers and have growth rate curves that lie almost directly on top of one another. The reason for the close agreement in these growth rate curves is illustrated by considering the S2 and A2 eigenmodes at A2's most unstable wavenumber, $kb^* = 5.07$ (Figure 3.17b). The perturbation shapes and magnitudes of the right side pairs are almost
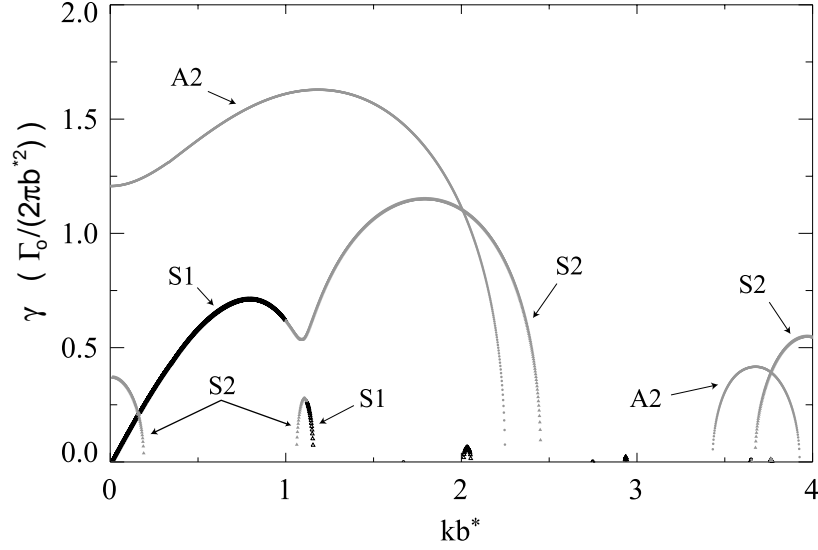
Figure 3.16: Growth rate curves for the co-rotating vortex pairs in Case 3 ($\Gamma = 2.5$, $d/b^* = 0.5$, $a/b^* = 0.075$). The S1 and A1 modes are denoted by black symbols and the S2 and A2 modes by gray symbols.
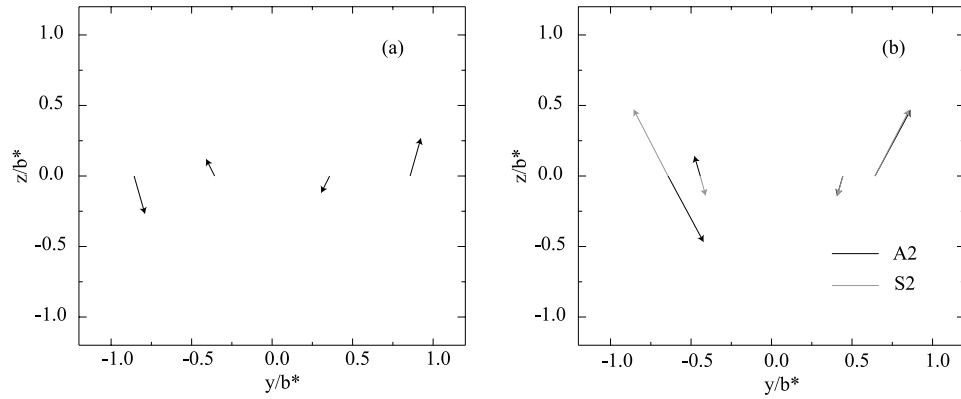
Figure 3.17: Most unstable mode shape for the co-rotating vortex pairs in (a) Case 3 (A2 mode at $kb^* = 1.18$) and (b) Case 4 (A2 mode at $kb^* = 5.07$). For Case 4, a comparison is made with S2 mode (gray arrows) at $kb^* = 5.07$.
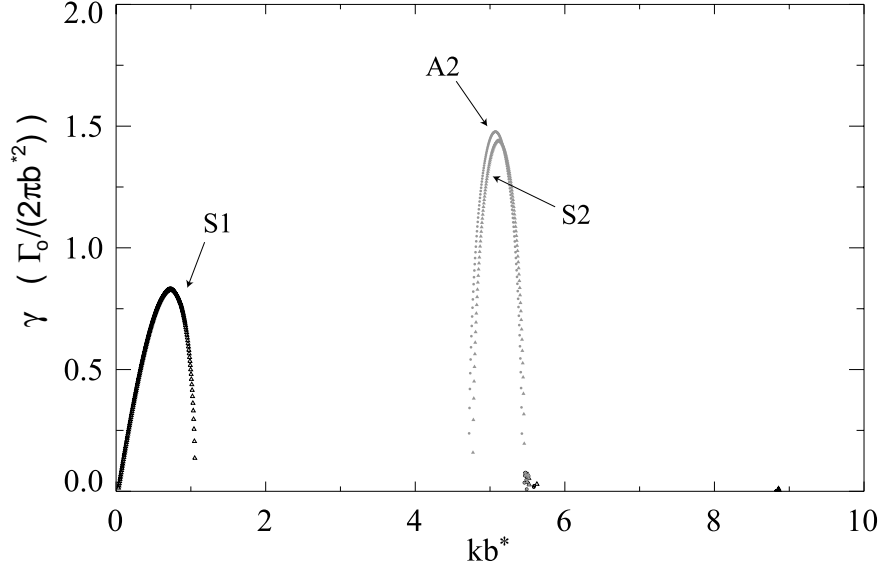
Figure 3.18: Growth rate curves for the co-rotating vortex pairs in Case 4 ($\Gamma = 2.5$, $d/b^* = 0.2$, $a/b^* = 0.03$). The S1 and A1 modes are denoted by black symbols and the S2 and A2 modes by gray symbols.

identical, while those of the left side pairs are out of phase in the axial direction by π radians. At this wider spacing between the vortex pairs, the effects of this phase difference are minimal, such that the perturbations shapes on the left sides of the S2 and A2 modes become equivalent to one another.

3.3.4 Transient Analysis of the Four Vortex Systems

To gain a deeper insight into how the long-wavelength perturbations grow in time, a transient analysis is performed on the counter-rotating and co-rotating pairs discussed in Sections 3.3.2 and 3.3.3. For each of the four cases, the vortex system is perturbed by the eigenmode corresponding to the most unstable wavenumber. The calculations are performed over one orbit period. The initial, total perturbation amplitude (Eq. 3.20) is taken to be $0.005d/b^*$ for the counter-rotating pairs and $0.15d/b^*$ for the co-rotating pairs. The reason for this difference in initial perturbation magnitudes is due to the large growth rates of the counter-rotating systems. If the initial perturbation magnitude is chosen to be

$15\%d$ for Cases 1 and 2, $|\eta_n|/(d/b^*)$ and $|\xi_n|/(d/b*)$ quickly grow to $O(1)$, invalidating the assumptions of the linear stability theory. Table 3.4 lists the initial disturbance amplitudes for all four cases.

Case	η_1	η_2	η_3	η_4	ξ_1	ξ_2	ξ_3	ξ_4
1	-2.6e-05	2.6e-05	4.0e-04	-4.0e-04	1.1e-04	1.1e-04	4.2e-04	4.2e-04
2	-2.5e-05	-2.5e-05	2.6e-04	2.6e-04	7.8e-05	-7.8e-05	2.3e-04	-2.3e-04
3	1.2e-02	1.2e-02	-8.1e-03	-8.1e-03	-4.8e-02	4.8e-02	1.8e-02	-1.8e-02
4	8.8e-03	8.8e-03	-1.2e-03	-1.2e-03	-1.9e-02	1.9e-02	4.7e-03	-4.7e-03

Table 3.4: Initial perturbations for the transient analysis of the counter-rotating (1-2) and co-rotating (3-4) cases (Table 3.2).

Transient Behavior of Counter-Rotating Systems

Figure 3.19 illustrates the time-varying perturbation amplitudes and orientations, ξ_i'/η_i', for the counter-rotating pairs. The solid lines in Figure 3.19a,c are the total perturbation amplitudes as given in Eq. 3.20, while the dashed and dotted lines are those of the right side tip (vortex number 2) and flap vortices (vortex number 4). The disturbance orientations, ξ_i'/η_i', are defined with respect to a coordinate system that rotates with the flap and tip vortices (Figure 3.10). For both counter-rotating cases, the perturbation amplitudes grow at the predicted rates with no visible transients. Note that the assumptions of the linear stability analysis, i.e. small perturbation amplitudes, soon become invalid as the perturbations grow to the order of the vortex separation distances. Prior to the breakdown of these assumptions, the tip vortex for Case 1, in which the pairs are located more closely to one another, exhibits a distinct transient in its orientation over the first quarter of the orbit period. Initially, the perturbation on the tip vortex rotates counter-clockwise, but shortly thereafter reverses direction and becomes fixed at one orientation. For both cases, the flap vortices remain at almost constant orientations over the entire orbit period, indicating that the flaps' self-induced rotation rates are balancing the azimuthal velocity
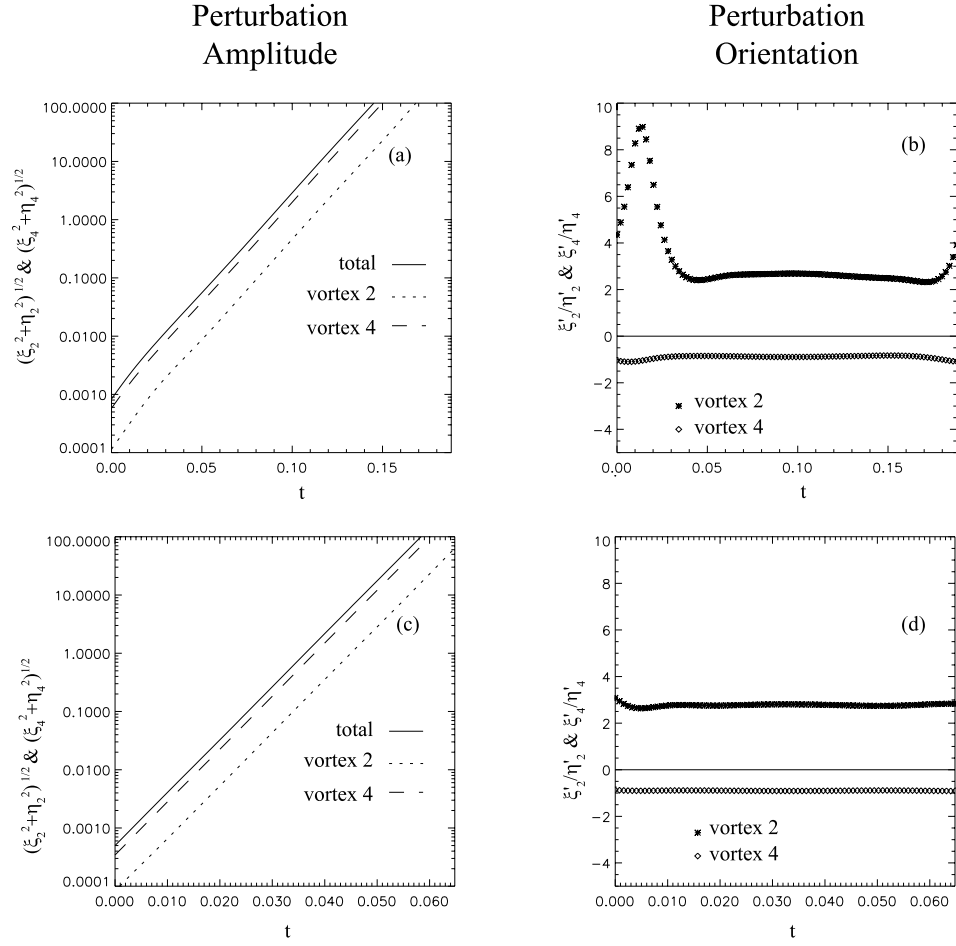
Figure 3.19: Transient perturbation amplitudes and orientations of the most unstable mode for the counter-rotating vortex pairs: (a-b) Case 1 (Γ = -0.6, $d/b^* = 0.1666$, $a/b^* = 0.025$) and (c-d) Case 2 ($\Gamma = -0.6, d/b^* = 0.1$, $a/b^* = 0.015$). The total perturbation magnitude is given by Eq. 3.20. The vortex system in Case 1 is perturbed at the most unstable wavenumber, $kb^* = 6.3$, and that of Case 2 at the most unstable wavenumber, $kb^* = 10.0$.
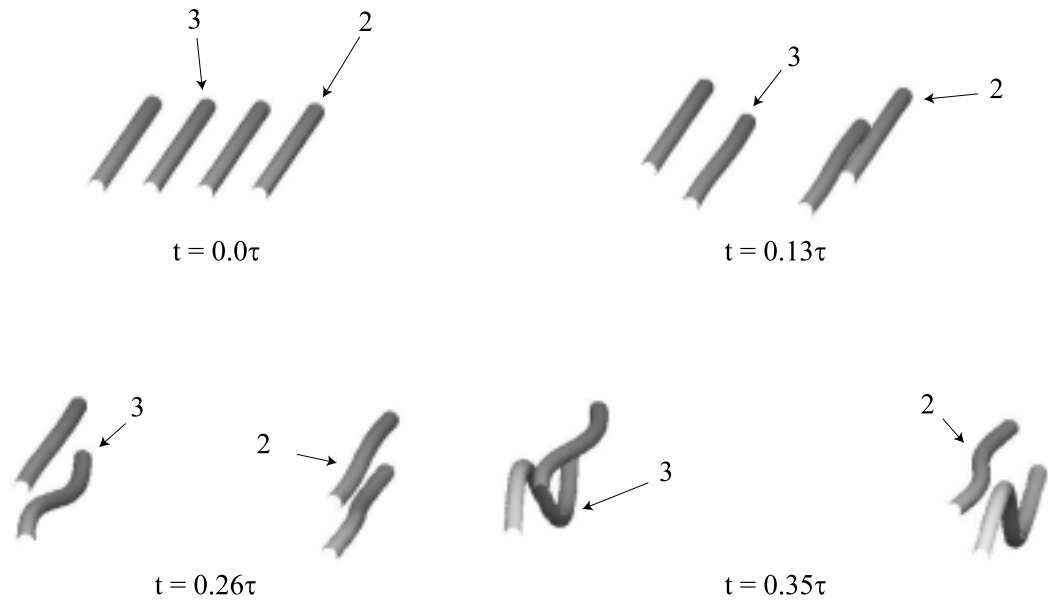
Figure 3.20: Three-dimensional views of the counter-rotating vortices for the transient analysis of the most unstable mode in Case 1 (Figure 3.19a-b) (Γ = -0.6, d/b^* = 0.1666, a/b^* = 0.025). The numbers in the figure denote vortices 2 and 3. Note that the snapshots of the orbit period are not equally spaced in time.
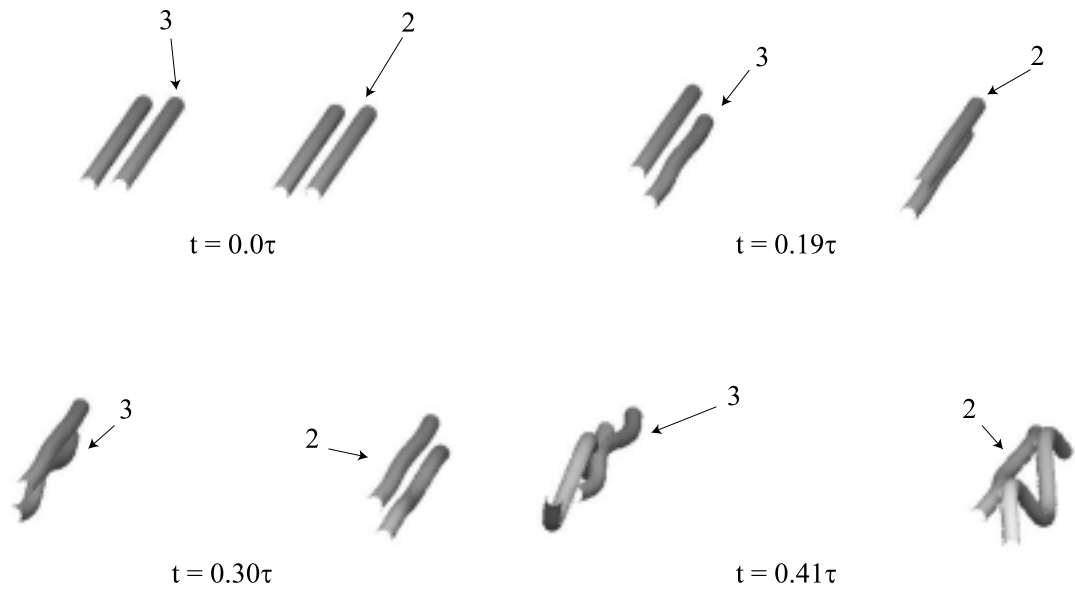
Figure 3.21: Three-dimensional views of the counter-rotating vortices for the transient analysis of the most unstable mode in Case 2 (Figure 3.19c-d) ($\Gamma = -0.6, d/b^* = 0.1$, $a/b^* = 0.015$). The numbers in the figure denote vortices 2 and 3. Note that the snapshots of the orbit period are not equally spaced in time.

component from the strain rate field of the tip vortices.

Figures 3.20 and 3.21 show a three-dimensional view of the transient behavior that better illustrates the evolution of the four-vortex system. The axial length of the vortices in Figures 3.20 and 3.21 is 1.0 such that one wavelength of the perturbation is shown for Case 1 and 1.6 wavelengths for Case 2. Although the linear stability theory becomes invalid for finite-size perturbations (by the final frame of both three-dimensional views, the assumptions of $|\xi_n|/d << 1$ and $|\eta_n|/d << 1$ are no longer valid), the three-dimensional views make it somewhat easier to speculate how the perturbations might continue to develop as the instability becomes non-linear. It is evident that as the disturbance amplitude increases, the minimum distance between the perturbations on vortices 1-3 and 2-4 decreases. At $t = 0$, the perturbations on vortices 1-3 and 2-4 are approximately separated by a distance d. As vortices orbit about one another, the disturbances on the weaker vortices (3,4) diverge in the strain rate fields of the tip vortices. This causes the disturbances on the weaker vortices to grow closer to the stronger vortices, as can be seen in Figure 3.20 (t = 0.35τ) and Figure 3.21 (t = 0.41τ). The linear stability theory discussed in this section cannot predict the non-linear behavior that would occur as vortices 1-3 and 2-4 approach one another. However, the work of Klein *et al.* [30] can be used to describe what is likely to happen as the instability becomes non-linear. One of the conclusions of [30] is that there is a finite-time collapse for a single pair of vortex filaments with a negative circulation ratio. This means that the perturbations on a counter-rotating vortex pair will grow and cause the vortices to touch one another in a finite time. Although the results of [30] are for a single counter-rotating pair, it was shown in Section 3.3.2 that the stability characteristics of the Cases 1 and 2 are very similar to those of a single, counter-rotating pair. With this observation, one can speculate that the counter-rotating vortex pairs in Cases 1 and 2 should also exhibit a finite time collapse.

This finite-time collapse for the four-vortex systems may occur in the manner shown in Figures 13 and 16 of [30], which are re-displayed in Figure 3.22. These figures demonstrate the non-linear interactions of a single vortex pair with a circulation strength ratio of $\Gamma = -0.5$. The vortex pair in Figure 3.22a has been perturbed in a symmetric manner (Eq. 5.2
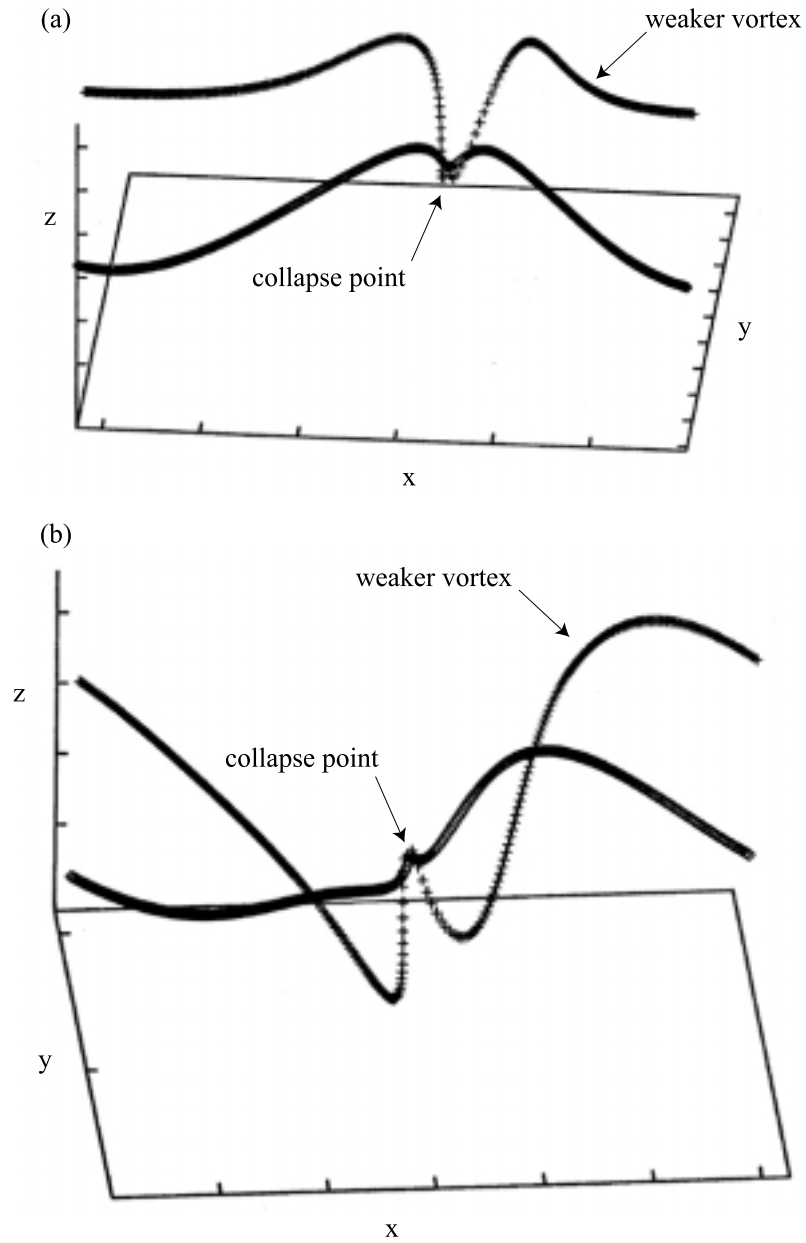
Figure 3.22: (a) Figure 13a and (b) Figure 16a from [30]. Both of these figures depict a counter-rotating vortex pair with $\Gamma = -0.5$. The vortex pair in (a) has been perturbed in a symmetric manner (Eq. 5.2 of [30]) at $t = 0$, while that in (b) has been perturbed with a symmetric helical disturbance (Eq. 5.4 of [30]) at $t = 0$. Note that the axes and labels have been modified by the present author for clarity.

of [30]) at $t = 0$, while that in Figure 3.22b has been perturbed with a symmetric helical disturbance (Eq. 5.4 of [30]) at $t = 0$. The temporal evolution of the vortex filaments is computed until the filaments make contact with one another or until a hairpin forms on one of the filaments. At this time, the asymptotic equations in [30] are no longer valid. The calculations in [30] do not include hairpin removal techniques ([11, 12]), which would allow for the reconnection of the vortex filaments and further investigation of their non-linear behavior. In Figure 3.22, the weaker vortex filament, loops around the stronger filament and is drawn in closer to it until the two filaments exhibit a finite-time collapse. During this time, the portion of the weaker filament farthest from the stronger filament remains at a large distance from the collapse point of the two filaments. So, if one could imagine copying Figure 3.22a or Figure 3.22b and placing this copy just to the left and right of Figure 3.22a or Figure 3.22b, a series of vortex hoops would emerge. Each of these hoops would begin and end at the collapse points in the x-direction of Figure 3.22. Although the calculations in [30] are done for a single vortex pair with initial conditions different than those described for Cases 1 and 2, the filament interaction described in [30] might occur between the vortices in the four-vortex systems. In Cases 1 and 2, the non-linear behavior may lead to the formation of vortex hoops if vortices 1-3 and 2-4 exhibit finite-time collapse.

Transient Behavior of Co-Rotating Systems

The co-rotating cases, displayed in Figure 3.23, demonstrate a different type of transient behavior. As expected, the total perturbation amplitudes grow significantly slower than those of the counter-rotating cases. Additionally, the disturbances on the flap and tip vortices rotate clockwise in the direction of their self-induced rotation rates, as is evident in the perturbation orientation plots in Figures 3.23b,d. An interesting observation is made from Case 3 by considering the portion of Figure 3.23a where $1.4 < t < 2.1$. Over this time range, the vortex 4 experiences a strong increase in its perturbation amplitude *and* a slowing in the time rate of change of its orientation. Both of these effects imply that the self-induced rotation rate of vortex 4 is partially balancing the rotational component of the strain field surrounding it. This incomplete balance is occurring in a portion of the strain

Perturbation
Amplitude

Perturbation
Orientation
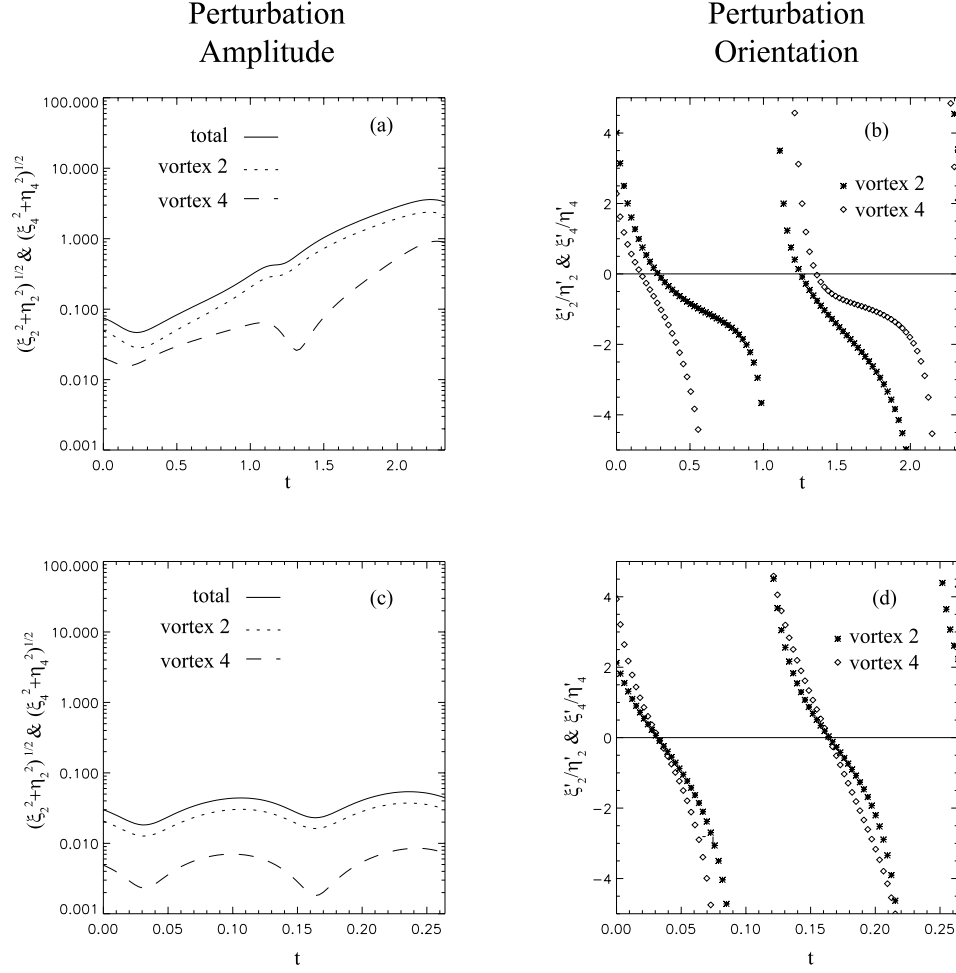
Figure 3.23: Transient perturbation amplitudes and orientations of the most unstable mode for the co-rotating vortex pairs: (a-b) Case 3 ($\Gamma = 2.5$, $d/b^* = 0.5$, $a/b^* = 0.075$) and (c-d) Case 4 ($\Gamma = 2.5, d/b^* = 0.2$, $a/b^* = 0.030$). The total perturbation magnitude is given by Eq. 3.20. The vortex system in Case 3 is perturbed at the most unstable wavenumber, $kb^* = 1.18$, and that of Case 4 at the most unstable wavenumber, $kb^* = 5.07$.
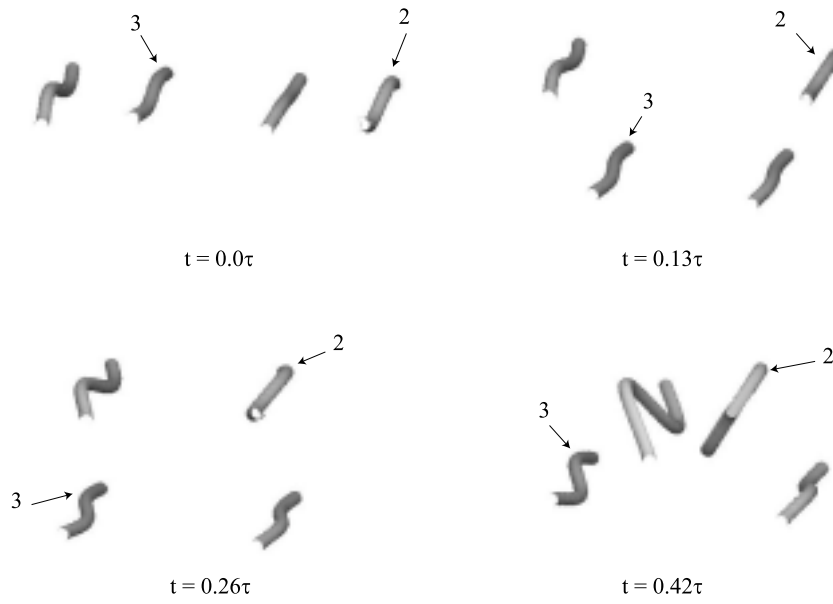
Figure 3.24: Three-dimensional views of the co-rotating vortices for the transient analysis of the most unstable mode in Case 3 (Figure 3.23a-b) ($\Gamma = 2.5$, $d/b^* = 0.5$, $a/b^* = 0.075$). The numbers in the figure denote vortices 2 and 3. Note that the snapshots of the orbit period are not equally spaced in time.
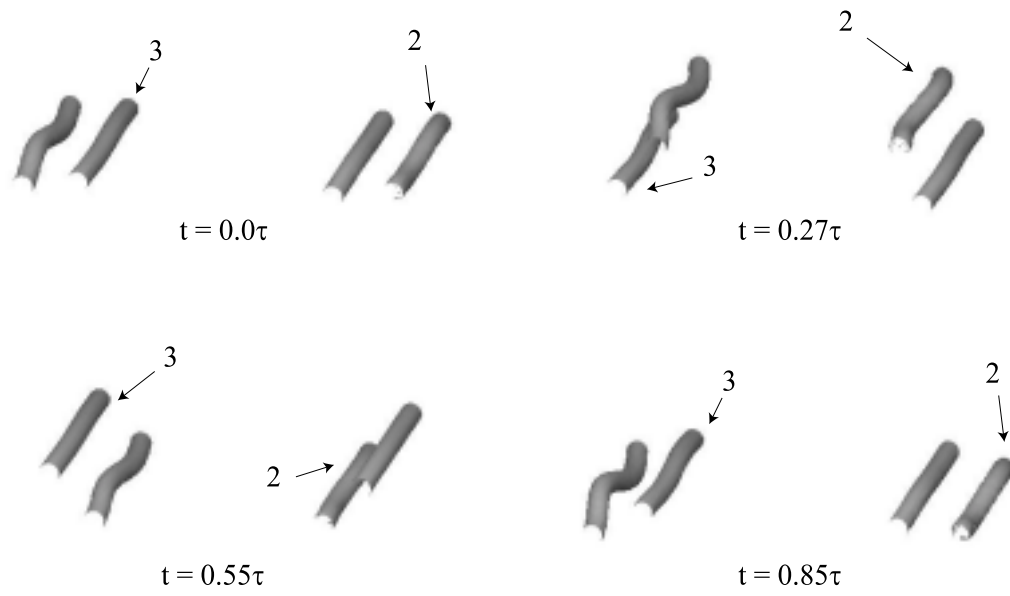
Figure 3.25: Three-dimensional views of the co-rotating vortices for the transient analysis of the most unstable mode in Case 4 (Figure 3.23c-d) ($\Gamma = 2.5, d/b^* = 0.2, a/b^* = 0.030$). The numbers in the figure denote vortices 2 and 3. Note that the snapshots of the orbit period are not equally spaced in time.

field that has a relatively large, positive, extensional component. During the latter portion of the orbit period, the perturbation amplitudes grow to the order of the flap/tip separation distance and the assumptions of the linear stability analysis become invalid. For Case 4, the disturbance amplitudes oscillate in a quasi-periodic manner over the orbit period, a behavior that is reminiscent of the neutrally stable oscillations for a single, co-rotating pair.

Figures 3.24 and 3.25 demonstrate three-dimensional views of the vortices for Cases 3 and 4. Note that the axial length of Figure 3.24 is 2π and that of Figure 3.25 for Case 4 is $\pi/2$. As was done previously with the counter-rotating vortex systems, a helpful exercise is to use the results of the linear stability theory to speculate about the types of non-linear interactions that might arise in the four-vortex systems. In addition to studying counter-rotating vortex pairs, Klein *et al.* [30] also analyzed co-rotating vortex pairs. One of the conclusions in [30] is that co-rotating vortex pairs do not exhibit finite time collapse. That is, vortex filaments in a single, isolated, co-rotating pair do not make contact with one another in a finite amount of time. With the counter-rotating pairs, it was rather straightforward to draw conclusions from the analysis in [30] and apply them to the four-vortex systems. The reason for this was that the four-vortex, counter-rotating systems have stability properties very similar to those of a single counter-rotating pair. However, this is not the case for co-rotating pairs. As discussed in Section 3.3.3, the additional co-rotating vortex pair brings about a stark change in the stability characteristics of a single, co-rotating vortex pair. While an isolated co-rotating pair is linearly stable to long wavelength perturbations, the four-vortex, co-rotating system is unstable. With this distinct difference in stability properties, it is difficult to apply the results of [30] for a single, co-rotating vortex pair to Cases 3 and 4. However, some observations can still be drawn from the results in Figure 3.23-3.25. For the closely-spaced pairs in Case 3, it can be seen that the disturbances on vortices 1 and 2 grow to the order of the distance between vortices 1-2 by the half orbit point. Subsequent non-linear behavior might initiate interactions between the oppositely-signed vortices 1 and 2. For Case 4, the perturbation amplitudes remain small ($|\eta_n|/(d/b^*) << 1$ and $|\xi_n|/(d/b^*) << 1$) over the first orbit period, suggesting that non-linear behavior would not be evident during this time. If the calculations for Case 4

were extended up to several orbit periods, the disturbance amplitudes would probably grow to the size of the separation distances of vortices 1-3 and 2-4, perhaps resulting in non-linear interactions between the flap and tip vortices.

3.4 Closing Remarks

The linear stability characteristics of two vortex pairs have been analyzed in this chapter. While a single, co-rotating vortex pair is stable to long-wavelength perturbations, the presence of an additional co-rotating pair brings about instability to the four-vortex system. On the other hand, the counter-rotating systems have growth rate curves that are very similar to those of a single, counter-rotating pair. *This indicates that the instability growth in the four-vortex, counter-rotating system is driven primarily by the strain rate field between the oppositely-signed vortices within each of the pairs.*

One interesting observation can be made by considering the growth rate curves of the counter- and co-rotating vortex systems. A comparison of the Figures 3.12, 3.15, 3.16, and 3.18 reveals that the maximum growth rates of the co-rotating pairs are almost two orders of magnitude smaller than those of the counter-rotating pairs. It is as though the inherent, linear stability of the single co-rotating pairs carries over into their four-vortex counterparts. The low growth rates of the co-rotating systems suggest that their instability growth may be difficult to observe in an actual vortex wake. However, the large growth rates for the counter-rotating pairs indicate that these eigenmodes may be the ones observed in the wakes of the triangular-flapped airfoil. *If these instabilities are observed, they should arise much sooner than the Crow-like, S1 mode and have a wavelength that is distinctly shorter.*

While Chapters 2 and 3 have focused upon the underlying physics and theoretical background of vortex stability, the remaining chapters will discuss the experimental research that was performed with triangular-flapped airfoils. Because the wakes of these airfoils consist of counter-rotating vortex pairs, the following chapters will emphasize the discussions in Chapters 2 and 3 that are related to counter-rotating vortices. For a complete discussion

on the experimental measurements made in co-rotating vortex wakes, the reader is referred to Chen *et al.* [9], Bristol *et al.* [7], and Bristol [8].

In the following chapter, the results of flow visualization measurements are presented and the non-linear behavior of counter-rotating vortex pairs is addressed. Chapters 5 and 6 will discuss the PIV measurements that were made in the wakes of triangular-flapped airfoils.

Chapter 4

Flow Visualization

4.1 Introduction

In order to obtain a more complete look at the trailing vortex wakes of triangular-flapped airfoils, a new set of flow visualization measurements were made at the U.C. Berkeley Richmond Field Station towing tank facility. Several changes in the experimental setup described in [35] were made in order to improve the quality of the flow visualization images. Because the resulting wakes are so three-dimensional and complex, volumetric flow visualization was a vital element in understanding the trailing vortex dynamics. The observations made with this technique provide more information about the flow physics than the two-dimensional PIV measurements. Furthermore, without the flow visualization data, the PIV data would have been difficult, if not impossible, to interpret at times.

4.2 Experimental Setup

The towing tank measures 70 m × 2.5 m and has a nominal water depth of 1.5 m. In the middle of the tank is the test section (Figure 4.1), which has glass windows that give an underwater view of the tank. A lightweight, aluminum carriage is used to tow the airfoils down the length of the tank at high speeds. The carriage is driven by a 5-hp computer-controlled motor (Parker Compumotor), which is located at the upstream end of
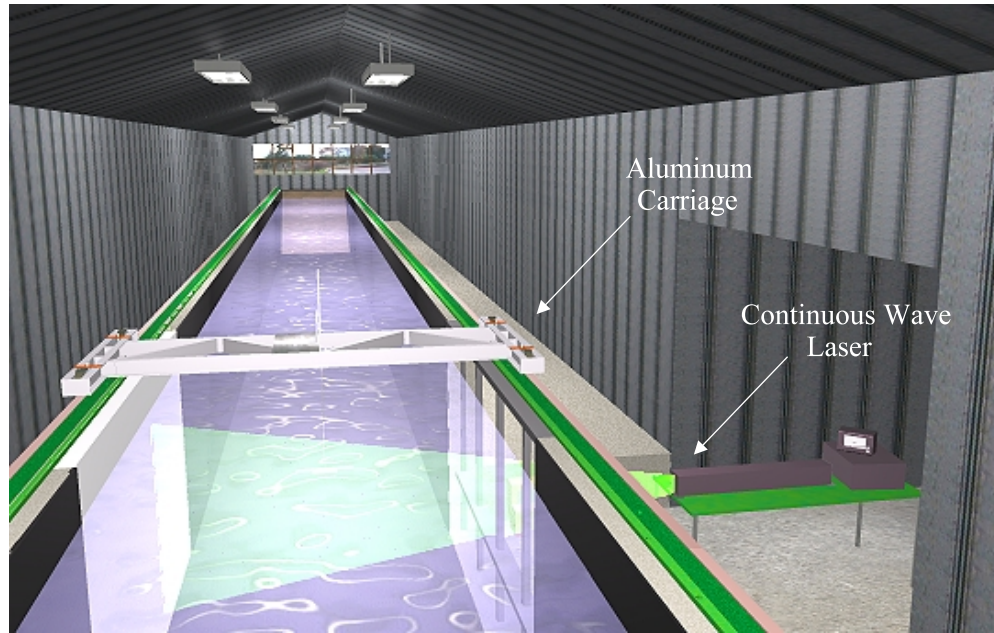
Figure 4.1: Downstream view of the Richmond Field Station towing tank facility. The CW laser will be discussed in the PIV measurements chapter.

the tank. The motor drives the carriage through a 122 m steel cable that loops around a drive pulley on the motor shaft and an idle pulley at the far end of the tank. The ends of the cable are attached to the front and rear of the carriage. To minimize the amount of droop in the cable and the subsequent oscillations of the carriage during acceleration, PVC cable suspenders are located every 3 m down the length of the tank. It should be noted that the motor/controller system was tuned so that the carriage quickly achieves its maximum velocity with a minimal amount of oscillations about the desired velocity. During an experiment, the carriage begins its motion at the upstream end of the tank and continues until it reaches the far end. The reason for doing this is that previous experiments have demonstrated that stopping the carriage causes the wake vortices to burst. This bursting phenomena slowly propagates upstream from the airfoil. Therefore, if the carriage is stopped too close to the test section, the data collected there will become contaminated by this effect.

A modular airfoil (Figure 4.2) is used in this experiment to generate the wake vortices. Depending on the type of lift distribution desired, different tabs and flaps can be attached

b = 400 mm

c = 66.7 mm

50%c TF

r = 170 mm

0.5c

75%c TF

0.75c

0.25b
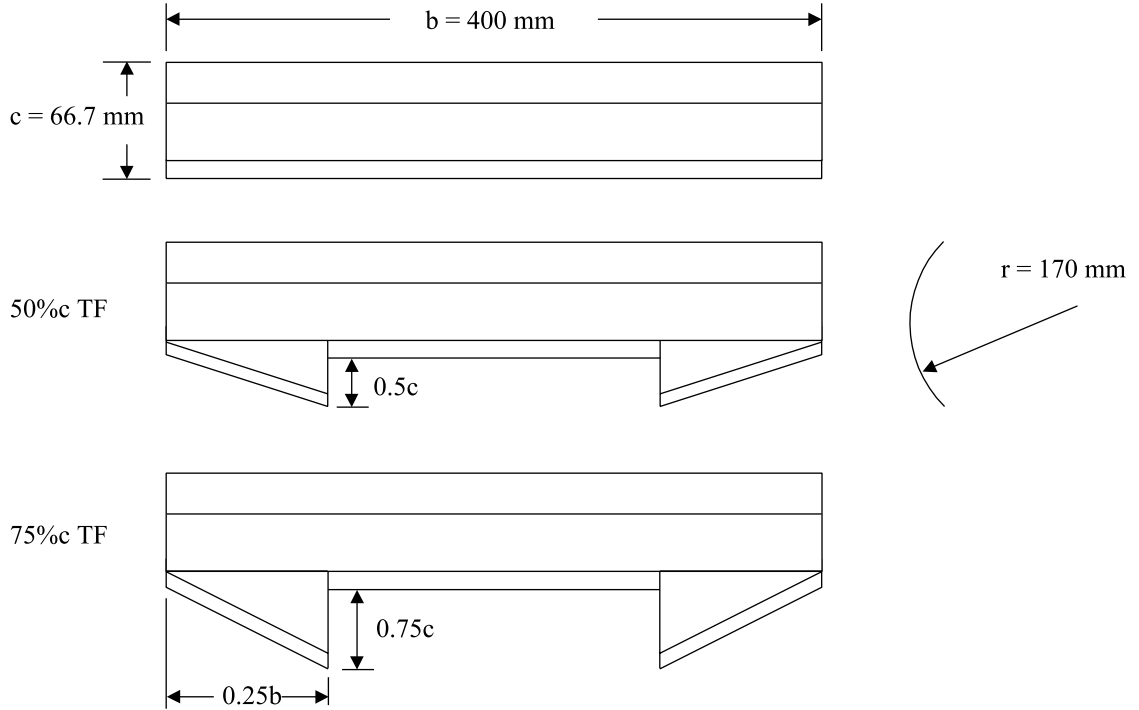
Figure 4.2: Planform and side view of the three airfoils used in the experiment.

to the trailing edge of the airfoil. The airfoil and the trailing edge tabs and flaps are made of 3.2 mm thick stainless steel sheet metal that is rolled to give a camber radius of 17 cm. The leading edge of the airfoil is tapered for the first 20 mm and the trailing edge tabs and flaps are tapered over the last 10 mm. On the underside of the airfoil are four 1.1 mm wide × 1.1 mm deep channels, which house the dye injection tubing. Once a set of tabs and flaps are bolted to the airfoil, the counter-sunk bolt holes and any gaps between the tabs and flaps are covered with clear, packing tape (3M), yielding a more streamlined surface. For this experiment, three airfoil configurations are utilized: a rectangular-shaped airfoil, which has a span, b, of 40.0 cm and a chord, c, of 6.67 cm; an airfoil that has outboard, triangular flaps, which have a span of 0.25b and a chord of 0.5c (denoted from hereafter as 50%c TF); and an airfoil that has outboard, triangular flaps, which have a span of 0.25b and a chord of 0.75c (denoted hereafter as 75%c TF).

The airfoils are attached to the carriage by a streamlined, stainless steel strut, which places them approximately 0.5 m beneath the water surface (Figure 4.3). The junction piece between the strut and the airfoil has the same cross-section as the strut and sits flush against the curved, upper surface of the airfoil. The streamlined portion of the strut is 5.1 cm wide $\times$ 6 mm thick $\times$ 76.2 cm long and has four 3.2 mm wide $\times$ 3.2 mm deep channels running along its length to accommodate the dye tubing used for flow visualization. Before conducting the experiments, flow visualization with particle streaking is performed on the strut wake to confirm that the strut is not yawed, an effect that could invalidate the wake vortex measurements. Slight adjustments were made to the strut's yaw angle so that its wake is as thin as possible. In order to adjust the airfoil's angle of attack, the strut can pivot on its mounting bracket, allowing the angle of attack to vary between $\pm 12^o$ in 1° increments.
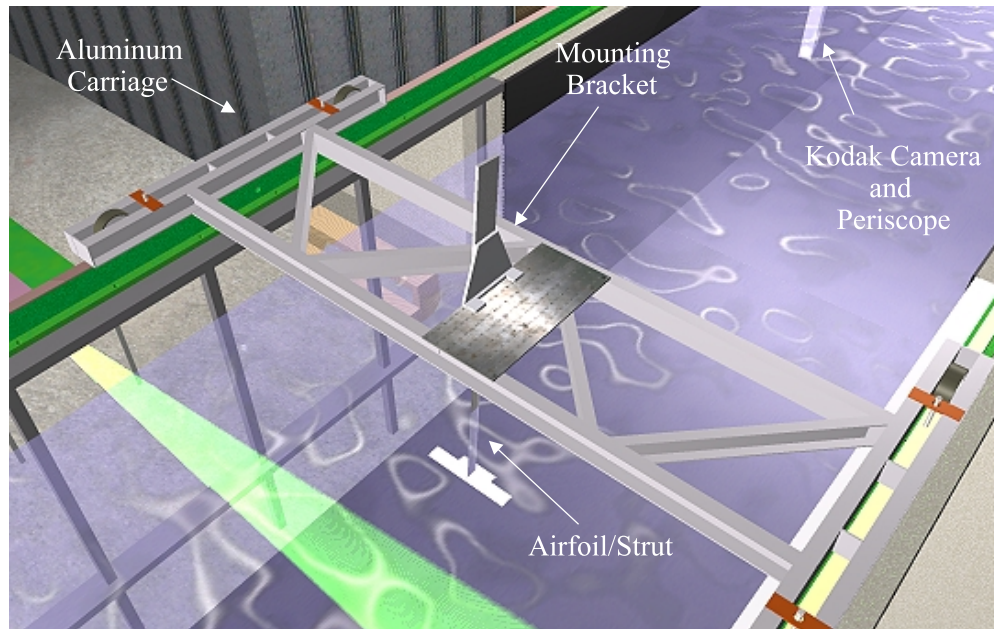
Figure 4.3: Top view of the aluminum carriage. The Kodak camera and periscope will be discussed in the chapter on PIV measurements.

Visualization of the trailing vortices is accomplished by injecting florescent dye into the vortex cores with the system shown in Figure 4.4. Four stainless steel tubes, 3.2 mm in diameter, are inserted into channels that run the length of the streamlined strut. These channels are then covered with modeling clay and a 76 cm piece of aluminum tape. The tape is positioned 1.25 cm from the leading edge of the strut. At approximately 2.5 cm from the end of the strut, the 3.2 mm tubes are joined to 19 gauge thin-walled, stainless tubes that passes through the airfoil and runs along its underside to the flaps and wing tips. Because the diameter of the 19 gauge tubing is 1.1 mm (or, as later PIV meausurements demonstrate, about 2% the diameter of vortex cores), the influence of these tubes on the vortex roll-up is assumed to be neglible. Clear packing tape (3M) is used to hold the 19 gauge tubing in the channels on the underside of the airfoil. To ensure a seal between the different diameter tubes, the scheme shown in Figure 4.5 is employed. A 3.2 cm diameter brass tube and a slanted-end piece of clear tubing (3.2 mm O.D. and 1.1 mm I.D.) are placed around the 19 gauge tubing between the airfoil and the 3.2 mm stainless steel tubing. When the airfoil is bolted into place, it pushes against the brass tubing, which forces the clear tubing into the 3.2 mm stainless steel tubing. The resulting junction forms a watertight seal up to 30 psi. Fluorescent, sodium salt dye (Sigma Chemical Company, No. F-6377) is used in this experiment and is mixed with water to the desired mass concentration. Two separate containers, which are fixed to the carriage, hold the different dye mixtures. The container that supplies dye to the flap vortices has a dye concentration of 2:100 and the container that supplies dye to the tip vortices has a dye concentration of 1:100. Both of these containers are open to the atmosphere, such that the dye is drawn into the vortices by the low pressure that exists in the vortex cores.

The test section of the towing tank is illuminated with blue light from seven slide projectors. The blue light is generated by placing a blue, low-pass, glass filter in the slide container of each projector. The projectors are located approximately 2 m from the viewing windows of the test section and are arranged in a manner similar to that shown in Figure 4.6. The motion of the dye is recorded with five video cameras: three analog cameras, whose video signals are recorded on three VCR's, and two VHS camcorders. An overhead
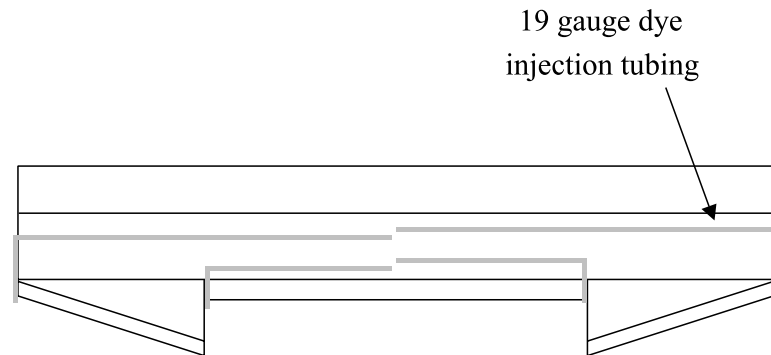
Figure 4.4: Dye injection tubing on the triangular-flapped airfoil. For the rectangular airfoil, only the tubes going to the wing-tips are installed.
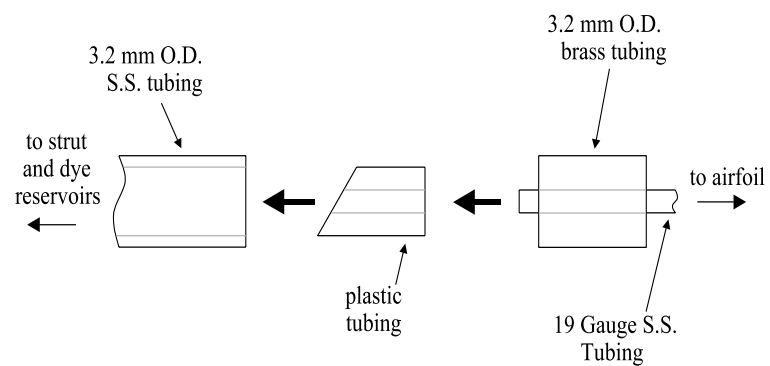
Figure 4.5: Sealing mechanism used to connect the 19 gauge tubes on the airfoils to the 3.2 mm dia. tubes on the strut.
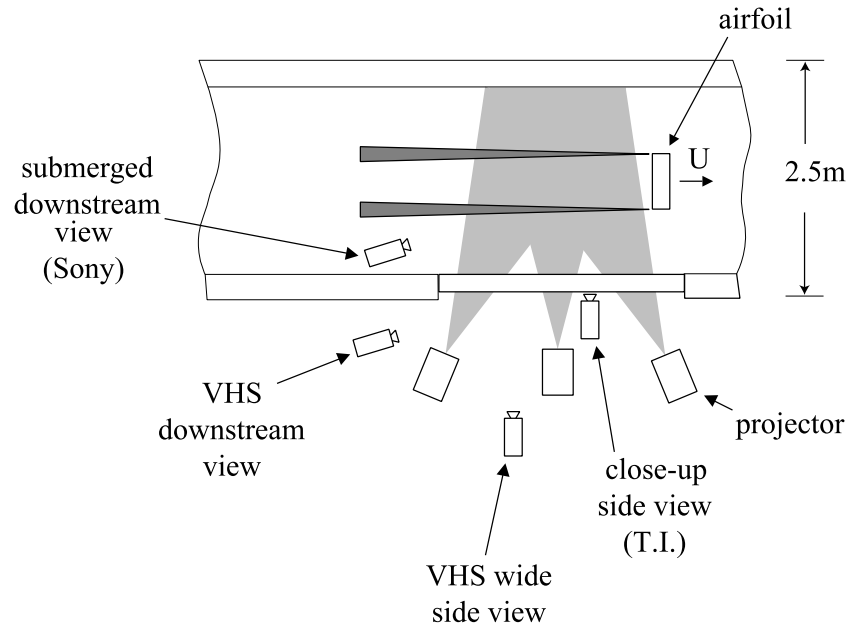
Figure 4.6: Schematic of the setup used for the flow visualization measurements. For clarity, not all of the projectors are shown.
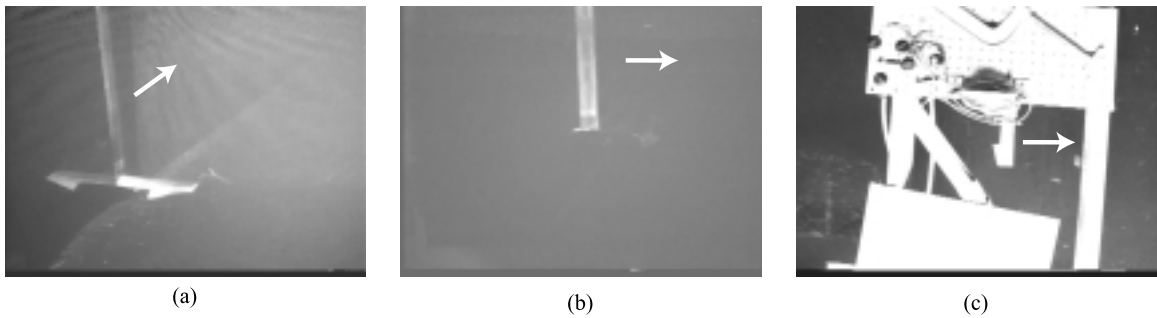
Figure 4.7: (a) Downstream, (b) close-up side, and (c) overhead reference views of the airfoil. The airfoil is at the same downstream location in each of the views. The arrows indicate the direction that the airfoil travels during the experiment.

view is provided by a Sony XC7500C (640 pixels × 480 pixels) camera with an 8 mm lens. By suspending the camera approximately 2 m above the water surface, the field of view at the airfoil depth is approximately 170 cm × 130 cm. One problem that is introduce this view is the distortion of the dye trails due to surface waves generated by the strut. In order to minimize these waves, metal and plastic gratings are placed on the left and right walls of the test section at the water surface. Consequently, the waves are dissipated at the walls rather than being reflected. A side view of the vortex wake is recorded by placing a Texas Instruments camera with an 8 mm lens against the glass panes in the test section. The camera is positioned at the same downstream location as the Sony camera. In this manner, the Sony and Texas Instruments cameras give two orthogonal views of the trailing vortex wake. The field of view from the Texas Instruments camera is approximately 103 cm × 77 cm at the airfoil centerline. Another Sony XC7500C camera gives a "three-quarters" downstream view of the test section. This camera is housed in a waterproof, cylindrical shell and is suspended in the test section such that its 8mm lens penetrates the water surface to a depth of about 10 cm. Figure 4.7 demonstrates reference images for these views. In each of the photos, the airfoil is located at the same downstream position in the test section.

The two VHS camcorders are used to provide overall views of the test section. One camcorder, located 3 m behind the Texas Instruments camera, gives a side view of the test section. An additional "three-quarters" downstream view is accomplished by placing the second camcorder at the upstream end of the test section. This camera is oriented so that it views the dye trails through the glass panes at an angle. Spatial calibrations are made for the overhead view and the two side views by filming a ruler at several depths and lateral locations in the test section. This information is later used to extract the instability wavelengths and other flow features that are recorded in the dye visualization images.

Because the 8 mm lenses used on the Sony and Texas Instruments cameras have such a short focal length, it was feared that the images captured with them would have a significant radial distortion, giving them a "fish-eye" appearance. In order to check for this distortion, a checkerboard grid, which had 2 cm × 2 cm black and white squares, was filmed with an 8 mm lens. Analysis of this image revealed that the radial distortion is minimal.

Therefore, it was deemed that the images filmed with the 8 mm lenses would not have to be digitally corrected for radial distortion.

A total of 24 flow visualization runs are made by varying the airfoil speed, angle of attack, and type of airfoil. These parameters are summarized in Table 4.1. The run numbers for the rectangular and triangular-flapped airfoils are not entirely consistent in Table 4.1. The reason for this is that the measurements are part of a larger set of flow visualization experiments. When discussing the results of the flow visualization, the type of airfoil used in a particular run will be mentioned so as to eliminate any confusion. During these experiments, the runs were spaced by approximately 20 minutes, allowing the water in the tank to become quiescent for the next run. At the end of each day of flow visualization, the tank was mixed with about $\frac{1}{4}$ of a gallon of non-color safe bleach (Longs brand) in order to bleach out the residual dye in the tank.

Before discussing the observations made in the wakes of the airfoils, a comment should be made on the interpretations of the dye visualizations. The dye is taken to be a marker of the vorticity in the flap and tip vortices. However, the dye does not mark all of the vorticity in the wake. The reason for this is that the dye is injected at only four distinct points and not along the entire vortex sheet generated by the airfoils. Since the molecular diffusivity of water is much smaller than its momentum diffusivity, the dye remains as a partial marker of the vortex sheet, which rapidly rolls up into vortices. Hence, in the rolled up wake, the dye marks vorticity, but not all vorticity is marked by dye. At larger downstream distances, only coherent structures that correlate well with themselves both spatially and temporally are discussed in the following sections. Therefore, if a large dispersal of dye is observed in the wake, no attempt is made to relate this to a large dispersal of vorticity. The PIV measurements will later be employed to quantify the spread of vorticity in the airfoil's wakes.

Run	Airfoil	U_o (cm/s)	α (degrees)
15	Rect.	500	3
16	Rect.	500	3
18	Rect.	500	2
21	Rect.	300	2
1	50% TF	500	2
2	50% TF	500	0
3	50% TF	500	-1
4	50% TF	300	2
5	50% TF	300	0
6	50% TF	300	-1
7	50% TF	500	2
8	50% TF	300	2
9	50% TF	500	0
10	50% TF	300	0
11	75% TF	500	2
12	75% TF	300	2
13	75% TF	500	0
14	75% TF	300	0
15	75% TF	500	-1
16	75% TF	300	-1
17	75% TF	500	2
18	75% TF	300	2
19	75% TF	500	0
20	75% TF	300	0

Table 4.1: Parameters for the flow visualization runs. The run numbers are not entirely con-sistent because these measurements are part of a larger set of flow visualization experiments.

4.3   Rectangular Airfoil Observations

The flow visualization data of the rectangular wing's wake (run 16, $U_o = 500$ cm/s, $\alpha = 3^o$) are shown in Figures 4.8 and 4.9. At $x/b = 0$, the airfoil is in the center of the test section. The vertical black lines in all of the top view images are shadows cast by two of the steel beams that support the test section windows. Note that the side view images are
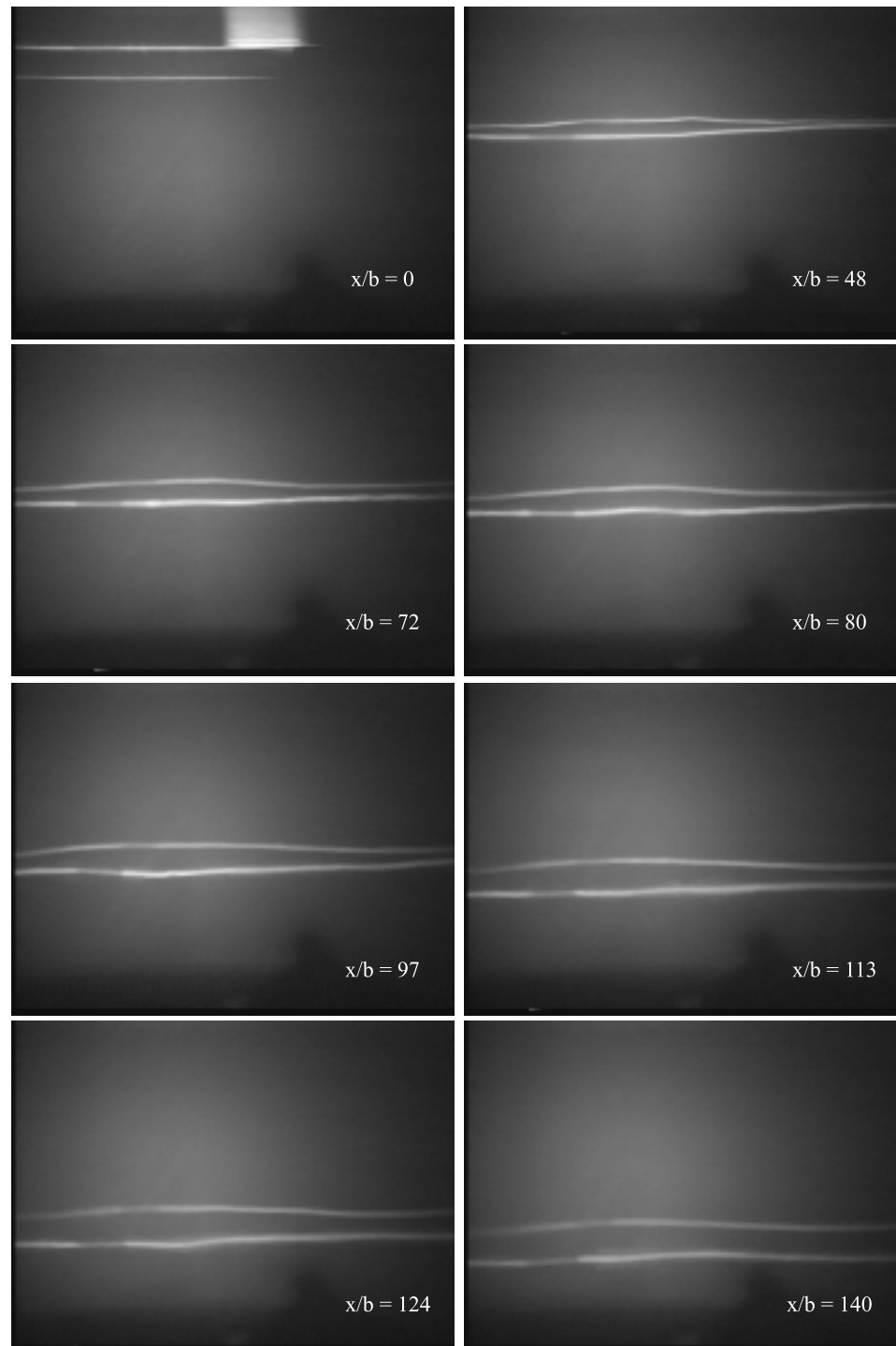
Figure 4.8: Close-up side view of the rectangular airfoil's wake (run 16, $U_o = 500$ cm/s, $\alpha = 3^o$). Note that the frames are not evenly spaced in x/b.
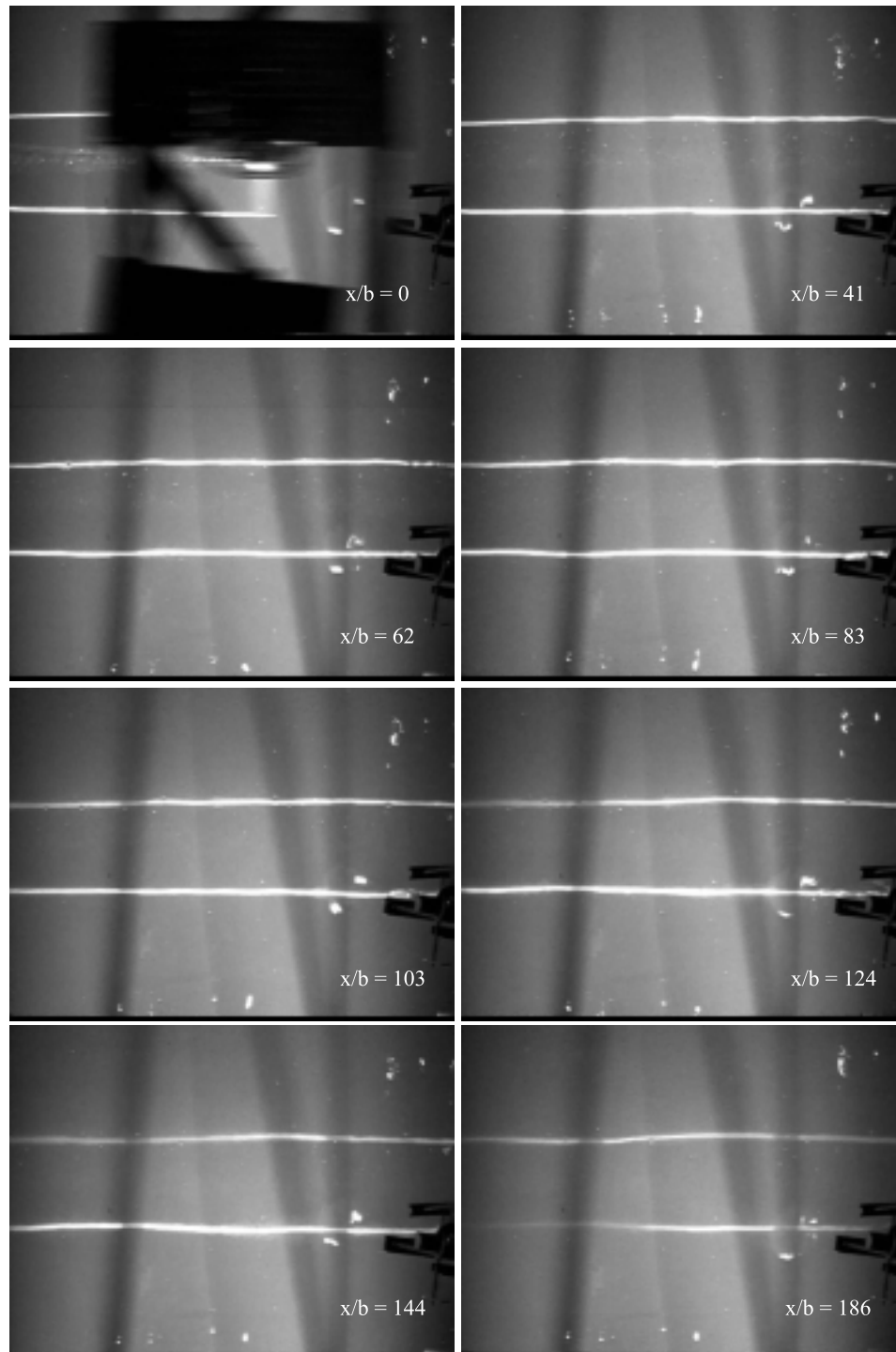
Figure 4.9: Top view of the rectangular airfoil's wake (run 16, $U_o = 500$ cm/s, $\alpha = 3.0^o$). Note that the frames are not evenly spaced in x/b.

slightly lower than the reference image shown in Figure 4.7b. The reason for repositioning the side view camera is to capture the rectangular airfoil's wake for as long as possible. When the runs with the triangular-flapped airfoils were performed, the side-view camera was raised to give the view in Figure 4.7b. It can be seen in Figures 4.8 and 4.9 that after the two wing-tip vortices form, they descend rather quietly in the test section. While not exactly parallel, the vortices display only a minimal amount of three-dimensional characteristics, which are evident in the slight undulations visible in the side view images. Additionally, solitons, or bulges in the vortex core sizes, are observed to travel upstream along the length of the vortices at a speed of order 0.5 m/s. Their velocity is not constant in time, but varies periodically as the solitons make their way through the test section. Unfortunately, the still, side-view images do not clearly demonstrate these observations of the solitons. As the vortices approach the bottom of the tank, they begin to exhibit signs of the long-wavelength, Crow instability (top view, $x/b = 144$ and 186). At later times, the vortices interact with the bottom of the tank and break apart. The other runs performed with the rectangular airfoil demonstrated similar characteristics as those described above.

4.4   Triangular-Flapped Airfoils Observations

Of the twenty flow visualization runs performed with the two triangular-flapped airfoils, an instability is observed to develop between the counter-rotating flap and tip vortices for all towing speeds and angles of attack. The qualitative behavior of the wake does not appear to depend strongly on the size of the triangular flaps. The instability initially occurs on the weaker flap vortices and has a wavelength that is on the order of one wingspan. The perturbation amplitudes on the flap vortices grow rapidly, such that the flap and tip vortices eventually make contact with one another. At larger downstream distances, the non-linear evolution of the vortices depends strongly upon the angle of attack. For runs in which $\alpha = 2.0^o$, there is a large exchange of dye across the airfoil centerline within 100 spans, regardless of the type of triangular-flapped airfoil. However, at -1°, the vortices remain on either side of the wake and exchange little, if any, dye across the airfoil centerline.

4.4.1 Observations for Run 1: 50%c TF, $\alpha = 2^o$, $U_o = 500$ cm/s

Figures 4.10-4.12 illustrate the dye visualization images of the downstream, close-up side, and top views at several downstream locations for run 1. The large bright spot in the side view images is due to the reflection of one of the projectors. The airfoil and four dye trails are visible in the three views at $x/b = 0$. After their initial formation, the flap and tip vortices orbit outwardly about their common vorticity centroids in a manner similar to that of the two-dimensional, potential vortex calculations (Section 3.2). PIV measurements in the wake of this airfoil at the same speed and angle of attack reveal that $\Gamma_f/\Gamma_t = -0.37$. At approximately 15 spans or 135° through the orbit period, stationary, instability waves are observed to rapidly develop on the weaker flap vortices. The wavelength of the instability is on the order of one wingspan or four times the separation distance between the flap and tip vortices. Note that this wavelength is shorter than that of the Crow instability between equal strength, counter-rotating vortices. The stationary, instability waves on the left and right flap vortices grow independently of one another. The distortion due to the surface waves is visible in the top view at $x/b = 18$ and 21. The perturbation amplitudes quickly grow such that the flap and tip vortices on the port-side make contact at about 20 spans and those on the starboard-side at 25 spans. During the time at which the instability is growing, the perturbations on the flap vortices remain at a relatively fixed orientation with respect to the rotating reference frame of the flap and tip vortices. This observation leads to the conclusion that the self-induced rotation rate of the flap vortices is balancing the rate of strain field from the tip vortices.

As the instability progresses, the flap vortices wrap around the tip vortices, forming "Ω"-shaped hoops that have a structure similar to Klein et al.'s [30] Figures 13 and 16. The spiral "feet" of these hoops behave like vortex rings and advect themselves inward toward each other. This extends the hoops in the vertical direction, as is evident in the side view images. By 45 spans, the hoops are oriented vertically and are flung across the center of the wake. As the hoops approach the airfoil centerline, they pinch off into vortex rings, occasionally colliding with rings from the opposite side of the airfoil. The vortex rings that make it to the opposite of the wake collide with the remnants of the tip vortices. As the
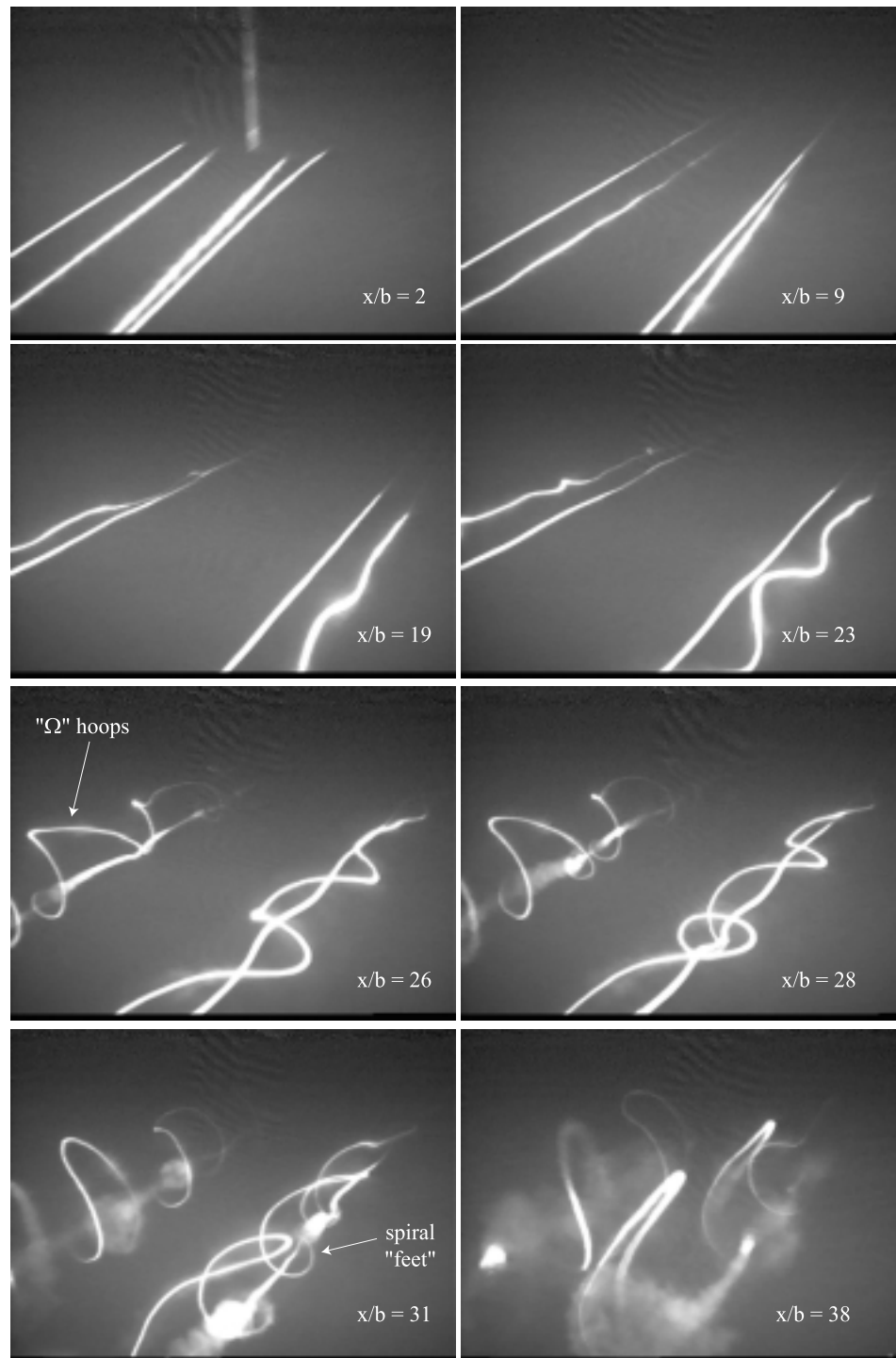
Figure 4.10: Downstream view of the triangular-flapped airfoil (run 1, 50%c TF, $U_o = 500$ cm/s, $\alpha = 2.0^o$). Note that the frames are not evenly spaced in x/b.
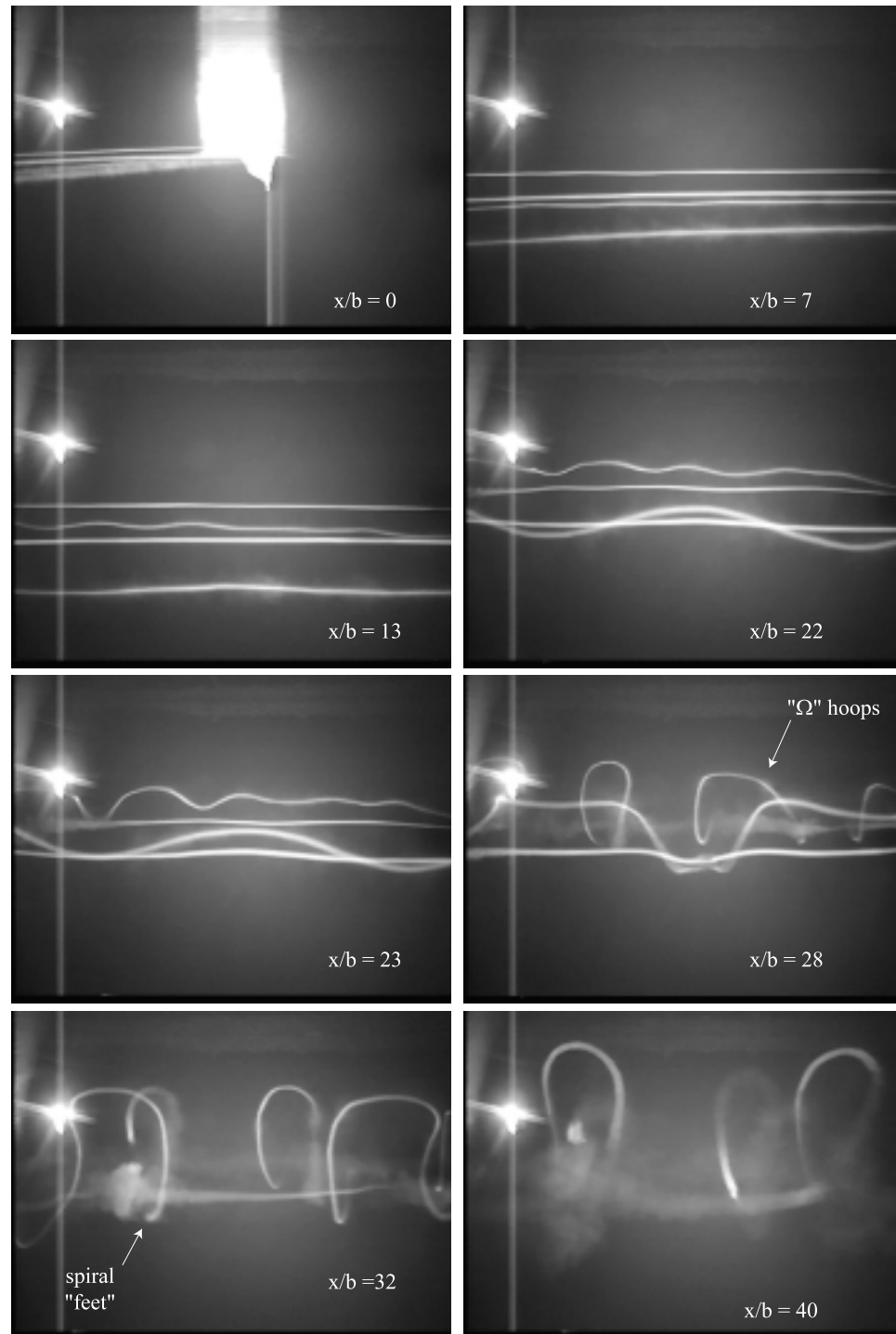
Figure 4.11: Close-up side view of the triangular-flapped airfoil (run 1, 50%c TF, $U_o = 500$ cm/s, $\alpha = 2.0\ ^o$). Note that the frames are not evenly spaced in x/b.
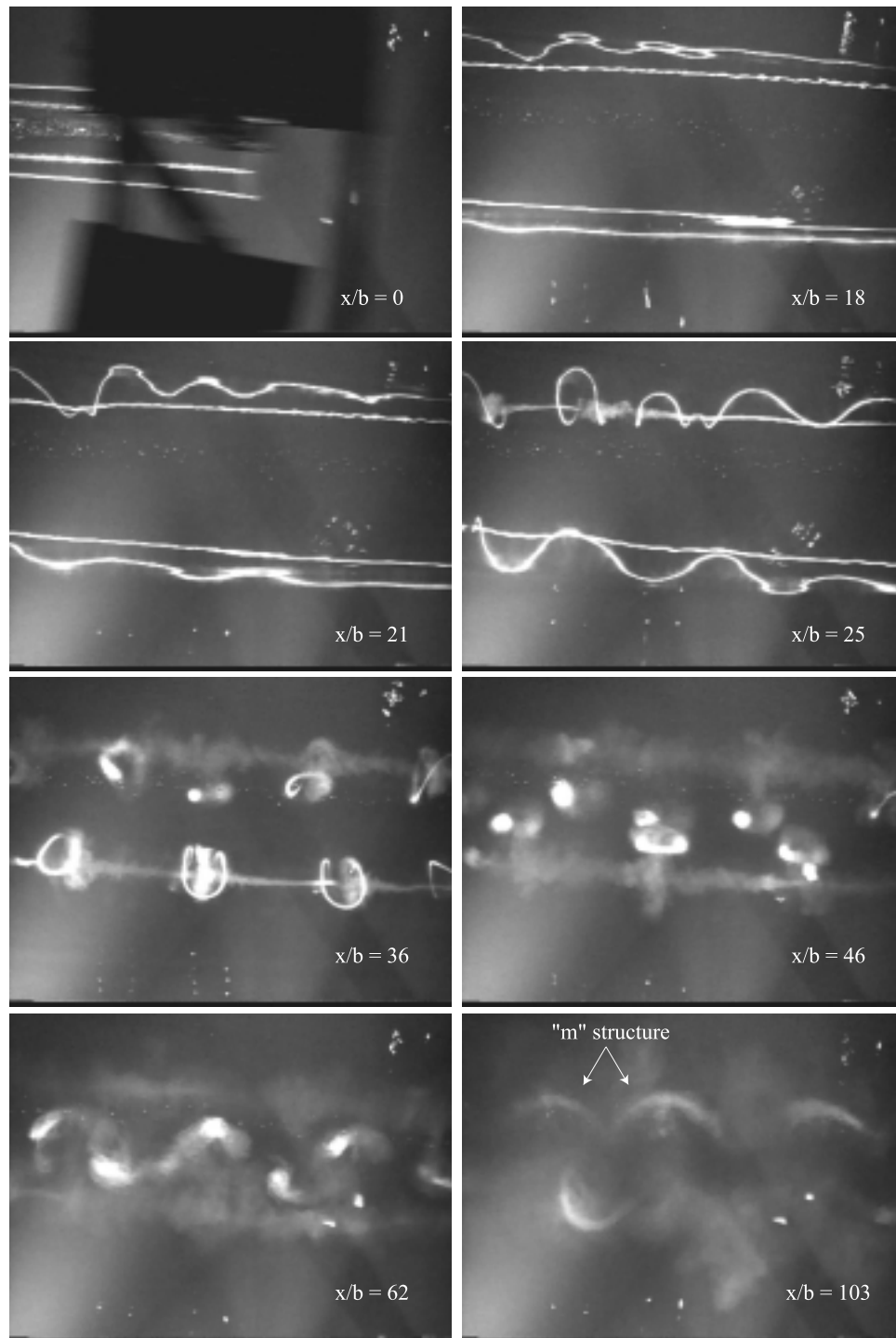
Figure 4.12: Top view of the triangular-flapped airfoil   (run 1, 50%c TF, $U_o = 500$ cm/s, $\alpha = 2.0^o$). Note that the frames are not evenly spaced in x/b.
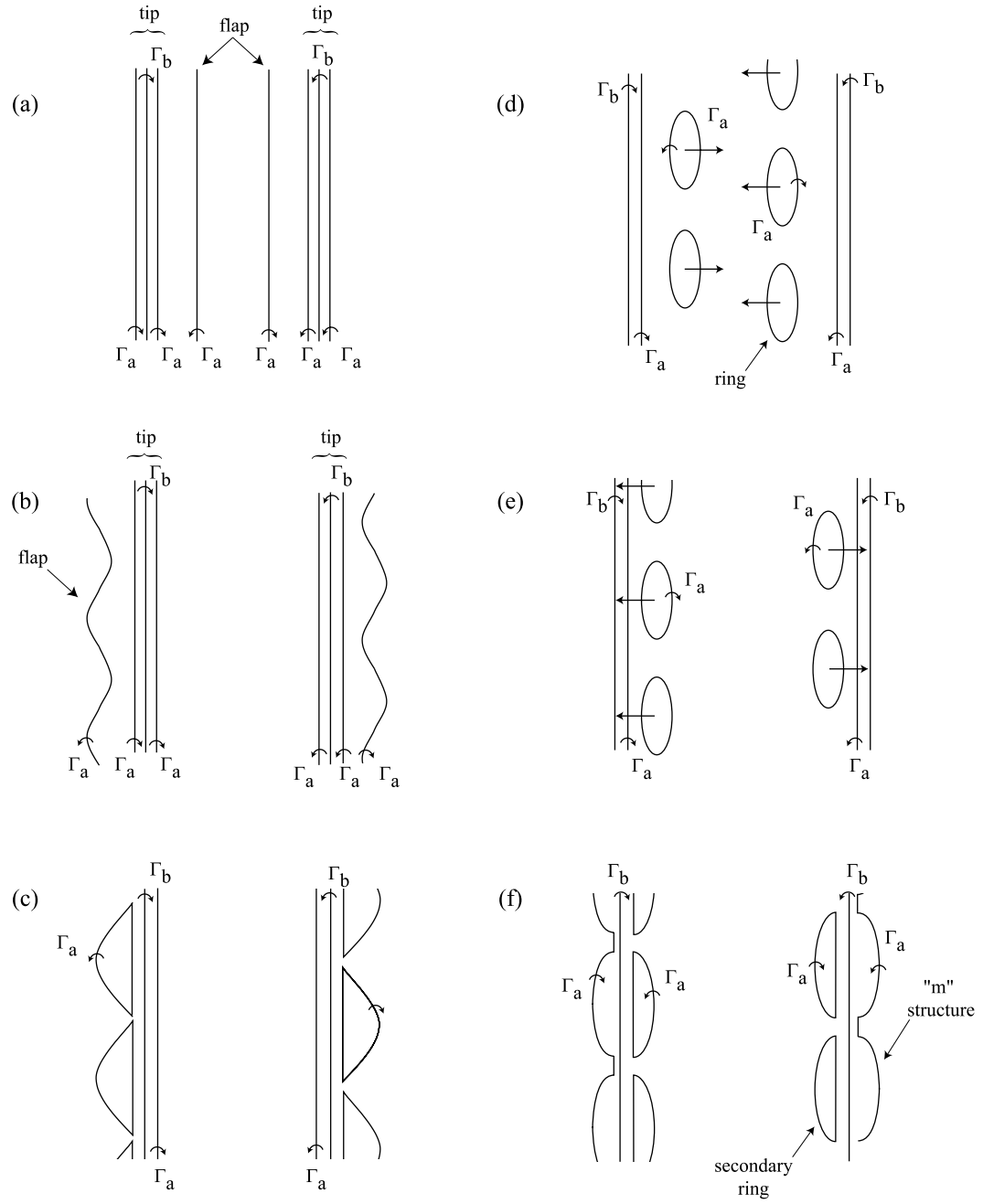
Figure 4.13: A filament model of the vortex interactions that are observed in the wake of the 50%c TF airfoil at $\alpha = 2.0^o$.

rings approach the tip vortices, their diameters increase roughly by a factor of two, resulting in a "m"-like structure in the wake, which is visible in the top view at $x/b = 103$. By 175 spans, the dye is completely dispersed in the test section and no coherent structures are visible in the wake. The downstream view and close-up side view do, however, indicate the presence of downwash at this downstream location.

To better understand the vortex-connection and re-connection processes that are occurring in the wake described above, a useful exercise is to model the vortices as vortex filaments and trace through the vortex interactions that occur in the wake. Let the flap and tip vortices have strengths of Γ_a and $2\Gamma_a + \Gamma_b$, respectively. These circulation strengths are chosen to make the following analysis more tractable, as will become evident shortly. Initially, the flap and tip vortices are parallel as shown Figure 4.13a. As the vortices orbit about one another, the flap filaments develop finite amplitude perturbations (Figure 4.13b), resulting in the contact of the flap and tip vortices (Figure 4.13c). Neglecting the spiraling effects and other details of the vortex connection process, the flap filaments join with the Γ_a portion of the tip filaments, forming closed vortex rings (Figure 4.13d). Assuming that there are no collisions in the center of the wake, the vortex rings travel to the opposite side of the wake (Figure 4.13e) and there interact with the tip vortices. To keep the circulation constant along the length of the filaments, the upper halves of the vortex rings connect with the remaining Γ_a portion of the tip filament, yielding the "m"-like structure observed in the flow visualization data (Figure 4.13f). Meanwhile, the bottom halves of the vortex rings form secondary vortex rings with the Γ_a portion of the tip filament. Due to the large dispersal of dye, it is difficult to clearly observe the existence of secondary rings in the flow visualization data.

4.4.2 Observations for Run 3: 50%c TF, $\alpha = $ -1°, $U_o = $ 500 cm/s

The flow visualization images for run 3 are shown in Figures 4.14-4.16 for several downstream locations. By decreasing the angle of attack to -1°, the instability exhibits a somewhat different behavior than that for the 2° case. The reason for this is that the flap vortex is relatively stronger with respect to the tip vortex at this angle of attack. PIV

measurements demonstrate that $\Gamma_f/\Gamma_t = -0.55$ at this towing speed and angle of attack. Additionally, this angle of attack causes the overall vortex strengths to be weaker so that the pressure in the vortex cores is higher than that of the 2° runs. Consequently, the vortices draw less dye into their cores, causing the dye trails in Figures 4.14-4.16 to appear fainter than those for run 1. By approximately 20 spans or 90° through the orbit period, a long wavelength instability, which is slightly larger than that of the 2° case, appears on the flap vortices. As this instability grows, the tip vortices also exhibit perturbations of the same wavelength, though their amplitude is smaller than the disturbances on the flap vortices (top view, x/b = 23-35). From the side-view images at 19-26 spans, a higher wavenumber instability can be seen on the flap vortices. The wavelength of this instability is on the order of the flap/tip separation distance. These instabilities were repeatedly observed in the -1.0^o runs for both triangular-flapped airfoils at $U_o = 300$ and 500 cm/s. The source of these instabilities is uncertain, but, given their short wavelength, they could be caused by higher order, radial modes that depend upon the internal structure of the vortices [50]. By 31 spans or 135° through the orbit period, the port-side flap and tip vortices make contact with one another. After a few more spans, the starboard-side pair does the same. As the vortices in either of the pairs make contact, the stronger tip vortices "reach out" to the flap vortices (side view, x/b = 35). The resulting structure of the flap and tip vortices bears a resemblance to Figure 13 of Klein [30], which is based on a non-linear filament calculation for a single vortex pair with $\Gamma = -0.5$.

The "Ω" hoops that develop from the flap vortices are slightly larger than those of the 2° degrees run due to the longer wavelength of the instability (top view, x/b = 39). As the hoops' "feet" spiral around the tip vortices, they advect themselves inward towards one another. This, in turn, extends the hoops vertically. While the flap vortices wrap around the tip vortices, the tip vortices exhibit a helical structure as illustrated in Figure 4.16 at $x/b = 50$. Eventually, the hoops pinch off into vortex rings, which travel upwards to the water surface. Unlike the 2° case, there is little exchange of dye across the airfoil centerline. By 125 spans, there are no coherent features visible in the wake. Additionally, the close-up side view and downstream view show that there is no evident downwash in the test section.
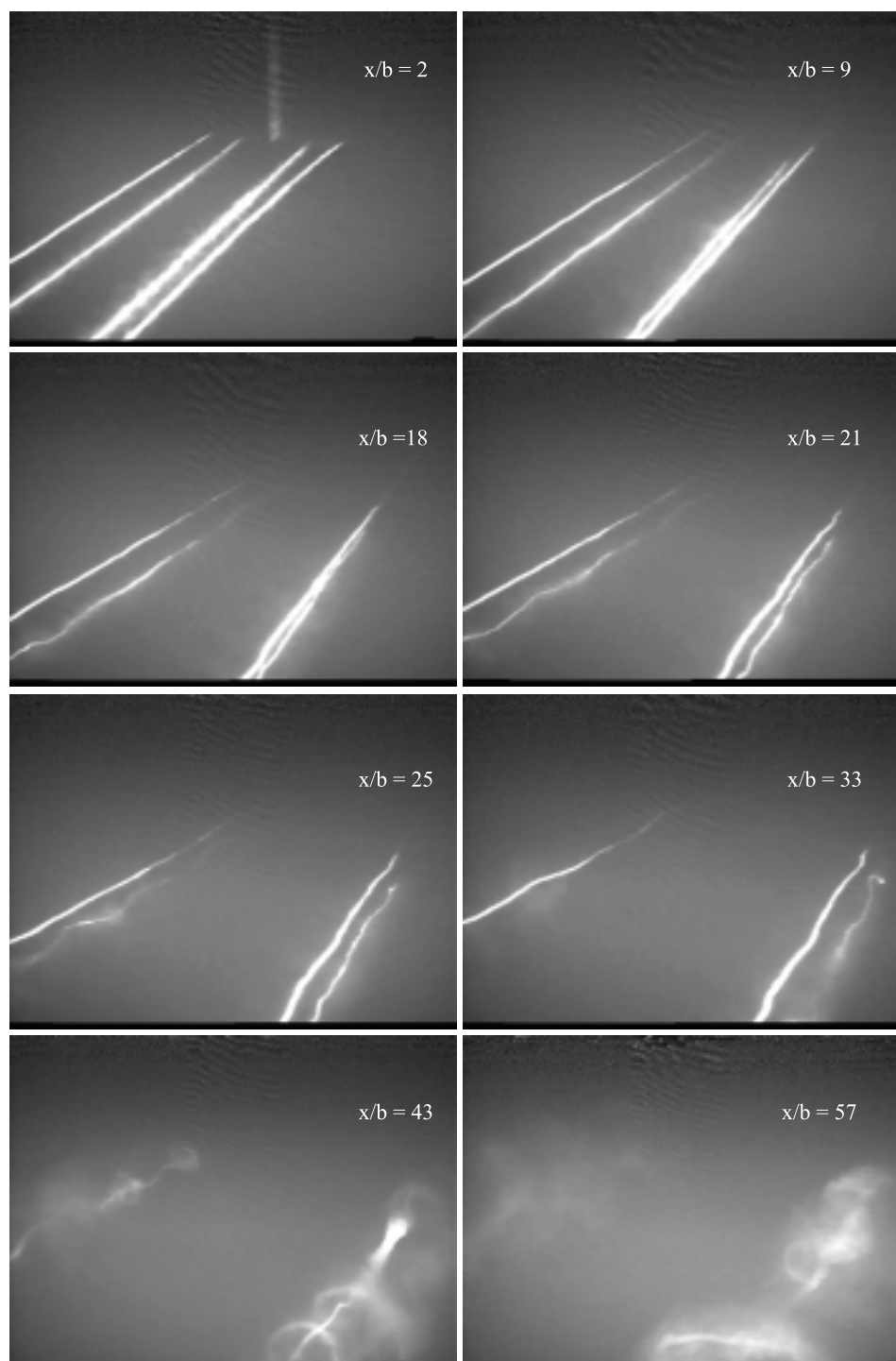
Figure 4.14: Downstream view of the triangular-flapped airfoil (run 3, 50%c TF, $U_o = 500$ cm/s, $\alpha = -1.0^o$). Note that the frames are not evenly spaced in x/b.
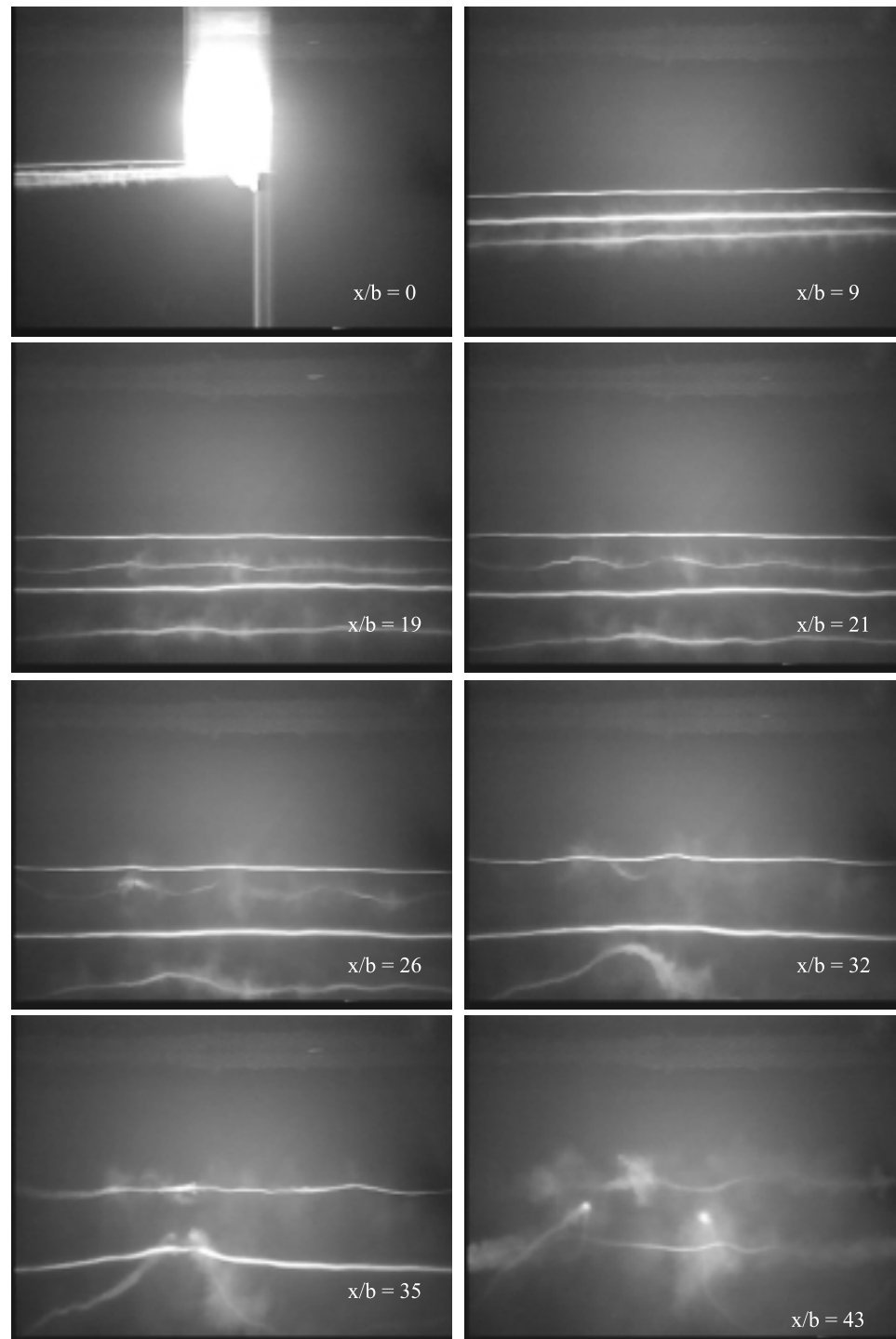
Figure 4.15: Close-up side view of the triangular-flapped airfoil (run 3, 50%c TF, $U_o = 500$ cm/s, α = -1.0^o). Note that the frames are not evenly spaced in x/b.
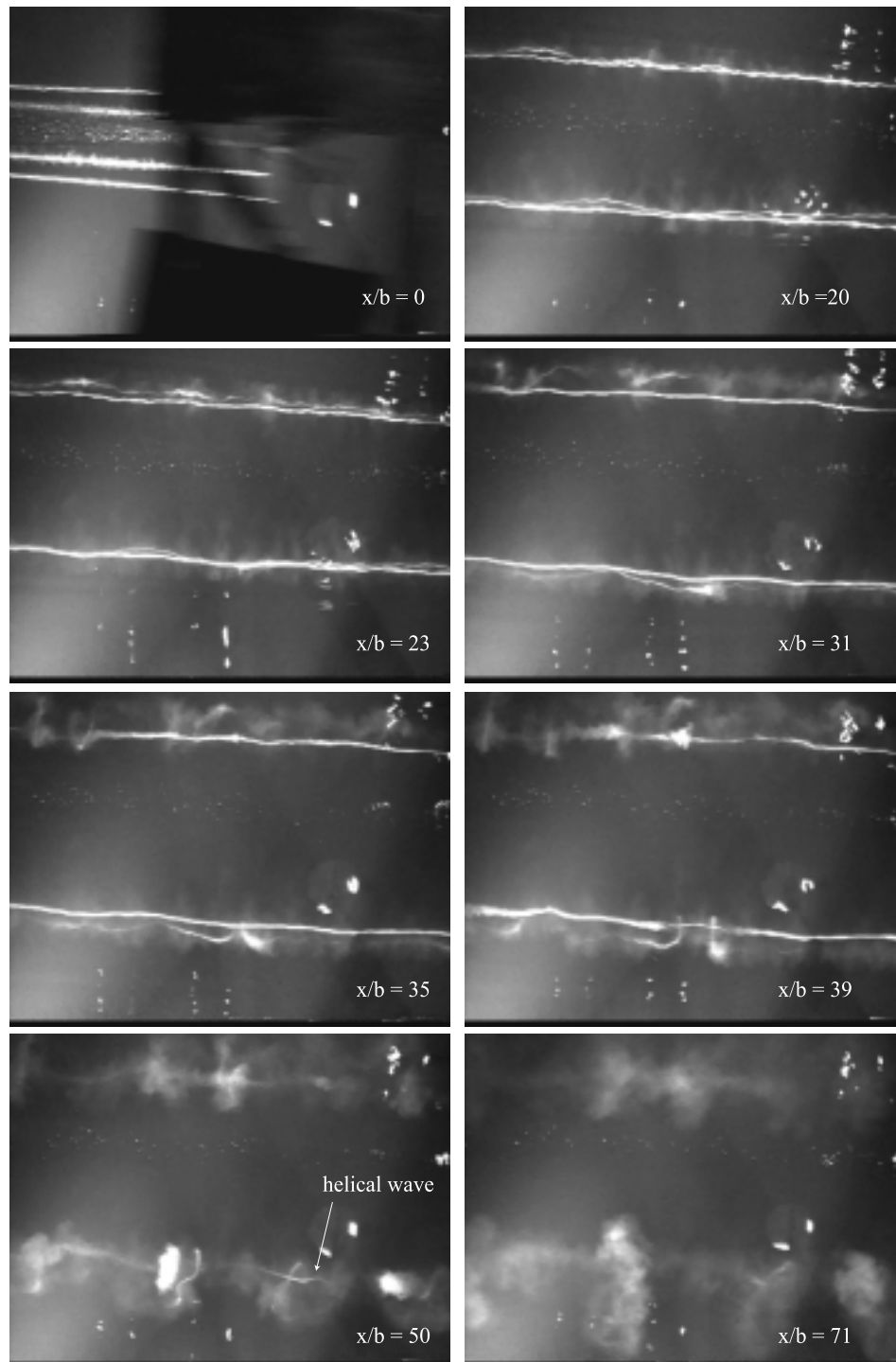
Figure 4.16: Top view of the triangular-flapped airfoil   (run 3, 50%c TF, $U_o = 500$ cm/s, $\alpha = $ -1.0^o). Note that the frames are not evenly spaced in x/b.

This is not to say that the wake has been completely dispersed, since it is probable that the dye is no longer marking the vorticity. The PIV measurements in Chapter 5 provide a more accurate analysis to the behavior of the wake at these large downstream distances. The flow visualization runs performed with the 75%c TF airfoil demonstrate similar qualitative features as those of the 50%c TF airfoil.

4.4.3 Comparsion with Previous Experiments and Numerical Simulations

A useful exercise is to pause in the discussion of the flow visualization data and to compare the observations described above with previous experimental and numerical work. A review of the open literature revealed that there are a few other observations of a similar type of instability between unequal strength, counter-rotating vortex pairs. One of the earlier observations of a similar type of instability can be found in flow visualization photographs taken of a 747 wake [14]. Figure 4.17 shows two of these photographs. During these flight tests, smoke was injected into the counter-rotating vortex pairs that formed from the inboard flaps. After the 747 passes overhead, a distinct sinuous instability is seen to develop along two of the vortices. If the top photo of the 747 is taken as a reference length, the wavelength of the instability appears to be on the order of one or two wingspans. Leonard [31] later modeled this 747 wake with a three-dimensional, time-dependent, inviscid calculation and obtained the results in Figure 4.18. Through private communication with Dr. Leonard, the author learned that the tip vortex in this calculation has a strength of 0.04, the outboard flap vortex a strength of 0.116, and the inboard flap vortex a strength of -0.04. It can be seen in Figure 4.18 that the inboard flap vortex develops a sinusoidal instability within 10 spans downstream of the generating wing. The wavelength of the instability is about equal to the initial distance between tip vortices. At larger downstream distances, the counter-rotating inboard and outboard flap vortices, which have a relative circulation strength ratio of -0.34, interact in a manner similar to that described above for the 50%c TF airfoil. The weaker inboard flap vortex wraps around the outboard flap vortex, forming "Ω"-shaped hoops.

t = 0 s   t ~ 15 s

Figure 4.17: Flow visualization in the wake of a 747 airliner [14]. Smoke is injected into the inboard flap vortices. The times at which the images were taken are shown beneath each of the photographs.
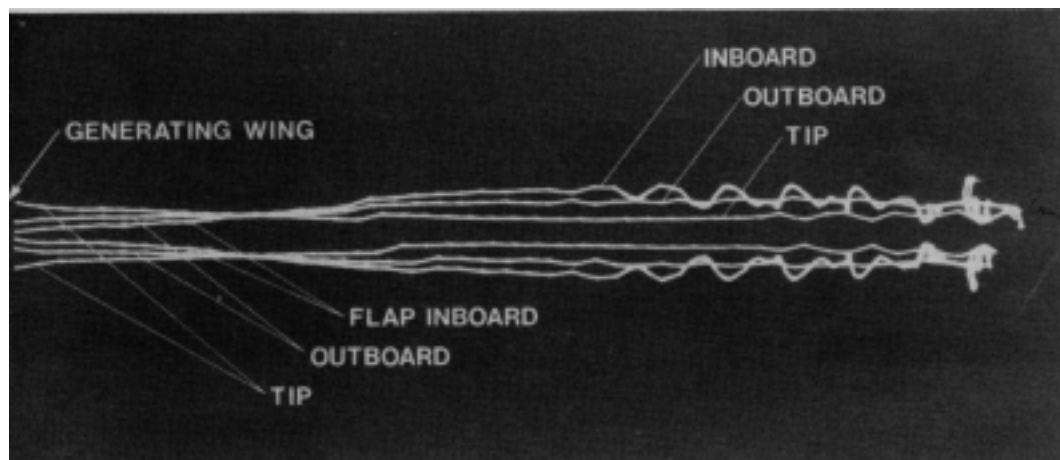
Figure 4.18: Numerical simulation [31] of the 747 wake [14] shown in Figure 4.17.

More recently, Quackenbush *et al.* [39, 40, 41, 42] have studied the interaction of unequal strength, counter-rotating vortex pairs in an effort to alleviate the sailplane wakes of military submarines. As discussed in Chapter 1, the goal of their project is to use shape memory alloys (SMA) to actively perturb the vortices and accelerate the breakup of the wake. The authors have modeled the flow of two counter-rotating vortex pairs with a Lagrangian-based vortex method, the results of which are shown in Figure 4.19. In this figure, the initial distance between the inboard and outboard vortices is $d = 0.275b$ and the circulation strength ratio of the vortices is $\Gamma = -0.58$, which yields a wake that is comparable to that discussed for run 3 in Section 4.4.2 (Γ = -0.55, d_o/b = 8.6 cm/40 cm = 0.22). The value of $d_o = 8.6$ cm is the initial separation distance between the flap and tip vortices and is obtained from the PIV data in Chapter 5. The vortices in Figure 4.19 have been perturbed at three wavelengths: $2b$, $4b$, and $8b$. The $8b$ perturbation is intended to excite the Crow instability between the oppositely-signed tip vortices. The results of [40] demonstrate that the $2b$ perturbation quickly becomes the most rapidly growing mode. The authors report that the time scales of the $2b$ mode are 3-10 times faster than that of the Crow instability. Although the core sizes are not known for the vortices in Figure 4.19, this difference between the time scales of the Crow instability and the instability between the inboard and outboard vortices does agree favorably with the growth rate curves in Figure 3.12 of a similar four-vortex system (Γ = -0.6, d/b = 0.33). Qualitatively, the four-vortex system in Figure 4.19 appears similar to wakes of the triangular-flapped airfoils. It should be noted that the vortex system in Figure 4.19 is generating an upwash. In Figure 4.19c, Ω-shaped hoops are forming as the weaker inboard vortices wrap around the outboard vortices. By Figure 4.19d, the hoops appear to be separating from the outboard vortices and transitioning to closed vortex rings.

However, the above studies did not emphasize theoretical or physical explanations for the causes of the observed instabilities between the unequal strength, counter-rotating vortex pairs. The following chapter will accomplish this by comparing the instability wavelengths in the wakes of the 50%c TF and 75%c TF airfoils with those predicted by the linear stability analyses described in Chapters 2 and 3.
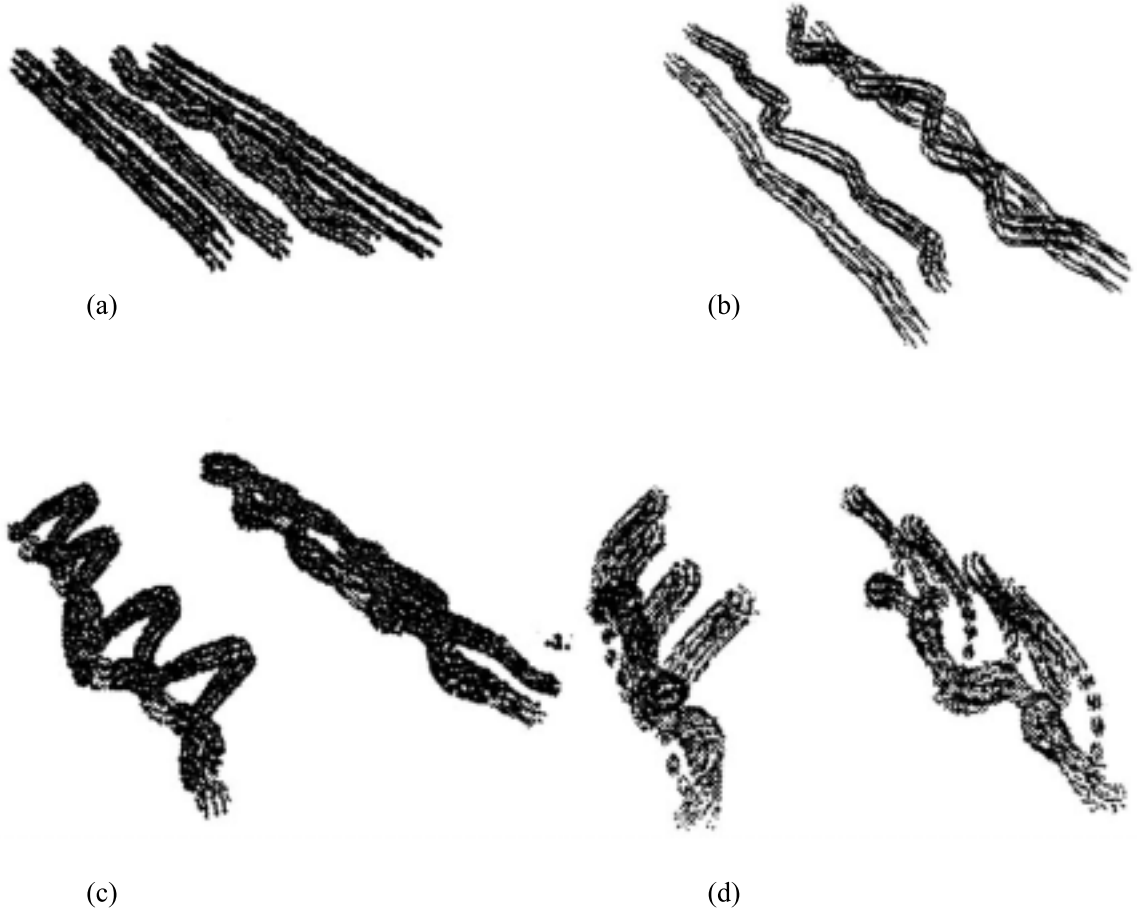
Figure 4.19: Numerical simulation of two counter-rotating vortex pairs from [40]. The inboard and outboard vortices have a relative circulation strength of $\Gamma = -0.58$ and a separation distance of $d/b = 0.275$. The initial perturbations are at wavelengths of $2b$, $4b$, and $8b$. Note that the wake is generating an upwash.

4.4.4   Finite-Time Collapse of the Counter-Rotating Vortex Pairs

As discussed in Section 3.3.4, one of the conclusions of Klein *et al.* [30] was that vortex pairs with negative circulation ratios have a finite-time collapse; that is, the oppositely-signed vortices contact one another in a finite amount of time. With the flow visualization data, it is possible to compare the observations of the present study with this conclusion.

For this analysis, the close-up side view is utilized to measure the time it takes the flap

and tip vortices to first touch one another. The point at which the airfoil is in the center of the field of view is taken to be $t = 0$. There are several challenges in measuring the collapse time with this view. Occasionally, the vortex pair closest to the camera blocks the far vortex pair, making it difficult to observe the exact moment the far pair makes contact. For the longer wavelength instabilities, the nodes of contact on the vortex pair closest to the camera sometimes occur outside the camera's field of view. Thus, for these runs, no collapse time for the closer vortex pair is recorded. In spite of these shortcomings, the measurements do provide an estimate of the collapse times for the different counter-rotating pairs.

The results of the measurements are plotted in Figure 4.20. The y-axis is the collapse time, $\tau_{col.}$, normalized by $\tau_{2D} = 4\pi^2 d_o^2/(\Gamma_t + \Gamma_f)$, which is the orbit time of two equivalent strength point vortices separated by a distance d_o. The relative circulation strengths of the vortex pairs are plotted on the x-axis. For the starboard pairs, the values of Γ_f/Γ_t and d_o are taken from the PIV measurements. However, no PIV measurements were made of the port-side vortex pairs. It is assumed that the port-side vortex pairs have the same relative circulation strengths and separation distances as those on the starboard-side. It can be seen in Figure 4.20 that there is some variation in the collapse time with Γ_f/Γ_t; however, no definite trends are apparent. What is consistently evident, though, is that the flap and tip vortices require on the order of one orbit time to make contact with each other. Furthermore, *all of the counter-rotating pairs in this study exhibit finite-time collapse, confirming the conclusion in* [30].

4.5 Closing Remarks

The flow visualization data provides an excellent, qualitative description of the instability that arises between the unequal strength, counter-rotating vortex pairs. With this data, the highly complex, three-dimensional, vortex interactions are easily identified as the instability becomes non-linear. The one drawback of the flow visualization is that it does not lend itself to other quantitative measurements, such as the circulation strengths of the vortices, their kinetic energy, and internal structure. When the dye becomes dispersed, it
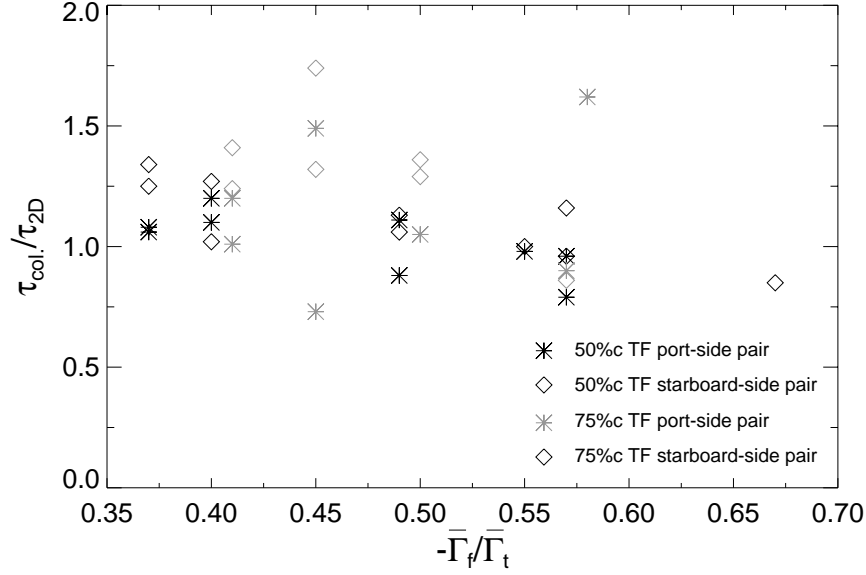
Figure 4.20: Collapse time, $\tau_{col.}/\tau_{2D}$, as a function of Γ_f/Γ_t. The collapse times of the port-side vortex pair are denoted by *'s and those of the starboard-side by diamonds. The collapse times of the 50%c TF airfoil are shown with black symbols and those of the 75%c TF airfoil with gray symbols.

is also difficult to determine what is occurring in the vortex wake. For these reasons, the two-dimensional PIV measurements discussed in the following chapter were carried out to quantify the behavior of the vortex wake at large downstream distances.

Chapter 5

PIV Measurements

5.1 Experimental Setup

Velocity and velocity gradient measurements of the vortex wakes were made with a particle imaging velocimetry (PIV) system, a schematic of which is shown in Figure 5.1. For a detailed view of the vortices, a Kodak Megaplus ES 1.0 (1008 pixels × 1018 pixels) digital camera is placed 4.5 m upstream of a 1 cm thick light sheet generated by a dual-head, pulsed YAG laser (New Wave Gemini). With a 50 mm Canon lens attached to this camera, the field of view at the light sheet is approximately 60 cm × 60 cm. Reference images of the rectangular and triangular-flapped airfoils are shown in Figure 5.2. Because the wakes of the triangular-flapped airfoils spread out so much, only the starboard half of triangular-flapped airfoil is imaged. To produce the light sheet, the laser's beams are passed through a cylindrical lens. The YAG laser and the camera are synchronized with one another through a counter card (Computer Boards CIO CTR-10) that generates five timing signals. The first signal is used to trigger the camera, which is operated in triggered, double exposure mode. When running in this mode, the camera can acquire image pairs at 15 Hz. By varying the timing settings on the counter card, the images within each pair can be separated anywhere from 1 microsecond to 33 milliseconds. For these measurements, the time between sequential PIV images ranges from 6 ms to 12 ms, depending on the airfoil speed. The other four timing signals trigger the Q-switch and lamp-fire inputs on each of
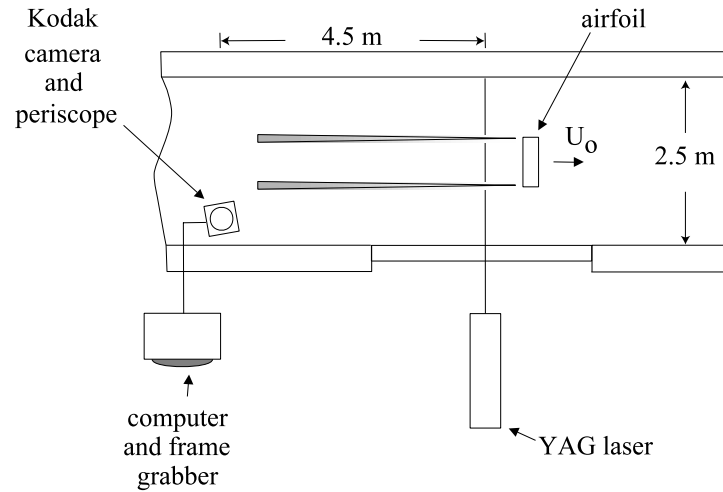
Figure 5.1: Schematic of the PIV system used to make quantitative measurements.

(a)   (b)
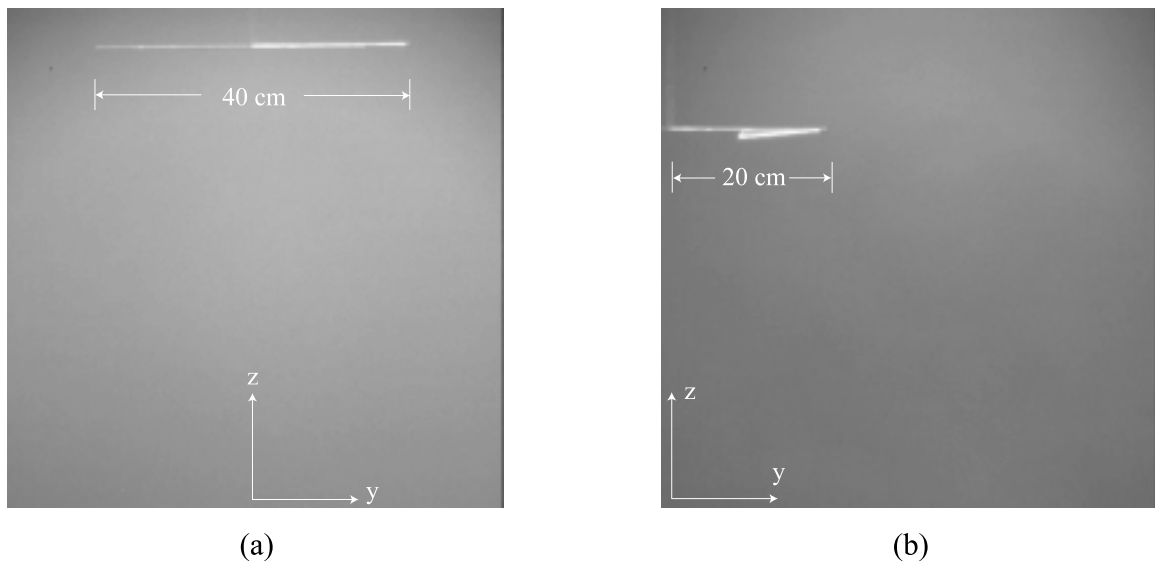
Figure 5.2: Reference image of (a) the rectangular airfoil and (b) the triangular-flapped airfoil in the view of the Kodak camera.

the laser heads. Because the beams from the laser heads are of slightly different diameters, the beams are passed through a metal pinhole ensuring that the light sheet is the about same thickness when either of the heads is firing.

The towing tank test section was seeded with 40 micron silver-coated spheres (Potters Industries) that have a specific gravity of 0.9. The Kodak camera views the particles through a periscope that places the camera approximately 120 cm beneath the water surface (Figure 5.3). To minimize the influence of the periscope on the wake vortices, the periscope is suspended only 15 cm from the tank wall. The images from the Kodak camera are transferred to a computer via a digital frame grabber (Matrox Genesis-LC). Since the images in a pair are so closely spaced in time, the frame grabber treats each monochrome image pair as a single color image. The program running the frame grabber then splits the color image into two monochrome images, which are then transferred to a buffer in the computer's memory. The number of images that can be sequentially grabbed is limited by the amount of memory on the computer. The computer used in this experiment has 1 GB of RAM, allowing a total of 850 images or about 28 seconds worth of data to be captured. After all of the images have been acquired, they are saved on the computer's hard drive.

For a wider view of the vortex wake, a second camera and laser setup was used. A Sony XC-7500C camera with a 50 mm lens is placed 10 m upstream of the test section and is focused upon a light sheet generated by at 10W CW laser (American Laser Corporation). The field of view with this camera is 96 cm × 72 cm. To spread the laser sheet out enough so that it covers this entire field of view, the laser beam is passed through two cylindrical lenses. The Sony camera is mounted in a waterproof, cylindrical shell and suspended 25 cm from the tank wall at a depth of 40 cm. The images of particle streaks from this camera are recorded with the same frame grabber/computer system described above. During the experiments, the Sony camera was used to obtain a first look at the vortex wakes by filming particle streaks in the test section. With the approximate trajectory and behavior of the wake known, the Kodak camera could then be re-oriented to capture the phenomena of interest. For the rectangular airfoil, this meant adjusting the Kodak camera so that the airfoil was at the top of the view (Figure 5.2a). However, for the triangular-flapped airfoils,
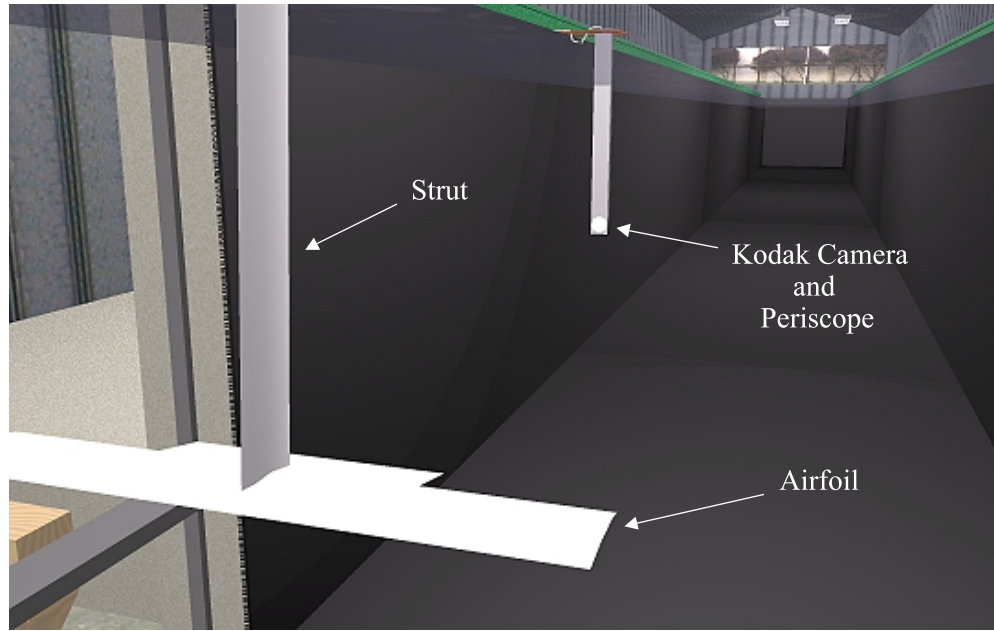
Figure 5.3: Upstream view of the periscope assembly.

the Kodak camera was positioned so that the airfoils were nearly centered in the field of view (Figure 5.2b).

A total of 11 runs with the rectangular airfoil and 24 runs with the triangular-flapped airfoils were done with the setup described above. The time between sequential runs was approximately twenty minutes. Because the particles tend to become dispersed after several runs, the test section of the tank was seeded every three to four hours during the data acquisition process. Additionally, several PIV images were recorded of the background flow in the test section prior to each run. With these images, the velocity fluctuations were calculated to be of order 1 cm/s.

5.2   Image Distortion Correction

One of the drawbacks of placing the Kodak camera/periscope assembly close to the tank wall is that it results in the camera capturing a skewed image of the vortex wake. A

tilt-and-shift lens could have removed this distortion, but one was not available during the experiments. To test the severity of the image distortion, a checkerboard grid made of black and white squares 2 cm × 2 cm was placed in the camera's field of view and recorded. The resulting image is shown in Figure 5.4. It is immediately apparent from this image that the horizontal lines in the grid do not appear horizontal, but at various angles. In addition, the black and white squares on the right side of the image are slightly larger than those on the left side. It was felt that this distortion was significant enough to lead to errors in the PIV measurements and, therefore, it needed to be digitally corrected.
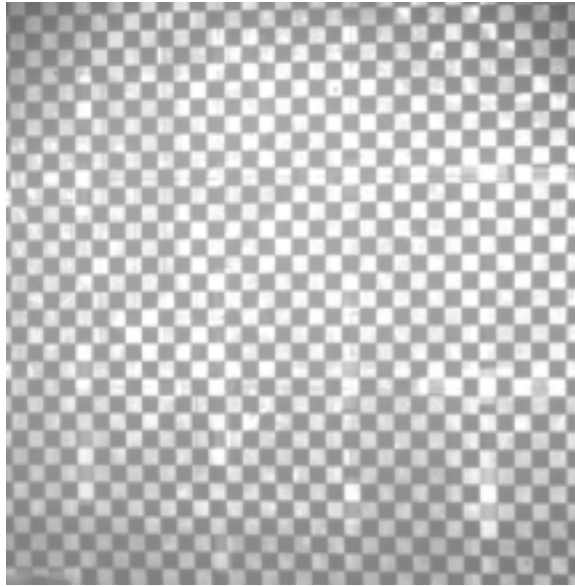
Figure 5.4: Checkerboard grid imaged by the Kodak camera from the periscope. The image distortion is noticeable in the horizontal lines that appear at various angles.

The first step in the correction process is to compute a mapping between the distorted and undistorted camera views. To accomplish this, the perspective drawing technique described in [6] is followed. Figure 5.5 demonstrates a schematic of the plan and elevation views of the grid when it is imaged by the Kodak camera. The variables h_o and w_o are the streamwise and lateral offsets of the camera from the right side of the distorted view.
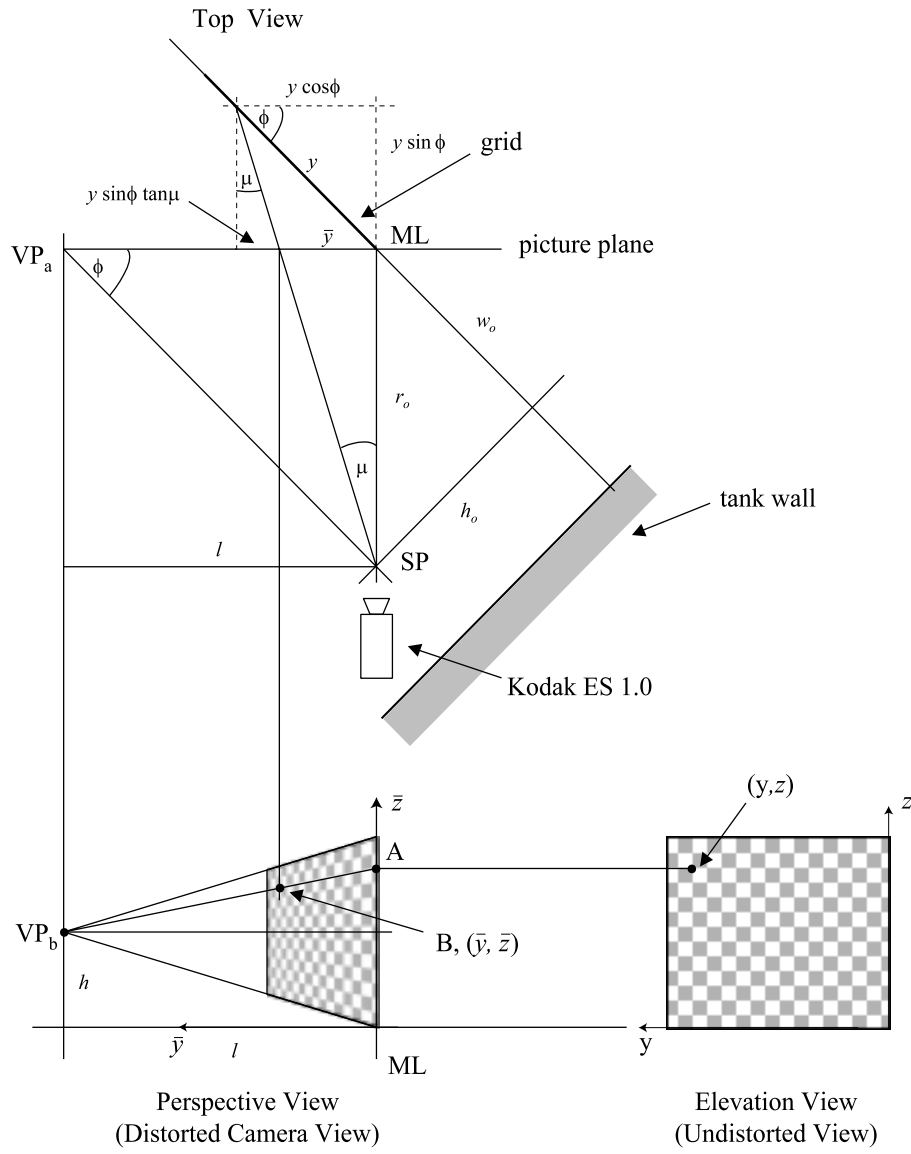
Figure 5.5: Geometric quantities used to compute the mapping between the undistorted and distorted camera views.

Therefore, the distance from the camera to the right side of this view is $r_o = \sqrt{h_o^2 + w_o^2}$. The picture plane in Figure 5.5 is called the upon which the grid is projected. For this analysis, the picture plane is taken to be parallel to the Kodak camera's CCD. The intersection of the right side of the grid and the picture plane is called the measuring line (ML). This is the only vertical line in the perspective view where true, vertical height measurements can be made. In the picture plane, the true distance y is mapped to a location $\bar{y}$. The distance $\bar{y}$ is found by drawing a line from the location y on the grid to the Kodak camera location, which is referred to as the station point (SP). The intersection of this line with the picture plane yields the distance $\bar{y}$. Before $\bar{y}$ can be calculated, the vanishing point must be found by drawing a line from the station point parallel to the grid. The intersection of this line and the picture plane is the vanishing point (VP_a), which is a distance l from the right side of the grid. After some geometry, one can show that the relationship between y and $\bar{y}$ is given by

$$y sin\phi \ \ tan\mu + \bar{y} = y cos\phi \tag{5.1}$$

where $tan\mu = \bar{y}/r_o$. Solving Eq. 5.1 for $\bar{y}$ yields

$$\bar{y} = \frac{y cos\phi}{1 + y sin\phi/r_o} \tag{5.2}$$

where $tan\phi = r_o/l$.

The next step is to find a mapping for the vertical location, $\bar{z}$, in the distorted view. This is accomplished by drawing vertical lines from the points ML, VP_a, and $\bar{y}$ to the area left of the elevation view. A horizontal line is extended from the point (y, z) in the elevation view to the vertical line that originated from the point ML. At the intersection point, A, of these two lines, another line is drawn to the vanishing point (VP_b), which has a vertical offset of h. The intersection point, B, gives the mapped location $(\bar{y}, \bar{z})$ of the point (y, z). It is immediately apparent that $\bar{z}$ is related to z by the relationship

$$z = \bar{z} + \bar{y}\frac{\bar{z} - h}{l - \bar{y}} \tag{5.3}$$

Substituting Eq. 5.2 for $\bar{y}$ into Eq. 5.3 and solving for $\bar{z}$ provides a one-to-one mapping between the undistorted and distorted camera views.
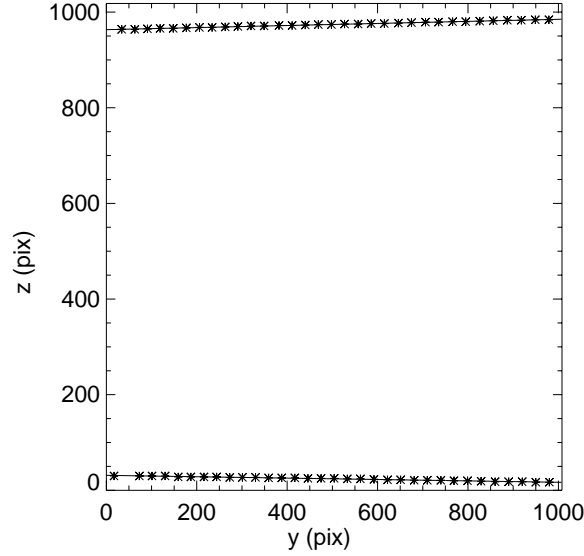
Figure 5.6: Top and bottom rows of the extrema from the convolution of Figure 5.4 with Eq. 5.4. The lines are fit to these data points with a least-squares method in order to obtain the vanishing point location, VP_b.

Before the skewed images can be digitally corrected, the variables h_o, w_o, l, and h need to be found. The streamwise and lateral offsets, h_o and w_o, can be obtained by simply making the necessary measurements of the experimental setup. On the other hand, l and h are calculated from the distorted grid image in Figure 5.4. In order to extract this information from Figure 5.4, it is necessary to fit lines to the distorted horizontal lines in Figure 5.4. A process similar to that described in Debevec [18] is followed to accomplish this task. A checkerboard filter,

$$\begin{pmatrix} 1 & \cdots & 1 & -1 & \cdots & -1 \\ \vdots & \ddots & \vdots & \vdots & \ddots & \vdots \\ 1 & \cdots & 1 & -1 & \cdots & -1 \\ -1 & \cdots & -1 & 1 & \cdots & 1 \\ \vdots & \ddots & \vdots & \vdots & \ddots & \vdots \\ -1 & \cdots & -1 & 1 & \cdots & 1 \end{pmatrix} \tag{5.4}$$

is convolved with the image in Figure 5.4. The size of the filter is 15×15, where the size

of the arrays of 1's is 8×8. When this filter lies on top of four squares that are similar to the filter, the convolution yields a local maximum. When the filter lies on top of four squares that are the inverse of the filter, the convolution gives a local minimum. With the local extrema locations known, the intersection points of the black and white squares are also known throughout the grid. Lines are fit with a least-squares method to the top and bottom rows of these points as shown in Figure 5.6. Where these lines intersect reveals the vanishing point distance, $l = 27,258$ pixels, and its vertical offset, $h = 405$ pixels.
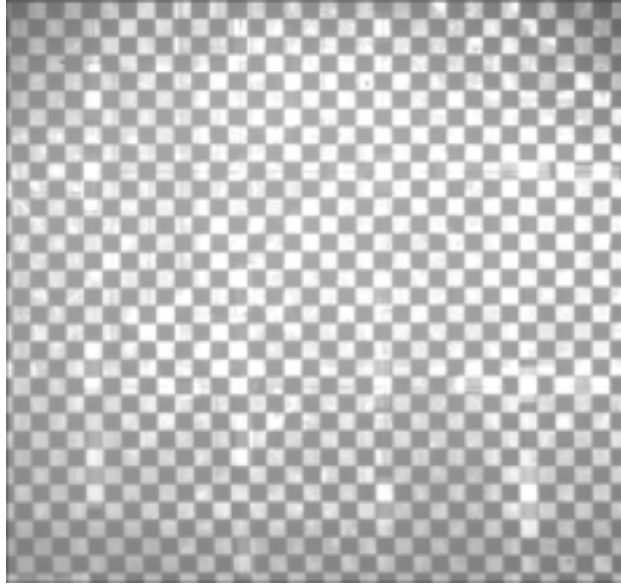
Figure 5.7: Checkerboard grid from Figure 5.4 that has been digitally corrected by the mapping in Eq.'s 5.2 and 5.3.

The digital correction process is carried out by using Eq.'s 5.2 and 5.3 to map a point (y, z) backwards to its corresponding distorted location, $(\bar{y}, \bar{z})$. A four-point interpolation scheme [1] is implemented to find the pixel intensity at the location $(\bar{y}, \bar{z})$. The pixel value is then transferred to the location (y, z) in the undistorted domain. This process is continued until the entire image is generated in the undistorted view. The final undistorted grid image is shown in Figure 5.7. Because of the correction procedure, the undistorted image (1086 pix $\times$ 1018 pix) is larger in the y-direction than the original image (1008 pix $\times$ 1018 pix).

Comparison of Figure 5.4 and 5.7 demonstrates that the horizontal grid lines now appear horizontal. Furthermore, the black and white squares are uniformly sized over the entire image. A FORTRAN program was written to perform this digital correction on the PIV images before they were processed to obtain the velocity and velocity gradient fields.

5.3 Image Processing

The PIV processing was performed on successive image pairs with an adaptive Lagrangian Parcel Tracking (aLPT) Sholl *et al.* [46] algorithm. This algorithm utilizes interrogation windows that are advected and deformed according to the local velocity and velocity gradient fields, improving the quality of the data in regions of strong deformation. The outputs of aLPT are the two-dimensional velocity vector field, u_i, and its gradient tensor, $\partial u_i / \partial x_j$, which is computed spectrally. For this experiment, processing of the 1086 pix $\times$ 1018 pix images results in data fields that are 66 bin $\times$ 62 bin, giving a resolution of 1 cm/bin. Appendix B lists the aLPT parameters that were used to process all of the experimental data.

5.4 Error Analysis of aLPT

Several tests are performed on aLPT to determine its accuracy in measuring the velocity and velocity gradient fields. These tests are accomplished by constructing PIV images in which the particles are advected according to a known velocity distribution. The images are rendered in IDL by generating a random distribution of particles over a 1008 $\times$ 1018 data array, which is the same size as the Kodak camera's CCD. Each particle has a Gaussian intensity distribution, where the width of the Gaussian is one data bin and the peak value is a random number between 0 and 255. The particle density is chosen so that the images appear comparable to those of the experimental data. A portion of an artificial particle image is displayed in Figure 5.8. Using a 2nd order Adams-Bashforth scheme with a time step of 0.0006 s, the particles are then advected by the velocity field of a Lamb-Oseen

vortex,

$$u_\theta(r) = \frac{\Gamma_o}{2\pi r}(1 - e^{-r^2/\sigma^2}) \tag{5.5}$$

After the tenth time step, a second image is rendered at that time step with the known particle locations.
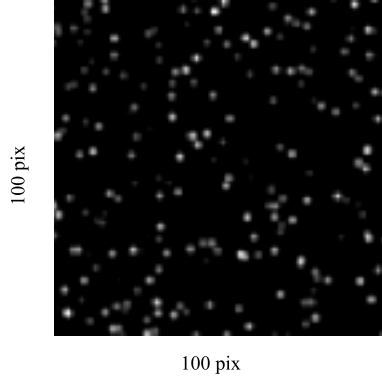
Figure 5.8: A portion of an artificial PIV image.

The circulation strength, Γ_o and core size, σ, of the Lamb-Oseen vortex are chosen to roughly match those of the experimental data. Later processing of the PIV data set reveals that the tip vortices from the triangular-flapped airfoils have an average circulation strength of about 1200 cm^2/s and an apparent core size of $\sigma_f = 3.1$ cm. The flap vortices have an average circulation strength of 600 cm^2/s and an apparent core size of $\sigma_t = 2.6$ cm. These values are used to generate the artificial PIV data, which is processed with aLPT. The processed vorticity data is fit with a Gaussian vorticity distribution,

$$\omega(r) = \frac{\Gamma_o}{\pi\sigma^2}e^{-r^2/\sigma^2} \tag{5.6}$$

allowing the measured circulation strengths and core sizes to be obtained. Two of the input parameters to aLPT are the cutoff, k_e, and exponent, n, of the Fourier filtering kernel,

$$1 - e^{-(k_e/k)^n} \tag{5.7}$$

which is used to filter the processed data in the frequency domain. The variable k_e is the wavelength (in the units of data bins) at the $1/e$ cutoff point of the filtering kernal. Figure 5.9 shows a plot of this filter. Initial processing of the experimental PIV data revealed that $k_e = 6$ and $n = 3$ minimized the amount of background noise, while still preserving the features of the individual vortices. Using these values of k_e and n, the accuracy of aLPT could be assessed by processing the artificial PIV data described above. The first two rows of Table 5.1 provide a comparison between the analytical and processed data for two vortices that have circulation strengths and apparent core sizes comparable to those observed in the experimental data. The normalized standard deviations,

$$\bar{\omega}_{stdev} = \frac{1}{max|\omega_{analy.}|}\sqrt{\frac{\sum_i^{n_x}\sum_j^{n_u}(\omega_{ij\ alpt} - \omega_{ij\ analy.})^2}{n_x n_y - 2}} \tag{5.8}$$

$$\bar{u}_{\theta stdev} = \frac{1}{max|u_{\theta analy.}|}\sqrt{\frac{\sum_i^{n_x}\sum_j^{n_y}(u_{\theta ij\ alpt} - u_{\theta ij\ analy.})^2}{n_x n_y - 2}} \tag{5.9}$$
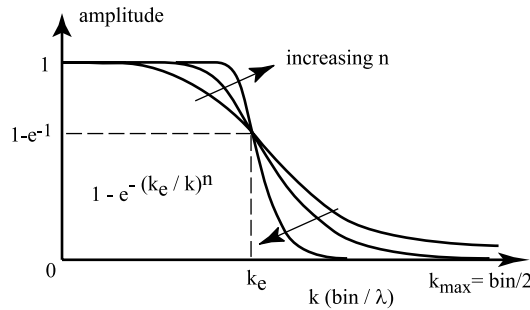
Figure 5.9: Filtering kernal used in aLPT to filter the processed data.

$\sigma_{analy.}$ (cm)	$\Gamma_{o\ analy.}$ (cm^2/s)	$max|\omega_{analy.}|$ $(1/s)$	σ_{alpt} (cm)	$\Gamma_{o\ alpt}$ (cm^2/s)	$max|\omega_{alpt}|$ $(1/s)$	$\bar{\omega}_{stdev}$	$\bar{u}_{\theta stdev}$
3.1	1200	39.7	3.5	1224	31.7	0.031	0.042
2.6	600	28.3	3.2	622	18.9	0.032	0.059
2.4	1200	66.3	3.1	1243	41.1	0.029	0.043
1.6	600	74.6	2.6	636	29.5	0.025	0.048

Table 5.1: Values of the vortex size, σ, circulation strength, Γ_o, and peak vorticity before and after processing with aLPT. The variables $\bar{\omega}_{stdev}$ (Eq. 5.8) and $\bar{u}_{\theta stdev}$ (Eq. 5.9) are the normalized standard deviations of the analytical and processed data. The variable $max|\omega_{analy.}|$ is found from $\Gamma_{o\ analy.}/(\pi\sigma_{analy.}^2)$, while $max|\omega_{alpt.}|$ is the maximum value of vorticity in the processed data field.

of the processed and analytical vorticity and azimuthal velocity data are also shown in this table. The value 2 in the above two equations comes from the two degrees of freedom in the vorticity fitting routine. The variables n_x and n_y are the array size of the processed data field. Selecting a step size of 16 pixels for the interrogation windows used in aLPT results in $n_x = 62$ and $n_y = 62$. This gives a resolution of about 1 cm between each data bin. From Table 5.1, it is evident that aLPT overestimates both the circulation strengths and core sizes. However, the peak vorticity, which is obtained by finding the maximum value of vorticity in the processed data field, is consistently underestimated. In later linear stability analyses of the experimental data, the circulation strengths and vortex core sizes are used and not the peak values of vorticity. Therefore, the errors incurred by the peak vorticity can safely be ignored in those analyses. While the errors in the circulation strengths are acceptable, those in the core sizes are not. The reason for this is that the linear stability analyses depend upon the vortices' self-induced rotation rates, which are a strong function of the vortices' core sizes (Figure 2.3). Therefore, a more accurate assessment of the vortices' sizes is needed. To reconcile these errors, an analysis is performed to determine the amount by which aLPT amplifies the actual core sizes. The last two rows in Table 5.1 summarize the findings of these calculations. When the artificial data is processed for a vortex of $\sigma = 2.4$ cm, aLPT yields a vortex of size 3.1 cm, the average, experimentally measured value of

the tip vortices. Similarly, a flap vortex of size 1.6 cm is reported to have a $\sigma = 2.6$ cm. With these values, a conversion can be found between the actual vortex size and the vortex size that aLPT yields. While not exact, a linear relationship,

$$\sigma_{act.}(cm) = a_1 \sigma_{alpt}(cm) + a_2 \tag{5.10}$$

is assumed to provide the conversion. Using the values of σ in the last two rows of Table 5.1, a_1 is found to be 1.6 and a_2 to be -2.56. The relationship in Eq. 5.10 is used in later linear stability analyses to provide a more accurate prediction of the vortex core sizes and, hence, the instability wavelengths.

Another test that is performed on aLPT is to compare the values of the Γ_o and $\int \omega dA$, which should, theoretically, be identical. Unfortunately, this is not the case. As displayed in Table 5.2, aLPT places a negative bias on the vorticity near the borders of the processed domain. If all of the vorticity is included in calculation of $\int \omega dA$, errors on the order of -40% result for both test cases. However, by cropping off the negatively-biased data by one or two rows and columns, the error can be reduced to a more reasonable level. Note that the relative error in $\int \omega dA$ is larger for the weaker vortex. Figure 5.10 illustrates some of the qualitative differences between the analytical and processed vorticity and azimuthal velocity distributions. It can be seen in Figure 5.10c that aLPT causes the vortex to be

	$\Gamma_{o\ analy.} = 1200\ (cm^2/s)$	$\Gamma_{o\ analy.} = 600\ (cm^2/s)$
$\int \omega dA$ (entire)	674	367
$\int \omega dA$ (cropped by 1)	1138	685
$\int \omega dA$ (cropped by 2)	1211	816

Table 5.2: Comparsion of $\Gamma_{o\ analy.}$ and $\int \omega dA$ for two test cases: $\Gamma_{o\ analy.} = 1200$ cm^2/s, $\sigma_{analy.} = 2.4$ cm; and $\Gamma_{o\ analy.} = 600$ cm^2/s, $\sigma_{analy.} = 1.6$ cm. The intergral is evaluated over the entire data fields and over data fields that are cropped by 1 or 2 rows and columns along the border.
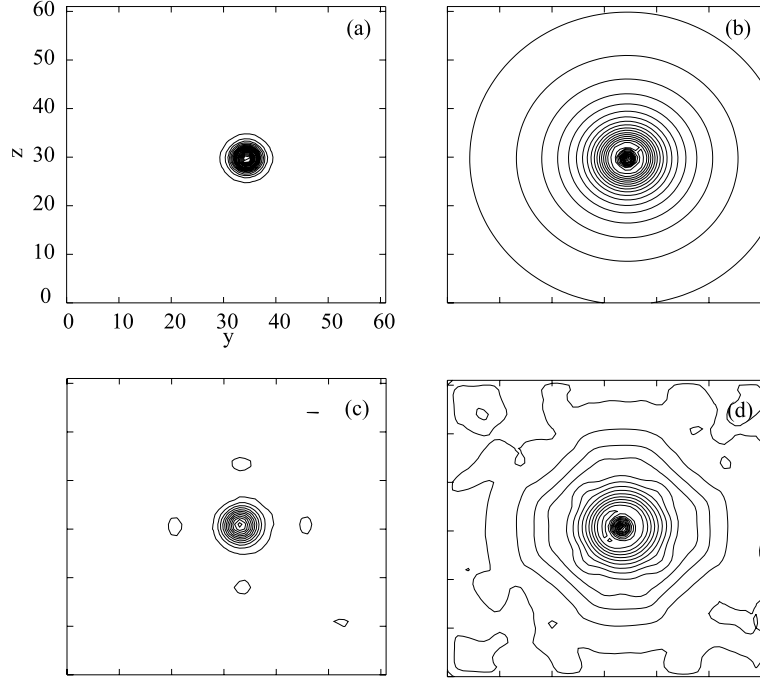
Figure 5.10: (a) Analytical vorticity field, (b) analytical azimuthal velocity field, (c) processed vorticity field, and (d) processed azimuthal velocity field for $\Gamma_o = 1200\ \ cm^2/s$ and $\sigma = 2.4\ \ cm$. The same contour levels are used in (a, c) and (b, d).

slightly slumped to the left and generates four false patches of vorticity around the processed vortex. Instead of being circular, the azimuthal velocity field has a diamond-like appearance at large radii from the vortex center.

The experimental PIV data is processed with the same aLPT parameters as those used above for the artificial data. Therefore, the errors in processing the artificial data can be used to approximate the errors of the actual PIV data. From the last two columns of Table 5.1, it can be seen that the normalized standard deviations between the analytical and processed azimuthal velocity and vorticity data are on the order of 5%. This value can be taken as an estimate of the experimental accuracy. However, it should be noted that the actual data contains out-of-plane motion, meaning that the axial velocity in the vortex wake carries particles through the light sheet. This loss of particles introduces additional errors, which have not been accounted for in the above analyses. Furthermore, the above analyses

have only been performed on an isolated vortex, while the experimental data consists of both one and two vortices. The presence of another vortex may cause additional errors in aLPT. In terms of the spatial resolution of the PIV data, the distance between the data bins is 1 cm with a 50% overlap between successive bins. The temporal resolution of the data depends upon the time between sequential data fields. During these experiments, the time separation between the data fields is 66 ms (15 Hz) such that time scales of the flow smaller than 133 ms cannot be accurately measured.

5.5 Image Brightening

Another consequence of Kodak camera's upstream location from the light sheet is that the particle images, which are exposed for only 6 ns, appear to be very dim. Examination of these images revealed that only the brightest particles are discernable. This led to the notion that there would be additional errors when the data were processed to obtain the velocity and velocity gradient fields. Preliminary processing of the PIV data confirmed these suspicions, as the resulting data was noisier than it ought to have been. The reason for the added noise is that the bright particles are weighted more heavily in the cross-correlation routine in aLPT. Consequently, the bright particles dominate over the dimmer ones, even though the dimmer ones comprise the majority of the flow. A solution to this problem was found by brightening the particle images and increasing their contrast.

The procedure to brighten and increase the image contrast is similar to one in [23]. The process begins by defining two variables, *high* and *low*, where pixel values above *high* are set to 255 and those below *low* are set to 0. The remaining pixel values are mapped according to the relationship,

$$p = \left(\frac{p_o - low}{high - low} \right)^{\kappa} \tag{5.11}$$

where p is the mapped pixel intensity, p_o the original intensity, and κ a term that defines the non-linearity of the mapping. Figure 5.11 displays three intensity mappings for $high = 90$, $low = 20$, and $\kappa = 0.5$, 1.0, and 2.0. For the set of PIV data measured in the towing tank, the values of *high* and *low* are taken to be 150% and 30% of the average pixel intensity of
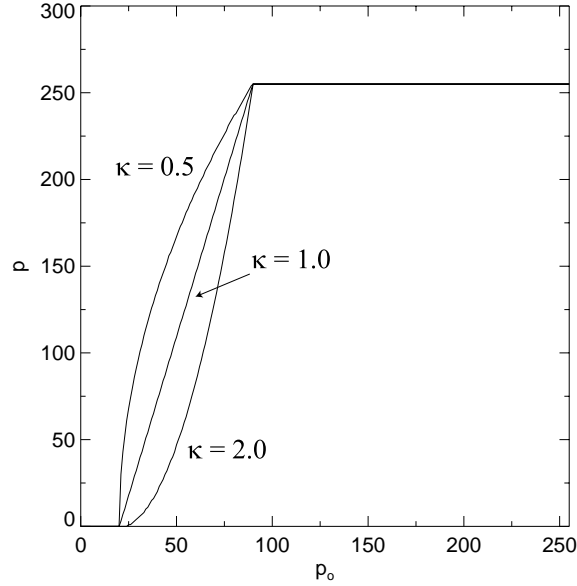
Figure 5.11: Three different brightness mappings using Eq. 5.11 with $high = 90$, $low = 20$, and $\kappa = 0.5$, 1.0, and 2.0.

each image and the value κ to be 1.5.

Figure 5.12 demonstrates the results of brightening an image with these parameters. The figure on the left is an enlarged portion of the original PIV image and the figure on the right is the same image after the brightening. It can be seen that there are more particles visible in the mapped image and that the particle intensity is more uniform over the entire field of view. In order to determine the mapping effects on the processed data, an image pair is brightened and processed and its output data compared with the processed data from the original images. The selected image pair was recorded in the wake of the 75%c TF airfoil and illustrates two unequal strength, counter-rotating vortices. The results of the processing are shown in Figure 5.13, which uses the same contours levels in both plots. It can be seen that not only are the vorticity contours of the mapped images less noisy, but that the peak vorticity and average cross-correlation coefficient values are higher for the brightened image pair.
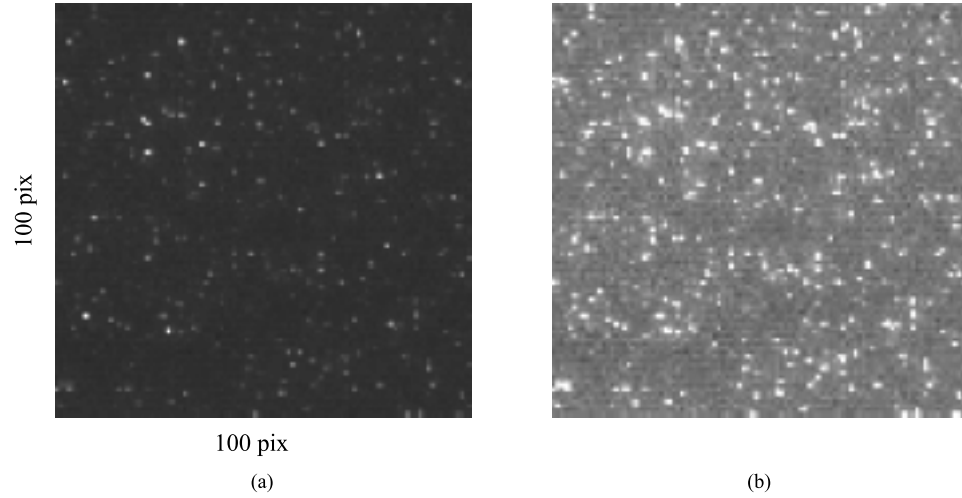
Figure 5.12: Portions (100 pix $\times$ 100 pix) of a typical PIV image: (a) original image (b) brightened image ($high = 150\%$ average pixel intensity, $low = 30\%$ average pixel intensity, $\gamma = 1.5$).
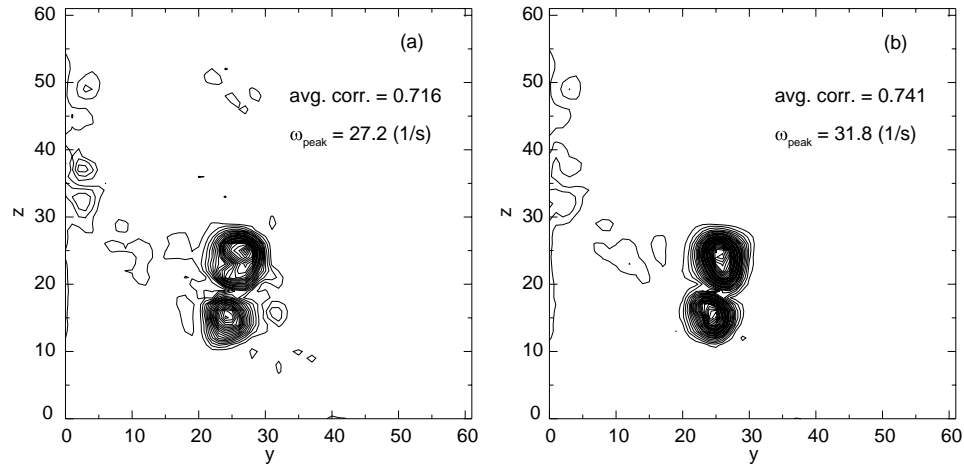
Figure 5.13: Vorticity contours obtained from processing (a) an original PIV image pair and (b) its brightened counterpart. The same contour levels are used in each plot.

5.6   Listing of the Image Pairs

When a large number of PIV images are processed, one of the inputs to aLPT is a list of the image pairs for a given run. Generating this list presents some difficulty because the experimental system used to capture the PIV data occasionally skips images. Consequently, a systematic pairing of images (for example, assuming that the even-numbered images are the first image in every pair and odd-numbered images are the second image in every pair) is not valid throughout an entire run. Since manual examination of each of the image pairs would be tedious, a computer code was written in IDL (Interactive Data Language) to automate this task.

The image list is started with the user inputting the first valid pair, say **image13.raw** and **image14.raw**. The code then proceeds by reading in the next two images (**image15.raw** and **image16.raw**) and computing their linear, Pearson correlation coefficient. The logic of this calculation is that the images within a pair have relatively small particle displacements between them, giving a correlation coefficient that is relatively high. On the other hand, images that do not belong in a pair have larger particle displacements, yielding a lower correlation coefficient. If the correlation coefficient is above the user-supplied threshold, which is typically 0.4, the two images are taken to be a pair and their names are added to the image list. The next two images (**image17.raw** and **image18.raw**) are then opened and evaluated. However, if the correlation coefficient is below the threshold level, it is assumed that one of the images in the pair has been lost. The previous pair's names (**image13.raw** and **image14.raw**) are copied to the present location in the image list and the next images to be evaluated are the second image in the current pair (**image16.raw**) and the one following it (**image17.raw**). This process is repeated until all of the valid image pairs in the run have been added to the image list.

5.7   Post-Processing of the PIV Data

With the two-dimensional velocity and velocity gradient fields obtained from aLPT, the flow statistics for a given run are calculated for the entire field of view, as well as for

the individual vortices. Post-processing of the PIV data from the rectangular and flapped airfoils was achieved with several codes written in IDL.

In order to characterize the trailing vortex wake of the triangular-flapped and rectangular airfoils, several integral quantities are computed, beginning with the first frame in which the airfoil enters the field of view. The analysis of the wake continues until the last frame in the run or until the vortices leave the camera's field of view, whichever comes first. The two-dimensional data fields (y, z) are cropped by 1 bin along all four edges to remove the spurious data that exists along the border of the measurement domain. The wake's total circulation is obtained from

$$\Gamma_o = \int \omega dA \tag{5.12}$$

and the position of the overall vorticity centroid from

$$\mathbf{y}_c = \frac{\int \mathbf{y} \omega dA}{\Gamma_o} \tag{5.13}$$

The descent velocity of the wake is calculated by weighting the velocity field with the vorticity field as in Bilanin *et al.* [4] and Marcus [32] to get

$$\mathbf{v}_c = \frac{\int \mathbf{v} \omega dA}{\Gamma_o} \tag{5.14}$$

For the rectangular airfoil, the expression in Eq. 5.13 is not employed because it would yield a nearly infinite value for the wake's centroid. Instead, the formula,

$$\mathbf{y}_c = \frac{\int \mathbf{y} |\omega| dA}{\int |\omega| dA} \tag{5.15}$$

is used to find the position of the rectangular airfoil's wake. The two-dimensional kinetic energy of the wake is found from

$$K.E. = \frac{1}{2} \int |\mathbf{v}|^2 dA \tag{5.16}$$

For the runs with the triangular-flapped airfoils, a measure of the overall vortex size on one half of the wake is taken to be

$$r_{eff} = \frac{\int (\mathbf{y} - \mathbf{y}_c) \omega dA}{\int \omega dA} \tag{5.17}$$

which is computed over the cropped data field. This size definition has the advantage in that it does not depend upon a model for the vortex structure, a feature that proves to be useful when the flap and tip vortices display highly three-dimensional behavior.

In addition to calculating flow statistics for the entire wake, analyses are performed on the individual vortices. The initial guesses for the locations of the flap and tip vortices (triangular-flapped airfoil) are taken to be the positions of the minimum and maximum values of vorticity, respectively. The initial guesses for the positions of the left and right tip vortices (rectangular airfoil) are found in a similar manner. The locations of the vortices are then iterated upon by shifting an 8 bin × 8 bin box (20 bin × 20 bin box for the rectangular airfoil) over the initial guesses for the flap and tip locations until the boxes' centers coincide with the vortices' centroids (Figure 5.14). The kinetic energy and descent velocity of the rectangular airfoil's vortices are found by calculating Eq.'s 5.14 and 5.16 within the 20 bin × 20 bin box. Because the 8 bin × 8 bin boxes occasionally overlap one another, a different type of analysis is performed for the flap and tip vortices.

To isolate the velocity and vorticity fields of the closely spaced flap and tip vortices, a line is first drawn from the flap centroid to the tip centroid. The minimum of the absolute value of vorticity and its location are then found along this joining line. Another line, perpendicular to the joining line, is drawn through this location and is taken to be the divider between the two vortices. The vortices are then surrounded by two rotated, 16 bin × 16 bin boxes. Within these boxes, the vortices' kinetic energy and updated centroid positions are calculated. Because the coordinate system of the boxes is rotated, the velocity and vorticity data within them are interpolated by fitting a second degree, polynomial surface to the nine data points nearest the data point of interest.

The structure of the individual vortices is obtained by fitting the circulation distribution of a Lamb-Oseen vortex,

$$\Gamma(r) = \Gamma_o(1 - e^{-r^2/\sigma^2}) \tag{5.18}$$

to the circulation data that is inside a 7 bin radius circle (9 bin radius for the rectangular airfoil), which is centered upon each of the vortices' centroids. With Γ_o and σ known from
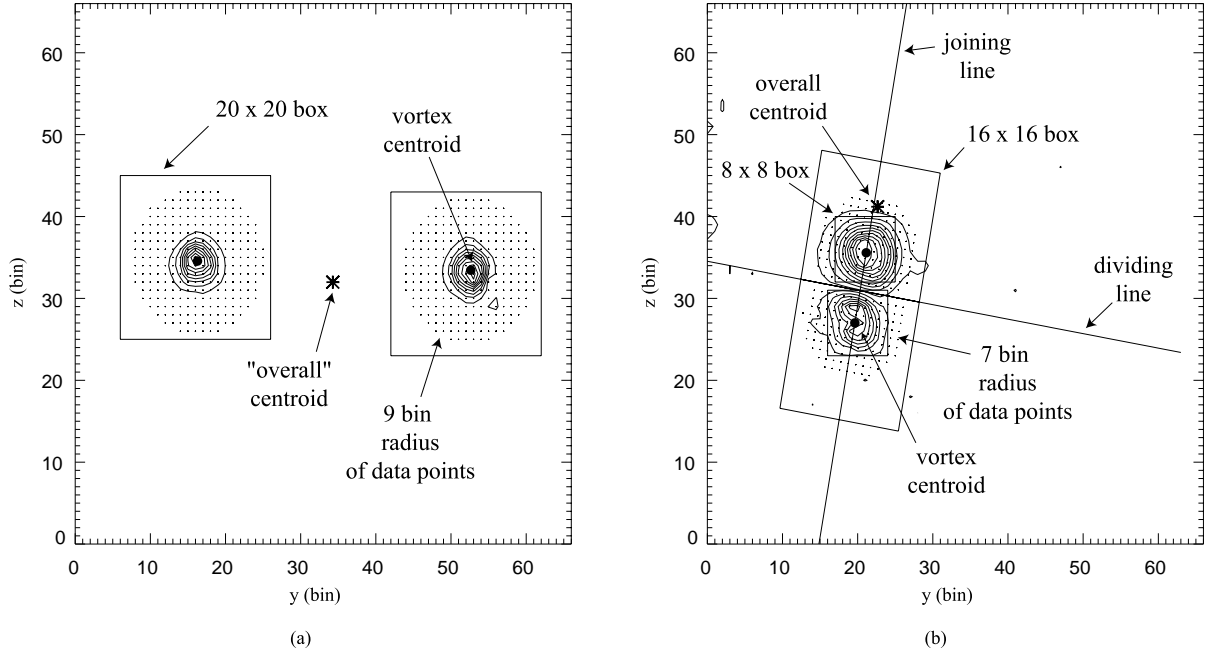
Figure 5.14: Integration regions that are used in the post-processing of the (a) rectangular airfoil, PIV data and (b) the triangular-flapped, airfoil PIV data.

the circulation fit, the vortices' core sizes can be found from

$$r_{max} = 1.12\sigma \tag{5.19}$$

which is the radial location of the maximum azimuthal velocity. The maximum azimuthal velocity is found by substituting the value of r_{max} in Eq. 5.19 into the azimuthal velocity distribution

$$u_\theta(r) = \frac{\Gamma_o}{2\pi r}(1 - e^{-r^2/\sigma^2}) \tag{5.20}$$

to obtain

$$u_{\theta max} = \frac{\Gamma_o}{2.24\pi\sigma}(1 - e^{-1.12^2}) \tag{5.21}$$

The peak value of vorticity is calculated by evaluating

$$\omega(r) = \frac{\Gamma_o}{\pi\sigma^2}e^{-r^2/\sigma^2} \tag{5.22}$$

at $r = 0$. Additionally, the descent velocity and kinetic energy of the flap and tip vortices are obtained by computing Eq.'s 5.14 and 5.16 within the circular regions.

For the triangular-flapped airfoil, analysis of the flap and tip vortices continues until the instability gives rise to three-dimensional effects in the measurement plane. This criterion is somewhat subjective, because it depends on where the light sheet cuts the vortex wake. Typically, the flap and tip vortices are examined until there is a rapid change in their core sizes or until they begin to merge with each other. After this point, calculations for the individual vortices cease and the analysis continues only for those values computed over the entire field of view. For the rectangular airfoil, the tip vortices are examined over the entire run.

5.8   Analysis of the Rectangular Airfoil Data

The results for the rectangular wing data are summarized in Tables 5.3 and 5.4. For the eleven runs that were conducted with this airfoil, the experimental data appear very similar from run to run even though the initial Re_Γ varies from 37,000 to 86,000. Changing the airfoil speed or angle of attack does shift the values of the measured quantities, but the trends in the data remain nearly the same.

The performance characteristics of the airfoil are shown in Figure 5.15, which illustrates the initial circulation as a function of the angle of attack, α, for $Re_c = 2.0 \times 10^5$ ($U_o = 300$ cm/s) and $Re_c = 3.3 \times 10^5$ ($U_o = 500$ cm/s). As α increases from 0° to 3°, the circulation, and, hence, the airfoil's lift increase, indicating that the airfoil is not stalling over this range of α. The spread in the data points at a given angle of attack and Re_c also gives an estimate of the repeatability of the PIV measurements. Note that the circulation is finite at $\alpha = 0^o$, indicative of the camber on the airfoil.

5.8.1   Vorticity Contours and Vortex Trajectories

Vorticity contours at several downstream distances are shown in Figure 5.16 for run 11 ($U_o = 500$ cm/s, $\alpha = 3^o$), in which $Re_\Gamma = 85,600$. The downstream distance, $x(t)$, is

Run	U_o (cm/s)	α (deg.)	$\frac{1}{2}(|\Gamma_{or}(0)| + |\Gamma_{ol}(0)|)$ (cm²/s)	$\bar{\Gamma}_{ol}$ (cm²/s)	$\bar{\Gamma}_{or}$ (cm²/s)
10	500	3	854	-869	883
11	500	3	856	-866	868
13	500	3	821	-851	868
23	500	3	829	-896	917
15	500	0	374	-359	361
16	500	0	383	-346	365
17	500	0	381	-349	361
18	500	2	721	-727	735
19	500	2	725	-723	743
20	500	2	760	-721	733
21	300	2	388	-364	362

Table 5.3: Run parameters for the rectangular airfoils: U_o, airfoil speed; and α, angle of attack. Several measured quantities: $\frac{1}{2}(|\Gamma_{ol}(0)| + |\Gamma_{or}(0)|)$, initial, total circulation; $\bar{\Gamma}_{ol}$, average left vortex circulation; and $\bar{\Gamma}_{or}$, average right vortex circulation.

Run	U_o (cm/s)	α (deg.)	$\overline{K.E.}$ (cm²/s²)	$\bar{r}_{rmax}/b$	$\bar{r}_{lmax}/b$
10	500	3	258,000	0.064	0.061
11	500	3	255,000	0.064	0.061
13	500	3	250,000	0.064	0.060
23	500	3	267,000	0.063	0.061
15	500	0	48,300	0.090	0.103
16	500	0	45,400	0.090	0.100
17	500	0	45,900	0.090	0.112
18	500	2	189,000	0.060	0.063
19	500	2	191,000	0.061	0.061
20	500	2	191,000	0.058	0.060
21	300	2	50,000	0.058	0.060

Table 5.4: Several measured quantities for the rectangular airfoil: $\overline{K.E.}$, average kinetic energy of the wake; $\bar{r}_{rmax}/b$, average core size of the right vortex; and $\bar{r}_{lmax}/b$, average core size for the left vortex. Note that the core sizes are based upon values of σ that have been corrected by Eq. 5.10.
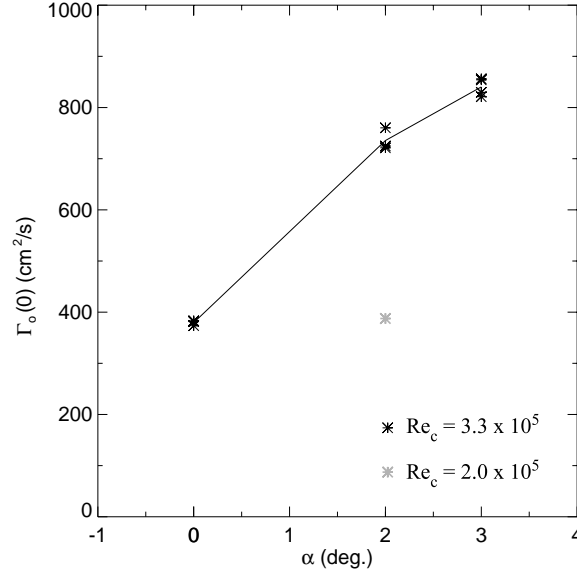
Figure 5.15: Total circulation, $\Gamma_o(t)$, at $x(t)/b = 0$ as a function of the angle of attack, α, for the rectangular airfoil.

found by evaluating $x(t) = U_o t$, where t is the time in seconds since the airfoil passed through the light sheet. At $x(t)/b = 0$, the tip vortices are rolling up from the vortex sheet generated by the airfoil, giving them an elongated shape. The initial separation distance between the left and right vorticity centroids is approximately 37 cm. The two counter-rotating vortices at the airfoil's centerline are due to either the boundary layer off the strut or corner vortices that form at the strut/airfoil junction. By 41 spans, the vortices have long since completed their roll-up process and are nearly circular in shape. Note that the left vortex is somewhat above the right vortex, which is a consequence of an asymmetry in the airfoil's or strut's construction. In the last two plots at $x(t)/b = 83$ and 125, the vortices appear almost exactly as they do at 41 spans; the only difference is that they have descended to a lower elevation in the tank.

The trajectories of the left and right vorticity centroids, as well as that of the entire wake, are shown in Figure 5.17. The horizontal and vertical positions of the wake are found from Eq. 5.15, which is calculated over the cropped data field. After the initial roll-up, the tip vortices descend vertically at nearly a constant rate. There is a slight shift in the
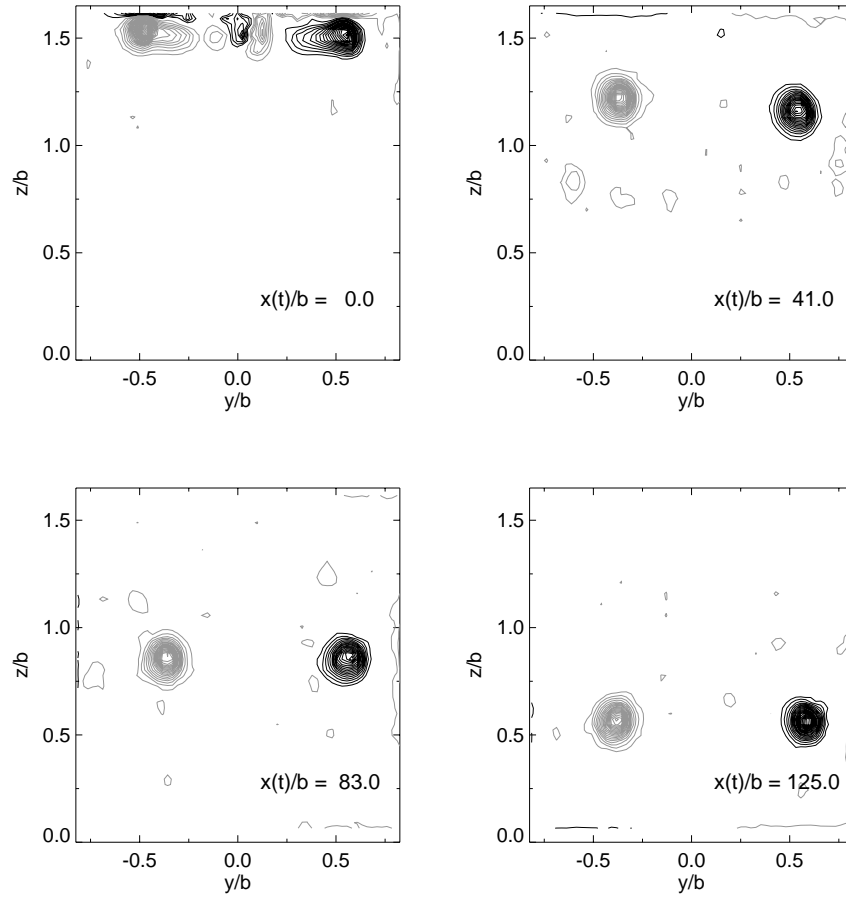
Figure 5.16: Vorticity contours at several downstream locations from the rectangular airfoil (run 11, $U_o = 500$ cm/s, $\alpha = 3^o$). The black contour levels indicate positive values of voriticty and gray contour levels negative values. The same contour levels are used in each of the plots.
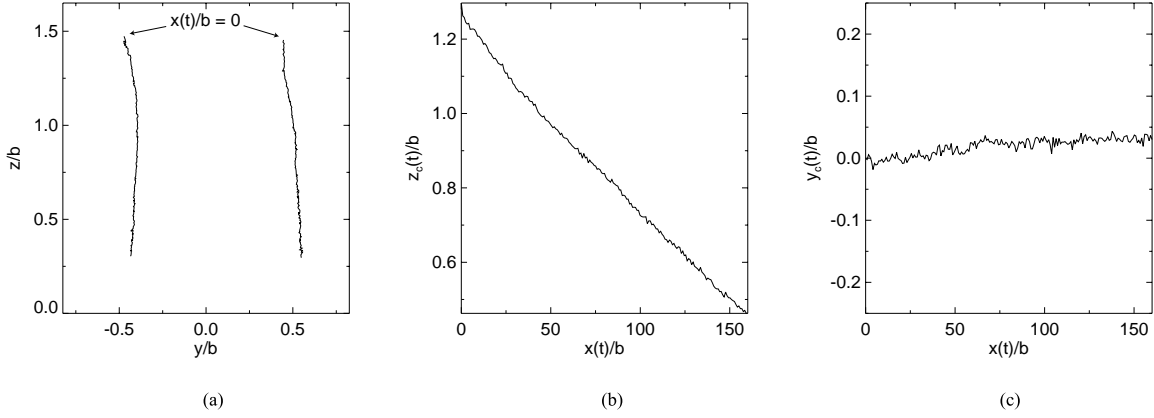
Figure 5.17: Vortex trajectories in the wake of the rectangular airfoil (run 11): (a) paths of the left and right tip vortices and the (b) vertical location, z_c, and (c) horizontal location, y_c, of the wake as a function of downstream distance.

horizontal position of the wake by $x(t)/b = 160$ (Figure 5.17c), which might be due to the slight asymmetry in the airfoil or strut. The nearly vertical paths of the vortices also indicate that the PIV measurement plane is high enough in the tank so that the vortices do not interact with their images across the tank's bottom. It should be noted that the vertical location of the wake ($z_c/b \approx 1.3$) at $x(t)/b = 0$ does not equal that of the individual vortices ($z/b \approx 1.5$). The reason is that the calculated value of z_c/b includes vorticity over the entire field of view, not just that of the tip vortices. Consequently, the non-zero vorticity beneath the tip vortices weights z_c/b to a value that is less than that of the individual tip vortices.

5.8.2 Isovorticity Surfaces

One means of visualizing the vorticity contour data over an entire run is to plot an isovorticity surface, which is generated by stacking contours of one vorticity level. Figures 5.18 and 5.19 illustrate isovorticity surfaces for the wake of the rectangular airfoil (run 11, $U_o = 500$ cm/s, $\alpha = 3^o$). There are three isovorticity surfaces of $|\omega|$ shown in these two figures: $|\omega| = 9.5$, 4.75, and 2.85 1/s. These vorticity levels are chosen to be 25%, 12.5%, and 7.5% of the maximum vorticity (uncorrected) at $x(t)/b = 0$. Figure 5.18 demonstrates a side view of the isovorticity surfaces, such that the vertical axis in the plot is the z-direction.
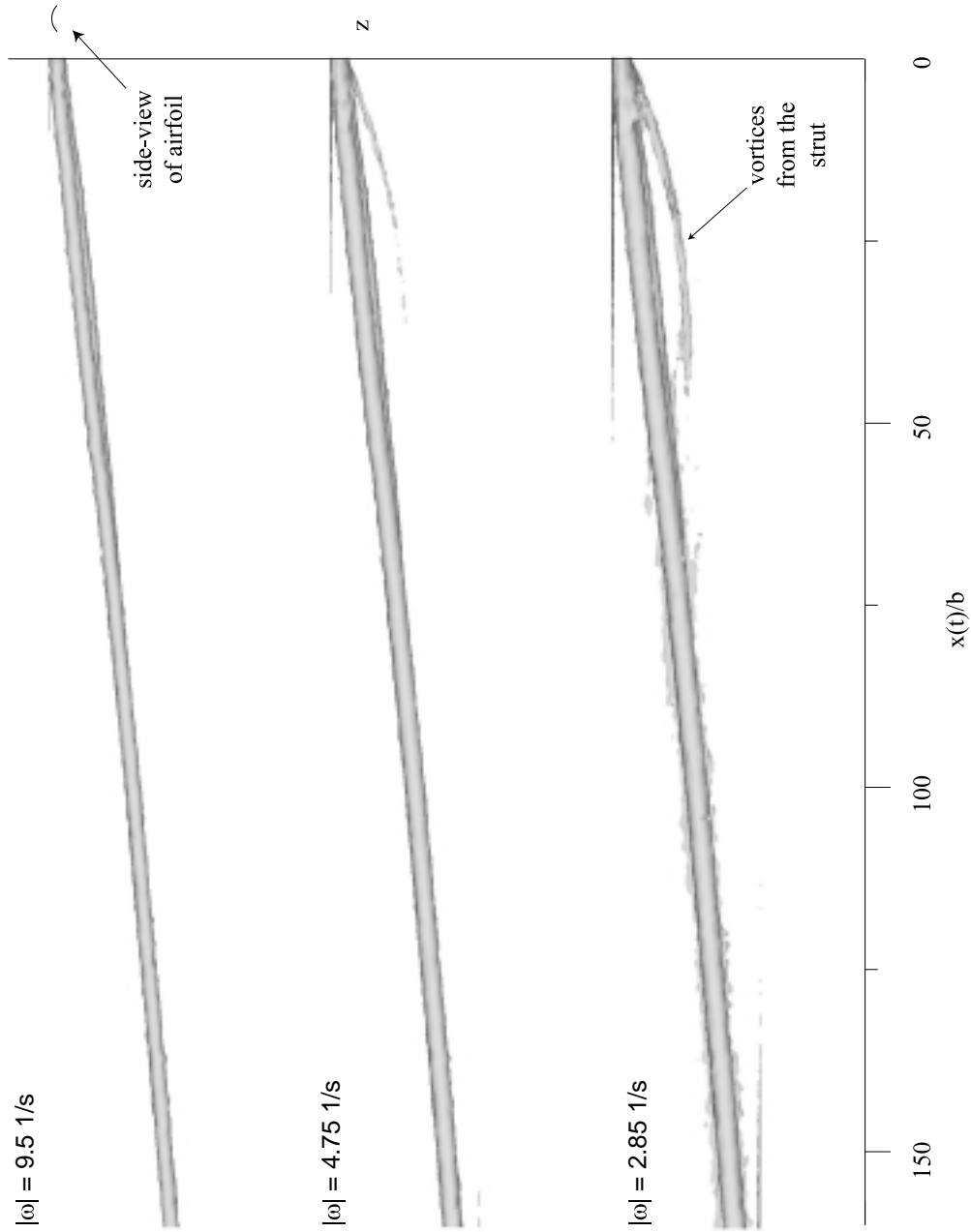
Figure 5.18: Side view of the isovorticity surfaces from the rectangular airfoil (run 11, $U_o = 500$ cm/s, $\alpha = 3^o$). The horizontal axis is the downstream distance, $x(t)/b$, from the airfoil.
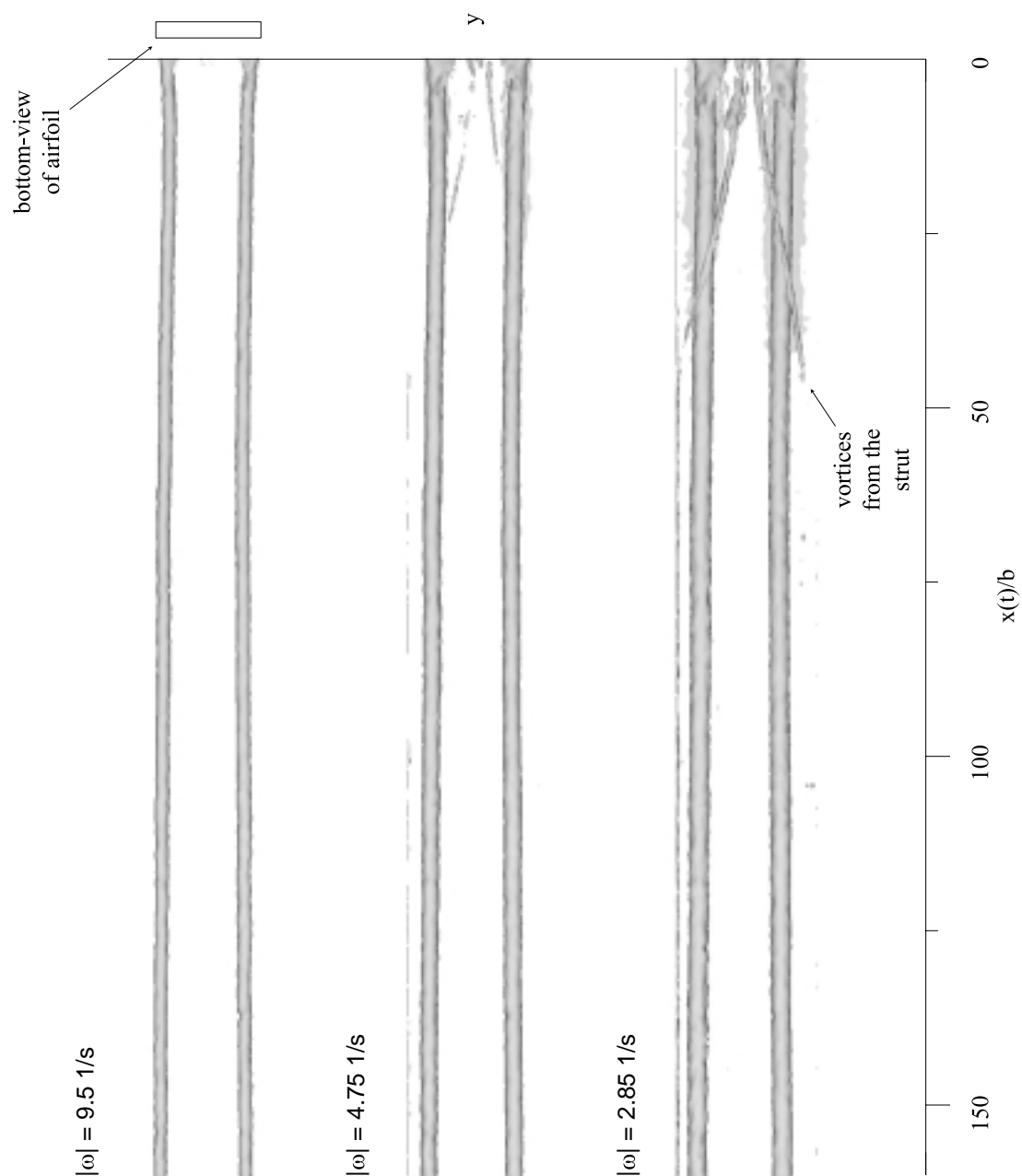
Figure 5.19: Bottom view of the isovorticity surfaces from the rectangular airfoil (run 11, $U_o = 500$ cm/s, $\alpha = 3^o$). The horizontal axis is the downstream distance, $x(t)/b$, from the airfoil.

The cross-section of the airfoil displayed in the upper-right corner is intended to orient the reader. The horizontal axis is the downstream distance, $x(t)/b$, from the airfoil. Figure 5.19 shows the same three isovorticity surfaces, but from a viewpoint of looking up at the wake from below. The vertical axis is the lateral direction, y, across the wake. Again, the figure of the airfoil in the upper right corner is placed there to orient the reader to the flow. The aspect ratio of these surfaces is not quite correct. The vertical and lateral scales are equal to one another, but the axial scale has been compressed.

It can be seen in the side-view surfaces that the wake descends at a nearly constant rate over the entire run. The slight difference in the elevation the right and left tip vortices is also evident in this view from $0 < x(t)/b < 75$. The smaller, counter-rotating vortex pair from the strut is evident in the side-view surfaces for $0 < x(t)/b < 50$. The bottom view of the surfaces illustrates the initial roll-up of tip vortices. From $0 < x(t)/b < 10$, the tip vortices move slightly inboard as the vortex sheet rolls up from the airfoil. Another important feature in Figure 5.19 is the lateral positioning of the wake. Note that there are little, if any, oscillations in the spacing between the tip vortices. This indicates that there are no visible signs of developing instabilities.

5.8.3 Two-Dimensional Kinetic Energy

The two-dimensional kinetic energy of the wake in run 11 is demonstrated in Figure 5.20. The rise and fall of the kinetic energy is due to the fact that the field of view does not encompass all of wake's kinetic energy. Therefore, the value of the kinetic energy depends somewhat upon the location of the vortices in the measurement plane. At $x(t)/b = 0$ and 160, the vortices are at the top and bottom of the camera's view, so that only a portion of the kinetic energy is measured. However, at $x(t)/b \approx 50$, the vortices are in the middle of the measurement plane, which results in a maximum value of the kinetic energy.

5.8.4 Vortex Strength and Structure

The internal structure of the vortices is measured by fitting their circulation distributions with that of a Lamb-Oseen vortex (Eq. 5.18). Figure 5.21a displays the values

of $\Gamma_o(t)$ as a function of the downstream distance from the airfoil. The circulation of the left vortex remains almost constant after the initial roll-up, while that of the right vortex experiences a slight decrease $x(t)/b = 160$. The vortex core sizes, $r_{max} = 1.12\sigma$, maximum azimuthal velocities, and peak vorticity values are shown in Figures 5.21(b-d). All three of
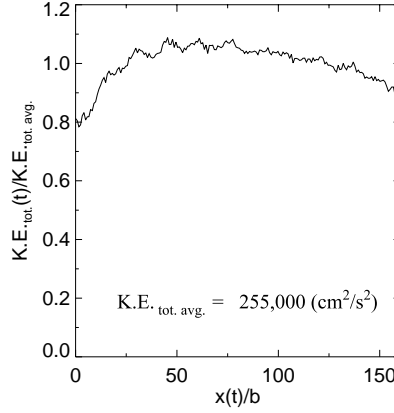
Figure 5.20: Two-dimensional kinetic energy as a function of downstream location for the rectangular airfoil (run 11).

these variables have been computed with values of σ that have been corrected with Eq. 5.10. The maximum azimuthal velocity is normalized by the wake's characteristic descent velocity, $V_o = \Gamma_o(0)/2\pi b_o^*$, where $\Gamma_o(0)$ is the average circulation of the left and right vortices at $x(t)/b = 0$ and b_o^* is the initial separation of the left and right vorticity centroids. The peak vorticity is normalized by the reciprocal of the wake's characteristic descent time, $2\pi b_o^{*2}/\Gamma_o(0)$. The sizes of the right and left vortices vary only slightly about their average values of 6.4%b and 6.1%b. Because of the low temporal resolution of the PIV measurements, it is difficult to say if the small variations of the core sizes are caused by solitons traveling through the laser sheet. The maximum azimuthal velocity and peak vorticity are also relatively constant over the run and exhibit no signs of viscous decay.

The radial distributions of the circulation, azimuthal velocity, and vorticity of the right vortex at $x(t)/b = 100$ are plotted in Figure 5.22. The Lamb-Oseen circulation fit appears to match the data well at this downstream location. In fact, for this particular run,
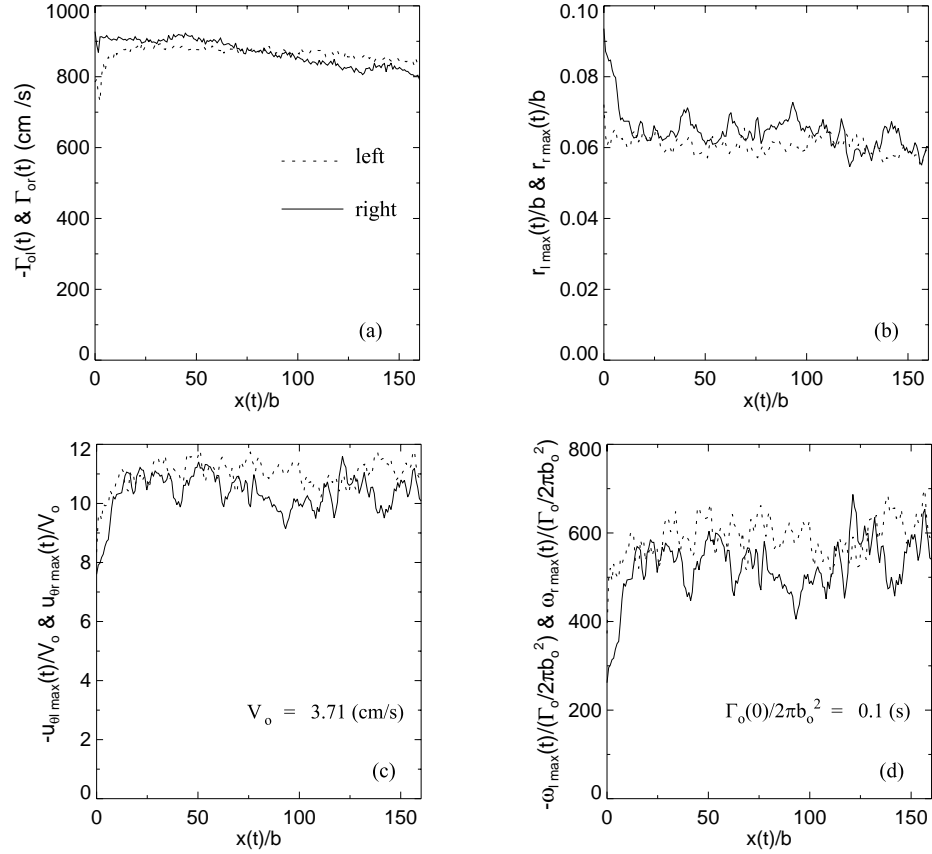
Figure 5.21: (a) Circulation, (b) vortex core sizes, (c) maximum azimuthal velocities, and (d) peak vorticity values as functions of downstream distance for the rectangular airfoil (run 11). The vortex core sizes, maximum azimuthal velocities, and peak vorticities have been computed with values of σ that are corrected with Eq. 5.10.
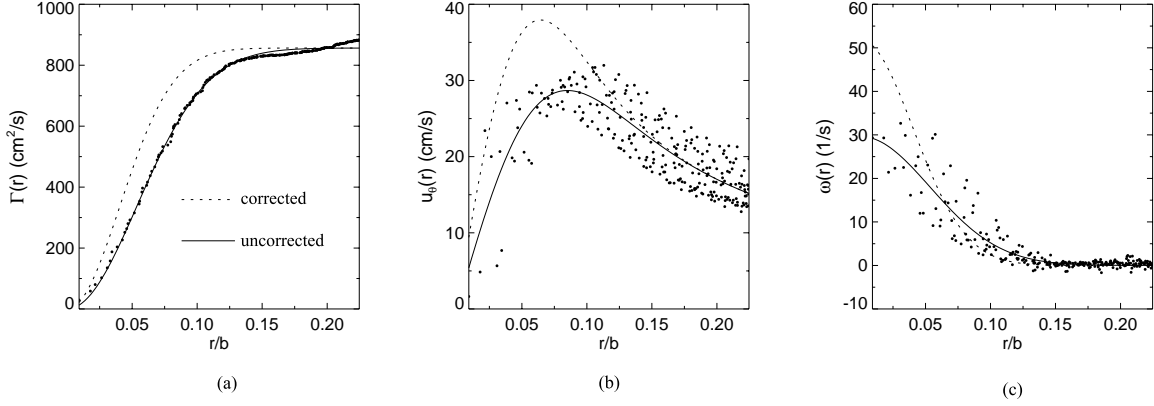
Figure 5.22: Radial distributions of (a) circulation, (b) azimuthal velocity, and (c) vorticity at $x(t)/b = 100$ for the rectangular airfoil (run 11). The radial distributions that are based upon a corrected values of σ (Eq. 5.10) are shown in dashed lines.

the average standard deviation of the circulation fits is roughly 1% of the vortices' total circulations. The vorticity and azimuthal velocity data exhibit larger variations about the Lamb-Oseen profiles. This is partially due to a lack of azimuthal symmetry about the vorticity centroid. Like the Lamb-Oseen vortex, the vorticity data is distributed compactly with irrotational flow outside of the vortex core. This is also evident in the azimuthal velocity's apparent $1/r$ dependence at larger radii. The dashed lines in Figure 5.22 denote the radial distributions that are based on a corrected value of the vortex core size, σ, and are more representative of the actual vortices. By decreasing the size of the vortex and keeping its strength, Γ_o, constant, the maximum azimuthal velocity and peak vorticity are increased to values that are greater than that of the experimental data.

The PIV data from the wakes of the rectangular airfoil confirm the observations that were made previously from the flow visualization data. Namely, that the equal strength, counter-rotating, vortex pairs evolve in a rather steady fashion with no evidence of bursting or decay. Given the quantitative analyses discussed above, it is probably safe to assume that if the towing tank were deeper, these vortex pairs would continue their quiet descent for several hundreds of spans longer.

5.9   Analysis of the Triangular-Flapped Airfoil Data

The results of the triangular-flapped airfoil runs are shown in Tables 5.5 and 5.6. The properties of the wakes prior to the non-linear effects of the instability were very repeatable. However, the unsteady, three-dimensional, and dynamic nature of these wakes is evident in the PIV data after the instability occurred. Consequently, the exact details of the flow physics vary at larger downstream distances from run to run.

Figure 5.23a illustrates the dependence of the initial circulation on the airfoil's angle of attack. The circulation is calculated over the field of view that has been cropped by one data bin along the border. As was the case with the rectangular airfoil, the circulation increases with increasing α. However, the average circulation of the flap vortices (Table 5.6) increases only marginally as the angle of attack was increased from -1.0^o to 2.0^o. This implies that the flow over the triangular flaps is probably stalling at the larger angles of attack. Figure 5.23b shows the ratio, $\bar{\Gamma}_{of}/\bar{\Gamma}_{ot}$, as a function of α for the two triangular-flapped airfoils. The "$^-$" in the previous sentence indicates that these are the time-average flap and tip circulations. It can be seen that the value of $\bar{\Gamma}_{of}/\bar{\Gamma}_{ot}$ depends strongly upon the angle of attack, but not so much upon the type of airfoil.

5.9.1   Vorticity Contours and Vortex Trajectories

The vorticity contours for a run in which $\bar{\Gamma}_{of}/\bar{\Gamma}_{ot} =$ -0.37 (run 39, $U_o =$ 500 cm/s, $\alpha = 2.0^o$, 50%c TF) are shown in Figure 5.24. Negative values of vorticity are labeled with gray contours and positive values with black contours. The same contour levels are used in each of the eight plots. At $x(t)/b = 0$, the flap and tip vortices are rolling up from the airfoil. The "comma"-like appearance of the tip vortex is due to the roll up of the vortex sheet along the trailing edge of the triangular flap. The vorticity shed from the strut can also be seen on the left side of the plot from $1.2 < z/b < 1.6$. By 18 spans, the counter-rotating pair has orbited about $3\pi/4$ radians. From the flow visualization data, the instability amplitude is finite at this downstream location, yet the vortices in this measurement plane exhibit no evidence of its presence. However, a rapid change in the vortices' core sizes occurs at 38
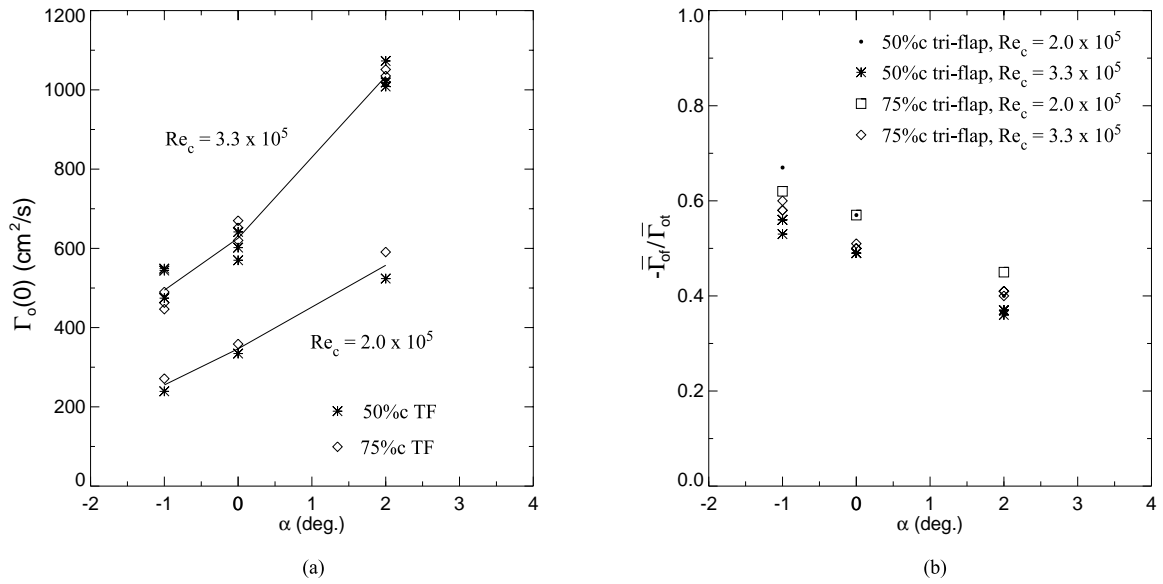
Figure 5.23: (a) Total circulation at $x(t)/b = 0$ and (b) the average value of $\bar{\Gamma}_{of}/\bar{\Gamma}_{ot}$ as functions of the angle of attack, α, for the triangular-flapped airfoils.

Run	$Wing$	U_o (cm/s)	α $(deg.)$	$\Gamma_{tot.}(0)$ (cm^2/s)	$\bar{\Gamma}_{of}$ (cm^2/s)	$\bar{\Gamma}_{ot}$ (cm^2/s)
38	50%c TF	500	2	1009	-612	1644
39	50%c TF	500	2	1018	-607	1640
40	50%c TF	500	2	1073	-605	1663
42	50%c TF	500	0	570	-599	1228
43	50%c TF	500	0	602	-609	1237
44	50%c TF	500	0	641	-601	1237
46	50%c TF	500	-1	474	-597	1073
47	50%c TF	500	-1	549	-594	1053
48	50%c TF	500	-1	544	-576	1087
69	50%c TF	300	2	524	-396	980
70	50%c TF	300	0	335	-439	773
71	50%c TF	300	-1	239	-444	663
50	75%c TF	500	2	1051	-689	1705
52	75%c TF	500	2	1035	-699	1715
53	75%c TF	500	2	1019	-698	1719
55	75%c TF	500	0	670	-653	1276
56	75%c TF	500	0	652	-655	1306
57	75%c TF	500	0	620	-629	1266
59	75%c TF	500	-1	463	-649	1085
60	75%c TF	500	-1	490	-642	1114
61	75%c TF	500	-1	447	-650	1122
64	75%c TF	300	0	359	-453	796
65	75%c TF	300	-1	271	-408	655
66	75%c TF	300	2	591	-454	1012

Table 5.5: Run parameters for the triangular-flapped airfoils: 50%c TF airfoil; 75%c TF airfoil; U_o, airfoil speed; and α, angle of attack. Several measured quantities: $\Gamma_{tot.}(0)$, initial, total circulation; $\bar{\Gamma}_{of}$, average flap circulation; and $\bar{\Gamma}_{ot}$, average tip circulation.

Run	$Wing$	U_o (cm/s)	α $(deg.)$	$\overline{K.E.}(cm^2/s^2)$	$\bar{r}_{tmax}/b$	$\bar{r}_{fmax}/b$
38	50%c TF	500	2	164,000	0.069	0.039
39	50%c TF	500	2	169,000	0.068	0.037
40	50%c TF	500	2	165,000	0.068	0.034
42	50%c TF	500	0	94,500	0.066	0.044
43	50%c TF	500	0	79,200	0.061	0.045
44	50%c TF	500	0	93,000	0.063	0.044
46	50%c TF	500	-1	60,700	0.061	0.050
47	50%c TF	500	-1	65,600	0.060	0.052
48	50%c TF	500	-1	71,800	0.064	0.048
69	50%c TF	300	2	70,500	0.071	0.044
70	50%c TF	300	0	45,600	0.068	0.050
71	50%c TF	300	-1	24,600	0.069	0.056
50	75%c TF	500	2	150,000	0.069	0.036
52	75%c TF	500	2	144,000	0.068	0.039
53	75%c TF	500	2	133,000	0.071	0.039
55	75%c TF	500	0	107,000	0.063	0.042
56	75%c TF	500	0	97,000	0.063	0.040
57	75%c TF	500	0	82,100	0.061	0.040
59	75%c TF	500	-1	56,400	0.063	0.050
60	75%c TF	500	-1	60,500	0.064	0.053
61	75%c TF	500	-1	55,300	0.068	0.048
64	75%c TF	300	0	32,000	0.068	0.050
65	75%c TF	300	-1	22,200	0.066	0.063
66	75%c TF	300	2	72,500	0.071	0.045

Table 5.6: Several measured quantities for the triangular-flapped airfoils: $\overline{K.E.}$, average kinetic energy; $\bar{r}_{tmax}/b$, average tip vortex size; and $\bar{r}_{fmax}/b$, average flap vortex size. Note that the core sizes are based upon values of σ that have been corrected by Eq. 5.10.
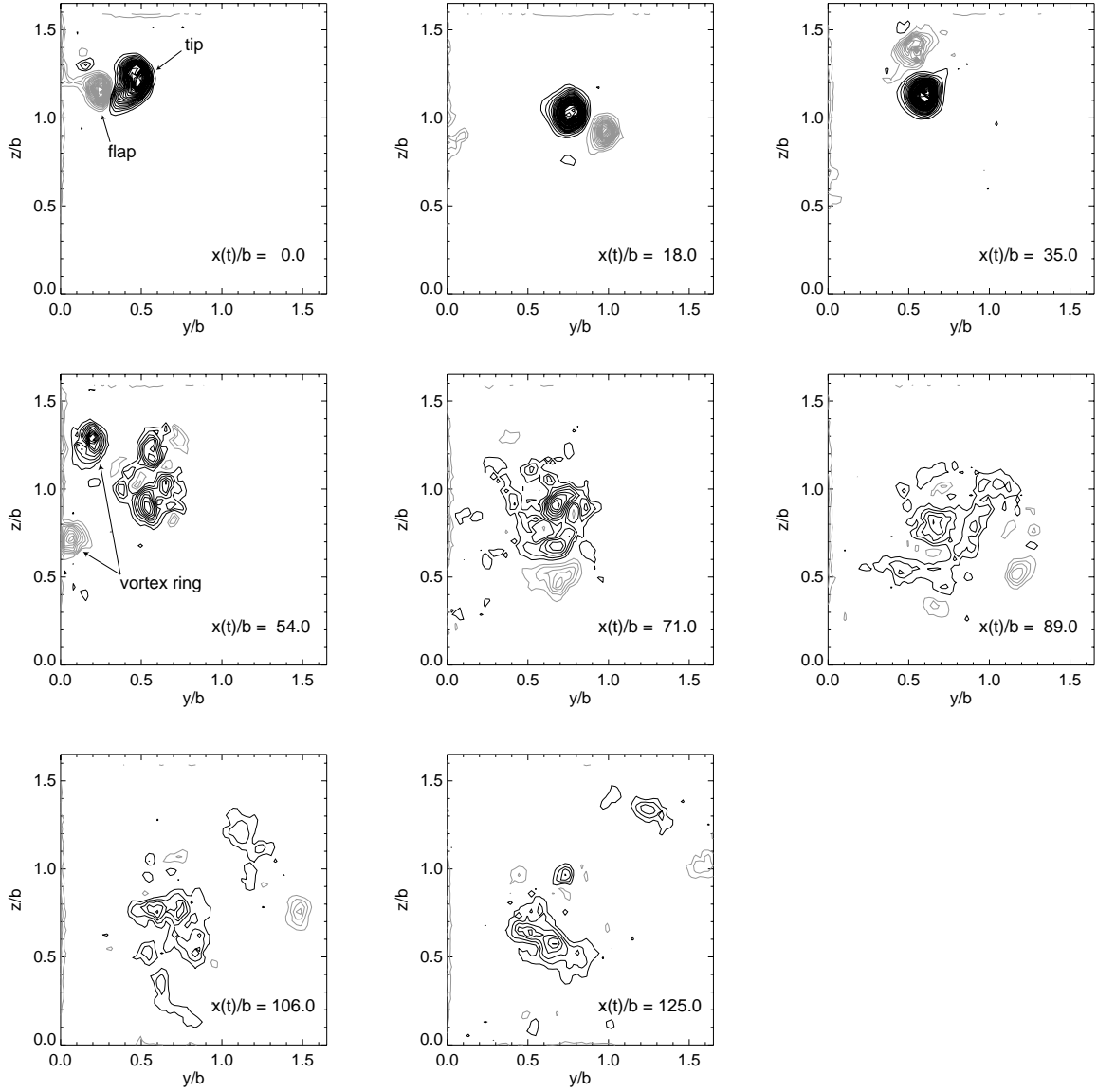
Figure 5.24: Vorticity contours at several downstream locations for $\bar{\Gamma}_{of}/\bar{\Gamma}_{ot}$ = -0.37 (run 39, U_o = 500 cm/s, $\alpha = 2.0^o$, 50%c TF). The black contour levels indicate positive values of voritcity and gray contour levels negative values. The same contour levels are used in each of the plots.

(a) (b)
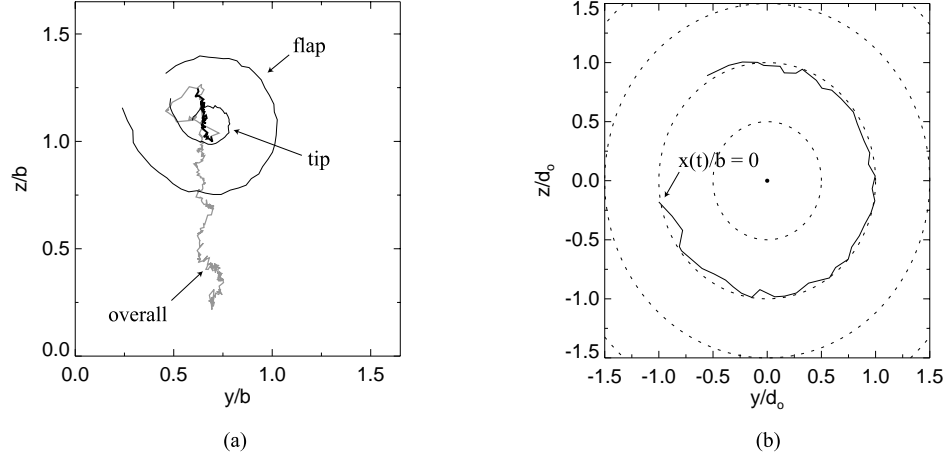
Figure 5.25: (a) Trajectories of the flap and tip vortices and overall centroid for $\bar{\Gamma}_{of}/\bar{\Gamma}_{ot}$ = -0.37 (run 39, U_o = 500 cm/s, α = 2.0^o, 50%c TF) (b) position of the flap vortex with respect to the tip vortex for $0 \leq x(t)/b < 38$.

spans (not shown) as the non-linear effects of the instability propagate through the measurement plane. At 54 spans, the tip vortex splits into two and a vortex ring enters the measurement plane from the left. This ring collides with the right-side tip vortex at 71 spans, which results in large patches of vorticity being spread across the field of view. By 125 spans, a few remnant patches of vorticity remain, although their peak values are significantly less than that at $x(t)/b = 0$.

The trajectories of the flap and tip vorticity centroids, as well as the centroid of the entire wake, are plotted for run 39 in Figure 5.25a for $0 \leq x(t)/b \leq 243$. The thin, black lines are the positions of the flap and tip vortices prior to the rapid change in vortex structure at 38 spans. The thick, black line denotes the centroid of the wake for $x(t)/b < 38$, while the gray line illustrates it for $x(t)/b \geq 38$. Initially, the flap and tip vortices follow curved paths as they orbit outwardly about their vorticity centroid. The position of the flap vortex with respect to the tip vortex during this time is shown in Figure 5.25b. The flap vortex's position is normalized by the initial separation distance, d_o, between the flap and tip vortices, which for this run is 9.82 cm. It is evident that the distance between the vortices remains almost constant. For other runs, the distance between the flap and tip vortices increases or decreases, depending on whether or not the light sheet cuts the wake

at a peak or trough of the instability on the flap vortex. While $x(t)/b < 38$ spans, the wake's centroid descends vertically downward. However, as the vortex ring enters the field of view, the position of the wake's centroid fluctuates largely. After the collision of the ring and the tip vortex, the overall centroid continues its vertical descent.

For larger values of $|\bar{\Gamma}_{of}/\bar{\Gamma}_{ot}|$, the vortex dynamics appear somewhat different. Figure 5.26 illustrates this in the vorticity contours for a run in which $\bar{\Gamma}_{of}/\bar{\Gamma}_{ot} =$ -0.53 (run 48, U_o = 500 cm/s, $\alpha = -1.0$, 50%c TF). At $x(t)/b = 54$, the tip vortex divides into smaller pieces and the flap vortex exits the measurement plane. In the subsequent contour plots, the sinusoidal instability results in an ejection of the flap vortex and its remnants towards the upper right hand corner of the contour plots. Notice that there is no exchange of vorticity across the airfoil centerline. Instead, the non-linear effects of the instability are confined to either side of the wake, which is consistent with the flow visualization measurements discussed in Section 4.4.2.

The vortex trajectories for $\bar{\Gamma}_{of}/\bar{\Gamma}_{ot} =$ -0.53 (Figure 5.27) also differ from those of $\bar{\Gamma}_{of}/\bar{\Gamma}_{ot} =$ -0.37 (run 39). As one would expect, the flap and tip vortices trace out circular arcs that have larger radii of curvature, which is simply due to the fact that the vortices are more equal in strength. One interesting result was that the wake has a noticeably reduced descent velocity after the instability occurs. This phenomenon was previously mentioned in the flow visualization observations (Section 4.4.2). In the flow visualization data, there appeared to be no distinct downwash in the test section for $x(t)/b > 125$ (Section 4.4.2). However, because the dye was so dispersed at these downstream locations, no conclusions could be made from that data. The overall centroid of the wake, which is plotted up to 330 spans downstream of the airfoil, illustrates this observation. For $x(t)/b > 38$, the overall centroid fluctuates largely at first, but then lingers in the vicinity of the tip vortex's final location for the remainder of the run. This behavior was consistently observed for the runs that had an angle of attack equal to -1.0^o. Unlike the runs at $\alpha = 2^o$, the overall centroid would remain in approximately the same location for the remainder of the run and not descend out of view. This is not to say that the wake has stopped descending completely.
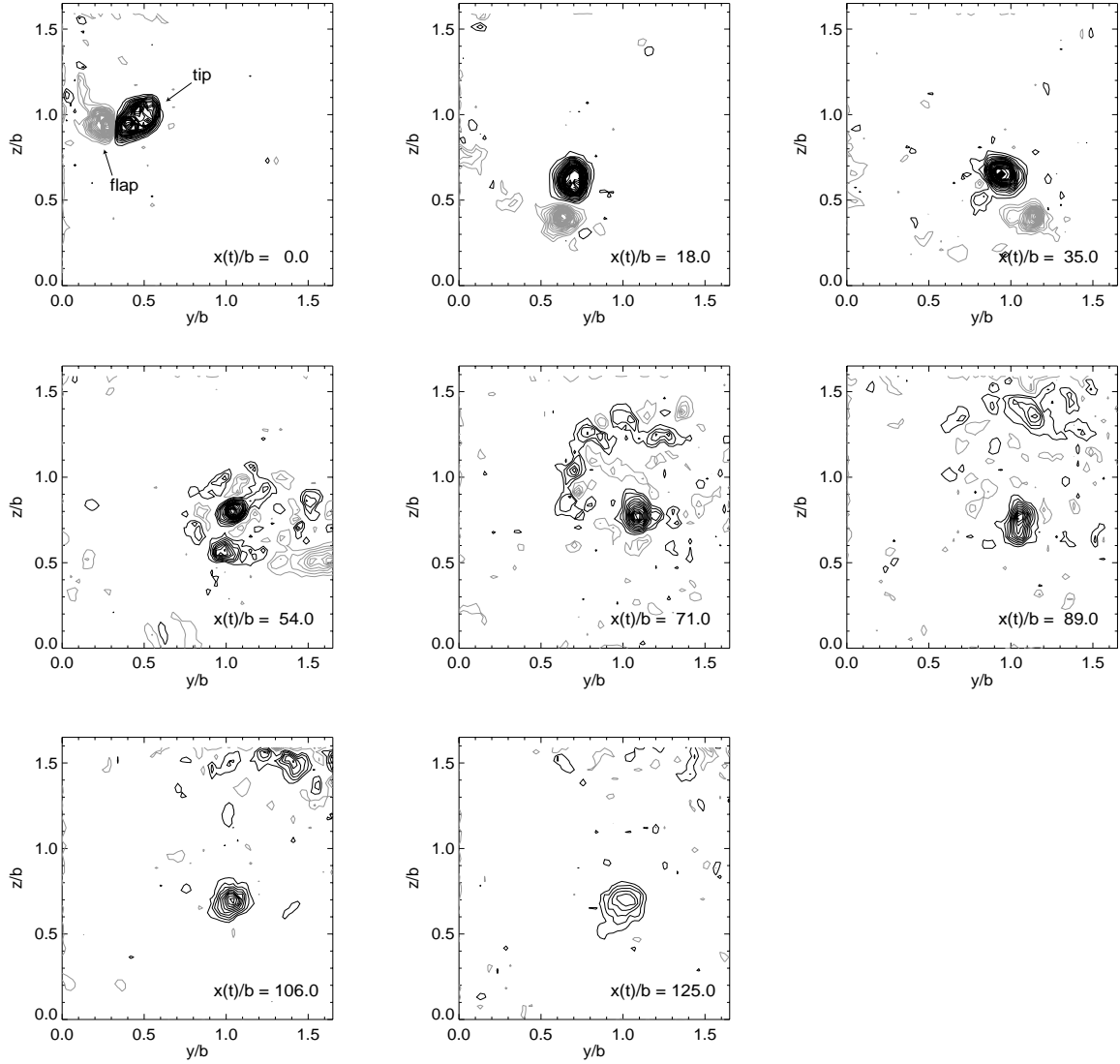
Figure 5.26: Vorticity contours at several downstream locations for $\bar{\Gamma}_{of}/\bar{\Gamma}_{ot} = $ -0.53 (run 48, $U_o = 500$ cm/s, $\alpha = -1.0^o$, 50%c TF airfoil). The black contour levels indicate positive values of voritcity and gray contour levels negative values. The same contour levels are used in each of the plots.
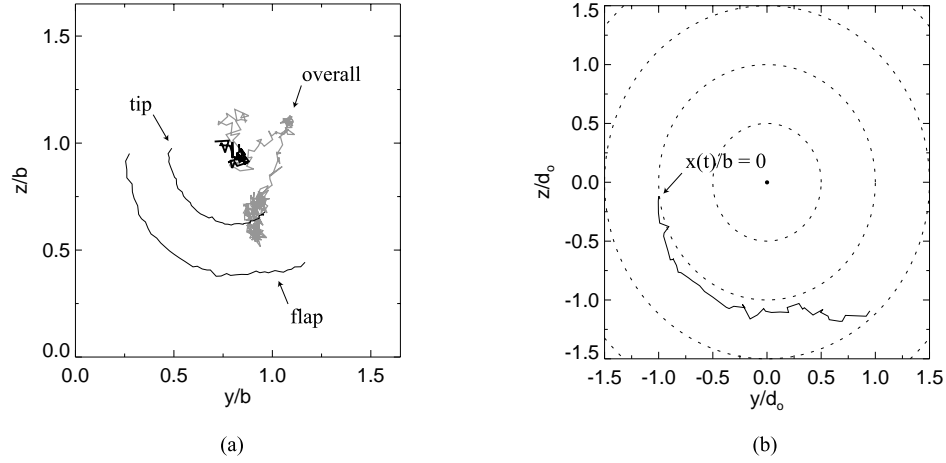
Figure 5.27: (a) Trajectories of the flap and tip vortices and overall centroid for $\bar{\Gamma}_{of}/\bar{\Gamma}_{ot} =$ -0.53 (run 48, $U_o = 500$ cm/s, $\alpha = -1.0^o$, 50%c TF) (b) position of the flap vortex with respect to the tip vortex for $0 \leq x(t)/b < 38$.

In fact, a review of the particle-streak data from the wide-view Sony camera revealed that there is a small, but finite, amount downwash in the wake at 330 spans downstream of the airfoil.

5.9.2   Isovorticity Surfaces

The isovorticity surfaces for run 39 ($U_o = 500$ cm/s, $\alpha = 2.0^o$, 50%c TF, $\bar{\Gamma}_{of}/\bar{\Gamma}_{ot} = -0.37$) are shown in Figures 5.28 and 5.29. Three surfaces of $|\omega|$ are shown: $|\omega| = 9.75$, 4.88, and 2.93 1/s. These values correspond to 25%, 12.5%, and 7.5% of the maximum vorticity (uncorrected) of the flap vortex at $x(t)/b = 0$. Figure 5.28 illustrates a side view of these surfaces, while Figure 5.29 shows their bottom view. The side view of the surfaces is taken from a vantage point of one located at the airfoil centerline and looking outboard to the triangular flap. Consequently, the flap vortex in Figure 5.28 is initially closest to the viewer. The dashed line at $x(t)/b = 38$ is the downstream distance at which the vortices exhibit a sudden change in their internal structure. Unlike the isovorticity surfaces for the rectangular airfoil (Figures 5.18 and 5.19), the surfaces in the wake of the 50%c TF airfoil are highly unsteady and are characterized by large changes in the vorticity distribution.
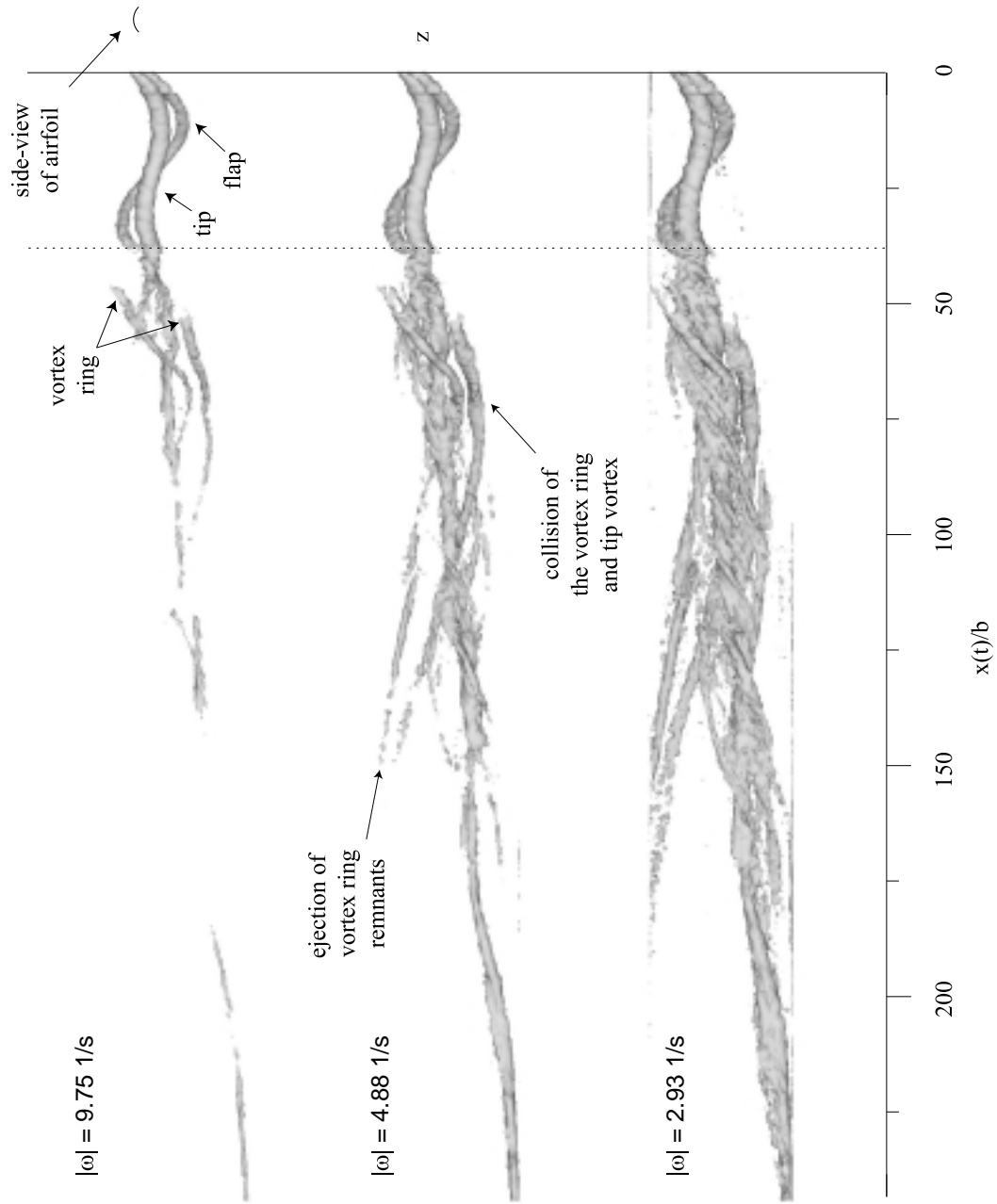
Figure 5.28: Side view of the isovorticity surfaces for run 39 ($U_o = 500$ cm/s, $\alpha = 2.0^o$, 50%c TF, $\bar{\Gamma}_{of}/\bar{\Gamma}_{ot} = -0.37$). The horizontal axis is the downstream distance, $x(t)/b$, from the airfoil.
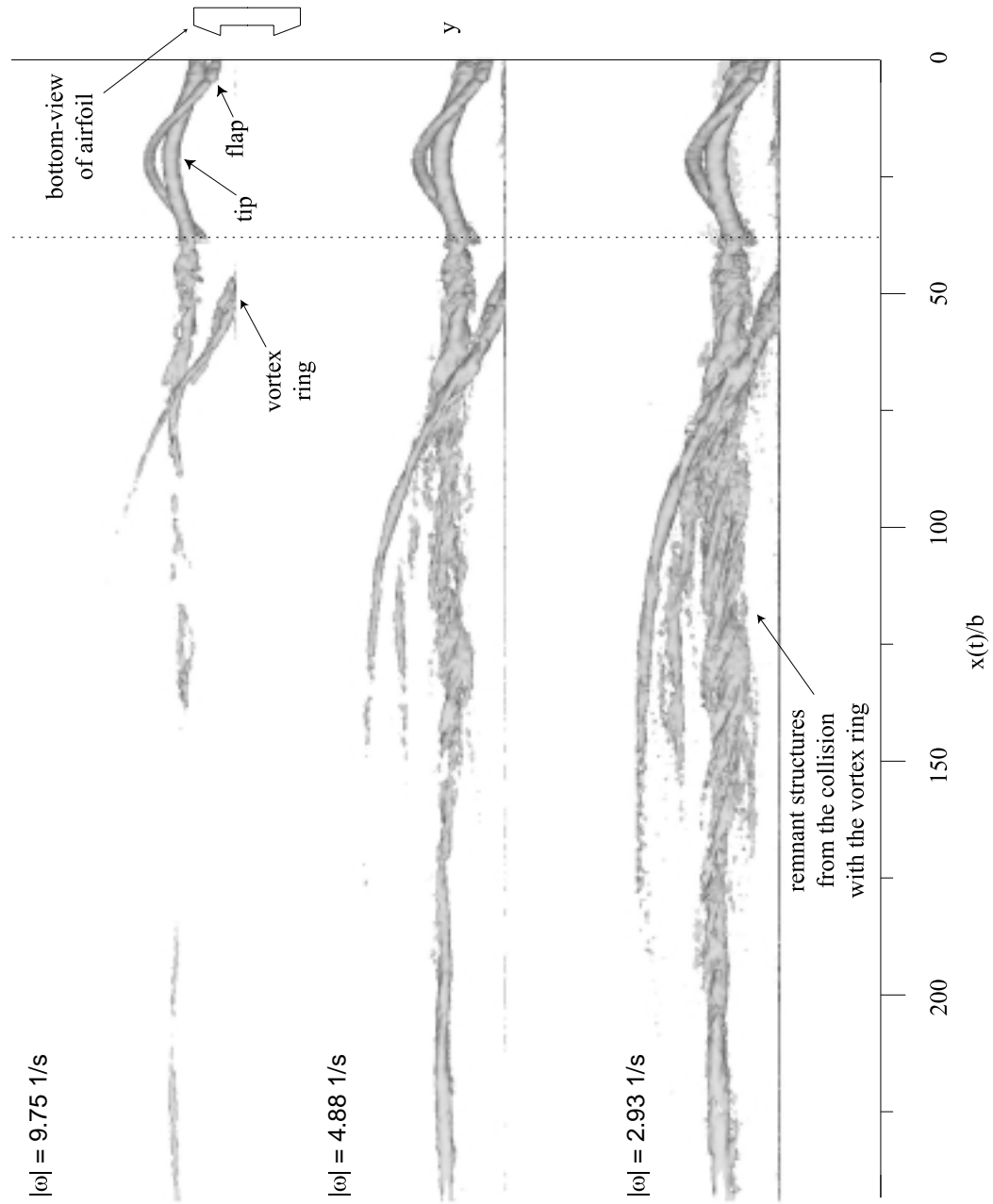
Figure 5.29: Bottom view of the isovorticity surfaces for run 39 ($U_o = 500$ cm/s, $\alpha = 2.0^o$, 50%c TF, $\bar{\Gamma}_{of}/\bar{\Gamma}_{ot} = -0.37$). The horizontal axis is the downstream distance, $x(t)/b$, from the airfoil.

One important comment that must be made is how these figures are interpreted. If this two-dimensional data were the only information available about the wake, it would be nearly impossible to imagine that the flap vortices are undergoing a sinuous instability, which leads to the formation of vortex hoops and rings. This clearly underscores the importance of the flow visualization data in this study. Therefore, the discussions in the following paragraphs are based upon not only the PIV data, but also the knowledge that was gained from the flow visualization data.

For $x(t)/b < 38$, the surfaces on the counter-rotating vortex pair are fairly smooth, indicating that the vorticity distribution is not varying significantly. At $x(t)/b{=}38$, the flap vortex seems to disappear from view. The reason for this is that the instability amplitude on the flap vortex has become finite, causing the flap vortex to pivot in the measurement plane. Consequently, the PIV data no longer captures the flap vortex. Note that for $x(t)/b \geq 38$, the isovorticity surfaces are no longer smooth, but are characterized by high frequency structures, demonstrating the unsteady, three-dimensional nature of the wake. At $x(t)/b \approx 50$, the vortex ring from the opposite side of the wake enters the field of view and eventually collides with the remnant tip vortex. The details of this collision are quite interesting as shown in Figure 5.28. For this slice of the wake, the vortex ring is swept under the tip vortex and ejected upwardly out of the measurement plane. It appears that the top portion of the vortex ring interacts strongly with the tip vortex. The effects of this collision cause the formation of small-scale structures, which orbit about the tip vortex and give rise to the helical shapes in the $|\omega| = 2.93$ and 4.88 1/s surfaces. The side view of the isovorticity surfaces demonstrates that for the remainder of the run, the wake, though highly disrupted, continues to descend in the test section.

The isovorticity surfaces for run 48 ($U_o = 500$ cm/s, $\alpha = -1.0^o$, 50%c TF, $\bar{\Gamma}_{of}/\bar{\Gamma}_{ot} = -0.53$), which has a larger value of $|\bar{\Gamma}_{of}/\bar{\Gamma}_{ot}|$, are shown in Figures 5.30 and 5.31. Again, these surface values correspond to 25%, 12.5%, and 7.5% of the maximum vorticity (uncorrected) of the flap vortex at $x(t)/b = 0$. Note that the axial scale for run 48 is different than that of run 39. The dashed line at $x(t)/b = 38$ denotes the downstream distance at which a sudden change is seen in the vortices' internal structure. For $x(t)/b \geq 38$, the tip
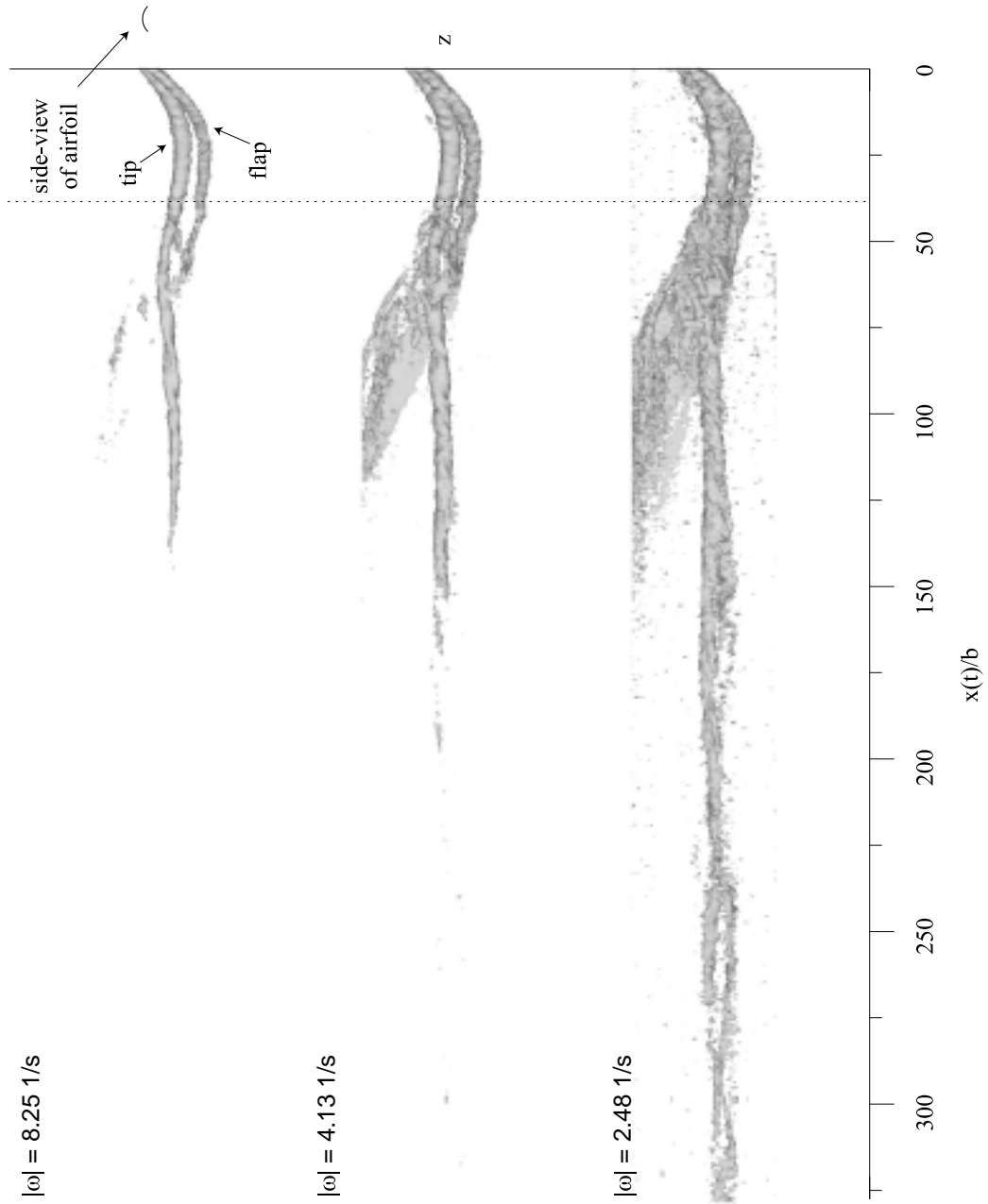
Figure 5.30: Side view of the isovorticity surfaces for run 48 ($U_o = 500$ cm/s, $\alpha = -1.0^o$, 50%c TF, $\bar{\Gamma}_{of}/\bar{\Gamma}_{ot} = -0.53$). The horizontal axis is the downstream distance, $x(t)/b$, from the airfoil.
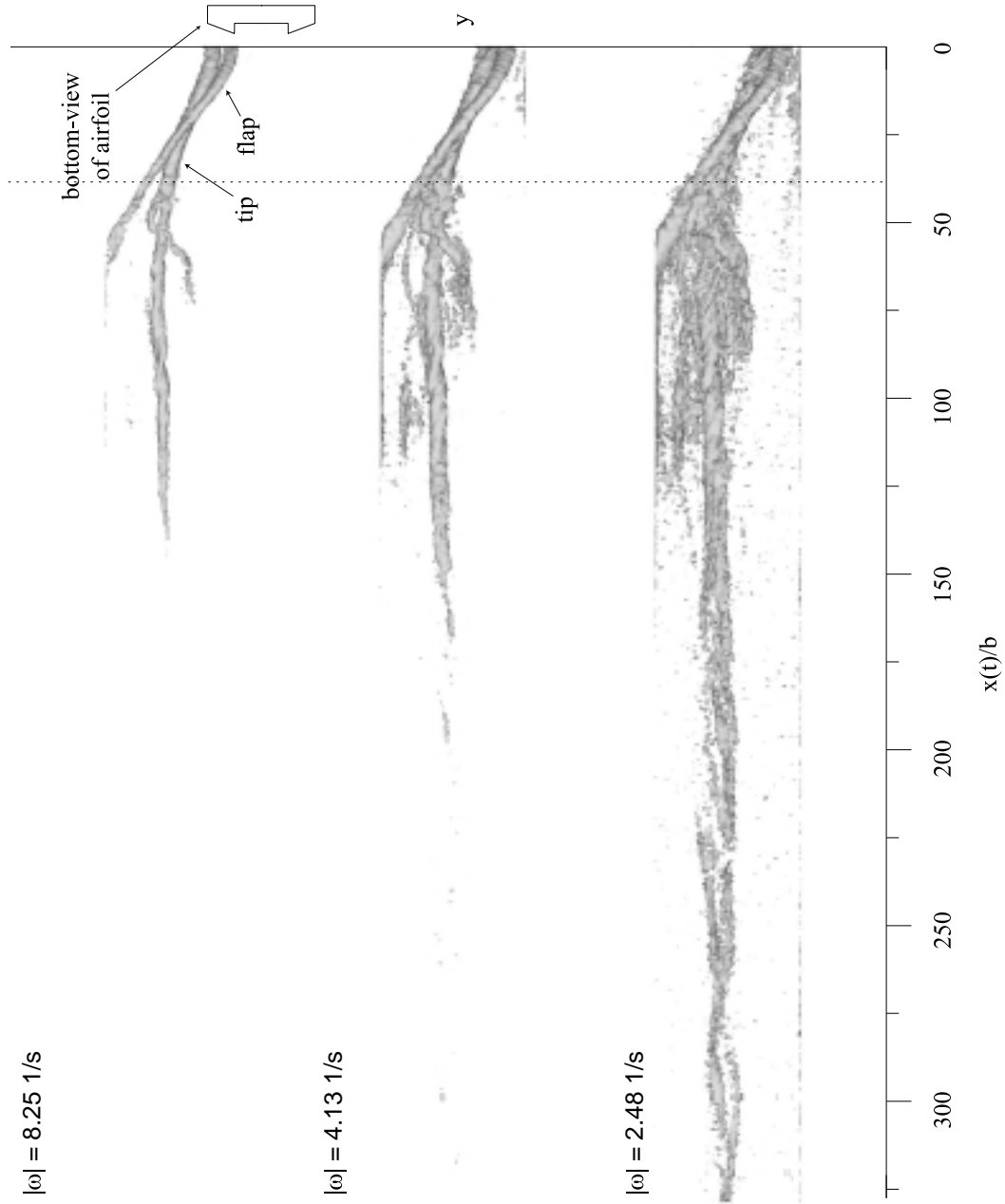
Figure 5.31: Bottom view of the isovorticity surfaces for run 48 ($U_o = 500$ cm/s, $\alpha = -1.0^o$, 50%c TF, $\bar{\Gamma}_{of}/\bar{\Gamma}_{ot} = -0.53$). The horizontal axis is the downstream distance, $x(t)/b$, from the airfoil.

vortex becomes shrouded with a cloud of small-scale structures as the non-linear effects of the instability propagate through the measurement plane. As discussed in Section 5.9.1, the sinusoidal instability on the flap vortex leads to the ejection of the flap vortex from the field of view at $x(t)/b \approx 75$.

One of the more noticeable features in these isovorticity surfaces is the reduction of the vorticity magnitude. For $x(t)/b \geq 150$, the vorticity magnitude drops below a value of 8.25 1/s. Furthermore, for $x(t)/b \geq 200$, only a few small patches of vorticity have magnitudes equal to 4.13 1/s. The descent characteristics of run 48 can also be seen in the side-view of the isovorticity surfaces. The data in Figure 5.30 demonstrates the reduced descent velocity of the wake after the instability has occurred. By 330 spans, the few remnant patches of the tip vortex are only slightly below the depth of the tip vortex at $x(t)/b = 100$.

5.9.3   Vortex Strength

After viewing the flow visualization and isovorticity surface data of the counter-rotating pairs, one question that arises is whether or not the circulation is conserved as the instability undergoes its non-linear evolution. For some runs, the circulation does remain relatively constant as shown in Figure 5.32a for run 55 ($U_o = 500$ cm/s, $\alpha = 0^o$, 75%c TF, $\bar{\Gamma}_{of}/\bar{\Gamma}_{ot} = $ -0.51). The dashed line at $x(t)/b = 36$ denotes the downstream location at which a sudden change occurs in the vortices' core structures. It is evident that the circulation decreases a small amount after 36 spans. Though in general, the circulation varies only slightly about its initial value of 670 cm^2/s.

Alternatively, the circulation does fluctuate strongly for some runs, such as that shown in Figure 5.32b for run 56 ($U_o = 500$ cm/s, $\alpha = 0^o$, 75%c TF, $\bar{\Gamma}_{of}/\bar{\Gamma}_{ot} = $ -0.50). Although the airfoil speed and angle of attack are identical to those of run 55, the trends in the circulation plot are completely different. At 75 spans, the circulation abruptly decreases by approximately 70%, which might give the impression that the circulation in the wake is suddenly decaying. However, this is not the case. The reason for the rapid "decay" in the wake's circulation is that the measurement plane does not contain all of the wake's vorticity. As the flap and tip vortices on both sides of the wake undergo their cooperative

instabilities, vortex hoops and rings enter and exit the field of view, causing the measured circulation to vary strongly. In this particular run, a vortex ring, which originates from the left flap vortex, enters the top of the measurement plane so that only the "negative" portion of the ring is imaged. Consequently, the "total" circulation plummets due to this additional negative vorticity. Notice that the circulation drops by a value comparable to the flap's circulation (Table 5.5). From 75 to 150 spans, the circulation steadily increases as the "positive" portion of the vortex ring enters the field of view and cancels its "negative" vorticity. By 150 spans, the circulation returns to a value close to that of $x(t)/b = 0$. Over the rest of the run, the circulation decreases more slowly as more and more of the vorticity is ejected from the field of view.
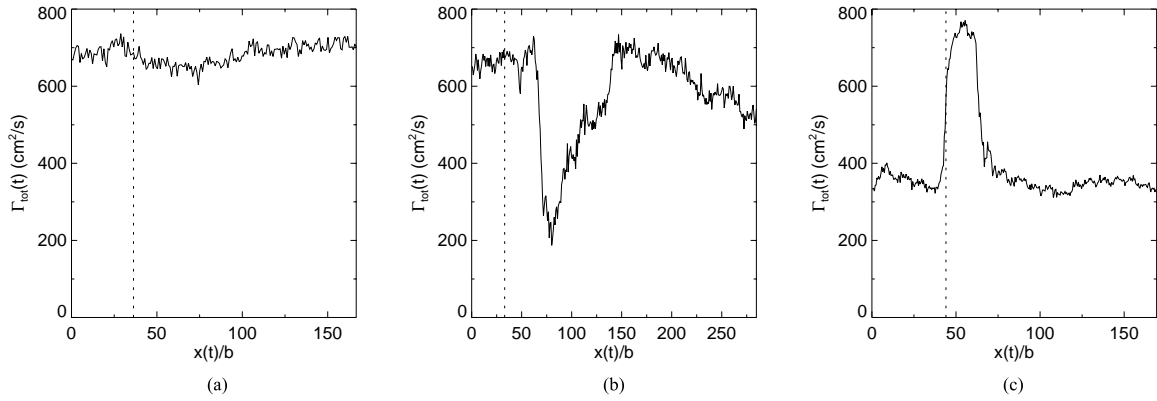
Figure 5.32: Various trends in the total circulation data. (a) run 55 (75%c TF, $\bar{\Gamma}_{of}/\bar{\Gamma}_{ot} =$ -0.51) (b) run 56 (75%c TF, $\bar{\Gamma}_{of}/\bar{\Gamma}_{ot}$ = -0.50) (c) run 70 (50%c TF, $\bar{\Gamma}_{of}/\bar{\Gamma}_{ot}$ = -0.57). The vertical dashed lines denote the downstream distances at which the flap and tip vortices undergo a rapid change in their structure.

Another example of a wake in which the circulation is not constant is shown in Figure 5.32c for run 70 ($U_o = 500$ cm/s, $\alpha = 0^o$, 50%c TF, $\bar{\Gamma}_{of}/\bar{\Gamma}_{ot}$ = -0.57). The measurement plane for this run intersects the flap's sinusoidal instability at a local peak, such that the observed distance between the flap and tip vortices increases as the instability evolves. Eventually, the instability amplitude grows so large that the flap vortex exits the field of view at 44 spans, resulting in an increase in "total" circulation. By 75 spans, the flap vortex

and its remnants re-enter the measurement plane and the circulation decreases to a value comparable to that of $x(t)/b = 0$. For the remainder of the run, no vortex rings enter or exit the measurement plane and the circulation remains relatively constant.

From these widely varying trends in the circulation data, it is difficult to conclude whether or not the flow is behaving inviscidly as the instability progresses. Viscous effects are more than likely occurring in the vortex re-connection and collision processes, but given the large Re_Γ of these vortices, the viscous length scales are too small to be a dominant factor in the evolution of these wakes. One trend evident over the entirety of some runs, such as run 55, or the portions of others, such as run 70 for $75 \leq x(t)/b \leq 170$, is that if no vorticity enters or exits the measurement plane, the circulation stays about constant despite the catastrophic events that are happening in the wake.

5.9.4 Two-Dimensional Kinetic Energy of the Wake

Perhaps, one of the more interesting integral quantities measured in the wakes of the triangular-flapped airfoils is the two-dimensional kinetic energy. In Section 5.8.3, it was shown that this quantity is relatively constant in the wakes of the rectangular airfoil. However, given the highly, three-dimensional wake of the triangular-flapped airfoils, one might expect that the two-dimensional kinetic energy would vary with downstream distance. Indeed, this was the case as Figure 5.33a illustrates for run 38 ($U_o = 500$ cm/s, $\alpha = 2.0^o$, 50%c TF, $\bar{\Gamma}_{of}/\bar{\Gamma}_{ot} = $ -0.37). Prior to 36 spans (vertical dashed line), the two-dimensional kinetic energy changes only slightly as the counter-rotating pair traverses the first three-quarters of its orbit period. Although the flow visualization data show that the instability becomes finite at 25 spans, the kinetic energy does not give an obvious indication of its presence at that downstream location. However, at 36 spans, the kinetic energy decreases by about 30% as the flap vortex is pivoted in the measurement plane by the instability. Consequently, the two-dimensional, PIV measurements no longer capture the flap vortex's total kinetic energy. Prior to 36 spans, the flap vortex comprises approximately 20% of the wake's kinetic energy. Therefore, the drop in the total kinetic energy is primarily due to
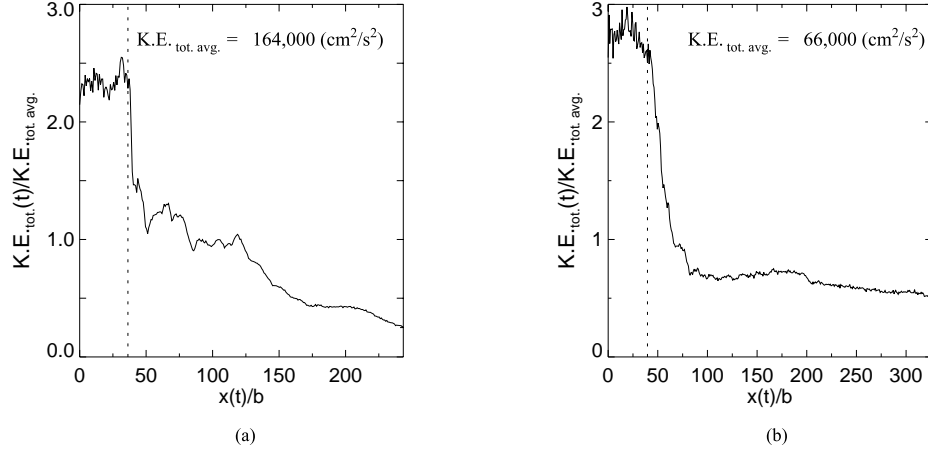
Figure 5.33: Two-dimensional kinetic energy as a function of downstream distance for the 50%c TF airfoil at small and large values of $|\bar{\Gamma}_{of}/\bar{\Gamma}_{ot}|$: (a) $\bar{\Gamma}_{of}/\bar{\Gamma}_{ot} = $ -0.37 (run 38, $U_o = $ 500 cm/s, $\alpha = 2.0^o$) (b) $\bar{\Gamma}_{of}/\bar{\Gamma}_{ot} = $ -0.56 (run 47, $U_o = 500$ cm/s, $\alpha = $ -1.0^o). The vertical dashed lines denote the downstream distance at which the flap and tip vortices undergo a rapid change in their core structures.

the pivoting of the flap vortex. The additional 10% decrease in the kinetic energy is, perhaps, due to either a disruption of the tip vortex's coherence or a slight pivoting of the tip vortex in the field of view. At approximately 50 spans, a vortex ring enters the measurement plane from the opposite side of the wake and impacts the tip vortex. Over the rest of the run, the wake's kinetic energy continues to slowly decay.

To illustrate the distribution of two-dimensional kinetic energy in the wake, Figure 5.34 shows contours of kinetic energy for run 38 ($U_o = 500$ cm/s, $\alpha = 2.0^o$, 50%c TF). The same contour levels are used in each of the eight plots. As the vortices roll up at $x(t)/b$ = 0, the kinetic energy has a compact distribution around the counter-rotating pair. At 54 spans, a vortex ring enters from the opposite side of the wake and its kinetic energy is visible on the left side of the contour plot. The vortex ring begins to collide with the remnants of the tip vortex at 71 spans, which subsequently spreads the kinetic energy over a large region of the measurement plane. For larger downstream locations, the peak values in the kinetic energy are markedly less than those in the contour plots prior to 36 spans.
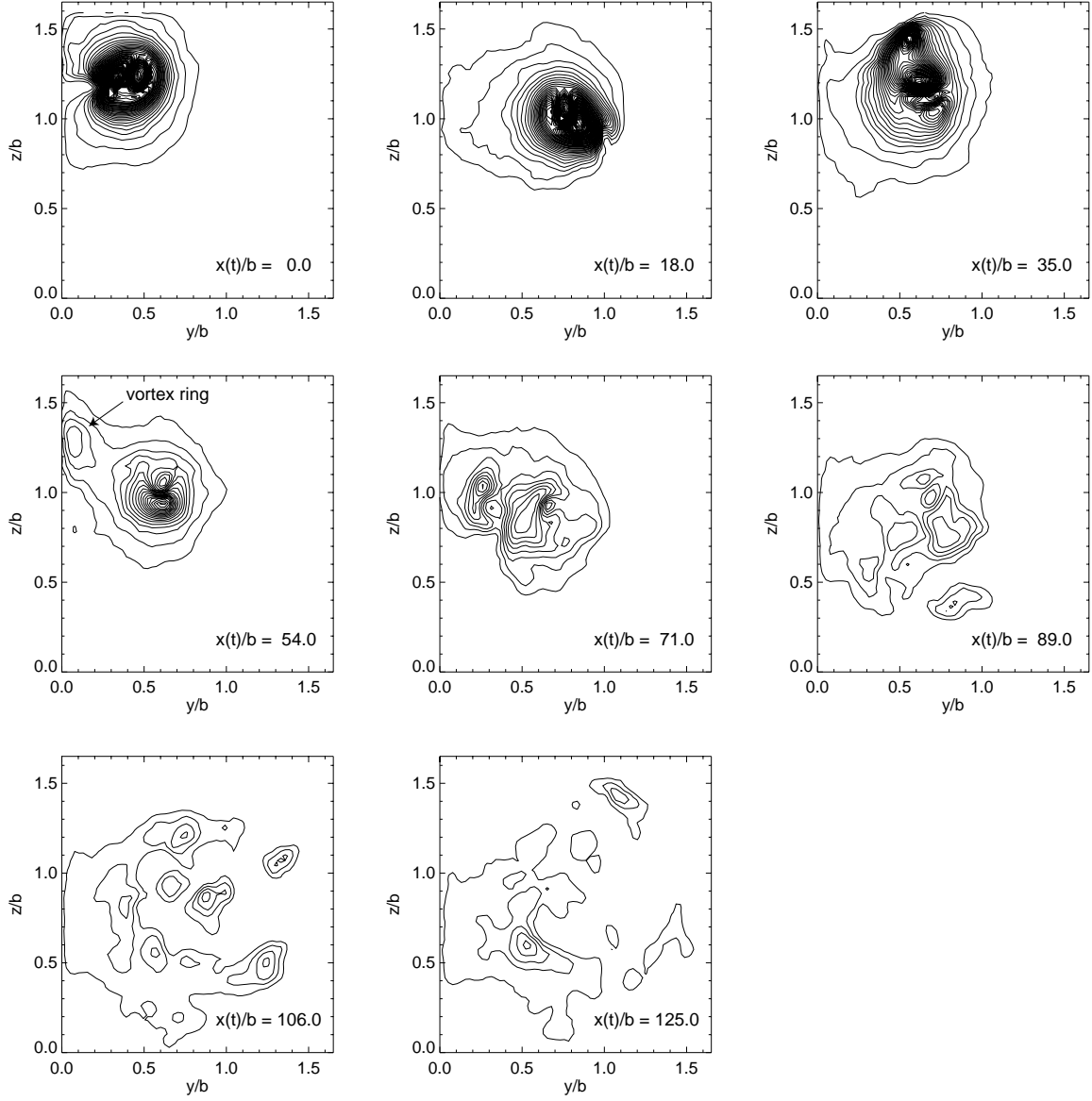
Figure 5.34: Contours of the two-dimensional kinetic energy for $\bar{\Gamma}_{of}/\bar{\Gamma}_{ot} = $ -0.37 (run 38, $U_o = 500$ cm/s, $\alpha = 2.0^o$, 50%c TF). The same contour levels are used in each of the plots.

For larger values of $|\bar{\Gamma}_{of}/\bar{\Gamma}_{ot}|$, the trends in two-dimensional, kinetic energy are somewhat different than those described above, regardless of Re_c. Figure 5.33b demonstrates this for a run in which $\bar{\Gamma}_{of}/\bar{\Gamma}_{ot}$ = -0.56 (run 47, U_o = 500 cm/s, α = -1.0^o, 50%c TF). One immediate difference between the kinetic energy of these two runs is that the kinetic energy in run 47 experiences a larger relative drop when the instability becomes evident at 40 spans. Before 40 spans, the flap vortex makes up about 20% of the flow's kinetic energy. However, the total kinetic energy decreases by approximately 70%, not 20%. Consequently, the drop in kinetic energy is not just due to the pivoting of the flap vortex in the measurement plane. The additional decrease in the kinetic energy arises from the pivoting and disruption of the tip vortex, which possesses about 50% of the wake's kinetic energy before 40 spans. This pivoting is visible in the flow visualization data on the starboard tip vortex in Figure 4.16 at $x(t)/b$ = 50. Over the rest of the run, the kinetic energy in Figure 5.33b does not decrease as much as it does in run 38. Rather, the value of the kinetic energy at 100 spans is close to its final value at 326 spans. Figure 5.35 displays contours of two-dimensional, kinetic energy for run 47. Initially, the distribution of kinetic energy appears similar to that of run 38. However, as the instability progresses, less and less of the two-dimensional, kinetic energy is present in the field of view. By 125 spans, the contour plot displays only a patch of kinetic energy, which is noticeably smaller than that of run 38 at the same downstream location.

The trends in the two-dimensional, kinetic energy described above are consistently observed in the PIV data for both the 50%c and 75%c triangular-flapped airfoils. When the instability first becomes evident in the measurement plane, the two-dimensional, kinetic energy always drops by a significant amount, regardless of $\bar{\Gamma}_{of}/\bar{\Gamma}_{ot}$. However, the residual decay of the kinetic energy does depend on $\bar{\Gamma}_{of}/\bar{\Gamma}_{ot}$. For larger values of $|\bar{\Gamma}_{of}/\bar{\Gamma}_{ot}|$, the kinetic energy does not decrease appreciably after its initial drop, as was shown above for run 47. Alternatively, for runs in which $|\bar{\Gamma}_{of}/\bar{\Gamma}_{ot}|$ is relatively small, like run 38, the kinetic energy continues to decay. There are a couple of reasons for this difference in decay characteristics. First, for the runs that have smaller values of $|\bar{\Gamma}_{of}/\bar{\Gamma}_{ot}|$, the instability leads to an exchange of vorticity from opposite sides of the wake. As the instability evolves,
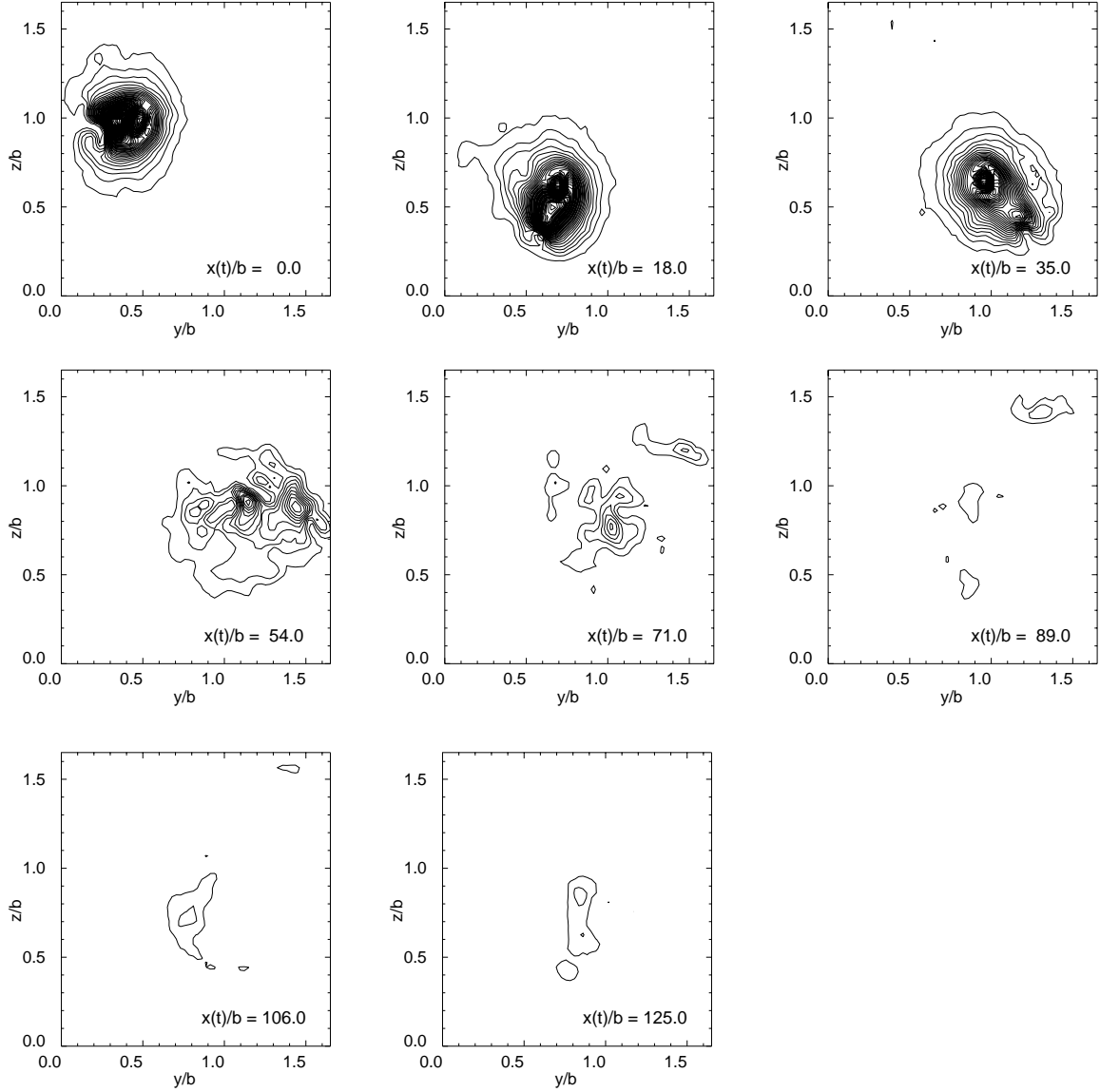
Figure 5.35: Contours of the two-dimensional kinetic energy for $\bar{\Gamma}_{of}/\bar{\Gamma}_{ot} = $ -0.56 (run 47, $U_o = 500$ cm/s, $\alpha = $ -1.0^o, 50%c TF). The same contour levels are used in each of the plots.

the flap vortices form coherent "Ω" hoops. The vortex rings that form from these hoops have cross-sections that are coherent and comparable in size to the original flap vortices. Although these rings are three-dimensional in nature, they possess a considerable amount of two-dimensional kinetic energy. Therefore, when they cross the airfoil centerline, the rings contribute to the total kinetic energy. As these rings collide and interact with the tip vortices, the flow becomes increasingly three-dimensional and the two-dimensional kinetic energy slowly decays. For larger values of $|\bar{\Gamma}_{of}/\bar{\Gamma}_{ot}|$, the non-linear behavior of the instability is confined to the opposite sides of the wake and there is little exchange vorticity across the airfoil centerline. Thus, no additional kinetic energy enters the field of view.

The second reason is due to the relative strengths of the flap and tip vortices. For runs in which $|\bar{\Gamma}_{of}/\bar{\Gamma}_{ot}|$ is small, the initial behavior of the instability does not significantly affect the tip vortex simply because it is much stronger than the flap vortex. As the flap vortex forms "Ω" hoops that pinch off into rings, the tip vortex does not pivot significantly in the measurement plane. This is evident in the flow visualization images in Figures 4.11 $(x(t)/b = 28, 32)$ and 4.12 $(x(t)/b = 25, 36)$ for a run in which $\bar{\Gamma}_{of}/\bar{\Gamma}_{ot} = -0.37$. As a result, a considerable amount of two-dimensional kinetic energy from the tip vortex remains in the field of view. This two-dimensional kinetic energy slowly becomes more three-dimensional over the rest of the run for the reasons explained above. However, for runs in which $|\bar{\Gamma}_{of}/\bar{\Gamma}_{ot}|$ is relatively large, the initial non-linear behavior affects not only the two-dimensional kinetic energy of the flap vortex, but also that of the tip vortex. Since the two vortices are more comparable in strength, the finite amplitude perturbations pivot and disrupt both the flap and tip vortices, causing a large drop in the wake's two-dimensional kinetic energy. The flow is so three-dimensional over the rest of the run that the two-dimensional kinetic energy remains at a small fraction of its initial value.

5.9.5   Vortex Structure

The structure and characteristics of the individual flap and tip vortices are analyzed in a manner similar to that of the rectangular airfoil. Consider run 46 ($U_o = 500$ cm/s, $\alpha = -1.0^o$, 50%c TF) in which $\bar{\Gamma}_{of}/\bar{\Gamma}_{ot} = $ -0.56. The circulations of the flap and tip vortices
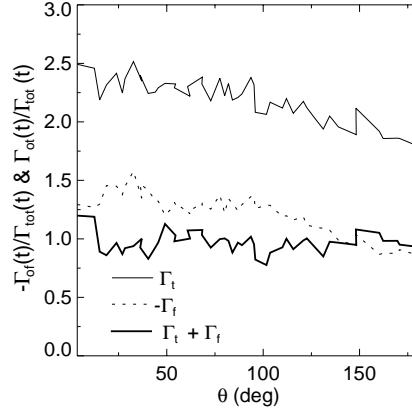
Figure 5.36: Circulation of the flap and tip vortices prior to the non-linear effects of the instability for run 46 ($U_o = 500$ cm/s, $\alpha = -1.0^o$, 50%c TF).

are plotted in Figure 5.36 over the first half of the orbit period, corresponding to the first 40 spans downstream of the airfoil. For $\theta > \pi$, the wake displays three-dimensional behavior and the individual vortices are no longer examined. Unlike the rectangular airfoil's tip vortices, which have relatively constant circulation strengths, the flap and tip vortices from the triangular-flapped airfoil have circulation strengths that decrease rather quickly. However, during this same period, the sum of the flap and tip circulations remains relatively constant. This leads to the conclusion that equal amounts of positive and negative vorticity are canceling along the interface of these two vortices. Similar trends are observed in other runs that also had relatively large values of $|\bar{\Gamma}_{of}/\bar{\Gamma}_{ot}|$.

The vortex core size, maximum azimuthal velocity, and peak vorticity of the flap and tip vortices are shown in Figure 5.37 for run 46. Note that the variables, r_{max}, $u_{\theta max}$, and ω_{max}, have been computed with values of σ that are corrected with Eq. 5.10. One interesting observation is the evidence for stretching and tilting of the flap vortex. The flow visualization data at this angle of attack and airfoil speed reveal that the perturbation on the flap vortex becomes finite by $\theta \approx \pi/2$ radians, causing the flap vortices to stretch and tilt. These three-dimensional effects are strongly evident in all three plots for the flap vortex, which demonstrates a large amplitude oscillation in r_{max}, $u_{\theta max}$, and ω_{max} at $\theta \approx \pi/2$ radians.
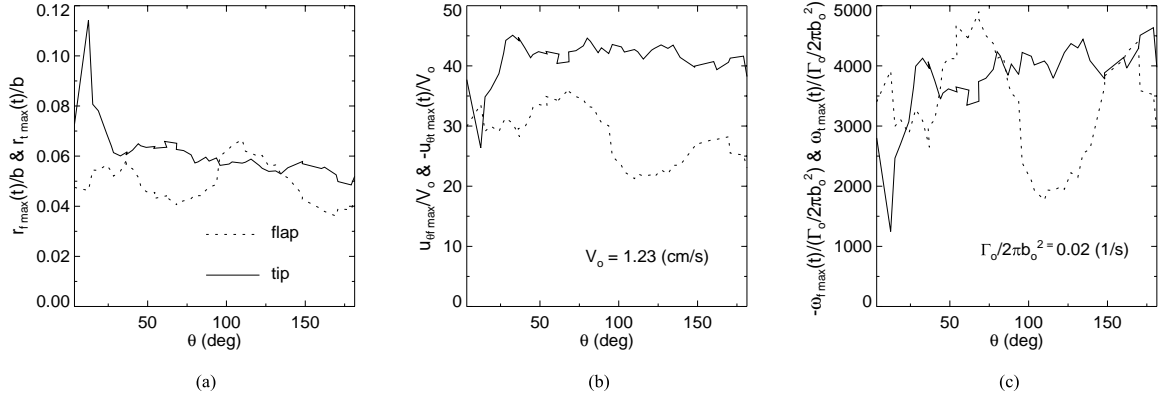
Figure 5.37: (a) Vortex core size, (b) maximum azimuthal velocity, and (c) peak vorticity of the flap and tip vortices as a function of orbit angle, θ, for run 46 ($U_o = 500$ cm/s, $\alpha = -1.0^o$, 50%c TF). Note that these plots are based upon corrected values of the vortex core size, σ (Eq. 5.10).

5.9.6   Effective Vortex Size

In order to assess how dispersed the wake becomes at large downstream distances, an effective core size (Eq. 5.17) is computed at each downstream location over the cropped field of view. This quantity has the advantage in that it does not rely upon fitting a particular analytical model to the circulation distribution, a feature that proves useful when the wake exhibits highly three-dimensional characteristics. One trend observed in the PIV data is that the effective core size varies strongly as a function of downstream distance. Figure 5.38 illustrates this for run 56 ($U_o = 500$ cm/s, $\alpha = 0^o$, 75%c TF, $\bar{\Gamma}_{of}/\bar{\Gamma}_{ot} = $ -0.5). The vertical dashed line at $x(t)/b = 33$ indicates the downstream distance at which the flap and tip vortices display a sudden change in their structures. Although the average core sizes of the flap and tip vortices are 4.0%b and 6.3%b (Table 5.6) from $0 \leq x(t)/b \leq 33$, the effective core size of the wake is much less. The reason is that the negative flap vortex is located farther from the wake's centroid than the positive tip vortex, causing the flap vortex to nearly cancel the contribution of the tip vortex to Eq. 5.17. As mentioned in a previous discussion of run 56 (Section 5.9.3), a vortex ring from the opposite side of the wake enters the top of the measurement plane at $x(t)/b = 75$, such that only the "negative" portion

of the ring is imaged. Due to the large distance between this negative patch of vorticity and the total centroid, the effective core size of the wake drops to a value that is less than zero. As the "positive" portion of the vortex ring enters the top of the measurement plane, r_{eff} increases to approximately 60%b, the largest value of any of the runs. Gradually, the vortex ring interacts with the remnants of the right-side tip vortex and the effective core size decreases. By 285 spans, r_{eff} is about 20%b, which is more than three times the initial size of the tip vortex. Observations from the other PIV experiments demonstrate that r_{eff}/b ranges from approximately 10%b to 40%b by the end of the runs, which typically occurs at about 250 to 300 spans downstream of the airfoil. On average though, the effective core size is 20%b at approximatetly 250 to 300 spans downstream of both triangular-flapped airfoils.
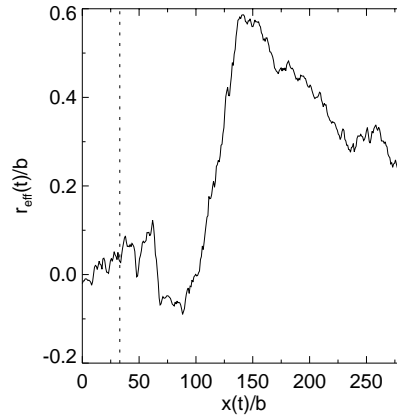
Figure 5.38: Effective vortex core size for run 56 ($U_o = 500$ cm/s, $\alpha = 0^o$, 75%c TF, $\bar{\Gamma}_{of}/\bar{\Gamma}_{ot}$ = -0.5) as a function of downstream distance. The vertical dashed line marks the downstream location at which the flap and tip vortices undergo a rapid change in their core structures.

5.9.7   Experimental and Theoretical Instability Wavelengths

With the core sizes, relative circulation strengths, and separation distances of the vortices known from the PIV data, it is now possible to compare the observed instability wavelengths from the flow visualization data with those predicted by the linear stability

analyses for two- (Section 2.3) and four-vortex systems (Section 3.3). As discussed in Chapter 4, there are three orthogonal views (a close-up side view, a wide side view, and an overhead view) of the test section that can be used to make these wavelength measurements from the flow visualization data. Unfortunately, each of these views has a drawback when calculating the unstable wavelengths. Although the close-up, side view provides good detail of the instability evolution, it is too close to the test section to measure several wavelengths. On the other hand, the wide side view gives a larger field of view, but the vertical bars holding the test section windows often obscure the instability peaks and troughs. The overhead vantage provides a wide field of view of the test section, but the surface waves from the strut initially distort the appearance of the dye trails. Considering each of these shortcomings, the overhead view is chosen since it typically yields the best measurements of the instability wavelengths. It is necessary, however, to not make measurements while the surfaces waves alter the flow visualization images. With this field of view, the spatial resolution of the flow is 0.26 cm/pixel or $0.007b$/pixel.

Another aspect of these wavelength measurements that requires discussion is the manner in which the peaks and troughs are identified. Due to the complexity of the flows, it is difficult to automate the peak and trough location process. Consequently, they are manually measured, which introduces some subjectivity. For the runs at $\alpha = 2.0^o$, the peaks and troughs are clearly identifiable. Yet, for the runs at -1.0^o, less dye is entrained into the vortices, making it difficult to perform wavelength measurements. In these cases, it is sometimes necessary to make an educated guess as to the instability wavelength. The instability wavelengths are measured over several downstream locations from the moment they are first observed until the moment the flap and tip vortices make contact with one another. Because the perturbations are finite in size when the instability is measured, a direct comparison with the results of the linear stability theory, which assumes that the perturbations are infinitesimal, is difficult. However, it is assumed that the most linearly-unstable mode will give rise to finite-size perturbations of the same wavelength, allowing an indirect comparison to be made. On average, the standard deviation of the measured wavelengths is approximately $0.15b$, which is noticeably greater than the spatial resolution

of the flow. The reason for this is that the instability wavelengths for each of the counter-rotating vortex pairs vary somewhat over the length of the test section.

There is an additional discrepancy between the four-vortex, linear stability model and the actual vortex wakes. Although this was not discussed in Section 3.3, one of the underlying assumptions of Crouch's [16] linear stability model is that the equilibrium flow of the four vortices is periodic; that is, the vortices continuously orbit about one another. With this assumption, Floquet theory can then be employed to solve for the instability growth rate. It is evident from the flow visualization data that the flap and tip vortices do not continuously orbit about one another. Rather, the instability amplitudes quickly become finite, which results in highly non-linear, non-periodic interactions. This leads to a fundamental difference between the actual wake behavior and that required by the four-vortex, linear stability model. Therefore, when the results of this model are compared to the experimental measurements, this crucial difference must be kept in mind.

Before computing the growth rate curves of the vortex systems, two corrections are made to the vortex sizes. The first is that from Eq. 5.10, which removes the artificial inflation that aLPT gives to the vortex size. The second correction accounts for the fact that the measured vortices have a circulation distribution that more closely follows that of a Lamb-Oseen vortex and not that of a Rankine vortex. Recall that the self-induced rotation rate discussed in Section 2.2.2 is for a Rankine vortex, which has a constant vorticity core, and not a Lamb-Oseen vortex. Therefore, it is necessary to find a Rankine vortex that has the same self-induced rotation rate as a Lamb-Oseen vortex. To accomplish this, the analysis of Widnall *et al.* [49] is used. For long wavelength perturbations, Widnall demonstrates that the self-induced rotation rate of an arbitrary vortex is given by

$$\bar{\varpi} = \frac{(ka)^2}{2} \frac{\Gamma}{2\pi a^2} \left(ln\frac{1}{ka} + A + ln2 - \gamma_e \right) \tag{5.23}$$

where A is a variable that depends upon the distribution of vorticity in the vortex core and $\gamma_e = 0.57721...$ is Euler's constant. For a Rankine vortex, $A = -0.25$ and for a Lamb-Oseen vortex $A = -0.058$. By substituting these two values of A into Eq. 5.23 and equating the self-induced rotation rate of a Rankine vortex to that of a Lamb-Oseen results in the

relationship,

$$a = 1.36\sigma \tag{5.24}$$

between the sizes of the two vortices. Equation 5.24 indicates that for long-wavelength perturbations, a Rankine vortex of core size a will have the same self-induced rotation rate as a Lamb-Oseen vortex of core size σ when $a = 1.36\sigma$.

The separation distance between the flap and tip vortices is taken from PIV measurements made at 0 spans downstream from the airfoils. The PIV measurements are performed on only the starboard-side of the wake, such that the port-side pair's separation distance and core sizes are not known. While not exact, it is assumed that the vortices on the port-side have the same separation distance and core sizes as those on the starboard-side. Additionally, the distance between the vorticity centroids on either half of the wake is computed by multiplying the distance from the starboard centroid to the airfoil centerline by two. For the unsteady, four-vortex stability analyses, the two vortex pairs are taken to be co-linear at $t = 0$. With the core sizes, relative circulation strengths, and separation distances known (see Table 5.7), the two- and four-vortex linear stability analyses can be carried out.

The growth rate curves for two of the experimental runs are shown in Figures 5.39 and 5.40. These plots are for the 50%c TF airfoil at $U_o = 500$ cm/s and $\alpha = 2^o$ (flow visualization runs 1,7 and PIV runs 38-40) and $U_o = 500$ cm/s and -1° (flow visualization run 3 and PIV runs 46-48). The dimensionless core sizes, relative circulation strengths, and separation distances for these runs are shown in Table 5.7. As done in Section 3.3, the growth rate curves in Figures 5.39 and 5.40 are plotted against two horizontal and two vertical axes. The left vertical and lower, horizontal axes are the instability growth rate and perturbation wavenumber for the four-vortex system, while the right vertical and upper, horizontal axes are the corresponding instability growth rate and perturbation wavenumber for the two-vortex system. The symbols in Figures 5.39 and 5.40 are the growth rates of the symmetric- and anti-symmetric modes (Eq. 3.18 and 3.19) for the four-vortex systems. The dashed curves are the growth rates of the two-vortex systems. The vertical dotted and dashed-dotted lines are the experimentally measured instability wavenumbers on the port-

and starboard-side flap vortices, respectively.

It can be seen in Figures 5.39 and 5.40 that the growth rate curves of the two- and four-vortex linear stability analyses follow similar trends. This indicates that the instability on the flap vortex is being driven primarily by the rate of strain field from the tip vortex and that the influence from the other vortex pair is minimal.
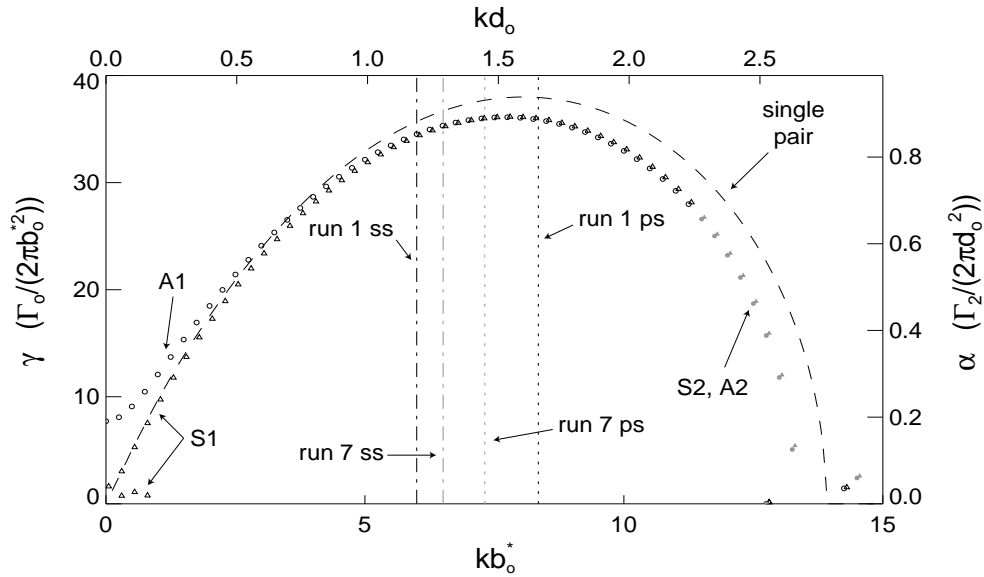
Figure 5.39: Instability growth rate curves from the two- and four-vortex linear stability analyses. The plots are based upon the average core sizes, relative circulation strengths, and initial separation distances from PIV runs 38-40 (50%c TF, $U_o = 500$ cm/s, $\alpha = 2.0^o$). The vertical lines indicate the observed instability wavenumbers on the port-side, "ps," and starboard-side, "ss," flap vortices from flow visualization runs 1 and 7 (50%c TF, $U_o = 500$ cm/s, $\alpha = 2.0^o$).
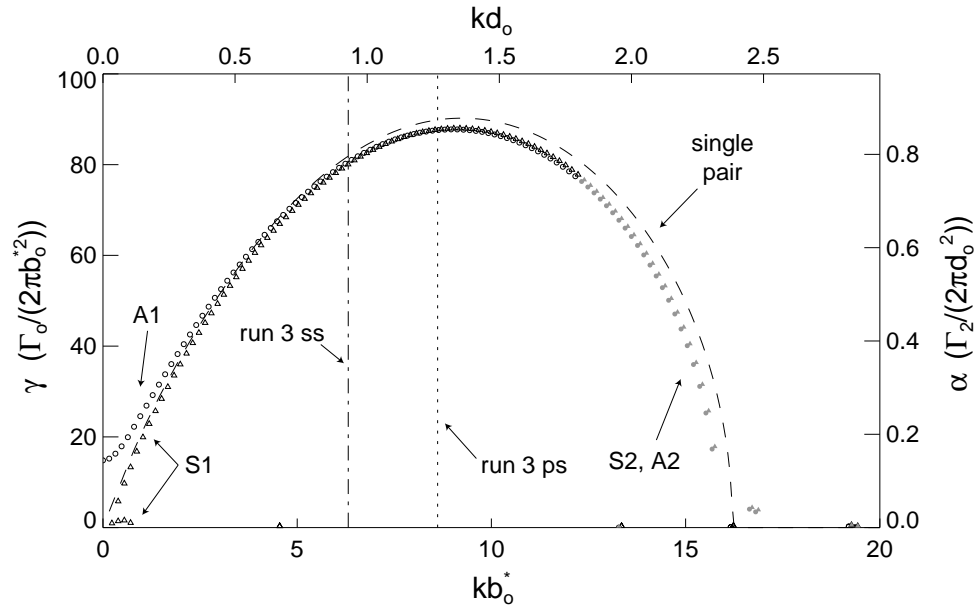
Figure 5.40: Instability growth rate curves from the two- and four-vortex linear stability analyses. The plots are based upon the average core sizes, relative circulation strengths, and initial separation distances from PIV runs 46-48 (50%c TF, $U_o = 500$ cm/s, α = -1.0^o). The vertical lines indicate the observed instability wavenumbers on the port-side, "ps," and starboard-side, "ss," flap vortices from flow visualization run 3 (50%c TF, $U_o = 500$ cm/s, α = -1.0^o).

Run FV	Run PIV	$\bar{\Gamma}_{of}/\bar{\Gamma}_{ot}$	b_o^* (cm)	a_t/b_o^*	a_f/b_o^*	d_o/b_o^*	λ_{ps}/b	λ_{ss}/b	λ_{one}/b	λ_{two}/b
1	38-40	-0.37	48.9	0.068	0.036	0.198	0.9	1.3	1.0	1.1
2	42-44	-0.49	58.3	0.053	0.037	0.154	0.9	1.2	1.0	1.0
3	46-48	-0.55	58.7	0.051	0.041	0.147	1.1	1.5	1.0	1.1
4	69	-0.40	65.0	0.053	0.033	0.144	0.7	0.9	0.9	0.7
5	70	-0.57	63.9	0.051	0.038	0.146	1.5	1.3	1.2	1.2
6	71	-0.67	71.4	0.047	0.038	0.127	2.3	1.8	1.2	1.4
7	38-40	-0.37	48.9	0.068	0.036	0.198	1.1	1.2	1.0	1.1
8	69	-0.40	65.0	0.053	0.033	0.144	0.8	0.8	0.9	0.7
9	42-44	-0.49	58.3	0.053	0.037	0.154	1.0	1.4	1.0	1.0
10	70	-0.57	63.9	0.051	0.038	0.146	1.0	1.0	1.2	1.2
11	50,52-53	-0.41	48.5	0.069	0.038	0.198	1.0	1.4	1.0	1.2
12	66	-0.45	54.7	0.063	0.040	0.152	1.0	1.2	0.8	0.8
13	55-57	-0.50	54.7	0.055	0.036	0.161	1.2	1.0	1.0	1.1
14	64	-0.57	65.6	0.050	0.037	0.145	1.1	–	1.2	1.2
15	59-61	-0.58	58.3	0.054	0.042	0.148	–	1.5	1.0	1.2
16	–	–	–	–	–	–	–	–	–	–
17	50,52-53	-0.41	48.5	0.069	0.038	0.198	0.9	1.0	1.0	1.2
18	66	-0.45	54.7	0.063	0.040	0.152	1.1	1.0	0.8	0.8
19	55-57	-0.50	54.7	0.055	0.036	0.161	1.2	1.3	1.0	1.1
20	64	-0.57	65.6	0.050	0.037	0.145	1.0	1.3	1.2	1.2

Table 5.7: Experimental instability wavelengths and the most unstable wavelengths of the two- and four-vortex linear stability analyses. Run FV is the flow visualization run number and Run PIV is the corresponding PIV run number. $\bar{\Gamma}_{of}/\bar{\Gamma}_{ot}$, average ratio of the flap circulation to the tip circulation from the PIV measurements; b_o^*, average, initial distance between the vorticity centroids on either side of the wake; a_t/b_o^*, average, dimensionless tip vortex size; a_f/b_o^*, average dimensionless flap vortex size; d_o, average, initial separation distance of the flap and tip vortices; b=40 cm, span of the airfoil; λ_{ps}/b, dimensionless instability wavelength on the port-side flap vortex; λ_{ss}/b, dimensionless instability wavelength on the starboard-side flap vortex; λ_{one}/b, the most unstable wavelength for a single, counter-rotating pair; and λ_{two}/b, the most unstable wavelength for two counter-rotating pairs.

This is even more evident in Figure 5.40, in which d_o/b_o^* has a somewhat smaller value of 0.147. The experimentally measured wavenumbers all lie within the range of unstable wavenumbers. While they do not coincide exactly with the most unstable wavenumbers of the linear stability analyses, they are reasonably close. It should be noted that the port-side flap vortex consistently exhibits a higher wavenumber instability than that on the starboard-side vortex. This may be due to an asymmetry in the strut or airfoil construction. The experimental and theoretical instability wavelengths for the other runs are summarized Table 5.7. Note that the results for a few of the runs are not shown in Table 5.7 because the dye trails are too faint for wavelength measurements to be made. As noted above, the experimental wavelengths are fairly close to those the predicted by the linear stability analyses. For the majority of the runs, the differences between the linear stability results of the single vortex pairs and those of the two-vortex pairs are small, indicating that the instability is caused by the interactions of the flap and tip vortices within each of the counter-rotating pairs. It should also be noted that, except for run 15 of the flow visualization data, the experimental wavelengths are on the order of one span or four times the separation distance of the flap and tip vortices. This wavelength is shorter than that of the classical Crow instability, which predicts a most unstable wavelength of order 8-10 times the separation distance. These observations are consistent with the calculations in Section 2.3, which demonstrate that the most unstable wavelength for an unequal strength, counter-rotating pair is shorter than that of an equal strength counter-rotating pair.

One possible reason for the difference between the theoretical and experimental wavelengths is that the self-induced rotation rate (Section 2.2.2) does not account for axial flow in the vortex core. During several preliminary experiments with these triangular-flapped airfoils, air bubbles were injected into the flap and tip vortices. The air bubbles, which became trapped in the vortex cores, were observed to travel in the same direction as the airfoil, indicating the presence of axial flow. Others [13, 19, 34] have also shown the existence of axial flow in vortex cores. For the present set of experiments, no axial flow measurements are made in the vortices, making it difficult to determine the strength of the axial flow and its distribution in the vortex cores. Another reason for the differences in the experimental

and theoretical wavelengths may be due to errors in equating the self-induced rotation rate of a Lamb-Oseen vortex to that of a Rankine vortex. The conversion factor in Eq. 5.24 is valid only in the long-wavelength limit. Therefore, applying Eq. 5.24 to shorter wavelength perturbations may cause small errors in the rotation rate of a Lamb-Oseen vortex. One final reason that may lead to the differences between the experimental and analytical wavelengths is that the linear stability models assume that the vortices are parallel and have no helix angle. Although the helix angle between the counter-rotating flap and tip vortices is relatively small, it is not zero and, therefore, it may introduce slight differences between the experimental and theoretical wavelengths.

5.10   Closing Remarks

The PIV data for the triangular-flapped airfoils provide a quantitative assessment of the counter-rotating pairs as they evolve in time. From the flow visualization data alone, it was previously difficult to make conclusions about the wakes at large downstream distances because of the dispersal of dye from the vortices. Now, however, questions about the wakes, such as their location, descent properties, kinetic energy, structure, and resulting distribution of vorticity, have been better analyzed.

Additionally, the PIV data makes it possible to compare the instability wavelengths observed in the flow visualization data with those of the linear stability analyses in Chapters 2 and 3. From these comparisons, it has been shown that linear stability models, which ignore the complicated details of the actual vortex wakes, predict instability wavelengths that are reasonably close to those seen experimentally. This demonstrates that the stability analyses are capturing the essential physics of the instability between the counter-rotating pairs. Furthermore, the similarities between the two- and four-vortex growth rate curves indicate that the instability is driven mostly by the strain rate field from the vortices within each of the vortex pairs.

Yet, one question that may arise from these measurements is how effective is this instability at alleviating the wake vortex hazard? Given the speed at which the instability

occurs, the rapid spreading of vorticity, and the three-dimensional nature of the resulting wake, the triangular-flapped airfoils appear to demonstrate signs of promise as an effective wake alleviation concept. In order to answer this question, the following chapter will address the wake alleviation properties of these triangular-flapped airfoils.

Chapter 6

Wake Alleviation Properties of the T.F. Airfoils

6.1 Introduction

When considering the flow visualization and PIV data of the triangular-flapped airfoils, it is evident that the wakes of these airfoils are markedly different than those of the rectangular airfoil. Unlike the rectangular airfoil's wakes, which are steady and compact in nature, the triangular-flapped airfoils' wakes are dynamic and more widely dispersed at similar downstream locations. Given these characteristics, the question naturally arises as to how effective are these triangular-flapped airfoils at reducing the wake vortex hazard?

Previous investigations [2, 15, 20, 24, 36, 37, 38, 48] of wake alleviation concepts have measured the dynamic forces on following aircraft to determine how effective a particular concept was at reducing the wake hazard. For flight test experiments, this often involved flying a smaller airplane into the wake of a larger, commercial transport. In more controlled experiments, various model planes and airfoils were positioned or towed in the wake of a larger, model airplane. Unfortunately, in the present experiment, it was not feasible to set up a similar type of test for the triangular-flapped airfoils. However, what is available in the current PIV data are the two-dimensional velocity fields in these airfoils' wakes from the moment of formation up to several hundred spans downstream. With this information,
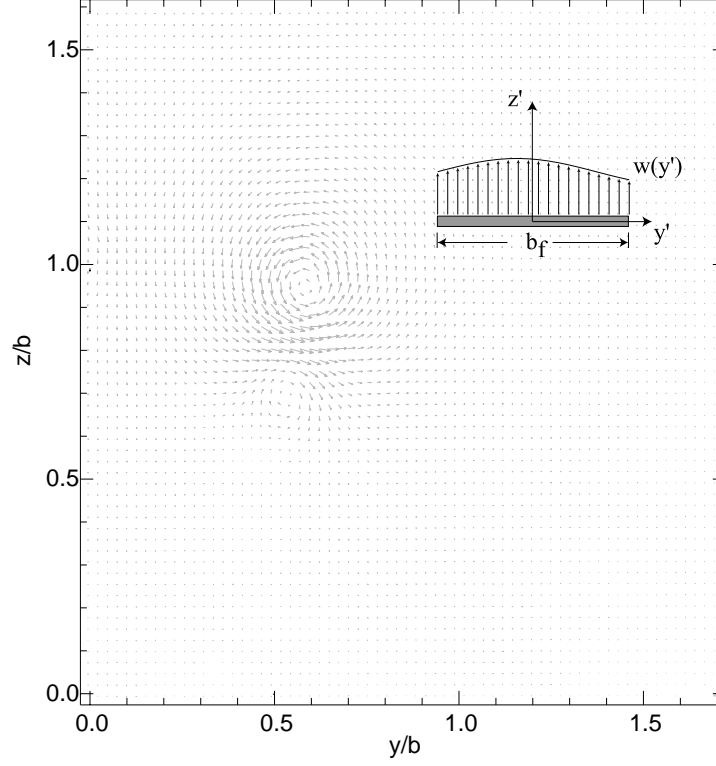
Figure 6.1: Schematic of the following wing in a typical velocity field.

it is possible to estimate the dynamic forces that a following wing might experience as it travels in the wakes of the triangular-flapped airfoils. Rossow [44] performed a similar type of analysis, but used an analytical velocity distribution instead of an experimental one. In the calculations to follow, an approach like that of [44] will be implemented using the measured velocity fields.

6.2   Mathematical Formulation

A schematic of the flow field is shown in Figure 6.1. The simulated, following wing is located at (y, z) and has a span of b_f. The (y', z') coordinate system is fixed with respect to the following airfoil and has its origin at the airfoil's center. The downwash on a differential portion of the following wing is given by $\frac{1}{2}C_{l\alpha}\alpha\ \rho U^2 c\ dy'$, where $C_{l\alpha}$ is the two-dimensional

lift-curve slope, α the flow inclination angle, and U the velocity of the following wing. If $\alpha \ll 1$, then $\alpha \approx tan\alpha = w(y', z')/U$, where $w(y', z')$ is the vertical component of the velocity field. For the PIV data, the maximum value of $|w/U|$ is about 0.15 so the assumption of small α is valid. Integrating the downwash over the span of the following wing gives

$$\int_{-b_f/2}^{b_f/2} \frac{1}{2}C_{l\alpha}\alpha \; \rho U^2 c \; dy' = \frac{1}{2}C_{l\alpha} \; \rho U^2 c \int_{-b_f/2}^{b_f/2} \frac{w(y', z')}{U}dy' \tag{6.1}$$

where it has been assumed that c is constant. Dividing Eq. 6.1 by b_f gives the average downwash on the following wing at the location (y', z'). For the sake of generality, only the quantity

$$D = \frac{1}{b_f} \int_{-b_f/2}^{b_f/2} w(y', z')dy' \tag{6.2}$$

will be used for the present analysis. The average rolling moment on the following wing is computed in a similar manner, by evaluating

$$\frac{1}{b_f} \int_{-b_f/2}^{b_f/2} \frac{1}{2}C_{l\alpha}\alpha \; \rho U^2 c \; y' \; dy' = \frac{1}{2}C_{l\alpha} \; \rho U^2 c \frac{1}{b_f} \int_{-b_f/2}^{b_f/2} y' \frac{w(y', z')}{U}dy' \tag{6.3}$$

Again, only the quantity

$$R = \frac{1}{b_f} \int_{-b_f/2}^{b_f/2} y'w(y', z')dy' \tag{6.4}$$

will be considered in the discussion to follow. The span of the following wing is taken to be $b_f = 20$ cm, or half that of the rectangular and triangular-flapped airfoils. Thus, the subsequent results simulate the effects that the vortex wakes have upon a smaller following wing. Repeating the calculations of Eq.'s 6.2 and 6.4 over the entire flow field yields a two-dimensional distribution of the downwash and rolling moment impinged upon the following wing. Given the finite span of the following wing, Eq.'s 6.2 and 6.4 cannot be computed along the left and right sides of the flow field. Therefore, the downwash and rolling moment data are cropped by $b_f/2 = 10$ cm on the left and right sides of the measurement plane.

6.3   Rectangular Airfoil

Before analyzing the wakes of the triangular-flapped airfoils, a useful exercise is to consider the wake of the rectangular airfoil, which can be considered as a baseline case. Figure 6.2 demonstrates contours of the downwash and rolling moment on the following wing, where the data is taken from Run 13 ($U_o = 500$ cm/s, $\alpha = 3.0^o$) at $x(t)/b = 50$. The positive contours are labeled in black and the negative ones in gray. The centroid locations of the left and right vortices are denoted by *'s and the $min(D(x(t), y, z))$ and the $max|R(x(t), y, z)|$ by black dots. Note the data fields are cropped along the left and right borders for the reason discussed above. It can be seen in Figure 6.2 that the rolling moment is greatest near the cores of the vortices, while the downwash is greatest somewhat inboard of the vortices. Qualitively, the plots on one side of the wake in Figure 6.2 appear similar to those in [44] for a single vortex. In order to study how the rolling moment and downwash vary as a function of $x(t)/b$, the variables $R' = max|R(x(t), y, z)|$ and $D' = min(D(x(t), y, z))$ are found at each downstream location. Calculating these quantities for the entirety of Run 13 yields the plots in Figure 6.3. As one might anticipate, the downwash and rolling moment exhibit very little decay over the 180 spans of measurements. Consequently, the wake of the rectangular airfoil is just as "dangerous" to the 20cm wing at 0 spans as it is at 180 spans.

Figure 6.3c shows the average correlation coefficient, $c.c._{avg}$, and the standard deviation of the correlation coefficient, $c.c._{std}$, for each processed data field from aLPT. This plot can be taken as a "goodness" measure of the PIV data during the run time. Note that for this run, the value of $c.c._{avg}$ remains slightly greater than 0.7. Additionally, $c.c._{std}$ is approximately equal to 0.1 over the entire run. For correlation values equal to 1, there is perfect correlation between the sequential particle images. This would occur when there is no fluid motion in the camera's field of view. When the correlation value equals 0, there is no correlation between the sequential images. The correlation value would equal 0 if the vortex wake is so three-dimensional that all of the particles in the first image leave the light sheet and are replaced with new ones by the time the second image is captured. In the
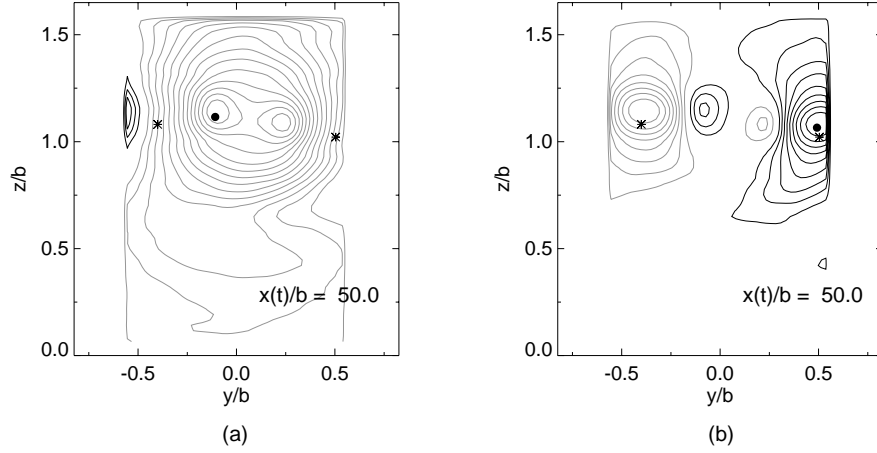
Figure 6.2: Contours of (a) downwash and (b) rolling moment in the wake of the rectangular airfoil (Run 13, $U_o = 500$ cm/s, $\alpha = 3.0^o$) at $x(t)/b = 50$. The *'s denote the location of the left and right vorticity centroids. The black dots denote the location of the $max|R(x(t), y, z)|$ and $min(D(x(t), y, z))$.
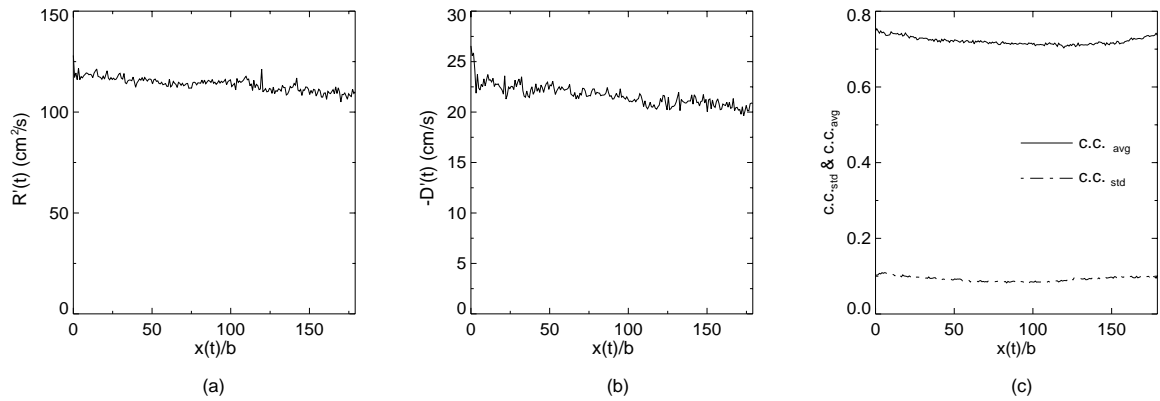
Figure 6.3: (a) Rolling moment, (b) downwash, and (c) average and standard deviation of the correlation coefficient data fields from aLPT as functions of downstream distance from the rectangular airfoil (Run 13, $U_o = 500$ cm/s, $\alpha = 3.0^o$).

following discussions, the plot in Figure 6.3c will be used as a reference to determine how "good" the PIV data is in the wakes of the triangular-flapped airfoils.

6.4 Triangular-Flapped Airfoils

Having established a baseline with the rectangular airfoil, the triangular-flapped airfoils can now be analyzed. Figure 6.4 illustrates the downwash and rolling moment for run 38 ($U_o = 500$ cm/s, $\alpha = 2.0^o$, 50%c TF, $\bar{\Gamma}_{of}/\bar{\Gamma}_{ot}$ = -0.37). The trajectories of the flap and tip vortices, as well as that of the overall centroid, are shown in Figure 6.4c to demonstrate that the wake does remain in the field of view during the measurement period. Prior to 36 spans (vertical dashed line), the rolling moment undergoes oscillations in which it has local maxima at $x(t)/b = 0$ and $x(t)/b \approx 25$ and a local minimum at $x(t)/b \approx 10$. The reason for this fluctuation is the changes in the counter-rotating pair's orientation. At $x(t)/b = 0$ and $x(t)/b \approx 25$, the flap and tip vortices are horizontally aligned and, therefore, impart a larger rolling moment on the following wing. At $x(t)/b \approx 10$, the vortices are vertically aligned and the corresponding rolling moment is less. At 36 spans, the vortex cores undergo a sudden change in structure, as the instability becomes non-linear. After this location, the rolling moment decreases substantially and continues to decay over the rest of the run. By 243 spans, the rolling moment has decreased by approximately 80% from its initial value.

The downwash for Run 38 is shown in Figure 6.4b. Like the trends of the rolling moment, the downwash decays considerably over the run as the wake becomes increasingly three-dimensional and incoherent. The average and standard deviation of the correlation coefficient from aLPT is shown in Figure 6.4d. Note that although $c.c._{avg}$ decreases somewhat over the course of the run, it remains at values comparable to those of the rectangular airfoil's wake. Likewise, $c.c._{std}$ has values that are about equal to those of the rectangular airfoil in run 13. This demonstrates that the time between the sequential particle images is small enough to reduce the amount of particles leaving the light sheet. Consequently, aLPT can measure the two-dimensional velocity and velocity gradient fields despite the fact that the wake becomes highly three-dimensional.
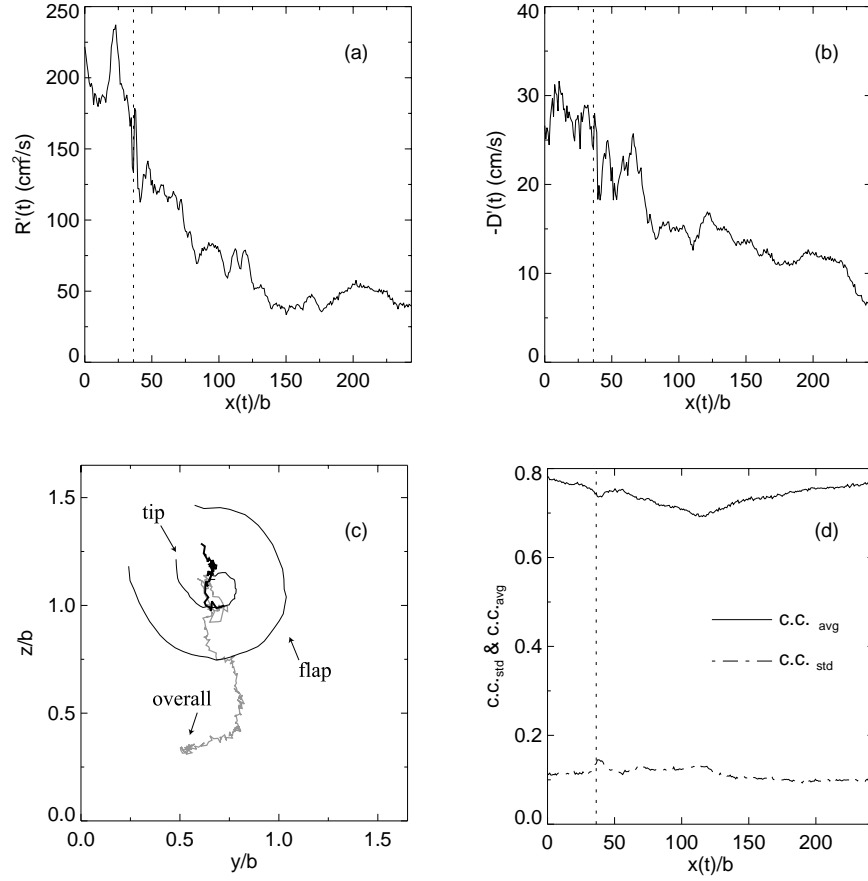
Figure 6.4: (a) Maximum rolling moment, R'(t), and (b) minimum downwash, D'(t), for Run 38 ($U_o = 500$ cm/s, $\alpha = 2.0^o$, 50%c TF, $\bar{\Gamma}_{of}/\bar{\Gamma}_{ot} = -0.37$). (c) Flap, tip, and overall vorticity centroids and (d) average and standard deviation of the correlation coefficient data fields from aLPT for Run 38.
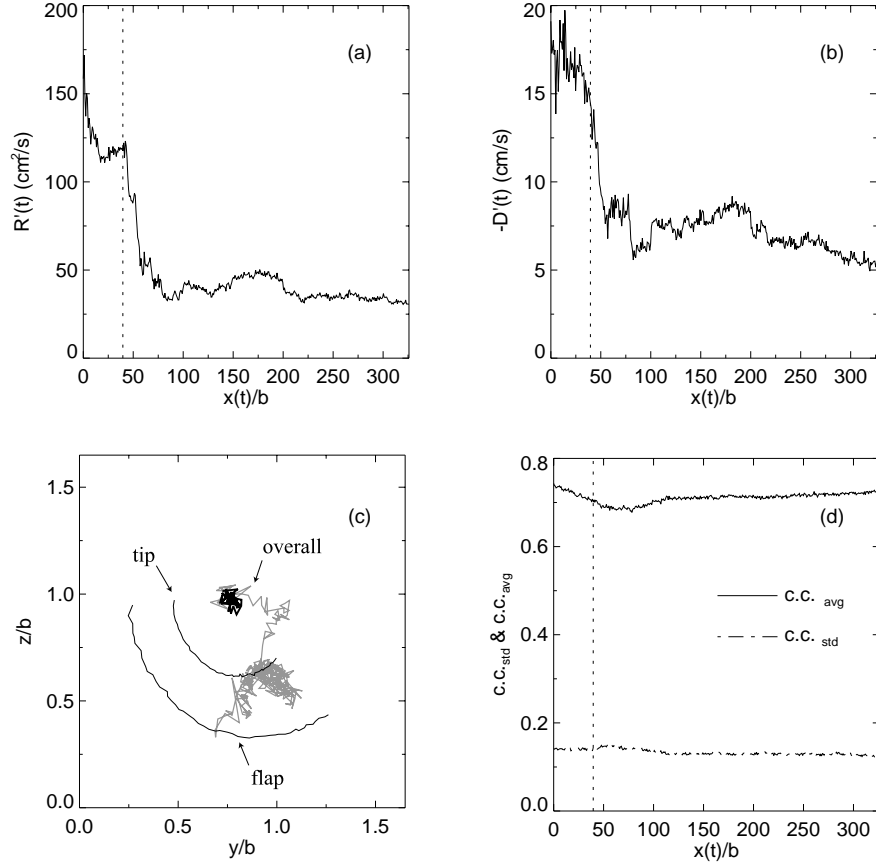
Figure 6.5: (a) Maximum rolling moment, R'(t), and (b) minimum downwash, D'(t), for Run 47 ($U_o = 500$ cm/s, $\alpha = -1.0^o$, 50%c TF, $\bar{\Gamma}_{of}/\bar{\Gamma}_{ot}$ = -0.56). (c) Flap, tip, and overall vorticity centroids and (d) average and standard deviation of the correlation coefficient data fields from aLPT for Run 47.

For larger values of $|\bar{\Gamma}_{of}/\bar{\Gamma}_{ot}|$, the trends in the downwash and rolling moment are somewhat different. In a manner similar to that of the two-dimensional kinetic energy (Section 5.9.4), the downwash and rolling moment typically do not continue to decrease after their initial drop. Figure 6.5 illustrates this for Run 47 ($U_o = 500$ cm/s, $\alpha = -1.0^o$, 50%c TF, $\bar{\Gamma}_{of}/\bar{\Gamma}_{ot}$ = -0.56). At 40 spans, the structure of the vortex cores suddenly changes and the rolling moment decreases. Over the rest of the run, both the downwash and rolling moment demonstrate little decay. Additionally, $c.c._{avg}$ and $c.c._{std}$ have values that are near those of the rectangular airfoil over the entirety of the run.

From the data in Runs 38 and 47, it can be seen that the downwash and rolling moment of the triangular-flapped airfoils behave in a manner quite unlike that of the rectangular airfoil. Although the dimensional values of R' and D' become less than those of the rectangular airfoil, a more accurate comparison should be made by non-dimensionalizing by the airfoils' lift, which is proportional to the circulation, Γ_o, and the initial separation distance, b_o^*, between the left and right vorticity centroids. To make a proper comparison, the lift of the rectangular and triangular-flapped airfoils is equated to the lift generated by simple horseshoe vortex, which has tip vortices separated by a distance, $b = 40$ cm. The expression that demonstrates this is $\Gamma_o b_o^* = \Gamma_h b$, where Γ_h is the circulation about the horseshoe vortex. For the rectangular airfoil in Run 13, $\Gamma_h = \Gamma_o b_o^*/b = ($ 821 cm^2/s 36.1 cm)/40 cm $= 741$ cm^2/s. On the other hand, $\Gamma_h = \Gamma_o b_o^*/b = ($ 1009 cm^2/s 48.5 cm)/40 cm $= 1223$ cm^2/s for Run 38 and $\Gamma_h = \Gamma_o b_o^*/b = (549$ cm^2/s 58.0 cm)/40 cm $= 796$ cm^2/s for Run 47. Figure 6.6 demonstrates plots of the dimensionless rolling moment, R'/Γ_h, and downwash, $D'/(\Gamma_h/b_f)$ for Runs 13, 38, and 47. Initially, the rolling moments of the 50%c TF airfoil are greater than that of the rectangular airfoil. As soon as the instability becomes evident in the measurement plane, the rolling moments of the triangular-flapped airfoil rapidly drop below the value for the rectangular airfoil. Because the wakes in Runs 13 and 38 descend out of view during the measurement period, their rolling moments are only plotted up to 180 and 243 spans, respectively, downstream of the airfoils.

The downwash of the triangular-flapped airfoil is less than that of the rectangular airfoil at $x(t)/b = 0$. When the non-linear effects of the instability propagate through the
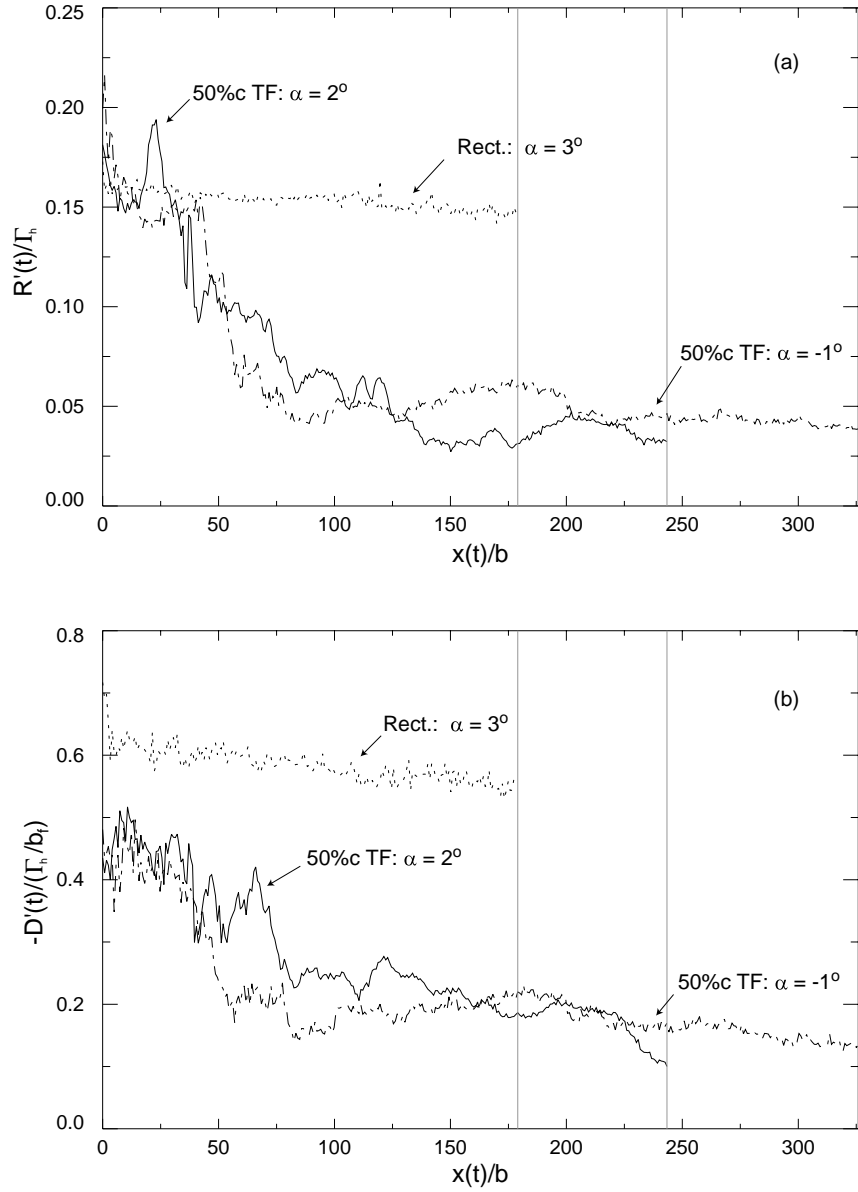
Figure 6.6: Dimensionless (a) maximum rolling moment, $R'(t)/\Gamma_h$, and (b) minimum downwash, $D'(t)/(\Gamma_h/b_f)$, as functions of downstream location for the rectangular airfoil (Run13) and the 50%c TF airfoil at 2.0^o (Run 38) and -1.0^o (Run 47).

measurement plane, the downwash begins to decrease. By 150 spans, the downwash of the triangular-flapped airfoil is approximately $\frac{1}{3}$ of the value for the rectangular airfoil.

To summarize the rolling moment and downwash data for all of the experimental runs, Figure 6.7 provides a comparison of $R'(t)/\Gamma_h$ and $D'(t)/(\Gamma_h/b_f)$ for the 50%c TF, 75%c TF, and rectangular airfoils at three downstream locations ($x(t)/b = 0$, 75, and 150). From Figure 6.7a-b, it can be seen that the rolling moment and downwash of the rectangular airfoil typically exhibit little decay during the measurement period. The rolling moment and downwash of the 50%c TF and 75%c TF airfoils are plotted in Figures 6.7c-f. The horizontal dashed lines in these figures represent the average values of $R'(t)/\Gamma_h$ and $D'(t)/(\Gamma_h/b_f)$ for the rectangular airfoil at $x(t)/b = 75$. It is evident that the rolling moment and downwash of the triangular-flapped airfoils decrease noticeably during the first 150 spans. Furthermore, by 75 spans, *the rolling moment and downwash of the triangular-flapped airfoils are always less than those of the rectangular airfoil.* For the 50%c TF airfoil, the greatest reduction in the rolling moment at $x(t)/b = 75$ occurs for Run 44 ($\bar{\Gamma}_{of}/\bar{\Gamma}_{ot} = -0.49$), in which $R'(t)/\Gamma_h$ is 62% less than the average value for the rectangular airfoil at the same downstream location. Also, the 50%c TF has the greatest reduction in the downwash in Run 42 ($\bar{\Gamma}_{of}/\bar{\Gamma}_{ot} = -0.49$), in which $D'(t)/(\Gamma_h/b_f)$ is 67% less than the average value for the rectangular airfoil at the same downstream location. For the 75%c TF airfoil at $x(t)/b = 75$, the reductions are somewhat similar: a 65% reduction in the rolling moment for Run 61 ($\bar{\Gamma}_{of}/\bar{\Gamma}_{ot} = -0.58$) and a 72% reduction in the downwash for Run 65 ($\bar{\Gamma}_{of}/\bar{\Gamma}_{ot} = -0.62$).

From the data in Figure 6.7, an important conclusion can be made: *the 50%c and 75%c triangular-flapped airfoils generate a wake that is significantly "safer" than that of the rectangular airfoil by 75 spans. Thus, the instability that arises in the wakes of the triangular-flapped airfoils demonstrates properties that make it a potential solution to the wake hazard problem.*
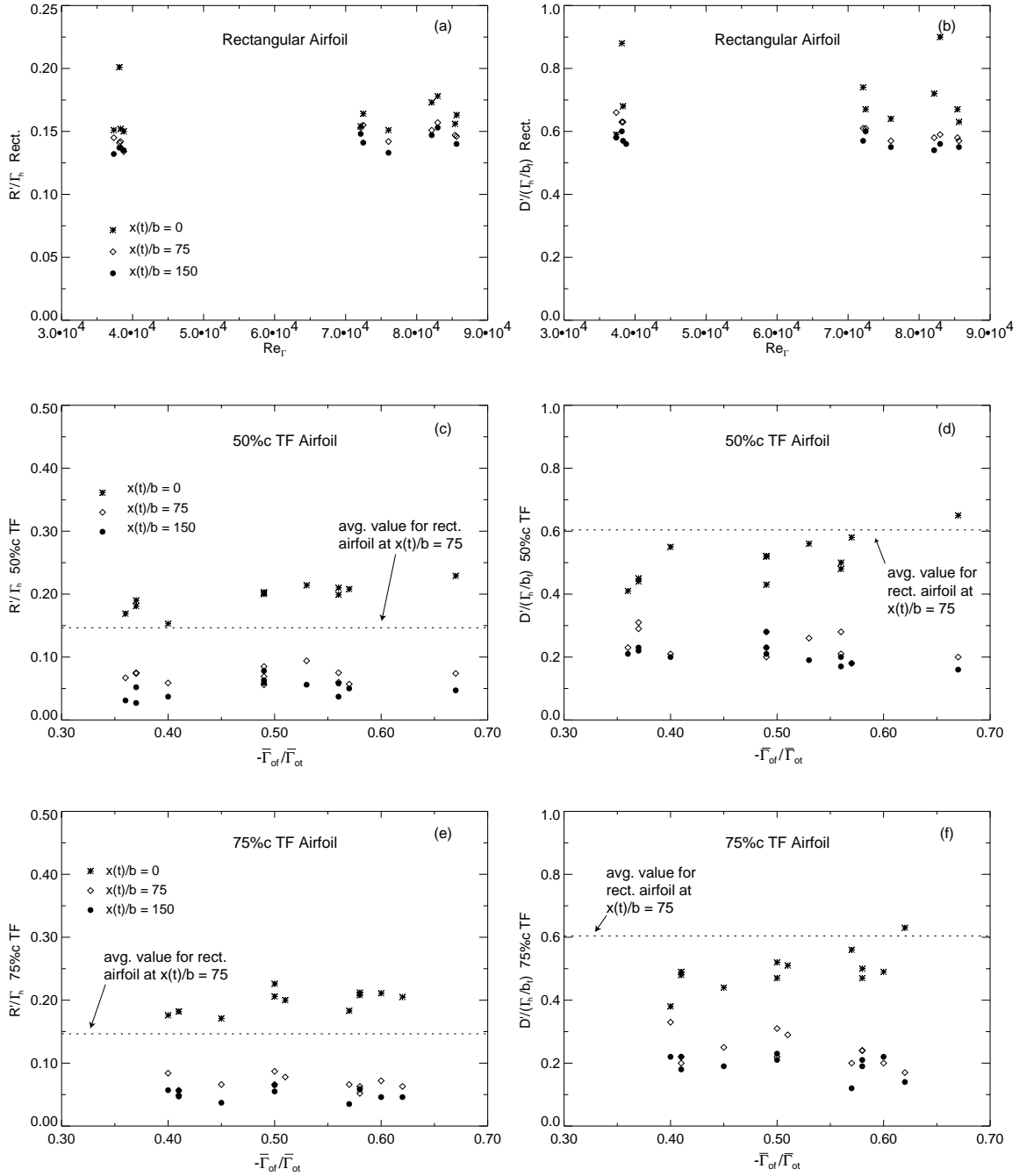
Figure 6.7: Dimensionless maximum rolling moment and minimum downwash for the rectanguar (a,b), 50%c TF (c,d), and 75%c TF (e,f) airfoils at $x(t)/b = 0$, 75, and 150.

6.5 Design Challenges

As with many of the proposed concepts for reducing the wake hazard, the triangular-flapped, airfoil design comes with its own set of challenges and disadvantages. The first is that of drag. By generating oppositely-signed control vortices, the induced drag on the airfoil will more than likely increase, making it less efficient. However, the triangular flaps would probably be extended only during take-off and landing, when following aircraft are relatively close. During landing, the additional drag would not be a problem, since the plane is decelerating anyway. But during take-off, the added drag would decrease the airplane's velocity and it may be necessary for the airplane to have more powerful engines.

The second disadvantage of this concept is that of structural modifications. In its present form, this wake alleviation concept operates by increasing the airfoil's outboard loading, which generates a larger bending moment in the wing. If this design were incorporated into an existing airplane, the increased bending moment would have to be compensated by strengthening the wing, resulting in an increase in its weight. Because the added weight will reduce the amount of cargo or passengers that can be carried, airline companies would not look favorably upon the utilization of this design. For the above two reasons, the use of outboard flaps would best be employed on a new aircraft design and not an existing one. Perhaps, a means of circumventing this shortcoming is to use other designs, such as vertically oriented flaps or the horizontal stabilizer, to generate oppositely-signed control vortices.

6.6 Design Advantages

Despite the challenges of this wake alleviation concept, it does possess several advantages. The first is that it is completely passive. Requiring no oscillating flaps or pulsed jets, the triangular-flapped, airfoil design functions by simply placing oppositely-signed vortices inboard of the tip vortices and using their energy to disrupt the coherence of the wake. If this design were employed in future airliners, there would be no concerns of degraded passenger comfort as there might be in a design that periodically varies the lift distribution

or vortex core sizes. Additionally, because the flaps do not oscillate, there would be fewer concerns about maintaining them against structural fatigue and wear.

The second advantage of this concept is that the instability between the flap and tip vortices evolves very rapidly when compared to the Crow instability, the mechanism that typically brings about the demise of the vortex wake. Following Crow's [17] analytical study of the long-wave instability for a counter-rotating vortex pair, numerous wake-alleviation concepts were tested in an effort to hasten this instability [2, 10, 21]. The hypothesis was that if this instability could be externally forced to grow, the linking of oppositely-signed tip vortices would form Crow rings, hence, changing the two-dimensional nature of the wake into a three-dimensional one. The resulting incoherent wake would pose less of a threat to following aircraft. However, one drawback of the Crow instability is its slow growth rate. Typically, it requires a few hundred spans to develop, making it a less attractive candidate for rapid wake attenuation. The primary reason for this slow growth rate is that the large spacing between the tip vortices reduces the rate of strain that they induce on each other. Because the rate of strain field is the driving mechanism of the instability's growth, it takes that much longer for the perturbations to become finite in size. On the other hand, by reducing the distance between oppositely-signed vortices, as is accomplished with the triangular-flapped airfoil, the instability can grow more rapidly. The flow visualization data in the wakes of the triangular-flapped airfoils demonstrate that the instability grows to a finite size typically within 15 spans downstream of the airfoil. By 150 spans, at which time the rectangular airfoil's wake is still descending peacefully, the two-dimensional nature of the triangular-flapped airfoil's wake has been completely transformed into a three-dimensional one.

The third advantage of this wake alleviation concept is that, although it is passive, its design does allow for the control of the non-linear evolution of the wake. By varying the relative circulation strength of the flap vortices from only -0.4 to -0.7, it has been shown that the behavior of the vortex wake can be widely altered. For smaller values of $|\bar{\Gamma}_{of}/\bar{\Gamma}_{ot}|$, there is a large exchange of vorticity across the airfoil centerline in the form of vortex rings. For larger values of $|\bar{\Gamma}_{of}/\bar{\Gamma}_{ot}|$, the vortices are confined to each side of the wake and

the instability leads to an upwards ejection of vorticity. Therefore, depending on the type of behavior desired in the vortex wake, the strength of the flap vortices can be adjusted accordingly.

Chapter 7

Conclusion

Through this study of the triangular-flapped airfoils' wakes, the theoretical stability characteristics of counter-rotating vortex pairs have been compared with experimental observations. The theoretical analyses discussed herein have demonstrated that the underlying physics for the instability of counter-rotating vortex pairs are the interactions of the rate of strain field on the vortices' self-induced rotation rates. The rate of strain field leads to the growth of an instability, while the self-induced rotation rate and the rotation rate of the pair stabilize perturbation growth. The linear stability analyses for a single, counter-rotating vortex pair and two, counter-rotating vortex pairs reveal that the most unstable wavelength for the unequal strength, counter-rotating pairs is shorter than that of classical Crow instability for an equal strength pair. The flow visualization measurements made in the wakes of the triangular-flapped airfoils qualitatively demonstrate the behavior of the counter-rotating pairs. The observed instability wavelengths agree favorably with those predicted by the linear stability calculations for equivalent two- and four-vortex systems. Furthermore, the flow visualization data illustrate how the non-linear, three-dimensional evolution of the vortex pairs varies as the relative strengths of the vortices are changed. For smaller values of $|\bar{\Gamma}_f/\bar{\Gamma}_t|$, there is a large exchange of vorticity across the airfoil centerline. However, for larger values of $|\bar{\Gamma}_f/\bar{\Gamma}_t|$, the non-linear vortex interactions remain confined on either side of the wake. The PIV measurements provide a quantitative assessment of the triangular-flapped airfoils' wakes. With the PIV data, it is shown that the two-dimensional

kinetic energy rapidly drops as the instability becomes non-linear and transforms the two-dimensional nature of the wake into a three-dimensional one. Due to the finite area of the two-dimensional PIV measurements, the total circulation of the counter-rotating pairs is often observed to vary in time as patches of vorticity enter and exit the measurement plane.

As mentioned in the Introduction, the original purpose in designing these triangular-flapped airfoils was to alleviate the wake vortex hazard. By introducing oppositely-signed control vortices near the tip vortices, two counter-rotating vortex pairs would be generated, where they could interact strongly from the moment they formed. It was thought that these interactions might lead to a sudden disruption in the wake's coherence. With the PIV measurements, it has been shown that the wakes of the triangular-flapped airfoils have an induced rolling moment and downwash that are always less than those of the rectangular airfoil by 75 spans. The results of this comparison lead to the conclusion that the triangular-flapped airfoil design has the potential for alleviating the wake vortex hazard.

Because of its ability to generate a "safer" wake, the concept of placing oppositely-signed, control vortices inboard of the tip vortices warrants further investigative research. In no way have the theoretical analyses and experimental measurements discussed in this work covered all possible research directions. Perhaps, future experiments could determine the minimum strength of the control vortices needed to disrupt the tip vortices and bring about destructive changes to the vortex wake. Other tests could be made by towing airfoils in the wakes of the triangular-flapped airfoils and measuring the induced rolling moment and downwash at different downstream locations with various flap and tip circulation strengths. To assess the drag penalty incurred by generating the additional pair of control vortices, wind tunnel experiments could be conducted with different triangular flap extensions. Finally, a better understanding of the non-linear vortex interactions may be accomplished by simulating the counter-rotating pairs with CFD analyses.

Appendix A

AIAA Journal Article

The following article was submitted to the *AIAA Journal* in November, 1999.

A Rapidly Growing Instability Mode in

Trailing Multiple-Vortex Wakes

Jason M. Ortega[*] and Ömer Savas[†]

University of California at Berkeley

I. Introduction

Following Crow's[1] analytical study of the long-wave instability for a counter-rotating vortex pair, numerous wake-alleviation concepts have been tested in an effort to hasten this instability mechanism.[2-5] The hypothesis was that if this instability could be externally forced to grow, the linking of oppositely signed tip vortices would form Crow rings, hence, changing the two-dimensional nature of the wake into a three-dimensional one. The resulting incoherent wake would have an accelerated destruction, causing it to pose less of a threat to following aircraft. However, one drawback of the Crow instability is its slow growth rate. Typically, it requires a few hundred wingspans to develop, making it a less attractive candidate for rapid wake attenuation. The primary reason for this slow growth rate is that the equal-strength, oppositely signed vortices are too widely spaced for this cooperative instability to rapidly occur. In order to circumvent this impediment and increase the growth rate, it is necessary to redesign the trailing vortex wake.

[*] Graduate Student, Department of Mechanical Engineering, University of California, Berkeley, CA 94720-1740. Student Member AIAA.
[†] Professor, Department of Mechanical Engineering, University of California, Berkeley, CA 94720-1740. Associate Fellow AIAA.

One means of accomplishing this is to construct a vortex wake that contains multiple vortex pairs, each of which has vortices that are located close to one another. This allows the vortices to develop cooperative instabilities and interact strongly in a time-scale much shorter than that for a single, widely spaced pair.[6] Recent towing tank experiments[7,8] have demonstrated this in the merger process of like-signed vortex pairs. By merely reducing the spacing between the flap and tip vortices from one-third of a span to one-sixth of a span, the vortices could interact more strongly with each other and quickly develop instabilities, decreasing the downstream distance to merger from 70 to only 10 spans. Another means is to generate oppositely signed vortices that have unequal strengths, resulting in a vortex wake that can decay by means other than the Crow instability. Leonard[9,10] presents numerical results from a vortex filament code in which unequal strength, oppositely signed flap vortices develop a sinusoidal instability that requires only 10 spans to grow to a finite size. Recently, Quackenbush et al.[11-13] have numerically explored a concept called "vortex leveraging" for alleviating the sailplane wake of a submarine. By periodically introducing control vortices by means of shape memory alloys (SMA), the flap vortices from the sailplane are spatially perturbed, causing them to interact with the oppositely signed tip vortices at downstream distances of 20 to 30 spans. Experimental verification, however, does not seem to be available at the present time.

In order to the test the two concepts discussed above, a series of flow visualization experiments were conducted. This paper presents the results of these tests

and describes a class of instabilities that is seen both within an unequal strength, counter-rotating vortex pair and between the vortex pairs on either side of a wing. We observe that a trailing vortex wake that has undergone this instability exhibits the formation of three-dimensional structures much sooner than the wake following the growth of the classical Crow instability.

II. Experimental Setup

Two wings (Figure 1) are employed for these experiments: a rectangular wing (a) that serves as the control wing, providing a reference against which the other wing is compared; and a wing that has triangular tip flaps (b). The wings are made of curved sheet metal of thickness 2.5 mm and both have a span, b, of 40cm, chord, c, of 6.7cm, and camber radius, R, of 17cm. The triangular flap extensions have widths of $d = 0.25b$. The leading and trailing edges are tapered and rounded to minimize flow separation. The experiments are performed at the U.C. Berkeley Richmond Field Station towing tank facility. The tank measures 2.4m wide by 70m long and has a nominal water depth of 1.5m. For this particular series of tests, an aluminum carriage is towed behind a motorized one, allowing a better top-view of the vortices from the instant they formed. The wings are attached to the aluminum carriage by a streamlined, stainless steel strut, which places them approximately 0.5m beneath the water surface. Recent PIV measurements[7] demonstrated that strut had minimal influence on the formation and ensuing dynamics of the wake vortices.

Flow visualization is performed by applying a mixture of fluorescent sodium salt (Sigma Chemical Company, No. F-6377) and corn syrup to the upper surface of the wings at the flaps and wing tips in 2.5cm wide strips (Figure 1). To increase the amount of time that this dye mixture lasts in the water, it is simmered over a heat source so that the majority of the water content is removed, giving it the consistency of hardened caramel. The dye is washed into the boundary layer on the top surface of the wing. The dyed fluid meets the fluid from the lower surface boundary layer to form the three-dimensional vortex sheet in the wake of the wing. Since the molecular diffusivity of water is much smaller than its momentum diffusivity, the dye remains as a partial marker of the vortex sheet, which rapidly rolls up into vortices. The dye is not a complete marker of the sheet, since the wing is partially painted with it. Hence, we argue that in the rolled up wake, all the dye marks vorticity, but not all vorticity is marked by the dye. At larger downstream distances, only coherent structures that correlate well with themselves both spatially and temporally are discussed. Therefore, if a large dispersal of dye is observed in the wake, no attempt is made to relate this to a large dispersal of vorticity.

The test section, located about half way down the length of the tank, is illuminated by passing a 10W CW laser beam through a spherical lens. The light cone thus generated allows for volumetric visualization of the flow field. A VHS camera is positioned about a meter upstream of the test section and views the wings and trailing vortices through the water surface. The surface waves generated by the strut cause some image distortion, but this does not have any significant effects on the flow observations.

Additional flow visualization images are obtained by viewing the trailing vortices through the side windows of the test section.

For each run, the wing is towed at a velocity, U, of 1.6 m/s ($Re_c = Uc/\nu = 107{,}000$, where ν is the kinematic viscosity of water) and at an angle of attack, α, of 2.0 degrees. Due to the different planform areas of the wings, the circulation strengths of the resulting wakes vary somewhat between the wings, though their values are of the same order of magnitude. Because the purpose of this study is to investigate the qualitative features of the wakes, these slight differences should not present a problem. The carriage begins its motion 20m upstream of the test section and continues until it reaches the end of the tank. Typically, 20 minutes are allowed to pass between runs, allowing the water in the tank to become quiescent. A total of seven flow visualization tests are performed: two with the rectangular wing having no flaps and five with the wing having triangular flaps.

III. Observations

Sequences of flow visualization images from video tape recordings are shown in Figure 2 for both wings. The columns correspond to images from the rectangular wing and the triangular-flapped wing. The rows correspond to the different downstream distances, z/b, from the wings. The frames labeled $z/b = 0$ show the wings just as they pass through the center of the test section. The streamwise ripples visible at $z/b = 0$ are the optical distortions due to the surface waves generated by the strut.

The first column in Figure 2 shows the counter-rotating vortex pair in the wake of the rectangular wing. This sequence of images is taken as the basis for comparison with the outboard-flapped wing experiments discussed below. Consistent with earlier studies in this facility[7,8] using the rectangular wing, the vortices shed from it indicate no signs of a long-wave instability during the observations. The vortices simply descend quietly until they proceed below the illuminated portion of the test section ($z/b = 150$, not shown). Observations of the rectangular wing's wake at much later times do show initial signs of the long-wave Crow instability. However, by this time, the wing has stopped and the vortex pair is nearing the tank floor. The behavior of the pair, therefore, is not investigated further.

The vortex wake of the wing with triangular flaps is shown in the second column of Figure 2. The tip vortices have the same senses of rotation as those for the rectangular wing, while each of the flap vortices have a sense of rotation that is opposite to that of the nearby tip vortices. Thus, two counter-rotating vortex pairs are generated. An estimate of the vortex strength ratios can be made by observing the paths of the vortices in a pair. The vortex pair rotates around its vorticity centroid in the reference frame of the descending wake. The initial separation of the pair and the location of their common centroid uniquely determine the ratio of their strengths. Because the mid-portion of the wing produces lift, the flap and tip vortices are of unequal strength, resulting in a circulation ratio $|\Gamma_{flap}/\Gamma_{tip}| < 1$, where $\Gamma_{flap,tip}$ are the vortex circulations.

quickly becomes the central event in the wake (Figure 3b-e). As the instability

progresses, the peaks on the flap vortices become tightly wrapped around the tip vortices,

forming "Ω"-shaped hoops (Figure 3d). The shape of the vortex pair just prior to the

formation of these hoops is similar to that in Figure 13 of Klein, et al.[14] The spiral "feet"

of these hoops advect themselves towards one other, causing the hoops to form closed

vortex rings (Figure 3e). These rings are then hurled towards the opposite side of the

wake. It is clear that this long-wave instability is a member of a more general class of

modes for arbitrary strength vortices. When the vortices are of the same sign, the vortex

pair is linearly stable to long wavelength perturbations.[15] However, when the vortices are

of opposite sign, the instability grows rapidly, as is evident in these flow visualization

images.

V. Growth Rate of the Instability Mode

We estimate the growth rate of the instability shown in Figure 2, in order to

compare it with the growth rates of other instabilities that exist between a single pair and

multiple pairs of trailing vortices. Using the image of the wing at $z/b = 0$ as a reference

length, the amplitude of the instability at $z/b = 23$, at which time the flap vortex has

orbited about π radians about the tip, is found to be approximately 6cm. The amplitudes

of the initial disturbances on the trailing vortices are taken to be on the order of the

boundary layer thickness at the trailing edge of the flap. As a conservative estimate, if

we approximate the flow over the wing by that of a turbulent boundary layer over a flat

plate, the boundary layer thickness is $0.37 \cdot x \cdot (Ux/v)^{-1/5} = 0.35$cm, where $x=1.58c=10.6$

cm (Schlichting).[16] With this information, the growth rate, α, of the instability can be

found from the expression, $y = y_o e^{\alpha t}$, where $y = 6$ cm is the perturbation amplitude at 23 spans, y_o the initial amplitude, and $t = (23$ spans$)$ x $(40$ cm/span$)$ / $(160$ cm/s$)$. Solving this expression for α yields a growth rate of 0.5 s^{-1}.

In order to compare the growth rate of this instability with that of the Crow[1] instability, it is necessary to calculate the characteristic time scale, $\tau_d = 2\pi d^2/\Gamma_{tip}$, of a single vortex pair. By performing this exercise, as done in Bristol[17], it is possible to determine if the instability on the flap vortex is driven by the rate of strain field, $\Gamma_{tip}/2\pi d^2$, of the neighboring tip vortex. To estimate Γ_{tip}, the root circulation about the wing is first estimated as $\Gamma_o = 250$cm^2/s from preliminary PIV measurements in the wake of the wing with triangular flaps. Next, we utilize the equation for the distance, $\underline{x}$, between the flap vortex and the vorticity centroid of the vortex pair. This can be found from the expression, $\underline{x} = \frac{1}{2}(\beta - b) + d = d \Gamma_{tip}/\Gamma_o$, where β is the distance between the vorticity centroids on either half of the wing. Computing the average distance between the tip vortices from $z/b = 0$ to 23 demonstrates that β is about equal to 45cm. Substituting the values of β, Γ_o, and d into the expression for $\underline{x}$ shows that $\Gamma_{tip} = 313$cm/s^2, giving a characteristic time scale of 2.0s and a dimensionless growth rate of $\gamma_d = 2.0$s$\cdot 0.5$s$^{-1} = 1.0$. When scaled in this manner, the estimated growth rate of this instability is on the order of that predicted by Crow[1] for two equal strength, oppositely signed vortices. The fact that the growth rate is of O(1) suggests that the straining field from the nearby tip vortex is responsible for the observed instability.

From an aircraft design point of view, the dimensionless growth rate can also be compared to that of a wing with multiple vortices. For this purpose, we define another characteristic time scale as that in Crouch,[6] which is $\tau_\beta = 2\pi\beta^2/\Gamma_o = 51s$. With this scaling, the dimensionless growth rate of the counter-rotating pair is $\gamma_\beta = 51s \cdot 0.5s^{-1} = 25$. The instability growth rate of a wake with multiple co-rotating pairs is taken to be 1.5,[6] the value for the A_2 mode (see Figure 2a of Crouch[6]) with $\delta = 0.3$ and $\Gamma_{flap}/\Gamma_{tip} = 0.5$). These values of δ and $\Gamma_{flap}/\Gamma_{tip}$ give a ratio of $d/b = 0.25$, allowing a rough comparison to be made with the triangular-flapped wing used in this study. It is interesting to note that the growth rate of the instability in Figure 2 is about 17 times greater than that of the A_2 mode in Crouch.[6] The growth rate data are summarized in Table 1.

Γ_f/Γ_t	γ_d	γ_β	*Source*
0	0.8		Crow[1]
+0.5		1.5	Crouch[6]
- 0.2	1	25	present experiments

Table 1. Instability growth rates.

VI. Closing Remarks

A rapidly growing instability mode is shown to exist between unequal, oppositely signed vortices in the wakes of wings. Having a wavelength of about one wingspan, this instability develops on the weaker flap vortices at approximately 20 spans downstream of the wing. All that is necessary to excite this instability is to place two unequal, oppositely

signed vortices close to one another where they can interact strongly. The rapid growth of the instability and the exchange of vorticity across the wing centerline suggest that this instability might be utilized as a means of controlling the vortex wake and, perhaps, reducing the wake hazard. PIV measurements are being conducted to provide a more quantitative assessment of the wakes of these wings.

References

[1]Crow, S.C., "Stability Theory for a Pair of Trailing Vortices", *AIAA Journal*, Vol. 8, No. 12, 1970, pp. 2172-2179.

[2]Chevalier, H., "Flight Test Studies of the Formation and Dissipation of Trailing Vortices," *Journal of Aircraft*, Vol. 10, No. 1, 1973, pp. 14-18.

[3]Dunham, R.E., Jr., "Unsuccessful Concepts for Aircraft Wake Vortex Minimization," *NASA Symposium on Wake Vortex Minimization*, edited by A. Gessow, NASA SP-409, 1976, pp. 221-250.

[4]Barber, M.R., Tymczyszyn, J. J., "Wake Vortex Attenuation Tests: A Status Report," *1980 Aircraft Safety and Operating Problems*, NASA CP-2170, 1981, pp. 387-408.

[5]Rossow, V. J., "Lift-Generated Vortex Wakes of Subsonic Transport Aircraft", *Progress in Aerospace Sciences,* Vol. 35, No. 6, 1999, pp. 507-660.

[6]Crouch, J. D., " Instability and Transient Growth for Two Trailing-Vortex Pairs," *Journal of Fluid Mechanics*, Vol. 350, 1997**,** pp. 311-330.

[7]Bristol, R., Ortega, J., Savas, Ö., "A Towing Tank Study of Airfoil Wake Vortices at Re_Γ of Order 10^5," AIAA Paper 99-3419, June 1999.

[8]Chen, A. Jacob, J. Savas, O, " Dynamics of Corotating Vortex Pairs in the Wakes of Flapped Airfoils," *Journal of Fluid Mechanics*, Vol. 383, 1999**,** pp. 155-193.

[9]Leonard, A., "Numerical Simulation of Interacting, Three-Dimensional Vortex Filaments," *Proceeding of the 4th International Conference on Numerical Methods in Fluid Dynamics*, Boulder Colorado, June 24-28, 1974, pp. 245-250; also published in *Lecture Notes in Physics*, Vol. 35, Springer-Verlag, Berlin, 1975.

[10]Corsiglia, V.R., Dunham, R.E., "Aircraft Wake Vortex Minimization by Use of Flaps," *NASA Symposium on Wake Vortex Minimization*, edited by A. Gessow, NASA SP-409, 1976, pp. 305-338.

[11]Quackenbush, T.R., Bilanin, A.J., McKillip, R.M., Jr., "Vortex Wake Control Via Smart Structures Technology," (Smart Structures and Materials 1996, Industrial and

Commercial Applications of Smart Structure Technologies, 27-29, February 1996) *Proceedings of the SPIE – The International Society for Optical Engineering*, Vol. 2721, 1996, pp. 78-92.

[12]Quackenbush, T.R., Bilanin, A.J., Batcho, P.F., McKillip, R.M., Jr., Carpenter, B.F., "Implementation of Vortex Wake Control Using SMA-Actuated Devices," (Smart Structures and Materials 1997, Industrial and Commercial Applications of Smart Structure Technologies, 4-6, March 1997) *Proceedings of the SPIE – The International Society for Optical Engineering*, Vol. 3044, 1997, pp. 134-146.

[13]Quackenbush, T.R., Batcho, P.F., Bilanin, A.J., Carpenter, B.F., "Design, Fabrication, and Test Planning for an SMA-Actuated Vortex Wake Control System," (Smart Structures and Materials 1998, Industrial and Commercial Applications of Smart Structure Technologies, 3-5, March 1998) *Proceedings of the SPIE – The International Society for Optical Engineering*, Vol. 3326, 1998, pp. 259-271.

[14]Klein, R., Majda, A.J., Damodaran, K., "Simplified Equations for the Interaction of Nearly Parallel Vortex Filaments," *Journal of Fluid Mechanics*, Vol. 288, 1995**,** pp. 201-248.

[15]Jimenez, J., "Stability of a Pair of Co-Rotating Vortices," *Physics of Fluids*, Vol. 18, No. 11, 1975.

[16]Schlichting, H., " Boundary-Layer Theory," 7th ed., McGraw-Hill, New York, 1979.

[17]Bristol, R. L., *Co-rotating Wake Vortex Instabilities*, Ph. D. Thesis, University of

California, Berkeley, 2000.

Figures

1. Wings: (a) rectangular planform, and (b) triangular flaps.

2. Video sequences: (a) rectangular planform, and (b) triangular flaps. The wing is in view in the first frame (z/b=0) of each column.

3. Instability mode-detail: photographs and outlines of dye concentrations. $\Delta z/b$ indicates the relative separation of the frames in (a)-(e). *lw*-long wave instabilities.

Figure 1.

Figure 2

(a) rectangular wing   (b) with triangular flaps

Figure 3

$\Delta z/b=0$

tip vortex

(a)

$\Delta z/b=7$

tip vortex

lw

(b)

$\Delta z/b=13$

tip vortex

lw

(c)

$\Delta z/b=19$

tip vortex

"Ω" hoops

(d)

$\Delta z/b=39$

tip vortex

vortex ring

(e)
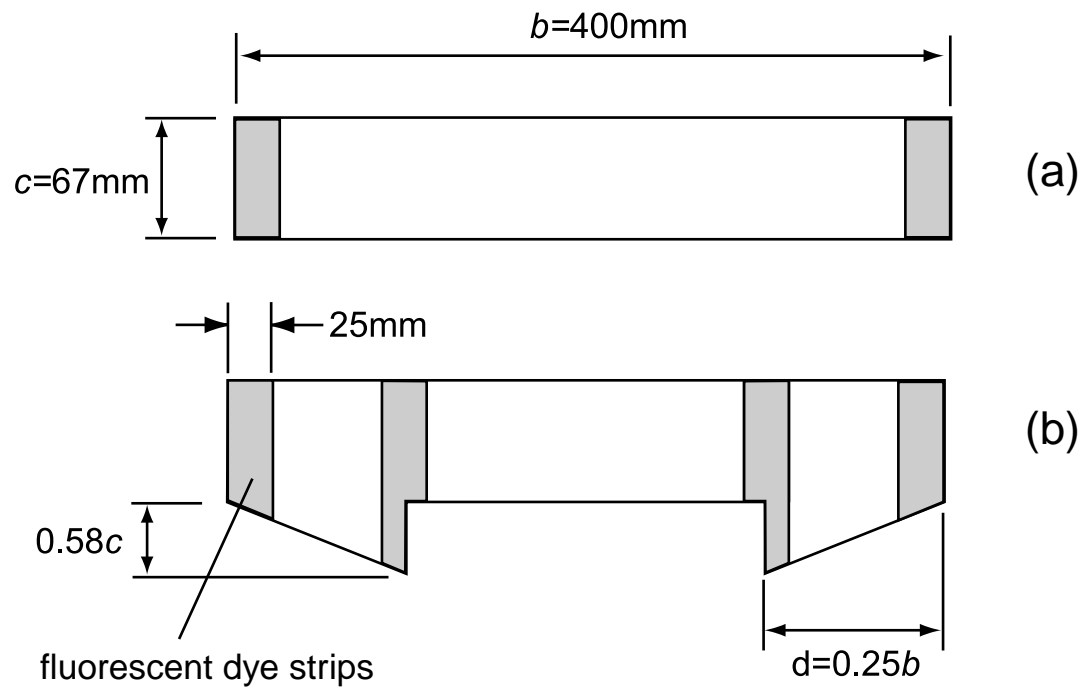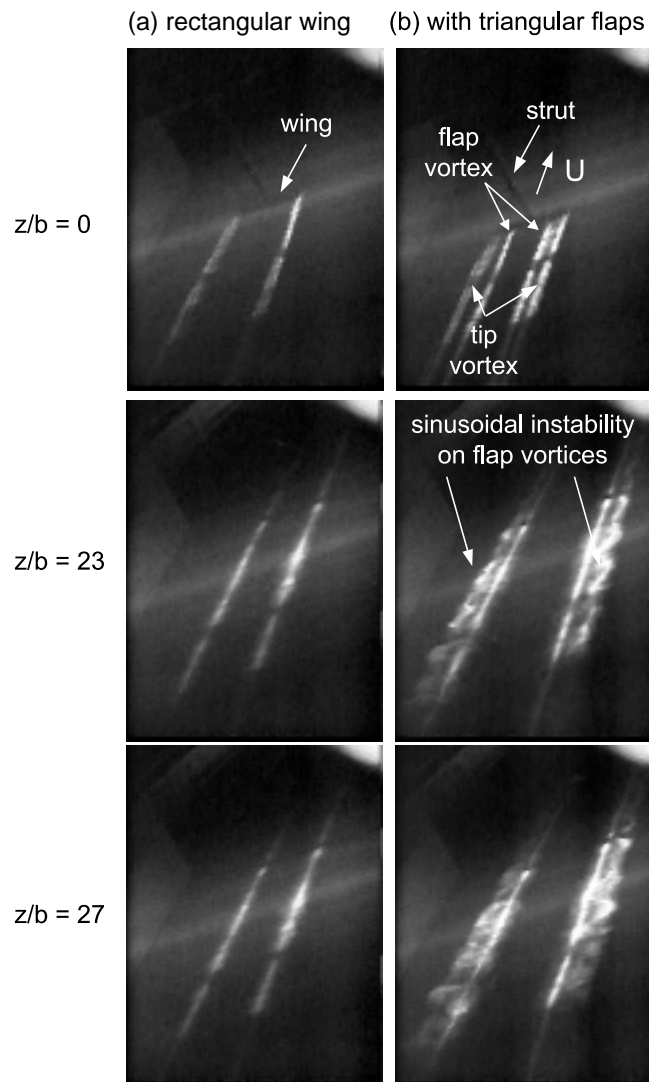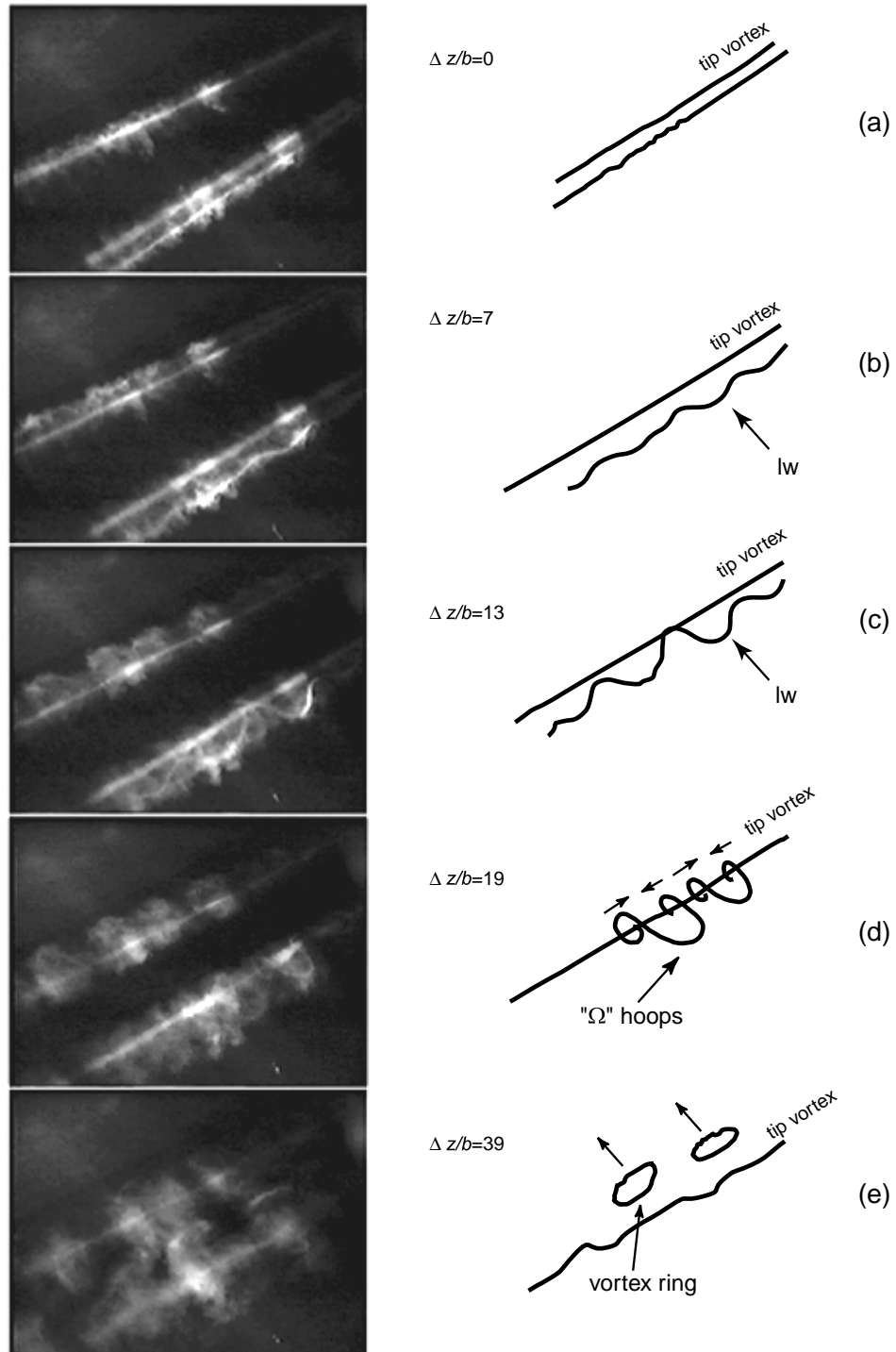
Appendix B

Processing Parameters for aLPT

The following are the parameters used in aLPT to process the particle image data:

```
lptmode, 0=singlepass, 1=small to large, 2=large to small, 3=LPT
4 2 1 1
file that contains the names of image files, prefix for outputfiles
img.txt
utns
image size nxc, nyc, pixr
1008 1018 8 1.00
flow size, nxf, nyf
1008 1018
flow offset, xf, yf
0 0
window size, nxw, nyw, 2**n
32 32
amod, min, max windows dimensions 2**n, correlaltion level corlvl
1 16 32 0.70
step size, nxs, nys
16 16
window type, wtype 1-7, see source listing
1
peak type, ptype 0=grid,1=parabolic,2=gaussian
2
laundary type, ltype 0=no laundering,1=rejection
1
extension parameter, 0= none, zero padding, 1= smooth (nth order)
2
filter widths (1/) fltrwx,fltrwy wavenlength in steps; exponent
6 6 3
wall parameters:  nwalls, parex, motion, intflag, outmask
0 0 0 0 0
wall geometry file
d:\naca0012\wall0012.raw
```

```
motion parameters:  dxcg, dycg ,rot
0.00 0.00 0.00
0.00 0.00 0.00
9.00 0.00 0.00
```

Bibliography

[1] Abramowitz, M., Stegun I. A., *Handbook of Mathematical Functions*, National Bureau of Standards, Applied Mathematics Series, **55**, 882, 1964.

[2] Barber, M.R., Tymczyszyn, J. J., "Wake Vortex Attenuation Tests: A Status Report," *1980 Aircraft Safety and Operating Problems*, NASA CP-2170, 387-408, 1981.

[3] Bilanin, A. J., Donaldson, C. D., Snedeker, R. S., "An Analytic and Experimental Investigation of the Wakes Behind Flapped and Unflapped Wings," AFFDL-TR-74-90, 1974.

[4] Bilanin, A. J., Teske, M. E., Williamson, G. G., "Vortex Interactions and Decay in Aircraft Wakes," *AIAA Journal*, **15**, 250-260, 1977.

[5] "Out of the Vortex," http://www.newscientist.com/nl/0722/vortex.html, *New Scientist*.

[6] Boyer, E. T., Meyers, F. D., Croft, F. M., Jr., Miller, M. J., Demel, J. T., *Technical Graphics*, John Wiley & Sons, Inc., 1991.

[7] Bristol, R., Ortega, J., Savaş, Ö., "A Towing Tank Study of Airfoil Wake Vortices at Re_Γ of Order 10^5," *AIAA Paper* 99-3419, June 1999.

[8] Bristol, R. L., *Co-operative Wake Vortex Instabilities*, Ph.D. Dissertation, University of California, Berkeley, 2000.

[9] Chen, A. Jacob, J. Savaş, O, "Dynamics of Corotating Vortex Pairs in the Wakes of Flapped Airfoils," *Journal of Fluid Mechanics*, **383**, 155-193, 1999.

[10] Chevalier, H., "Flight Test Studies of the Formation and Dissipation of Trailing Vortices," *Journal of Aircraft*, **10**, No. 1, 14-18, 1973.

[11] Chorin, A. J., "Hairpin Removal in Vortex Interactions," *Journal of Computational Physics*, **91**, 1-21, 1990.

[12] Chorin, A. J., "Hairpin Removal in Vortex Interactions II," *Journal of Computational Physics*, **107**, 1-9, 1993.

[13] Ciffone, D. L., Orloff, K. L., "Axial Flow Measurements in Trailing Vortices," *AIAA Journal*, **12**, No. 8, 1154-1155, 1974.

[14] Corsiglia, V.R., Dunham, R.E., "Aircraft Wake Vortex Minimization by Use of Flaps," *NASA Symposium on Wake Vortex Minimization*, edited by A. Gessow, NASA SP-409, 305-338, 1976.

[15] Croom, D. R., "Development of the use of Spoilers as Vortex Attenuators," *NASA Symposium on Wake Vortex Minimization*, edited by A. Gessow, NASA SP-409, 337-357, 1976.

[16] Crouch, J. D., "Instability and Transient Growth for Two Trailing-Vortex Pairs," *Journal of Fluid Mechanics*, **350**, 311-330, 1997.

[17] Crow, S. C., "Stability Theory for a Pair of Trailing Vortices," *AIAA Journal*, **8**, No. 12, 2172-2179, 1970.

[18] Debevec, P., *Modeling and Rendering Architecture from Photographs*, Ph.D. Thesis, University of California, Berkeley, 1996.

[19] Devenport, W. J., Vogel, C. M., Zsoldos, J. S., "Flow Structure Produced by the Interaction and Merger of a Pair of Co-Rotating Wing-Tip Vortices," *Journal of Fluid Mechanics*, **394**, 357-377, 1999.

[20] Dunham, R.E., Jr., "Unsuccessful Concepts for Aircraft Wake Vortex Minimization,"

NASA Symposium on Wake Vortex Minimization, edited by A. Gessow, NASA SP-409, 221-250, 1976.

[21] Dunham, R.E., Jr., "Exploratory Concepts Found to Be Unsuccessful for Aircraft Wake Vortex Minimization," *NASA Symposium on Wake Vortex Minimization*, edited by A. Gessow, NASA SP-409, 218-257, 1976.

[22] Hallock, J. N., Wake Vortex Bibliography. *http://www.volpe.dot.gov/wv/wv-bib.html.*

[23] Interactive Data Language (IDL), Research Systems, Inc., 1998.

[24] Jacobsen, R. A., Barber, M. R., "Flight-Test Techniques for Wake-Vortex Minimization," *NASA Symposium on Wake Vortex Minimization*, edited by A. Gessow, NASA SP-409, 191-217, 1976.

[25] Jimenez, J., "Stability of a Pair of Co-Rotating Vortices," *Physics of Fluids*, **18**, No. 11, 1580-1581, 1975.

[26] Kelvin, Lord, "Vibrations of a Columnar Vortex," *Phil. Mag*, **10**, 155-168, 1880.

[27] Klein, R., Majda, A. J., "Self-Stretching of a Perturbed Vortex Filament. I. The Asymptotic Equation for Deviations from a Straight Line," *Physica D*, **49**, 323-352, 1991.

[28] Klein, R., Majda, A. J., "Self-Stretching of Perturbed Vortex Filaments. II. Structure of Solutions," *Physica D*, **53**, 267-294, 1991.

[29] Klein, R., Majda, A. J., "An Asymptotic Theory for the NonLinear Instability of Antiparallel Pairs of Vortex Filaments," *Physics of Fluids*, **5**, No. 2, 369-379, 1993.

[30] Klein, R., Majda, A.J., Damodaran, K., "Simplified Equations for the Interaction of Nearly Parallel Vortex Filaments," *Journal of Fluid Mechanics*, **288**, 201-248, 1995.

[31] Leonard, A., "Numerical Simulation of Interacting, Three-Dimensional Vortex Filaments," *Proceeding of the 4th International Conference on Numerical Methods in*

Fluid Dynamic, Boulder Colorado, June 24-28, 245-250, 1974; also published in *Lecture Notes in Physics*, **35**, Springer-Verlag, Berlin, 1975.

[32] Marcus, P. S., "Vortex Dynamics in a Shearing Zonal Flow," *Journal of Fluid Mechanics*, **215**, 393-430, 1990.

[33] McCormick, B.W., *Aerodynamics, Aeronautics, and Flight Mechanics*, John Wiley & and Sons, 1995.

[34] Ortega, J. M., "Three-Dimensional Trailing Vortex Structure in the Near Wake of a Rectangular Airfoil," Masters Thesis, University of California, Berkeley, 1998.

[35] Ortega, J. M., Savaş, Ö, "A Rapidly Growing Instability Mode in Trailing Multiple-Vortex Wakes," submitted to *AIAA Journal*, November, 1999.

[36] Patterson, J. C., Jr., "Vortex Attenuation Obtained in the Langley Vortex Research Facility," *Journal of Aircraft*, **12**, No. 9, 745-749, 1975.

[37] Patterson, J. C., Jr., Hastings, E. C., Jr., Jordan, F. L., Jr., "Ground Development and Flight Correlation of the Vortex Attenuating Spline Device," *NASA Symposium on Wake Vortex Minimization*, edited by A. Gessow, NASA SP-409, 275-302, 1976.

[38] Patterson, J. C., Jordan, F. L., Jr., "Thrust Augmented Attenuation," *NASA Symposium on Wake Vortex Minimization*, edited by A. Gessow, NASA SP-409, 258-274, 1976.

[39] Quackenbush, T.R., Bilanin, A.J., McKillip, R.M., Jr., "Vortex Wake Control Via Smart Structures Technology," (Smart Structures and Materials 1996, Industrial and Commercial Applications of Smart Structure Technologies, 27-29, February 1996) *Proceedings of the SPIE - The International Society for Optical Engineering*, **2721**, 78-92, 1996.

[40] Quackenbush, T.R., Bilanin, A.J., Batcho, P.F., McKillip, R.M., Jr., Carpenter, B.F., "Implementation of Vortex Wake Control Using SMA-Actuated Devices," (Smart

Structures and Materials 1997, Industrial and Commercial Applications of Smart Structure Technologies, 4-6, March 1997) *Proceedings of the SPIE - The International Society for Optical Engineering*, **3044**, 134-146, 1997.

[41] Quackenbush, T.R., Batcho, P.F., Bilanin, A.J., Carpenter, B.F., "Design, Fabrication, and Test Planning for an SMA-Actuated Vortex Wake Control System," (Smart Structures and Materials 1998, Industrial and Commercial Applications of Smart Structure Technologies, 3-5, March 1998) *Proceedings of the SPIE - The International Society for Optical Engineering*, **3326**, 259-271, 1998.

[42] Quackenbush, T.R., Bilanin, A.J., Carpenter, B.F., "Test Results for an SMA-Actuated Vortex Wake Control System," (Smart Structures and Materials 1999, Industrial and Commercial Applications of Smart Structure Technologies, March 1999) *Proceedings of the SPIE - The International Society for Optical Engineering*, **3674**, 84-94, 1999.

[43] Rennich, S. C., *Accelerated Destruction of Aircraft Wake Vortices*, Ph.D. Thesis, Stanford University, 1997.

[44] Rossow, V. J., "Inviscid Modeling of Aircraft Trailing Vortices," *NASA Symposium on Wake Vortex Minimization*, edited by A. Gessow, NASA SP-409, 4-54, 1976.

[45] Rossow, V. J., "Lift-Generated Vortex Wakes of Subsonice Transport Aircraft," *Progress in Aerospace Sciences*, **35**, No. 6, 1999.

[46] Sholl, M. J., Savaş, Ö., "A Fast Lagrangian PIV Method for Study of General High-Gradient Flows," *AIAA Paper* No. 97-0493, 1998.

[47] Saffman, P. G., *Vortex Dynamics*, Cambridge Univ. Press, New York, NY, 1992.

[48] Stickle, J. W., Kelly, M. W., "Ground-Based Facilities for Evaluating Vortex Minimization Concepts," *NASA Symposium on Wake Vortex Minimization*, edited by A. Gessow, NASA SP-409, 123-154, 1976.

[49] Widnall, S. E., Bliss, D. B., Zalay, A., "Theoretical and Experimental Study of the Stability of a Vortex Pair," *Aircraft Wake Turbulence and Its Detection*, Plenum Press, 305-338, 1971.

[50] Widnall, S. E., Bliss, D. B., Tsai, C.-Y., "The Instability of Short Waves on a Vortex Ring," *Journal of Fluid Mechanics*, **66**, No. 1, 35-47, 1974.